

From Ternary Zintl Solids to Molecular Nanoarchitectures: Between Match and Mismatch of p-Block Metal Atoms in Multimetallic Zintl Clusters

Zur Erlangung des akademischen Grades einer

Doktorin der Naturwissenschaften
(Dr. rer. nat.)

von der KIT-Fakultät für Chemie und Biowissenschaften
des Karlsruher Instituts für Technologie (KIT)

genehmigte
Dissertation

von

M.Sc. Shangxin Wei

1. Referentin: Prof. Dr. Stefanie Dehnen
2. Referentin: PD Dr. Masooma Ibrahim
Tag der mündlichen Prüfung: 12.12.2024

Eidesstattliche Erklärung

Die eidesstattliche Versicherung ist in der Regel schriftlich abzugeben. Die Möglichkeit einer Aufnahme der eidesstattlichen Versicherung zur Niederschrift bleibt unberührt. Die schriftliche Erklärung hat folgenden Wortlaut:

Eidesstattliche Versicherung gemäß § 13 Absatz 2 Ziffer 3 der Promotionsordnung des Karlsruher Instituts für Technologie für die KIT-Fakultät für Chemie und Biowissenschaften:

1. Bei der eingereichten Dissertation zu dem Thema

From Ternary Zintl Solids to Molecular Nanoarchitectures: Between Match and Mismatch of p-Block Metal Atoms in Multimetallic Zintl Clusters

handelt es sich um meine eigenständig erbrachte Leistung.

2. Ich habe nur die angegebenen Quellen und Hilfsmittel benutzt und mich keiner unzulässigen Hilfe Dritter bedient. Insbesondere habe ich wörtlich oder sinngemäß aus anderen Werken übernommene Inhalte als solche kenntlich gemacht.

3. Die Arbeit oder Teile davon habe ich bislang nicht an einer Hochschule des In- oder Auslands als Bestandteil einer Prüfungs- oder Qualifikationsleistung vorgelegt.

4. Die Richtigkeit der vorstehenden Erklärungen bestätige ich.

5. Die Bedeutung der eidesstattlichen Versicherung und die strafrechtlichen Folgen einer unrichtigen oder unvollständigen eidesstattlichen Versicherung sind mir bekannt.

Ich versichere an Eides statt, dass ich nach bestem Wissen die reine Wahrheit erklärt und nichts verschwiegen habe.

Ort und Datum

Unterschrift

Eidesstattliche Versicherung

Belehrung

Die Universitäten in Baden-Württemberg verlangen eine Eidesstattliche Versicherung über die Eigenständigkeit der erbrachten wissenschaftlichen Leistungen, um sich glaubhaft zu versichern, dass der Promovend die wissenschaftlichen Leistungen eigenständig erbracht hat.

Weil der Gesetzgeber der Eidesstattlichen Versicherung eine besondere Bedeutung beimisst und sie erhebliche Folgen haben kann, hat der Gesetzgeber die Abgabe einer falschen eidesstattlichen Versicherung unter Strafe gestellt. Bei vorsätzlicher (also wissentlicher) Abgabe einer falschen Erklärung droht eine Freiheitsstrafe bis zu drei Jahren oder eine Geldstrafe.

Eine fahrlässige Abgabe (also Abgabe, obwohl Sie hätten erkennen müssen, dass die Erklärung nicht den Tatsachen entspricht) kann eine Freiheitsstrafe bis zu einem Jahr oder eine Geldstrafe nach sich ziehen.

Die entsprechenden Strafvorschriften sind § 156 StGB (falsche Versicherung an Eides Statt) und

§ 161 StGB (fahrlässiger Falscheid, fahrlässige falsche Versicherung an Eides Statt).

§ 156 StGB: Falsche Versicherung an Eides Statt

Wer vor einer zur Abnahme einer Versicherung an Eides Statt zuständigen Behörde eine solche Versicherung falsch abgibt oder unter Berufung auf eine solche Versicherung falsch aussagt, wird mit Freiheitsstrafe bis zu drei Jahren oder mit Geldstrafe bestraft.

§ 161 StGB: Fahrlässiger Falscheid, fahrlässige falsche Versicherung an Eides Statt

Absatz 1: Wenn eine der in den § 154 bis 156 bezeichneten Handlungen aus Fahrlässigkeit begangen worden ist, so tritt Freiheitsstrafe bis zu einem Jahr oder Geldstrafe ein.

Absatz 2: Strafflosigkeit tritt ein, wenn der Täter die falsche Angabe rechtzeitig berichtigt. Die Vorschriften des § 158 Absatz 2 und 3 gelten entsprechend.

Ort und Datum

Unterschrift

Versicherung gemäß § 13 Absatz 2 Satz 2 Ziffer 5 der Promotionsordnung des Karlsruher Instituts für Technologie (KIT) für die KIT-Fakultät für Chemie und Biowissenschaften

1. Einen erheblichen Verstoß gegen die Grundsätze guter wissenschaftlicher Praxis habe ich bislang nicht begangen.
2. Es gab bisher keine Promotionseignungsprüfung oder gleichwertige Prüfung an einer Universität oder dieser gleichgestellten Hochschule, an der ich erfolglos teilgenommen habe.
3. Diesem Promotionsverfahren gingen keine anderen Promotionsverfahren voran und ich bin in keinen weiteren Promotionsverfahren Kandidatin.
4. Ein entgeltliches Vertragsverhältnis, das eine gewerbliche Promotionsberatung zum Gegenstand hat und zur Unselbstständigkeit zumindest einer Promotionsleistung führen kann, besteht bzw. bestand nicht.
5. Die „Regeln zur Sicherung guter wissenschaftlicher Praxis am Karlsruher Institut für Technologie (KIT)“ habe ich beachtet.
6. In die Dissertation wurden Vorveröffentlichungen einbezogen, bei denen ich im Rahmen einer Mitautorenschaft jeweils einen signifikanten Teil selbstständig erbracht habe. Eine Aufstellung mit den Angaben:

Autoren/Autorinnen:

Titel der Vorveröffentlichung:

Veröffentlicht in:

Ausführliche Darlegung des selbstständig erbrachten, signifikanten Beitrages der Vorveröffentlichung oder der zur Veröffentlichung eingereichten Arbeit:

ist dieser Erklärung beigelegt. Die Aufstellung ist Bestandteil dieser Erklärung.

7. Die Dissertation oder Teile davon wurden nicht bei einer anderen Fakultät als Dissertation eingereicht.

8. Die Richtigkeit der vorstehenden Erklärungen bestätige ich.

Ort und Datum

Unterschrift

Declaration

I hereby declare that:

1. I have authored the present work independently.
2. This thesis has not been submitted to any other university.
3. I have not used sources other than those specified and cited in the bibliography.
4. Where I have consulted the published work of others, this is always clearly attributed.
5. The electronic version of the work is consistent with the written version.
6. I have acknowledged all main sources of help.

The presented work was carried out in the period from 22.06.2020 to 29.10.2024 (22.06.2020–31.12.2022 at Philipps-Universität Marburg, 01.01.2023–29.10.2024 at Karlsruhe Institute of Technology) under the supervision of Prof. Dr. Stefanie Dehnen.

Abstract

Binary Zintl anions cover a variety of the p-block elements, which can be combined with d- or f-block metals atoms. This results in an extensive collection of heterometallic combinations with novel molecular architectures that are inaccessible from homoatomic Zintl anions. In fact, the choice of the two elements within the heteroatomic precursor plays a vital role in the type of clusters that might form, which is mainly influenced by the relative size and electron affinity within the two p-block elements. Binary anions containing elements of similar sizes and electron affinities (a “match” case), such as $(\text{Ge}_2\text{As}_2)^{2-}$ and $(\text{Ge}_3\text{As})^{3-}$, can either 1) retain their original units as bridging or terminating ligands in products from reactions with a series of d^{10} phenyl and mesityl metal complexes, as seen in $[\text{PhZn}(\text{Ge}_3\text{As})]^{2-}$ (Ph = phenyl), $[\text{Zn}_3(\text{Ge}_3\text{As})_4]^{6-}$, $[\text{MesZn}(\text{Ge}_3\text{As})]^{2-}$ (Mes = mesityl), as examples; or 2) undergo fragmentation and reorganization process to form heteroatomic or intermetallic clusters, $[\{\text{Cp}^*\text{Ni}\}_2(\text{Ge}_6\text{As}_2)]^{2-}$, $[\{\text{RuCp}^*\}_4(\text{GeR})_x(\text{Ge}_4\text{As}_{4-x})]^{2-}$ ($x = 0, 2$, R = unknown substituent), and $[\text{Mn}_2@\text{Ge}_x\text{As}_{24-x}]^{9-}$, that are less structurally related to the parent units, upon reaction with group 7, 8, and 10 decamethylcyclopentadienide (Cp^*) complexes. In contrast, the “mismatch” combination of Ga and Bi behaves differently. By modulating the Lewis-acidic environment in the reaction sphere, different metal complexes were combined with Ga/Bi-based intermetallic solids, giving rise to the formation of a series of Bi-based clusters, where Ga is often absent and tends to be released as elemental gallium. The Lewis acids can either induce the formation of larger aggregates of $\{\text{Bi}_n\}$ units, such as $[\text{Bi}@\text{Ga}_8(\text{Bi}_2)_6]^{3-/5-}$, and $(\text{Ga}_2\text{Bi}_{16})^{4-}$, or be incorporated into the cluster framework itself as shown in $[\{(\text{cod})\text{Ru}\}_4\text{Bi}_{18}]^{4-}$ (cod = 1,5-cyclooctadiene). Additionally, the Lewis-acidic metal complex can be coordinated by the simplest building block released by the Ga/Bi system, Bi_2^{2-} , as seen in $[\{(\text{C}_7\text{H}_{11})(\text{C}_7\text{H}_{13})\text{Ru}\}_2\text{Bi}_2]^{2-}$, which causes a partial hydrogenation of the ligands present to form a stable complex. The product spectra of these two systems exemplify the great influence of the relative sizes and electron affinities of the selected elements. In the case of Ge and As, the formed clusters contain both Ge and As atoms connected in a soluble form due to their similar atomic sizes and electron affinities. In contrast, for Ga and Bi, which have very different sizes and electron affinities, the lighter Ga tends, though not always, to form metal precipitation, yet the much heavier polybismuthide units remain available for coordination of transition metal complex fragments to form binary Zintl clusters. In addition, the nature of the transition metals, as well as the ligands, also show subtle impacts on the type of the formed clusters, as seen in both systems.

Table of Contents

Abstract.....	i
Table of Contents	iii
Abbreviations	v
1 Introduction.....	1
1.1 History and Development of Zintl Anions	1
1.2 Intermetallic Phases, Zintl Phases, Zintl Solids.....	2
1.3 Zintl Anions as Precursors – Homoatomic and Heteroatomic Anions	4
1.4 Synthesis of Zintl Clusters – from Zintl Anions or Zintl Phases/Solids to Heteroatomic Clusters and Intermetalloid Clusters	5
1.4.1 Synthesis of Zintl Clusters from Homoatomic Units	6
1.4.2 Synthesis of Zintl Clusters from Heteroatomic Units	13
1.4.3 Synthesis of Zintl Clusters from Other Miscellaneous Units	24
1.5 Electronic Situation and Structures of Zintl Clusters	25
1.5.1 Concept of Electron-Precise Zintl Anions and Clusters	25
1.5.2 Concept of Electron-Deficient Zintl Anions and Clusters.....	26
2 Research Objectives and Questions.....	27
3 Behavior of “K₂GeAs” Solids in the Formation of Ternary Ge/As-based Clusters	29
3.1 Introduction.....	29
3.2 Synthesis and Investigation of the Ternary “K ₂ GeAs” solids.....	30
3.3 <i>Pseudo</i> -Tetrahedral Ge/As Clusters as Ligands in the Coordination Sphere of d ¹⁰ Metals.....	32
3.3.1 Syntheses, Structures and Bonding	32
3.3.2 Assembly of One to Four Ge/As-based <i>pseudo</i> -Tetrahedra in the Coordination Sphere of d ¹⁰ Metals	44
3.4 Expansions of <i>pseudo</i> -Tetrahedral Ge/As Anions.....	50
3.4.1 Syntheses, Structures and Bonding	50
3.5 Conclusion	65
4 Behavior of “K₅Ga₂Bi₄” in the Formation of Bi-based Anionic Clusters.....	67
4.1 Introduction.....	67
4.2 Understanding and Elucidating the Formation and Relationship of Bi-Rich Nanostructures	69
4.2.1 Syntheses, Structures, and Bonding	69
4.2.2 Understanding and Elucidating the Formation of Bismuth-rich Nanoclusters	82
4.3 Inducing In-Situ Hydrogenation in the Coordination Sphere of Ru ²⁺ Ions with Bi ₂ ²⁻	88

4.3.1 Syntheses, Structures and Bonding.....	88
4.3.2 Hydrogenation Study of $[\{(C_7H_{11})(C_7H_{13})Ru\}_2Bi_2]^{2-}$	92
4.4 Conclusions.....	97
5 Summary.....	99
6 Experimental Section.....	101
6.1 General.....	101
6.2 General Methods.....	102
6.3 Syntheses of Ternary Zintl Solids.....	103
6.4 Syntheses of Zintl Compounds.....	106
7 Appendix.....	113
7.1 Crystal Structure Measurements and Data.....	113
7.1.1 Data Collection and Refinement.....	113
7.1.2 Crystal Data and Details of the Structure Determinations.....	114
7.1.3 Structural Details.....	128
7.2 Micro-X-ray Fluorescence Spectroscopy (μ -XFS) Analysis and Energy- Dispersive X-ray Spectroscopy (EDS) Analysis.....	137
7.3 Electrospray Ionization Mass Spectrometry (ESI-MS) Investigations.....	152
7.3.1 Mass Spectra of Zintl Solids and Crypt-222 in Solution.....	152
7.3.2 Mass Spectra of Re-dissolved Single-Crystals.....	154
7.3.3 Time-dependent Mass Spectra of the Reaction Solutions.....	165
7.4 Quantum Chemical Investigations.....	178
7.4.1 Compounds $[K(crypt-222)]_2(1)_{0.9}(Ge_2As_2)_{0.1} \cdot 0.9tol - [K(crypt-222)]_26$	178
7.4.2 Compounds $[K(crypt-222)]_27 \cdot 2en - [K(crypt-222)]_29 \cdot solv$	183
7.4.3 Compounds $[K(crypt-222)]_{3.67}10 - [K(crypt-222)]_{412} \cdot solv$	184
7.4.4 Compound $[K(crypt-222)]_{213} \cdot solv$	187
Bibliography.....	189
Publication List.....	205

Abbreviations

A	alkali metals
Ae	alkaline earth metals
An	actinides
Ar	aryl
ccp	cubic close-packed
cod	1,5-cyclooctadiene
Cp	cyclopentadienide, C ₅ H ₅
Cp ^{'''}	1,2,4-tri-tert-butyl-cyclopentadienide
Cp [#]	tetramethylcyclopentadienide, C ₅ Me ₄ H
Cp*	decamethylcyclopentadienide, C ₅ Me ₅
crypt-222	4,7,13,16,21,24-hexaoxa-1,10-diazabicyclo[8.8.8]hexacosane
Cy	cyclohexyl
dppe	1,2-bis(diphenylphosphino)ethane
EA	electron affinity
EDS	dispersive X-ray spectroscopy
en	ethane-1,2-diamine
eq	equation
ESI-MS	electrospray ionization mass spectrometry
Et	ethyl
DMF	N,N-dimethylformamide
DFT	density functional theory
HOMO	highest occupied molecular orbital
hmds	bis(trimethylsilyl)amides, N(SiMe ₃) ₂
Hyp	tris(trimethylsilyl)silane, Si(SiMe ₃) ₃
<i>i</i> Pr	isopropyl
IR	infrared
L/R	ligands
LMOs	localized molecular orbitals
Ln	lanthanides
LUMO	lowest unoccupied molecular orbital
Mes	mesityl
μ -XFS	micro-X-ray fluorescence spectroscopy
nacnac	[(N(C ₆ H ₃ <i>i</i> Pr ₂ -2,6)C(Me)) ₂ CH] [−]
NMR	nuclear magnetic resonance
Ph	phenyl
Pn	pnictogens
PPh ₃	triphenylphosphine
PXRD	powder X-ray diffraction
py	pyridine
SCXRD	single crystal X-ray diffraction
SEN	skeleton electron number
solv	solvent
SOMO	singly occupied molecular orbital
<i>t</i> Bu	tert-butyl
THF	tetrahydrofuran
tol	toluene

Tr	triels
Tt	tetrels
VEC	valence electron concentration
VEN	valence electron number
X	halogens
XRD	X-ray diffraction
xs	excess
18-crown-6	1,4,7,10,13,16-hexaoxacyclooctadecane

1 Introduction

1.1 History and Development of Zintl Anions

Interest in polyatomic main group anionic clusters began with the exploration of the reaction between lead and antimony with an ammonia solution of sodium in 1891 by Joannis.^[1] The formed green and red solutions, for lead and antimony respectively, were interpreted as a redox event between the p-block metal and the sodium, later suggested to result in the anions Pb_9^{4-} , and Sb_7^{3-} from electrolysis studies carried out by Smyth, Kraus, and Peck.^[2–5] Extensive investigations from Zintl and coworkers further proved the existence of negatively charged main group (semi-)metals in alkali metal liquid ammonia solutions via potentiometric titration methods.^[6] Moreover, Zintl recognized that dissolving the binary intermetallic phases such as Na_4Tt_9 ($\text{Tt} = \text{Sn}, \text{Pb}$) in liquid ammonia directly would lead to the same solutions containing the polyanions of dissolving the corresponding metals, which built up the connection between salt-like intermetallic phases and soluble (semi-)metal polyanions.^[7] After his pioneering work, such main group polyanion clusters and intermetallic phases have been named in Zintl's honor.

In initial studies, despite of the existence of polyanionic clusters, it proved impossible to isolate crystalline samples from ammonia. To tackle this issue, Kummer et al. used ethane-1,2-diamine (en) instead of liquid ammonia as the solvent, which established a practical route towards a room temperature synthesis.^[8,9] Later, Corbett and coworkers applied sequestering agents like crypt-222 (4,7,13,16,21,24-hexaoxa-1,10-diazabicyclo[8.8.8]hexacosane) to successfully aid in the crystallization of the bare main group elemental clusters.^[10,11] Therefore, the structure of salt-like compounds could be determined using X-ray diffraction methods, and the first structurally verified polyanions were Sn_9^{4-} , and Sb_7^{3-} , respectively.^[8,10,12,13]

Aforementioned movements paved the way for fast developments in the chemistry of main group polyanionic clusters. Subsequent studies in this field, including the exploration of novel intermetallic phases and extension of such phases into solution, and further react with metal complexes, will be introduced within following sections respectively. A brief overview of the development of main group polyanions is shown in Figure 1.1.

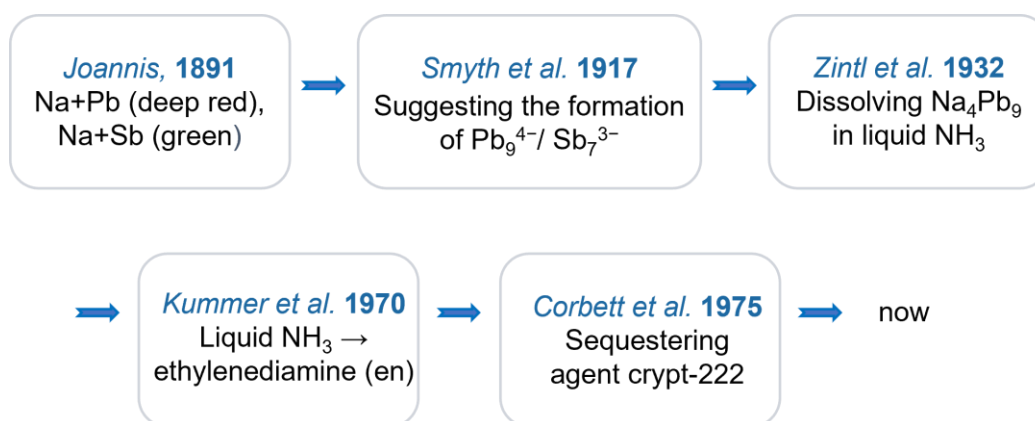


Figure 1.1: Timeline of the historical development of main group polyanions.

1.2 Intermetallic Phases, Zintl Phases, Zintl Solids

As introduced above, intermetallic phases serve as an important class of starting materials towards the formation of main group polyanions, and are also used extensively towards modern functional materials, such as those used in the aeronautic industry.^[14–16] Therefore, understanding intermetallic phases including the structures and properties, remains a meaningful field to explore.

Intermetallic phases comprise two or more metallic/semi-metallic elements with a fixed composition and ordered packing pattern.^[17] Well-known examples are Hume-Rothery phases, Laves phases, as well as Zintl phases. These phases have different properties in terms of either stoichiometric element composition, valence electron concentration, or packing mode. Hume-Rothery phases contain elements of similar electronegativity but different numbers of valence electrons and different crystal structures, so that the site of one element cannot be substituted by another element in larger amounts without impacting the structure. Valence electron concentration (VEC) stands as the sole factor that defines the Hume-Rothery phases, with the formula: $VEC = \frac{\sum \text{valence electrons}}{\sum \text{atoms}}$, where the value of VEC ranges between 1 and 2.^[18,19] Typical Hume-Rothery phases are CuZn, Cu₉Al₄, and Au₅Al₃. Laves phases are intermetallic compounds with a formula form of BC₂, which correlates to the packing density. In a Laves phase, an ideal atomic ratio of two atoms would fulfill the equation: $r_B/r_C = (3/2)^{1/2} \approx 1.225$, which results in a space filling of 71%.^[20] No general electronic concept has been devised for describing the Laves phases, as such phases cover a broad range of elemental compositions with either small or large electronegativity difference. Examples of Laves phases are MgCu₂, and MgZn₂. Both contain transition metal tetrahedra with magnesium atoms filling the cavities in the substructure network, though the former is a cubic close-packed (ccp) type, whereas the latter is a hexagonal type.^[21]

Different to the phases mentioned above, Zintl phases have a strict definition of composition, composing of alkali or alkaline earth metals and much more electronegative group 13–15 (semi-)metals, or even transition metals.^[22–25] For instance, Na₄Tt₉ (Tt = Sn, Pb), and A₃Pn₇ (A/Pn = Li, Na, Cs/P, Li, Na, K, Rb, Cs/As, Rb, Cs/Sb) belong to Zintl phases, which are interpreted by transferring valence electrons from the less electronegative metals to the p-block elements, thus

the p-block elements fulfill the 8–N rules.^[26–38] The structure of the two type of Zintl phases mentioned here are molecular cages of p-block element atoms surrounded by alkali metal atoms. Generally, the anionic substructure of binary, ternary or quaternary phases, show a broad variety, ranging from molecular units, 1D strands or 2D layers, to 3D networks. Some examples are presented in Figure 1.2.

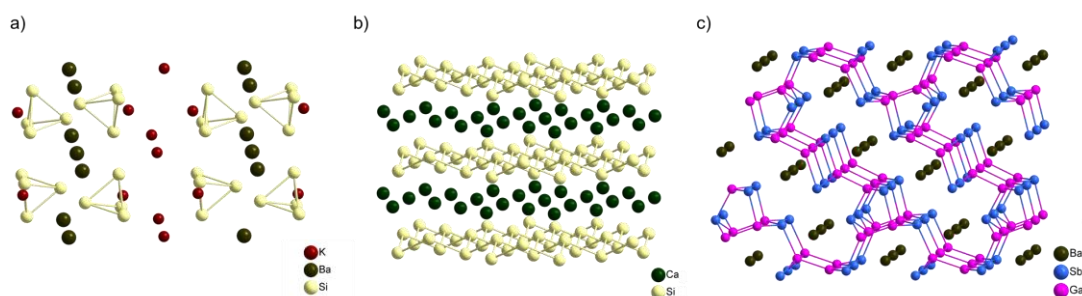


Figure 1.2: Examples of Zintl phases: a) K_2BaSi_4 contains molecular Si_4^{4-} units balanced by K^+ and Ba^{2+} cations; b) CaSi_2 contains two dimensional layers, $\infty\{\text{Si}_2^{2-}\}$, embedded by Ca^{2+} cations; c) BaGa_2Sb_2 is based on a 3-dimensional framework, $\infty^3\{(\text{Ga}_2\text{Sb}_2)^{2-}\}$.^[39–41]

Owing to the unique electronic properties of Zintl phases, a tapestry of diverse clusters form upon reactions of such phases or anions extracted from them with Lewis-acidic, mostly transition metal complexes, in a heterogenous solution mixture. The Lewis-acidic metal ions often trigger bond breaking and formation reactions of the Zintl anions, leading to the formation of larger aggregates, though the specific details of these complex processes still remains unknown. The mixed p/d-block or p/f-block (semi-)metal clusters that are obtained from such reactions are named Zintl clusters. Such clusters can often have special electronic properties and unique bonding situations that will be discussed further in Section 1.5.

Synthesis of Zintl phases usually involves heating main group (semi-)metals, and sometimes transition metals, together to several hundreds of degrees. For instance, the elements are mixed together a) in a fused niobium/tantalum tube with a designed temperature profile in an oven, or b) in a silica tube filled with noble gas (mostly argon), then heated stepwise either in a furnace, or using an oxygen torch. The resulting product is a fine, lustrous, metallic powder, sometimes pyrophoric, which can be ground in a pestle and mortar. Examples syntheses are shown in equations 1.1–1.4 below.^[42–45]

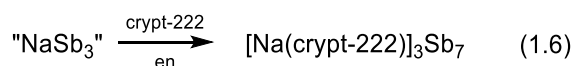
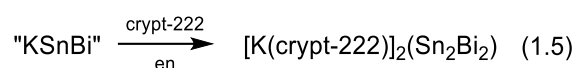


Note that the resulting product might represent a solid mixture comprising a major phase with an elemental composition different from what has been used for the elements, and the rest of product might exist in the form of an element or another phase. In this case, one uses the nomi-

nal composition of the elements as initially combined in quotation marks to name the obtained solids (see eqs 1.3 and 1.4).

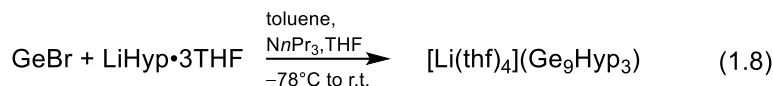
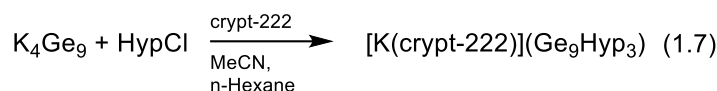
1.3 Zintl Anions as Precursors – Homoatomic and Heteroatomic Anions

Extractions of well-defined Zintl phases or solid mixtures, as described above, with sequestering agents, such as crypt-222, or 18-crown-6 (1,4,7,10,13,16-hexaoxacyclooctadecane), using polar solvents, like liquid ammonia, or en, leads to the formation of Zintl polyanions in the form of $[A(\text{crypt-222})]^+$ ($A = \text{Na}, \text{K}, \text{Rb}$) or $[A(18\text{-crown-6})]^+$ salts ($A = \text{K}, \text{Rb}$).^[13,44,46–49] Extracted compounds might either a) form salts retaining the original structure of the anionic part within the Zintl phases/solids, or b) undergo decompositions and rearrangements in the solution, thus form anions with structures that do not match the original element ratio of the starting phases/solids. Examples of Zintl phases/solids that have been extracted are presented in equations 1.5 and 1.6 below.^[50,51]



Either the resulting salts of Zintl anions or the Zintl phases/solids themselves can be applied as precursors for follow-up chemistry. Zintl anions, extracted from the appropriate Zintl phases, are typically tetrahedral or nine-atom cages. To date, known species are homoatomic anions Tt_4^{4-} ($\text{Tt} = \text{Si}, \text{Ge}, \text{Sn}, \text{Pb}$),^[42,52–57] Tt_9^{4-} ($\text{Tt} = \text{Si}, \text{Ge}, \text{Sn}, \text{Pb}$),^[46,58–71] Pn_7^{3-} ($\text{Pn} = \text{P}, \text{As}, \text{Sb}, \text{Bi}$),^[13,47,51,72–81] and heteroatomic anions $(\text{TrBi}_3)^{2-}$ ($\text{Tr} = \text{Ga}, \text{In}, \text{Tl}$),^[44,82] and $(\text{Tt}_2\text{Pn}_2)^{2-}$ ($\text{Tt/Pn} = \text{Ge/P}, \text{Ge/As}, \text{Ge/Sb}, \text{Sn/Sb}, \text{Sn/Bi}, \text{Pb/Sb}, \text{Pb/Bi}$),^[50,83–89] binary seven-atom, eight-atom, and nine-atom cages also exist, such as $(\text{Tl}_4\text{Bi}_3)^{3-}$,^[43] $(\text{Sn}_3\text{Sb}_4)^{6-}$,^[86] $(\text{Tt}_4\text{Pn}_4)^{2-}$ ($\text{Tt/Pn} = \text{Sn/Sb}, \text{Sn/Bi}$),^[90–92] $(\text{Sn}_5\text{Sb}_3)^{3-}$,^[93] $(\text{Sn}_3\text{Bi}_5)^{3-}$,^[94] $(\text{Tr}_4\text{Bi}_5)^{3-}$ ($\text{Tr} = \text{In}, \text{Tl}$),^[44,82] and $(\text{Tt}_7\text{Pn}_2)^{2-}$ ($\text{Tt/Pn} = \text{Ge/P}, \text{Ge/As}, \text{Sn/Bi}, \text{Pb/Bi}$),^[83,84,89,95] yet are limited in application, owing to the relatively low yields they are isolated in. Recently, crystalline salts comprising homoatomic Bi_2^{2-} dumbbells have been selected as another candidate of the starting material (see Section 1.4.3).^[96–100]

Besides the aforementioned precursors, modified Zintl anions with silyl moieties represent another class of Zintl chemistry precursors.^[101–109] Silyl groups are the most commonly used types of substituents for the Ge_9^{4-} anions, approached by direct metathesis reactions of Zintl phases with halide derivatives, resulting in the formation of $(\text{Ge}_9\text{Hyp}_3)^-$ ($\text{Hyp} = \text{Si}(\text{SiMe}_3)_3$), for instance.^[110] Alternatively, reactions involving subhalides of p-block (semi-)metals with alkali metal salts of corresponding silyl substituents in solution at low temperature can yield the same compounds.^[111] Representative reactions are shown in equations 1.7 and 1.8. Lowering the charge of the anion alters the solubility and stability of the modified cage compared to the naked anion, thus leading to different types of products when using ligand-decorated clusters as precursors (see Section 1.4.1.3).



1.4 Synthesis of Zintl Clusters – from Zintl Anions or Zintl Phases/Solids to Heteroatomic Clusters and Intermetalloid Clusters

Investigation of Zintl clusters has become a multifaceted field that includes the formation of novel clusters with respect to elemental combinations and structural architectures, as well as further studies on their electronic properties and reactivity.^[112,113] As mentioned in Section 1.3, either salts of molecular Zintl anions or Zintl phases/solids serve as the source of Zintl precursors for further reactions. Routes towards larger clusters are mainly realized in two ways: a) combinations of Zintl phases/solids plus sequestering agents with main group/transition metal complexes or b) combinations of salts comprising Zintl anions with main group/transition metal complexes. Most of such reactions are carried out in en.

To date, a plethora of beautiful heterometallic or intermetalloid cluster structures have been synthesized from such reactions, yet the pathway of cluster formation is poorly investigated in most cases. Nonetheless, the reagents show great impact on the range of the products, which include a) solvents, b) sequestering agents, c) transition metal complexes, and d) Zintl precursors. The evolution of the chemistry involving Zintl clusters (Section 1.1) has highlighted the importance of using polar amines as solvents and sequestering agents (points a and b), which not only optimize the solubility of phases or neat solids with high electron density per atom, but also support the isolation of crystalline products. Transition metal complexes have numerous factors which can be controlled to alter their reactivity: the metal atom itself, the ligand type, and the coordination number. This will be discussed in detail in Sections 3 and 4. Another key factor remains the Zintl precursors, which will be discussed in this section, addressing homoatomic and binary anionic units.

Note that in this thesis, the term “intermetalloid clusters” refers exclusively to endohedral clusters, with the general formulas $[\text{M}_x@E_y]^{q-}$ or $[\text{M}_x@E_y\text{M}_z]^{q-}$, where M represents a transition metal, lanthanide, or actinide atom, and E denotes one or more types of p-block (semi)metal atoms. In contrast, Zintl clusters lacking an endohedral atom will be denoted as “heterometallic clusters”.

1.4.1 Synthesis of Zintl Clusters from Homoatomic Units

1.4.1.1 Activation of P₄ and As₄ as Inspiration for Zintl Chemistry

Starting from a tetrahedral molecule, white phosphorus, P₄, being the archetypal example for such units, plays a vital role in many industrial processes as a precursor for the synthesis of organophosphorus compounds.^[114] The activation of P₄ with transition metal and main group complexes has yielded a large number of species ranging from compound exhibiting a metal-phosphorus triple bond and metal-P₄ complexes to polyphosphorus species with tens of phosphorus atoms.^[115–124] Synthesis of the heavier analogue As₄ requires freshly prepared reagents, owing to its sensitivity to light, air and moisture; therefore, corresponding derivatives have been studied less intensively.^[125,126] Similar to many P₄ derivatives, the products obtained upon reactions of As₄ tend to keep the tetrahedra intact, or break one of the Pn–Pn bond (butterfly-shaped; Pn = P, As) via various coordination modes.^[127–131] Examples of the activation of P₄, resulting in different types of products, are shown in Figure 1.3 below. Note that, while in Section 1, all d-/f-block metals are drawn in black for clarity, the d-/f-block metals in the following sections will be drawn in specific colors for emphasis.

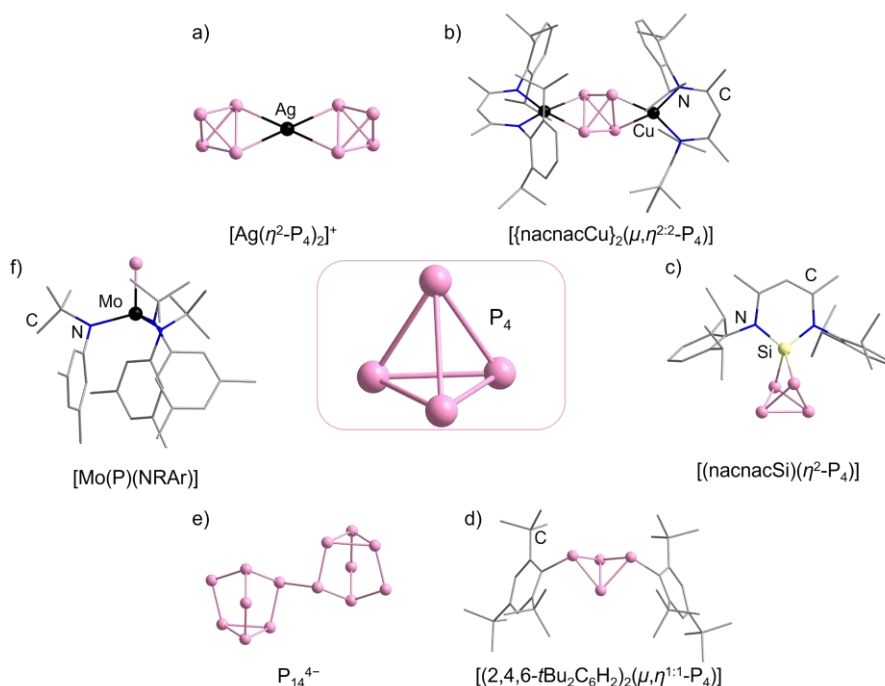


Figure 1.3: Examples of molecular structures showing the activation of P₄ with transition metal and main group complexes. Cases, in which P₄ remains intact and coordinates to metal fragments in different fashions: $[\text{Ag}(\eta^2\text{-P}_4)_2]^+$ (a)^[118] and $[\{\text{nacnacCu}\}_2(\mu, \eta^{2:2}\text{-P}_4)]$ (b)^[119]; $\text{nacnac} = \text{N}(\text{C}_6\text{H}_3\text{iPr}_2\text{-2,6-C}(\text{Me})_2\text{CH})^-$, iPr = isopropyl. Cases, in which a P–P bond in P₄ was broken: $[(\text{nacnacSi})(\eta^2\text{-P}_4)]$ (c)^[120] and $[(2,4,6\text{-tBu}_2\text{C}_6\text{H}_2)_2(\mu, \eta^{1:1}\text{-P}_4)]$ (d)^[121]. Case, in which P₄ reacts with Li in liquid ammonia to form a polyphosphide: P_{14}^{4-} (e)^[122]. Case, in which P₄ reacts with Mo(NRAr) to form a P–metal triple bond: $[\text{Mo}(\text{P})(\text{NRAr})]$ (f)^[123]; $\text{R} = \text{C}(\text{CD}_3)_2\text{CH}_3$, $\text{Ar} = 3,5\text{-C}_6\text{H}_3\text{Me}_2$. Hydrogen atoms are omitted for clarity.

1.4.1.2 Synthesis of Zintl Clusters from Tetrahedral Tt_4^{4-} Units

The investigations of P_4 and As_4 activation have caused interest in activating tetrahedral Zintl anions, as well. Homoatomic tetrahedral anions, Tt_4^{4-} ($Tt = Si, Ge, Sn, Pb$), exist in the solid state. However, an overall charge of $4-$ results in a high negative charge density per atom which consequently causes a solubility issue when dissolving these phases. Early research on the reactivity of Tt_4^{4-} anions has therefore mainly remained in solid-state chemistry. For instance, $[Zn(\eta^3-Ge_4)_2]^{6-}$ and $[Cd_3(\mu, \eta^{3:3}-Pb_4)_4]^{10-}$ (Figures **1.4a** and **1.4b**) are found to exist in the solids Cs_6Ge_8Zn and K_6Pb_8Cd , respectively (the latter co-crystallized with two additional Pb_4^{4-} units),^[132,133] infinite chain-like extensions $\frac{1}{\infty}\{[Au(\mu, \eta^{2:2}-Tt_4)]^{3-}\}$ ($Tt = Sn, Pb$; Figure **1.4c**) have been observed in Cs_3AuTt_4 .^[134]

In a solvent-based approach, primarily using liquid ammonia, Rb_4Sn_4 reacts with $[ZnPh_2]$ ($Ph = \text{phenyl}$) to give $[(\mu^2-Sn_4)Zn(\eta^3-Sn_4)]^{6-}$ (Figure **1.4d**).^[135] An A_4Tt_4 phase represents the most obvious precursor to provide Tt_4^{4-} units. Besides that, phases containing a mixture of anions have also served as precursors, though. For instance, the $K_{12}Sn_{17}$ phase composed of two Sn_4^{4-} and one Sn_9^{4-} units per formula unit, reacts with $[ClAu(PPh_3)]$ to give $[Au(\eta^2-Sn_4)_2]^{7-}$ (Figure **1.4e**).^[136] Similarly the $K_6Rb_6Ge_{17}$ phase, comprising two Ge_4^{4-} and one Ge_9^{4-} units per formula unit, reacts with $[ZnPh_2]$ to form $[Ph_2Zn(\eta^2-Ge_4H)]^{3-}$ (Figure **1.4f**), where the Zn atom retains both ligands besides being coordinated by Ge_4^{4-} .^[137] A series of $[\{MesCu\}_2(\mu, \eta^{3:3}-Tt_4)]^{4-}$ ($Tt_4 = Si_4, Ge_4, Si_{3.3}Ge_{0.7}$, $Mes = \text{mesityl}$) clusters (Figure **1.4g**) were synthesized by reacting different phases with $CuMes$ in liquid ammonia, as well.^[138–140] A recent study from Sun and co-workers has shown that the combination of $K_{12}Ge_{17}$ and $[MPh_2]$ ($M = Zn, Cd$) in an en solution leads to the formation of $[Zn_6(\mu, \eta^{2:2:2}-Ge_4)_4]^{4-}$, and $[Cd_6(\mu, \eta^{2:2:2}-Ge_4)_4]^{4-}$, (Figure **1.4h**) respectively.^[141] In all of the mentioned cases, the Tt_4^{4-} tetrahedron has remained intact, with no cleavage of the $Tt-Tt$ bonds, different from the chemistry of Pn_4 where cleavage of the bond is commonly observed.

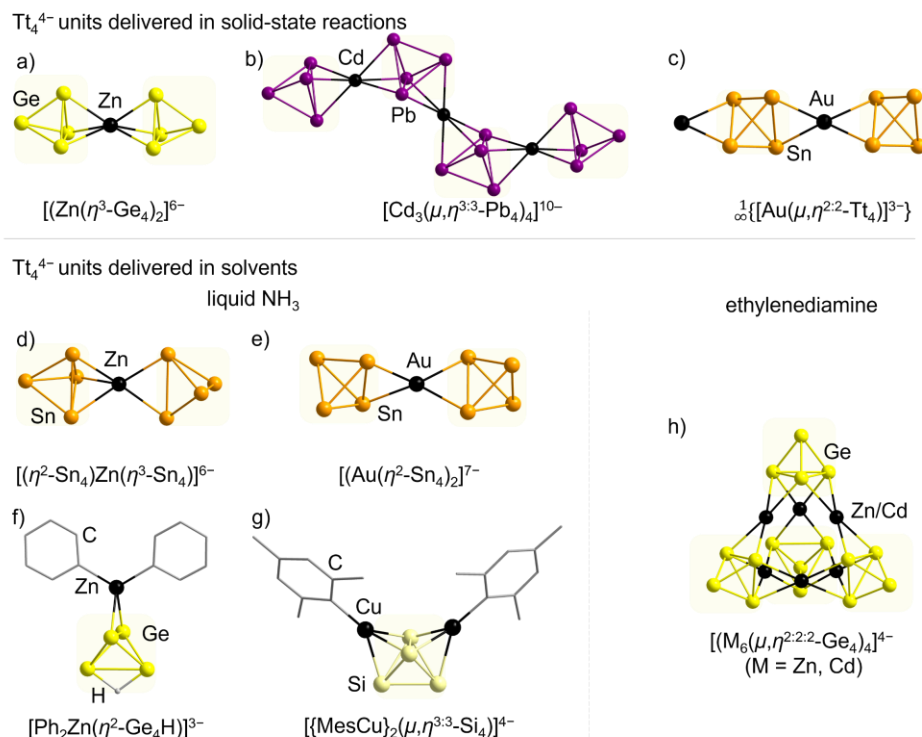


Figure 1.4: Examples of molecular structures of clusters derived from homoatomic Tt₄⁴⁻ units (Tt = Si, Ge, Sn), including solid-state compounds (above the solid line) or species obtained from solution (below the solid line): $[(\text{Zn}(\eta^3\text{-Ge}_4)_2)]^{6-}$ (a),^[132] $[\text{Cd}_3(\mu, \eta^{3:3}\text{-Pb}_4)_4]^{10-}$ (b),^[133] $\frac{1}{\infty}[\text{Au}(\mu, \eta^{2:2}\text{-Tt}_4)]^{3-}$ (Tt = Sn, Pb; c),^[134] $[(\eta^2\text{-Sn}_4)\text{Zn}(\eta^3\text{-Sn}_4)]^{6-}$ (d),^[135] $[(\text{Au}(\eta^2\text{-Sn}_4)_2)]^{7-}$ (e),^[136] $[\text{Ph}_2\text{Zn}(\eta^2\text{-Ge}_4\text{H})]^{3-}$ (f),^[137] $[\{\text{MesCu}\}_2(\mu, \eta^{3:3}\text{-Tt}_4)]^{4-}$ (Tt = Si, Ge; g),^[138–140] $[(\text{M}_6(\mu, \eta^{2:2:2}\text{-Ge}_4)_4)]^{4-}$, (M = Zn, Cd; h).^[141] Note that Tt₄⁴⁻ units retained in the products are emphasized by a light yellow background, and besides 1.4f, all the hydrogen atoms are omitted for clarity.

1.4.1.3 Synthesis of Zintl Clusters from Pn₇³⁻ Units

Pn₇³⁻ (Pn = P, As, Sb, Bi), which features a nortricyclane-like topology, was also used as a precursor in Zintl chemistry. The distinct structural motif of Pn₇³⁻ underscores the variety of bonding and topological configurations that group 15 elements can adopt in different charge states. In phases like A₃Pn₇ (A/Pn = Li, Na, K, Rb, Cs/P, As, Sb) and Ae₃Pn₁₄ (Ae/Pn = Sr, Ba/P, As), discrete Pn₇³⁻ units are surrounded by alkali or alkaline earth metal cations.^[26–29,31–38] The heaviest analogue, Bi₇³⁻, was also synthesized, by extraction of a mixture of K₅Bi₄, crypt-222, and [(C₆H₆)Cr(CO)₃] in pyridine, but so far not explored in corresponding reactions.^[74]

Pn₇³⁻ (Pn = P, As, Sb) can coordinate as such to transition metal complexes. Archetypal examples of an η² coordination mode (Figure 1.5a) include $[\text{Ph}_2\text{InP}_7]^{2-}$, $[\text{M}(\eta^2\text{-Pn}_7)_2]^{4-}$ (M/Pn = Zn, Cd/P, Zn/As), and $[\text{As}_7\text{Hg}_2\text{As}_7]^{4-}$. $[\text{M}(\eta^2\text{-Bi}_7)_2]^{4-}$ (M = Zn, Cd) have been known to exist as well, which were synthesized, however, in a different approach, by using binary anions (TlBi₃)²⁻ or ternary solids “K₅Ga₃Bi₄” instead (see Section 1.4.2.3).^[142–145] The μ,η^{1:1} coordination mode related to polyphosphide P₁₆²⁻ was exemplified by $[\text{As}_7\text{TtAsAs}_7]^{3-}$ (Tt = Sn, Pb), $[\text{M}_2(\mu, \eta^{1:1}\text{-Pn}_7)_2]^{4-}$ (M/Pn = Zn, Cd/P, Zn/As), and $[\text{M}_2(\mu, \eta^{1:1}\text{-Bi}_7)_2]^{4-}$ (M = Zn, Cd).

$\text{P}_7\text{H}_2]^{2-}$ ($\text{M} = \text{Ag, Au}$; Figure **1.5b**), and $[\text{As}_7\text{Au}_2\text{As}_7]^{4-}$.^[145–148] Pn_7^{3-} coordinates to transition metal fragments in an η^4 fashion, as seen in $[\{(\text{CO})_3\text{M}\}(\eta^4\text{-P}_7)]^{3-}$ ($\text{Pn/M} = \text{P, As, Sb/Cr, Mo, W}$; Figure **1.5c**).^[149] $[\text{Pd}_2(\mu, \eta^{2:2}\text{-As}_7)_2]^{4-}$ and $[\text{Cu}_2(\mu, \eta^{3:1}\text{-As}_7)_2]^{4-}$ feature two M^{2+} centers coordinated in a $\mu, \eta^{2:2}$ and $\mu, \eta^{3:1}$ fashion by two homoleptic As_7^{3-} units (Figures **1.5d**, **1.5e**), respectively.^[142,150] These clusters are mainly synthesized from reactions involving A_3Pn_7 , especially in the cases of As and Sb. This is mainly attributed to the favorable stoichiometric ratio of alkali metals and group 15 elements in the extracted salt, and the lower cost of K compared to other alkali metals. Clusters that are less structurally related to a Pn_7^{3-} unit, such as $[\text{Pd}_7\text{As}_{16}]^{4-}$ (Figure **1.5f**), and $[\text{Ni}_5\text{Sb}_{17}]^{4-}$ (Figure **1.5g**), represent rearranged products composed of $\{\text{Pn}_n\}$ units and transition metal atoms, and are known to be obtained from similar reactions.^[150,151]

Reactions of Pn_7^{3-} with transition metal complexes can yield a few intermetalloid clusters, like $[\text{M}@\text{Pn}_8]^{q-}$ ($\text{M/Pn/q} = \text{Mo/As/2, Mo/Sb/3, Nb/As/3, Nb/Sb/3, Cr/As/3}$), and $[\text{Pn}@\text{M}_{12}@\text{Pn}_{20}]^{q-}$ ($\text{Pn/M/q} = \text{As/Ni/3, Sb/Pd/3,4}$).^[152–157] The former consists of a puckered ring of eight group 15 atoms coordinating a central transition metal atom (Figure **1.5h**), while the latter is regarded as an “onion-type” cluster comprising of a Pn_{20} dodecahedron encapsulating an Pn-centered M_{12} icosahedron (Figure **1.5i**). Again, these clusters are not structurally related to the Pn_7^{3-} units.

Clusters derived from Pn_7^{3-} anions exhibit a tendency to retain their original shape as versatile building blocks when forming heteroatomic clusters, yet are less likely than their group 14 cousins to incorporate endohedral transition metals. Some examples of clusters that have emerged from Pn_7^{3-} anions are shown in Figure **1.5**.

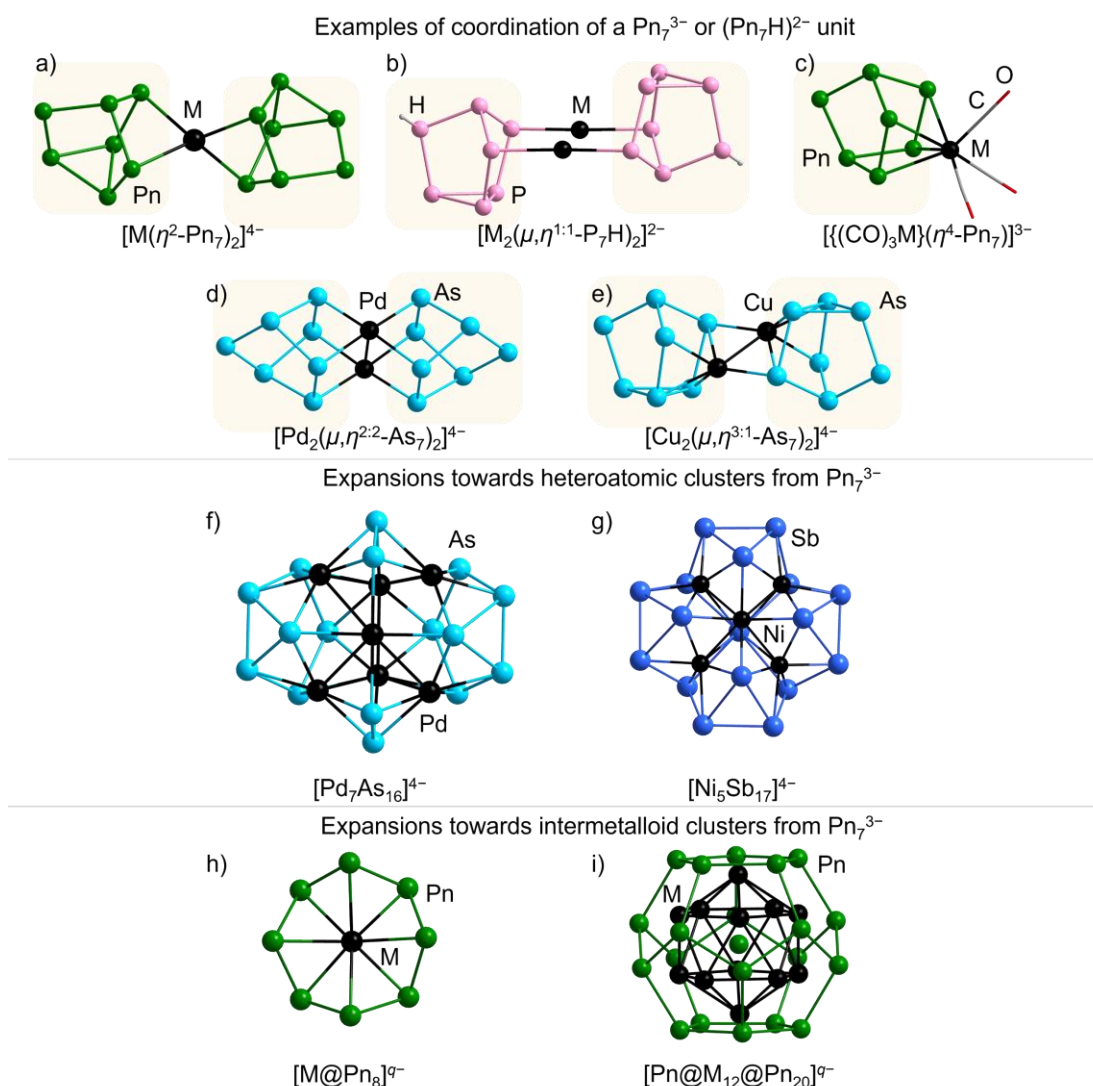


Figure 1.5: Examples of molecular structures of clusters derived from homoatomic Pn_7^{3-} anions ($\text{Pn} = \text{P}, \text{As}, \text{Sb}$). (a) – (e) Represent coordination complexes of clusters with different coordination modes: $[\text{M}(\eta^2\text{-Pn}_7)_2]^{4-}$ ($\text{M/Pn} = \text{Zn, Cd/P}, \text{Zn/As}; \text{Zn, Cd/Bi}$),^[142–145] $[\text{M}_2(\mu, \eta^{1:1}\text{-P}_7\text{H})_2]^{2-}$ ($\text{M} = \text{Ag}, \text{Au}$),^[147] $[\{(\text{CO})_3\text{M}\}(\eta^4\text{-Pn}_7)]^{3-}$ ($\text{Pn/M} = \text{P, As, Sb/Cr, Mo, W}$),^[149] $[\text{Pd}_2(\mu, \eta^{2:2}\text{-As}_7)_2]^{4-}$,^[150] $[\text{Cu}_2(\mu, \eta^{3:1}\text{-As}_7)_2]^{4-}$,^[142] (f) – (e) Represent expansions towards heteroatomic clusters: $[\text{Pd}_7\text{As}_{16}]^{4-}$,^[150] and $[\text{Ni}_5\text{Sb}_{17}]^{4-}$,^[151] (h) – (i) Represent expansions towards intermetalloid clusters: $[\text{M}@\text{Pn}_8]^{q-}$ ($\text{M/Pn/q} = \text{Mo/As/2}, \text{Mo/Sb/3}, \text{Nb/As/3}, \text{Nb/Sb/3}, \text{Cr/As/3}$),^[152–154] and $[\text{Pn}@\text{M}_{12}@\text{Pn}_{20}]^{q-}$ ($\text{Pn/M/q} = \text{As/Ni/3}, \text{Sb/Pd/3,4}$)^[155–157]. Note that the Pn_7^{3-} units retained in the products are emphasized by light yellow background.

1.4.1.4 Synthesis of Zintl Clusters from Tt_9^{4-} Units

The larger homoatomic units, Tt_9^{4-} ($\text{Tt} = \text{Ge}, \text{Sn}, \text{Pb}$), featuring a mono-capped square antiprismatic structure, have been extensively studied in different aspects, encompassing in-situ oxidation, oligomerization, functionalization with metal-ligand fragments, modification by vertex addition, and insertion of interstitial atoms.^[101,158]

The combination of KGe/KGe_{1.8} with crypt-222 leads to the formation of an ionic compound containing both Ge₉⁴⁻ (*C*_{4v} symmetry) and Ge₉²⁻ (*D*_{3h} symmetry) anions (Figure **1.6a**, **1.6c**), whereas the addition of crypt-222 to an en solution of K₄Ge₉ produces Ge₉³⁻ anions, the symmetry of which, lies in between of *C*_{4v} and *D*_{3h} (see Figure **1.6b**).^[58,64–67,159–161] Interestingly, these three species, with different charges, were found to coexist in the same solution according to co-crystallization experiments. Therefore, Sevov and his colleagues have proposed an equilibrium equation: Ge₉⁴⁻ \rightleftharpoons Ge₉³⁻ + e⁻ \rightleftharpoons Ge₉²⁻ + 2e⁻, observed from treating K₄Ge₉ with [SbPh₃].^[162] This equation suggests the transformations between differently charged {Ge₉} units occur with a small energy barrier.

Subsequent studies afforded dimers (Ge₉–Ge₉)⁶⁻ (Figure **1.6d**), trimers (Ge₉=Ge₉=Ge₉)⁶⁻ (Figure **1.6e**), tetramers (Ge₉=Ge₉=Ge₉=Ge₉)⁸⁻, and interconnected chains $\infty\{-(\text{Ge}_9^{2-})-\}$ (Figure **1.6f**) from various K/Ge phases or solids and crypt-222 or 18-crown-6 in en.^[66,162–170] These findings convey information of potential kinetic redox processes in these systems.

Functionalization of Ge₉^{q-} (*n* = 2, 3, 4) units with metal-ligand fragments results in exo-bonded substituents. Examples include (Ph₂Sb–Ge₉–Ph)²⁻ (Figure **1.6g**), (Ph₂Sb–Ge₉–SbPh₂)²⁻, and (Ph₂Sb–Ge₉–Ge₉–SbPh₂)⁴⁻, synthesized by nucleophilic attack of a silyl or metal complex fragment in a corresponding metathesis reaction.^[171]

Treatment of Tt₉⁴⁻ anions with transition metal complexes leads to the formation of heteroatomic clusters, such as [{(CO)₃M}(η⁴-Tt₉)]⁴⁻ (M/Tt = Cr/Sn, Mo/Sn, W/Sn, Cr/Pb, Mo/Pb, W/Pb) (Figure **1.6h**), and (PhZnTt₉)³⁻ (Tt = Si, Ge, Sn, Pb), that can be understood as products of vertex addition reactions.^[172–177] Intermetalloid clusters like [M@Sn₉]⁴⁻ (M = Co, Ni), [M@Tt₉]³⁻ (M/Tt = Ni/Ge, Ni/Cu/Sn, Cu/Pb; Figure **1.6i**), are formed by encapsulation of a central atom of the transition metal complex.^[45,178–181] Clusters of [{η⁴-(M@Sn₉)}Ni(L)]³⁻ (M/L = Co/CO, Co/C₂H₄, Ni/CO), [{η³-(M@Tt₉)}M'(L)]^{q-} (M/Tt/M' = Ni/Ge/Ni, L/*q* = PPh₃/2, en/3, CO/2, CCPh/3; Tt = Sn, M(=M')/L/*q* = Pt/ PPh₃/2, Pd/SnCy₃/3 (Cy = cyclohexyl); M/Tt/M'/L/*q* = Ni/Ge/Pd/PPh₃/2; M = Co, Tt = Sn, *q* = 3, M'/L = Pt/PPh₃, Au/Ph) display both properties, highlighting the flexibility in the modification of Tt₉⁴⁻ units.^[182–186]

Moving to ligand-decorated Tt₉^{q-} clusters, the well-known species, (Tt₉Hyp₃)⁻ (Tt = Ge, Sn, mostly with Ge), reacting with transition metal complexes also leads to of vertex addition or the formation of coordination clusters.^[103,109,187–190] Examples are [{(CO)₃M}(η⁵-Ge₉Hyp₃)]⁻ (M = Cr, Mo, W), and [(Hyp)M'(Tt₉Hyp₃)M(Tt₉Hyp₃)M'(Hyp)]^{q-} (M'/Tt/M/*q* = Zn/Ge/Pt/0, Au/Sn/Au/-1; Figure **1.6j**).^[103,188–190]

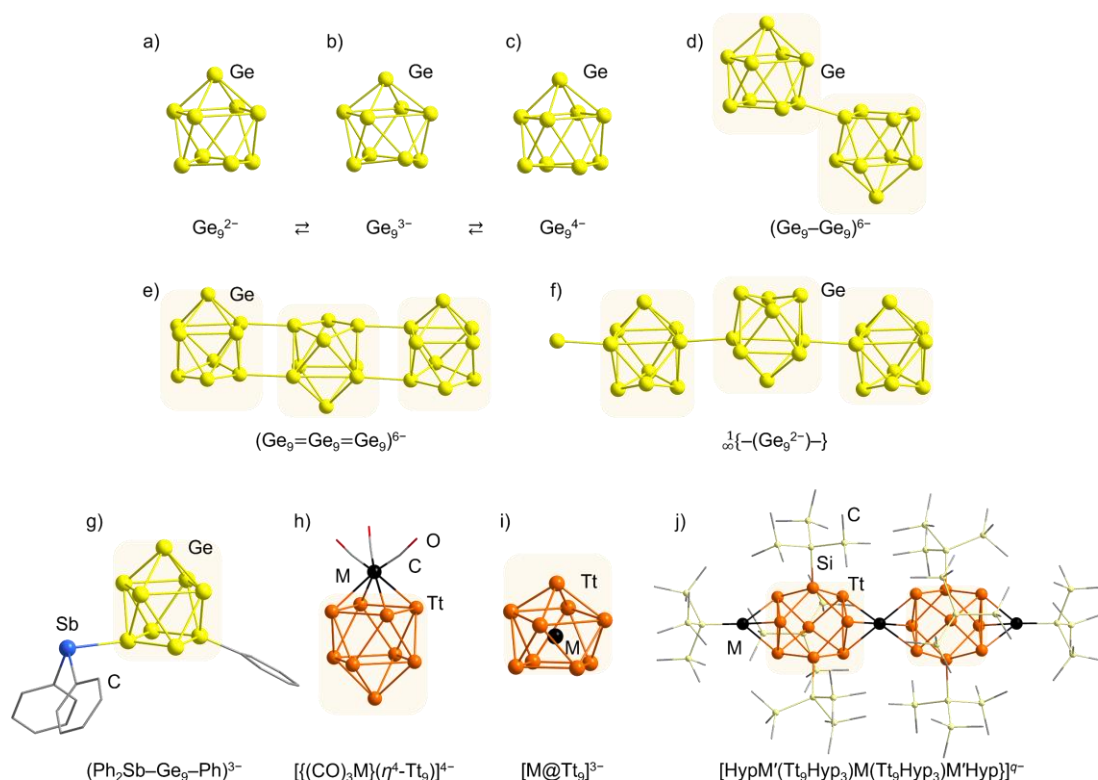


Figure 1.6: Molecular structures of Ge_9^{q-} : Ge_9^{2-} (a),^[58] Ge_9^{3-} (b),^[159–161] Ge_9^{4-} (c)^[58,64–67]. Examples of oligomerization and polymerization of Ge_9^{q-} ($q = 2, 3, 4$): $(\text{Ge}_9-\text{Ge}_9)^{6-}$ (d),^[66,162–164] $(\text{Ge}_9=\text{Ge}_9=\text{Ge}_9)^{6-}$ (e),^[165,166] and $\frac{1}{\infty}\{-(\text{Ge}_9^{2-})-\}$ (f)^[168,170]. Examples of molecular structures of clusters formed by homoatomic Tt_9^{4-} units: $(\text{Ph}_2\text{Sb}-\text{Ge}_9-\text{Ph})^{3-}$ (g),^[171] $[(\text{CO})_3\text{M}](\eta^4-\text{Tt}_9)^{4-}$ ($\text{M}/\text{Tt} = \text{Cr}/\text{Sn}, \text{Mo}/\text{Sn}, \text{W}/\text{Sn}, \text{Cr}/\text{Pb}, \text{Mo}/\text{Pb}, \text{W}/\text{Pb}$; h),^[172–176] $[\text{M}@\text{Ge}_9]^{3-}$ ($\text{M}/\text{Tt} = \text{Ni}/\text{Ge}, \text{Ni}/\text{Cu}/\text{Sn}, \text{Cu}/\text{Pb}$; i)^[179–181], and $[\text{HypM}'(\text{Tt}_9\text{Hyp}_3)\text{M}(\text{Tt}_9\text{Hyp}_3)\text{M}'(\text{Hyp})]^q-$ ($\text{M}'/\text{Tt}/\text{M}/q = \text{Zn}/\text{Ge}/\text{Pt}/0, \text{Au}/\text{Sn}/\text{Au}/-1$; j)^[189,190]. Note that the Tt_9^{q-} units retained in the products are emphasized by light yellow background, and all the hydrogen atoms are omitted for clarity.

Expansions of Tt_9^{4-} units result in reorganized structures, some of which maintain a deltahedral motif while others adopt different shapes. Icosahedral clusters were isolated from reactions between Tt_9^{4-} and transition metal complexes. Examples are $[\text{M}@\text{Tt}_{12}]^{q-}$ ($\text{M}/\text{Tt}/q = \text{Ni}, \text{Pd}, \text{Pt}/\text{Pb}/2, \text{Rh}, \text{Ir}/\text{Sn}/3, \text{Co}/\text{Ge}/3, \text{Au}/\text{Pb}/3$), $[\text{Mn}@\text{Pb}_{12}]^{3-}$, and $[\text{Ru}@\text{Ge}_{12}]^{3-}$.^[191–198] Notably, $[\text{Co}@\text{Ge}_{12}]^{3-}$ (Figure 1.7a) and $[\text{Ru}@\text{Ge}_{12}]^{3-}$ (Figure 1.7b) differ significantly from an icosahedral symmetry.^[195,198] The former is elongated along one C_5 axis, thus two “layers” are far separated, whereas the latter is non-deltahedral, and as such has no relationship at all with an icosahedron; it can be viewed as a fusion of two sites of dewar-benzene-like Ge_6 fragments. Larger deltahedral clusters with one or two endohedral atoms are accessible through similar reactions, and often adopt oblong shapes. For instance, $[\text{Pd}_2@\text{Tt}_{18}]^{4-}$ ($\text{Tt} = \text{Ge}, \text{Sn}$), prepared from K_4Tt_9 and $[\text{Pd}(\text{PPh}_3)_4]$, is regarded as a fusion of two $[\text{M}@\text{Tt}_9]^{4-}$ clusters (see Figure 1.7c);^[199,200] the 17-vertex $[\text{Ni}_2@\text{Ge}_{13}\text{Ni}_4(\text{CO})_5]^{4-}$ cluster (Figure 1.7d) can be viewed as two icosahedra $\{\text{Ni}@\text{Ge}_9\text{Ni}_3(\text{CO})_2\}$ and $\{\text{Ni}@\text{Ge}_7\text{Ni}_5(\text{CO})_5\}$ fused via a $\{\text{Ni}_2\text{Ge}_3\}$ pentaatomic-plane.^[184]

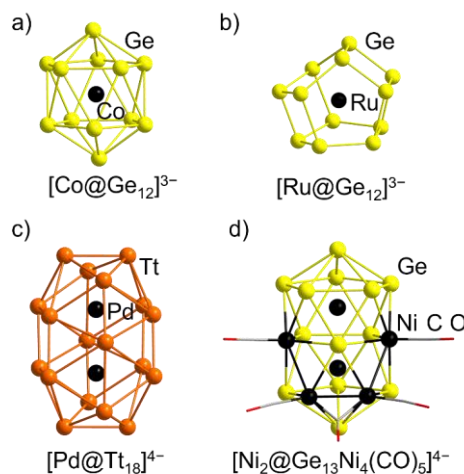


Figure 1.7: Selected examples of molecular structures that are less relevant to Tt_9^{q-} units: $[\text{Co}@\text{Ge}_{12}]^{3-}$ (a)^[195] and $[\text{Ru}@\text{Ge}_{12}]^{3-}$ (b)^[198] are distorted icosahedral clusters, $[\text{Pd}@\text{Tt}_{18}]^{4-}$ (Tt = Ge, Sn; c)^[199,200] and $[\text{Ni}_2@\text{Ge}_{13}\text{Ni}_4(\text{CO})_5]^{4-}$ (d)^[184] both demonstrate an oblong shape.

Typically, clusters obtained from reactions of Tt_9^{4-} units tend to form coordination clusters, as observed for the smaller units, yet with flexible degrees of distortions in terms of elongation, or compression.

1.4.2 Synthesis of Zintl Clusters from Heteroatomic Units

As mentioned in Section 1.3, binary *pseudo*-tetrahedral Zintl anions stand for the heteroatomic precursors that have been widely employed nowadays. Combining group 15 atoms with negatively charged group 13 or group 14 atoms results in heteroatomic *pseudo*-tetrahedral molecules with a lower negative charge ($2-$), compared to homoatomic Tt_4^{4-} anions.^[43,44,50,83–89,92] This leads to a lower electron density per atom within the tetrahedron, and therefore, to a better solubility in various polar solvents. Employing binary *pseudo*-tetrahedra as precursors enriches the product spectrum in terms of different elemental combinations and novel topologies. Problems arise, however, in determining the ratio and position of two involved p-block elements when they are not distinguishable from SCXRD (single crystal X-ray diffraction) measurements, which applies, in particular, to elements with nearly identical electron numbers such as Ge vs. As, Sn vs. Sb, Tl/Pb vs. Bi.

Despite the extensive combinations possible in the $(\text{TrPn}_3)^{2-}$ and $(\text{Tt}_2\text{Pn}_2)^{2-}$ systems, only a few are actually currently realized. Systematic DFT (density functional theory) studies concerning the existence of potential binary *pseudo*-tetrahedral Zintl anions suggested that a few more species with yet unexplored elemental combinations could be accessible.^[201] This relies on the ratio of covalent radii of the two elements within the tetrahedron. Another factor that addresses the use of such *pseudo*-tetrahedral anions in following reactions is the difference of the electron affinity: two elements with similar electron affinity are more likely to retain their covalent bond. In fact, the formation of novel binary *pseudo*-tetrahedral anions is influenced by various factors, and the mechanism underlying these reactions remain unclear in most cases. Nevertheless, the

binary anions that have been structurally characterized and reacted underscore the importance of the relative size and electron affinity between the two elements. The covalent radius, electron affinity, and electronegativity of group 13-15 elements are listed in Table 1.1.^[202–207] A snapshot of the employed binary *pseudo*-tetrahedra and the formed clusters not only helps to understand the reactivity of the precursors, but also provides insight towards understanding the formation pathway. Moreover, it serves as a keystone of introducing potential applications, such as catalytic studies.

Table 1.1: Overview of covalent radius, first electron affinity (EA), and electronegativity (EN, Pauling electronegativity) of group 13-15 elements of periods 3-6.

	Group 13 r_{cov} (Å), EA (eV), EN	Group 14 r_{cov} (Å), EA (eV), EN	Group 15 r_{cov} (Å), EA (eV), EN
Period 3	Al 1.21, 0.43, 1.61	Si 1.11, 1.39, 1.90	P 1.07, 0.75, 2.19
Period 4	Ga 1.22, 0.30, 1.81	Ge 1.20, 1.23, 2.01	As 1.19, 0.81, 2.18
Period 5	In 1.42, 0.38, 1.78	Sn 1.39, 1.11, 1.96	Sb 1.39, 1.05, 2.05
Period 6	Tl 1.45, 0.32, 2.04	Pb 1.46, 0.36, 2.33	Bi 1.48, 0.94, 2.02

1.4.2.1 Synthesis of Zintl Clusters from Lighter *pseudo*-Tetrahedral Units

$(\text{Ge}_2\text{P}_2)^{2-}$ (Figure 1.8a) and $(\text{Ge}_2\text{As}_2)^{2-}$ (Figure 1.8b) anions represent *pseudo*-tetrahedral anions composed of the lightest elements that were successfully isolated to date, yet the reactivity of both anions has been barely investigated.^[83,84] The atomic numbers of Ge and As atoms are nearly identical, therefore, these two elements cannot be distinguished via SCXRD measurements alone. Quantum chemical calculations are used to determine the most suitable positions of Ge and Pn atoms, as shown in Figures 1.8b, d, f–I (and similarly in all following figures), where the corresponding atom types are drawn in two-colored fashion. Note that in cases in which several conformers are possible, the more probable atom site is indicated by the dominant color.

When heated, elemental Ge, P, and As can react with Nb or Ta tubes, producing significant amount of side phases that can pollute the desired K/Ge/Pn phase. This massively reduces the yield of the extracted salts, and hinders the exploration of ternary cluster formation based on $(\text{Ge}_2\text{Pn}_2)^{2-}$ (Pn = P, As) units. To avoid this issue, a carbonized silica tube needs to be used during the heating process instead of Nb or Ta tubes. A successful synthesis as well as subsequent studies of the ternary K/Ge/As solids will be introduced in Section 3.

Upon extracting the solid with the nominal composition “ $\text{K}_2\text{Ge}_2\text{P}_2$ ” with crypt-222 and en, salts containing $(\text{Ge}_2\text{P}_2)^{2-}$ anions crystallize as the major compound, along with minor amounts of $[\text{K}(\text{crypt-222})]_2(\text{Ge}_7\text{P}_2)$ (Figure 1.8c).^[83] If undisturbed for several weeks, the $(\text{Ge}_2\text{P}_2)^{2-}$ salt will re-dissolve in the solution and larger amount of the salt of $(\text{Ge}_7\text{P}_2)^{2-}$ anions are observed, which therefore can be viewed as oxidation products of the *pseudo*-tetrahedral $(\text{Ge}_2\text{P}_2)^{2-}$ anions. The reactivity of $(\text{Ge}_2\text{P}_2)^{2-}$ is demonstrated by the reaction with the d-block complex $[\text{CdPh}_2]$ giving rise to the formation of a pinwheel shape cluster, $[\text{Cd}_3(\mu, \eta^{2:3}\text{-Ge}_3\text{P})_3]^{3-}$ (Figure 1.8e).^[83] The

replacement of a P atom with a Ge atom in the *pseudo*-tetrahedral units in this cluster suggests the existence of an equilibrium between $(\text{Ge}_2\text{P}_2)^{2-}$, and $(\text{Ge}_3\text{P})^{3-}$ plus $(\text{GeP}_3)^-$ anions, though the latter one has not been observed either as a free anion or coordinated to a metal center yet. The $[\text{Cd}_3(\mu, \eta^{2:3}\text{-Ge}_3\text{P})_3]^{3-}$ cluster consists of three Cd atoms forming a nearly isosceles triangle, which is further coordinated by three $(\text{Ge}_3\text{P})^{3-}$ units either in a μ, η^2 -type or μ, η^3 -type fashion. Interestingly, all three P atoms point outwards, therefore resulting in the observation of only Ge and Cd connections within the cluster yet. Another cluster, $[\text{Au}_6(\mu, \eta^{2:2:2}\text{-Ge}_3\text{As})(\mu, \eta^{2:2:2}\text{-Ge}_2\text{As}_2)_3]^{3-}$ (Figure 1.8f), emerged from the reaction of $(\text{Ge}_2\text{As}_2)^{2-}$ salts with $[\text{MeAu}(\text{PPh}_3)]$ in en.^[208] It is a supertetrahedral cluster composed of four *pseudo*-tetrahedral units connecting by an octahedron of six Au atoms. Again, an in-situ atom exchange process occurred in one of the $(\text{Ge}_2\text{As}_2)^{2-}$ units, which led to the formation of a $(\text{Ge}_3\text{As})^{3-}$ unit that was included in the cluster.

In addition to the reactions using $(\text{Ge}_2\text{Pn}_2)^{2-}$ salts to obtain coordination clusters as above, the extraction of a K/Ge/As solids obtained in Ta ampoules enabled the identification of five species, binary anions $(\text{Ge}_2\text{As}_2)^{2-}$ and $(\text{Ge}_7\text{As}_2)^{2-}$ (Figure 1.8d), and ternary intermetalloid clusters $[\text{Ta}@\text{Ge}_6\text{As}_4]^{3-}$, $[\text{Ta}@\text{Ge}_8\text{As}_4]^{3-}$, and $[\text{Ta}@\text{Ge}_8\text{As}_6]^{3-}$ (with the latter two anions coexisting in the same compound on two independent sites; Figures 1.8g – 1.8i).^[84] The formation of $(\text{Ge}_2\text{As}_2)^{2-}$ and $(\text{Ge}_7\text{As}_2)^{2-}$ indicates a similar trend of cluster growth as observed in the Ge/P system. Clearly, the reactions between the K/Ge/As mixtures and the tube material Ta resulted in three unexpected ternary clusters, each incorporating a formally fivefold charged Ta^{5+} atom. $[\text{Ta}@\text{Ge}_6\text{As}_4]^{3-}$ (Figure 1.8g) can be regarded as an intermediate resulting from a reaction of initially formed $(\text{Ge}_7\text{As}_2)^{2-}$ with elemental Ta and subsequent fragmentation and addition steps, on the way toward the large clusters. In addition, the latter two clusters are isostructural to $[\text{V}@\text{Ge}_8\text{As}_4]^{3-}$ (Figure 1.8h) and $[\text{Nb}@\text{Ge}_8\text{As}_6]^{3-}$ (Figure 1.8i), respectively, which are equally accessed through extractions of corresponding quaternary solids.^[209] The study of the mentioned multimetallic clusters of the Ge/As family shed light on possible mechanisms of cluster growth, which not only provides insight towards the formation of possible novel ternary clusters in the Ge/As system, but also advances the understanding of cluster chemistry in general.

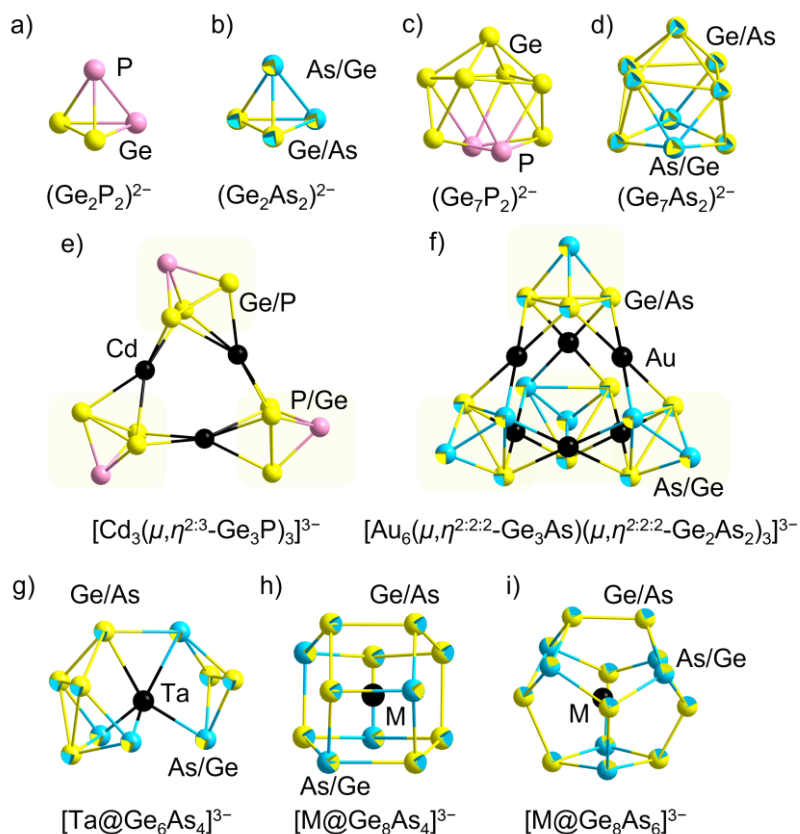


Figure 1.8: Molecular structures of the lightest heteroatomic *pseudo*-tetrahedral units, $(\text{Ge}_2\text{P}_2)^{2-}$ (a) and $(\text{Ge}_2\text{As}_2)^{2-}$ (b), and of anions formed upon (partial) oxidation of $(\text{Ge}_7\text{P}_2)^{2-}$ (c) and $(\text{Ge}_7\text{As}_2)^{2-}$ (d),^[83,84] known coordination complexes prepared from $(\text{Ge}_2\text{Pn}_2)^{2-}$ to date: $[\text{Cd}_3(\mu, \eta^{2:3}\text{-Ge}_3\text{P})_3]^{3-}$ (e),^[83] and $[\text{Au}_6(\mu, \eta^{2:2:2}\text{-Ge}_3\text{As})(\mu, \eta^{2:2:2}\text{-Ge}_2\text{As}_2)_3]^{3-}$ (f)^[208]. Intermetalloid clusters that formed by extractions of quaternary solids: $[\text{Ta}@\text{Ge}_6\text{As}_4]^{3-}$ (g), $[\text{M}@\text{Ge}_8\text{As}_4]^{3-}$ (M = Ta, V; h), and $[\text{M}@\text{Ge}_8\text{As}_6]^{3-}$ (M = Nb, Ta; i).^[84,209] In the case of Ge/As-based species, the corresponding atom types are drawn in two-colored fashion, with the more probable atom being indicated by the dominate color. Note that the $(\text{Ge}_2\text{Pn}_2)^{2-}$ units retained in the products are emphasized by light yellow background, and all the hydrogen atoms are omitted for clarity.

By now, the reactivity of $(\text{Ge}_2\text{P}_2)^{2-}$ and $(\text{Ge}_2\text{As}_2)^{2-}$ anions has been investigated only fragmentally. So far, the treatment of these two units with various transition metal complexes predominantly afforded only the coordination clusters mentioned above. Similar to homoatomic Tt_4^{4-} units, the lighter binary analogues tend to keep intact, sometimes involving atom exchange processes.

1.4.2.2 Synthesis of Zintl Clusters from Sb-based *pseudo*-Tetrahedral Units

Pseudo-tetrahedral units containing heavier elements (i.e., In/Sn/Sb, Tl/Pb/Bi), tend to, yet not always, undergo fragmentation and rearrangement processes. To date, Sb only appears to form binary *pseudo*-tetrahedral units with group 14 elements, such as $(\text{Sn}_2\text{Sb}_2)^{2-}$, $(\text{Pb}_2\text{Sb}_2)^{2-}$, and the recently isolated $(\text{Ge}_2\text{Sb}_2)^{2-}$.^[85,86,88] Sn and Sb represents the best-matching pair of the group 14/15 elemental combinations, owing to their exactly identical covalent radii (1.39 Å). As a result, the clusters that have emerged from $(\text{Sn}_2\text{Sb}_2)^{2-}$ are diverse. For instance, $(\text{Sn}_2\text{Sb}_2)^{2-}$

(Figure 1.9a) can behave similarly to the lighter elements' *pseudo*-tetrahedra mentioned above,^[86] retaining the original unit as an intact ligand and coordinating to transition metal atoms, like $[\text{Au}(\eta^2\text{-Sn}_2\text{Sb}_2)_2]^{3-}$ (Figure 1.9b), which was obtained by treatment with $[\text{BrAu}(\text{PPh}_3)]$ or $[\text{MeAu}(\text{PPh}_3)]$.^[210,211] Reorganized clusters, such as $[\{\text{M}(\text{Sn}_5\text{Sb}_3)\}_2]^{4-}$ ($\text{M} = \text{Cu}, \text{Au}$; Figure 1.9c), have been found to form in reactions with different d^{10} metal complexes, $[\text{LCu}(\text{NCMe})]$ ($\text{L} = \text{nacnac}$), and $[\text{MeAu}(\text{PPh}_3)]$, respectively.^[208,212] The structure of $[\{\text{M}(\text{Sn}_5\text{Sb}_3)\}_2]^{4-}$ can be viewed as two monomeric $\{\text{M}(\text{Sn}_5\text{Sb}_3)\}$ subunits linked by multicenter Sn–M contacts. The heavier analogues are also known for the combination of Sn/Bi and Pb/Bi (see below). In addition, reacting the phase K_8SnSb_4 , which was previously used as the source of $(\text{Sn}_2\text{Sb}_2)^{2-}$, with $[\text{M}(\text{CO})_6]$ ($\text{M} = \text{Cr}, \text{Mo}$), gives rise to the heteroatomic clusters, $[\{(\text{CO})_3\text{M}\}_2(\text{Sn}_2\text{Sb}_5)]^{3-}$ ($\text{M} = \text{Cr}, \text{Mo}$; Figure 1.9d), the structures of which can be viewed as an $\{\text{Sn}_2\text{Sb}_5\}$ unit coordinating two $\{\text{M}(\text{CO})_3\}$ fragments.^[213] The reactivity of this phase is further demonstrated by the reactions with AgMes , and $[\text{ClCu}(\text{PPh}_3)]$, respectively, leading to the formation of the clusters $[\{\text{M}(\text{Sn}_2\text{Sb}_5)\}_2]^{4-}$ ($\text{M} = \text{Ag}, \text{Cu}$; Figure 1.10e), which again possess two $\{\text{Sn}_2\text{Sb}_5\}$ subunits linked by a diamond-shaped $\{\text{M}_2\text{Sb}_2\}$ unit.^[213]

$[\text{Co}@\text{Sn}_6\text{Sb}_6]^{3-}$, $[\text{Co}_2@\text{Sn}_5\text{Sb}_7]^{3-}$, and $[\text{Ni}_2@\text{Sn}_7\text{Sb}_5]^{3-}$ are examples of intermetalloid clusters obtained from $(\text{Sn}_2\text{Sb}_2)^{2-}$, which are related in structure yet different in details.^[214] $[\text{Co}@\text{Sn}_6\text{Sb}_6]^{3-}$ (Figure 1.9f) and $[\text{Co}_2@\text{Sn}_5\text{Sb}_7]^{3-}$ (Figure 1.9g) are both synthesized from reactions of $(\text{Sn}_2\text{Sb}_2)^{2-}$ and $[\text{K}(\text{THF})_x][\text{Co}(\text{cod})_2]$ ($\text{THF} = \text{tetrahydrofuran}$, $\text{cod} = 1,5\text{-cyclooctadiene}$), containing one, or two interstitial Co^- atoms encapsulated in two fused square antiprism, respectively. This leads to a different atom composition of Sn and Sb observed in the two cluster molecules. In the isostructural $[\text{Ni}_2@\text{Sn}_7\text{Sb}_5]^{3-}$ cluster, two more Sb atoms are assigned to match the required electron count, as a Ni^0 atom is isoelectronic with a Co^- anion. Similar to Ge and As, the relative position of Sn and Sb atoms, as well as the electronic structure of these three clusters were determined by DFT calculations, which generally serve as an essential and powerful tool in the characterization of Zintl clusters.

An extensive study using $(\text{Sn}_2\text{Sb}_2)^{2-}$ reveals the influence of 4f or 5f metal ions on the formation of intermetalloid clusters, $[\text{M}@\text{Sn}_{14-x}\text{Sb}_x]^{q-}$ ($\text{M}/x/q = \text{La}/8/3, \text{La}/7/4, \text{Ce}/7/4, \text{U}/7/3, \text{U}/6/4$; Figures 1.9h – 1.9j).^[90] The cluster structures are analogues to those of known homologues, $[\text{Ln}@\text{Tt}_7\text{Bi}_7]^{4-}$ ($\text{Ln}/\text{Tt} = \text{La}, \text{Ce}/\text{Sn}, \text{La}, \text{Nd}, \text{Gd}, \text{Sm}, \text{Tb}/\text{Pb}$) and $[\text{U}@\text{Pb}_7\text{Bi}_7]^{3-}$, featuring six pentagonal and three square faces.^[215–217] To meet the required total number of valence electrons, the clusters, which differ in the ratio of Sn and Sb atoms and the type of interstitial atom, possess an overall charge of either 3– or 4–. The bonding of the atoms of the cluster shell is in agreement with the Zintl-Klemm-Busmann concept, either featuring three-bonded group 15 atoms or *pseudo*-group 15 atoms with a group 14 atom carrying a 1– charge (for more details, see Section 1.5.1).

The $[\{\text{Au}(\text{Pb}_5\text{Sb}_3)\}_2]^{4-}$ cluster, isostructural with the lighter Sn/Sb analogues (see Figure 1.9c), represents the only expansion of the $(\text{Pb}_2\text{Sb}_2)^{2-}$ anion to date.^[208] This cluster forms upon fragmentation and reorganization of the $(\text{Pb}_2\text{Sb}_2)^{2-}$ anion, driven by different sizes and significantly different electron affinities of Pb and Sb atoms.

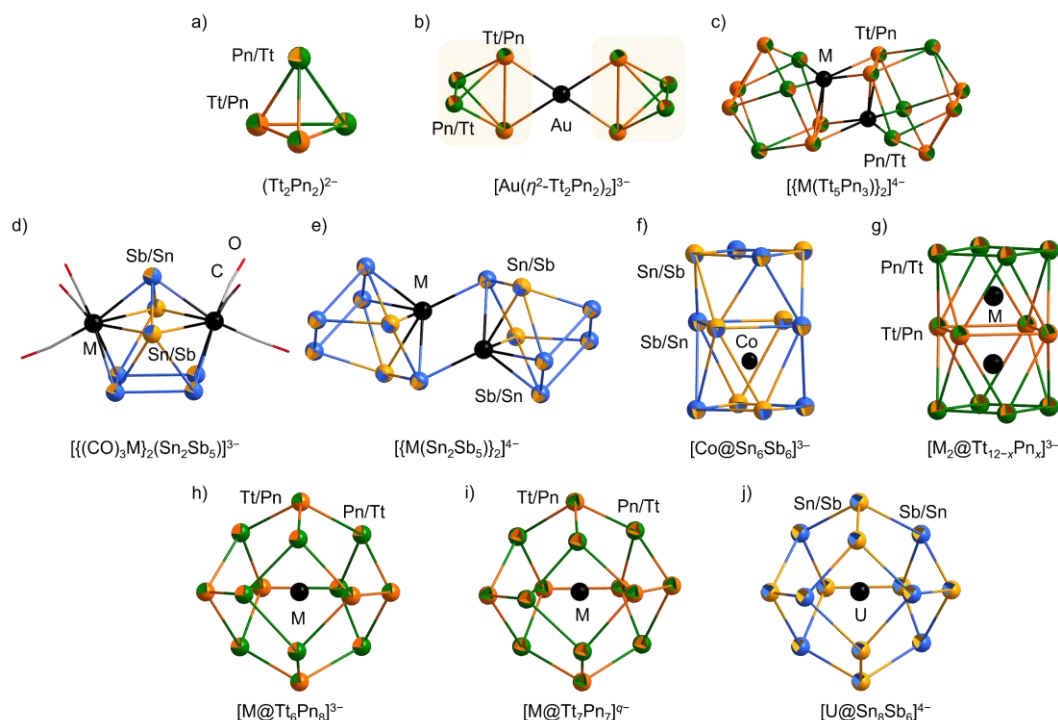


Figure 1.9: Molecular structures of $(Tt_2Pn_2)^{2-}$ ($Tt/Pn = Sn/Sb, Pb/Sb, Sn/Bi, Pb/Bi$; a),^[50,86–89] and a series of clusters obtained from $(Tt_2Pn_2)^{2-}$ anions: $[Au(\eta^2-Tt_2Pn_2)_2]^{3-}$ ($Tt/Pn = Sn/Sb, Sn/Bi, Pb/Bi$; b),^[211,212,223,224] $[M(Tt_5Pn_3)_2]^{4-}$ ($M/Tt/Pn = Cu, Au/Sn/Sb, Au/Pb/Sb, Au/Sn/Bi, Au/Pb/Bi$; c),^[208,212] $[(CO)_3M]_2(Sn_2Sb_5)^{3-}$ ($M = Cr, Mo$; d),^[213] $[M(Sn_2Sb_5)_2]^{4-}$ ($M = Ag, Cu$; e),^[213] $[Co@Sn_6Sb_6]^{3-}$ (f),^[214] $[M_2@Tt_{12-x}Pn_x]^{3-}$ ($M/Tt/Pn/x = Co/Sn/Sb/7, Ni/Sn/Sb/5, Ni/Sn/Bi/5, Ni/Pb/Bi/5$; g),^[89,214] $[M@Tt_6Pn_8]^{3-}$ ($M/Tt/Pn = La/Sn/Sb, La,Ce,Nd/Pb/Bi$; h),^[90,217,221] $[M@Tt_7Pn_7]^{9-}$ ($M/Tt/Pn/q = La,Ce/Sn/Sb/4, U/Sn/Sb/3, La,Ce/Sn/Bi/4, U/Pb/Bi/3, La,Nd,Gd,Sm,Tb/Pb/Bi/4$; i),^[90,215,217] and $[U@Sn_8Sb_6]^{4-}$ (j)^[90]. Similar as in the case of Ge/As-based species, the corresponding atom types are drawn in two-colored fashion, with the more probable atom being indicated by the dominate color. Considering intrinsic disorder problems, this also applies in the Sn/Bi-based and Pb/Sb-based clusters, although Sn and Bi, as well as Pb and Sb are generally distinguishable via SCXRD measurements. Note that $(Tt_2Pn_2)^{2-}$ units retained in the products are emphasized by light yellow background.

The recent exploration of $(Ge_2Sb_2)^{2-}$ unit started with the “ K_2GeSb ” solid, which comprises, in a small fraction, a crystalline compound with the composition of $K_{12}Ge_{3.5}Sb_6$. Extraction of $K_{12}Ge_{3.5}Sb_6$ led to the formation of salts of $(Ge_2Sb_2)^{2-}$ and $(Ge_4Sb_{12})^{4-}$ (Figures 1.10a, 1.10b).^[85] The addition of $[MeAuPPh_3]$ under the same reaction condition yields a larger cluster, $(Ge_4Sb_{14})^{4-}$ (Figure 1.10c). $(Ge_4Sb_{12})^{4-}$ and $(Ge_4Sb_{14})^{4-}$ are structurally related, and both of them can be regarded as combinations of $\{Ge_x\}$ and $\{Sb_y\}$ subunits. This has also been observed in clusters obtained from other “mismatch” elemental combinations, such as Ge/Bi. Indeed, $(Ge_4Sb_{14})^{4-}$ is isostructural with the heavier analogue $(Ge_4Bi_{14})^{4-}$ (see Section 1.4.3) and both clusters can be described as two norbornadiene-like $\{Pn_7\}$ units connected via a central $\{Ge_4\}$ chain.^[218] While $[MeAuPPh_3]$ is not part of the product, it seems to play a role in assembling the p-block anions into larger units in this reaction.

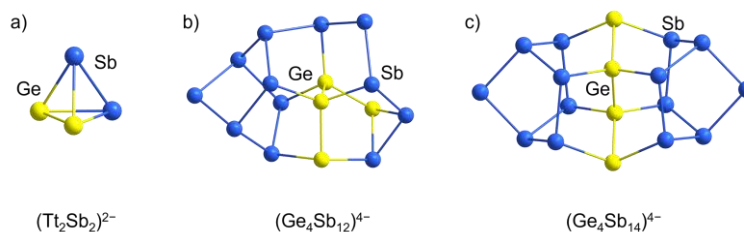


Figure 1.10: Molecular structures of $(\text{Ge}_2\text{Sb}_2)^{2-}$ (a), $(\text{Ge}_4\text{Sb}_{12})^{4-}$ (b), and $(\text{Ge}_4\text{Sb}_{14})^{4-}$ (c).^[85]

1.4.2.3 Synthesis of Zintl Clusters from Bi-based *pseudo*-Tetrahedral Units

With regards to the heaviest elemental combinations of the *pseudo*-tetrahedral anions, the most prominent examples are the $(\text{TrBi}_3)^{2-}$ ($\text{Tr} = \text{Ga}, \text{In}, \text{Tl}$) and $(\text{Tt}_2\text{Bi}_2)^{2-}$ ($\text{Tt} = \text{Sn}, \text{Pb}$) anions.^[44,82,87,89,92] Considering $(\text{Tt}_2\text{Bi}_2)^{2-}$ first, $(\text{Sn}_2\text{Bi}_2)^{2-}$ and $(\text{Pb}_2\text{Bi}_2)^{2-}$ have been studied extensively. It could be expected that owing to the difference in covalent radii and electron affinities between the elements that their chemical reactivities would also differ. Sn has a smaller covalent radius than Bi, whereas Pb is very similar in size ($\text{Sn} = 1.39 \text{ \AA}$, $\text{Pb} = 1.46 \text{ \AA}$, $\text{Bi} = 1.48 \text{ \AA}$). And with respect to the electron affinities, Pb is significantly smaller compared to Bi while Sn has a greater electron affinity than Bi ($\text{Sn} = 1.11 \text{ eV}$, $\text{Pb} = 0.36 \text{ eV}$, $\text{Bi} = 0.94 \text{ eV}$).

Previous reactions involving $(\text{Pb}_2\text{Bi}_2)^{2-}$ units show a preference of forming intermetalloid clusters. For instance, $[\text{K}(\text{crypt-222})]_2(\text{Pb}_2\text{Bi}_2) \cdot \text{en}$ combined with $[\text{Pd}(\text{PPh}_3)_4]$ in en yields $[\text{Pd}@\text{Pd}_2\text{Pb}_{10}(\text{Bi}_3)_2]^{4-}$ (Figure 1.11a) as its $[\text{K}(\text{crypt-222})]^+$ salts.^[219] The molecular structure of the cluster features a Pd-centered $\{\text{Pd}_2(\text{Pb/Bi})_{10}\}$ icosahedron with two $\eta^3\text{-(Pb/Bi)}_3^-$ triangular units attached. Since Pb and Bi are not distinguishable by SCXRD measurements, DFT calculations are applied to determine the most stable conformers. This is adapted by giving an average nuclear charge on each site of the Pb/Bi shell, and determining the potential energy for each atom (first order perturbation theory in the nuclear charge). From this, the formula of the cluster can be summarized as $[\text{Pd}@\text{Pb}_{10-2x}\text{Bi}_{2x}\{\text{Pd}(\eta^3\text{-Bi}_{3-x}\text{Pb}_x)\}_2]^{4-}$ ($x = 0, 1$), with Pb and Bi atoms assigned on the most preferable positions, which also works in other d- or f-block/Pb/Bi intermetalloid clusters. Examples are $[\text{Zn}@\text{Zn}_5\text{Pb}_3\text{Bi}_8]^{4-}$, and $[\text{Ni}_2@\text{Pb}_7\text{Bi}_5]^{3-}$, obtained by treating $(\text{Pb}_2\text{Bi}_2)^{2-}$ with $[\text{ZnPh}_2]$, and $[\text{Ni}(\text{cod})_2]$, respectively;^[89] $[\text{Ln}@\text{Pb}_6\text{Bi}_8]^{3-}/[\text{Ln}@\text{Pb}_3\text{Bi}_{10}]^{3-}$ ($\text{Ln} = \text{La}, \text{Ce}, \text{Nd}$), $[\text{Ln}@\text{Pb}_7\text{Bi}_7]^{4-}/[\text{Ln}@\text{Pb}_4\text{Bi}_9]^{4-}$ ($\text{Ln} = \text{La}, \text{Nd}, \text{Gd}, \text{Sm}, \text{Tb}$), and $[\text{U}@\text{Pb}_4\text{Bi}_9]^{3-}/[\text{U}@\text{Pb}_7\text{Bi}_7]^{3-}$, that were synthesized by reacting $(\text{Pb}_2\text{Bi}_2)^{2-}$ with corresponding $[\text{Ln}(\text{C}_5\text{Me}_4\text{H})_3]$ or $[\text{An}(\text{C}_5\text{Me}_4\text{H})_3]$ complexes.^[216,217]

Notably, most Sn/Bi clusters are homologous to the heavier Pb/Bi clusters, such as $[\text{Zn}@\text{Zn}_5\text{Sn}_3\text{Bi}_8]^{4-}$, $[\text{Ni}_2@\text{Sn}_7\text{Bi}_5]^{3-}$, and $[\text{Ln}@\text{Sn}_7\text{Bi}_7]^{4-}/[\text{Ln}@\text{Sn}_4\text{Bi}_9]^{4-}$ ($\text{Ln} = \text{La}, \text{Ce}$).^[95,215,220] The cluster $[\text{Zn}@\text{Zn}_5\text{Tt}_3\text{Bi}_8]^{4-}$ ($\text{Tt} = \text{Sn}, \text{Pb}$; Figure 1.11b) can be viewed as a $\{\text{Zn}_5\text{Tt}_3\text{Bi}_3\}$ delta-hedron with a central Zn atom, surrounded by five additional Bi atoms in a pentagram-like style.^[89,95] In the structure of $[\text{Ni}_2@\text{Sn}_7\text{Bi}_5]^{3-}$ (Figure 1.9g), two interstitial Ni atoms are incorporated in two fused square antiprism $\{\text{Tt}_7\text{Bi}_5\}$ analogous to the aforementioned Co/Sn/Sb clusters.^[220] The Pb/Bi clusters tend to crystallize with higher yields, which, might be attributed better size matching of the atoms and smaller surface polarities owing to more similar electro-

negativities. In addition, smaller Pb–Bi bond energies help in lowering the energy barrier for transformation in the solvents under inert conditions.

A series of group 14/Bi intermetalloid clusters containing an interstitial lanthanide or actinide atom can be classified according to their vertex count: 13-vertex cages (Figure 1.11c) or 14-vertex cages (Figures 1.9h and 1.9i).^[215–217] The 13-vertex group 14/Bi cages possess a “cap” composed of four-square faces, and a “bowl-type” lower part containing four pentagons and a square plane (bottom), with a 4:9 ratio of group 14 and Bi atoms. The four-bonded central Bi atom in the cap has a formal charge of 1+, while the neighboring Bi atoms are 1– charged, owing to strongly polarized bonds from the central Bi atom towards the neighboring atoms according to DFT calculations. The 14-vertex cages, isostructural to the lighter Sn/Sb analogues, possess a 7:7 ratio of group 14/Bi composition in accordance with the +3 charge of the encapsulated Ln cation. Note that the reaction of $(\text{Sn}_2\text{Bi}_2)^{2-}$ with $[\text{Pd}(\text{dppe})_2]$ (dppe = 1,2-bis(diphenylphosphino)ethane) in en affords a less spherical 14-vertex cluster, $[\text{Pd}_3@\text{Sn}_8\text{Bi}_6]^{4-}$ (Figure 1.11d), comprising three central Pd atoms.^[221] Moreover, this cluster contains more Sn atoms; it cannot be explained in terms of any classical bonding concept.

Clusters $[\text{Au}(\eta^2\text{-Tt}_2\text{Bi}_2)_2]^{3-}$ (Figure 1.9b), and $[\{\text{Au}(\text{Tt}_5\text{Bi}_3)\}_2]^{4-}$ (Figure 1.9c), are formed by reacting $(\text{Tt}_2\text{Bi}_2)^{2-}$ (Tt = Sn, Pb) with $[\text{MeAu}(\text{PPh}_3)]$ in different solvents (en was used for synthesizing the former, and py was used for synthesizing the latter).^[208,222,223] Their structures are analogous to those of the lighter Sn/Sb clusters. Note that the moderate reactivity of $[\text{MeAu}(\text{PPh}_3)]$ also allows for the mere coordination of intact *pseudo*-tetrahedra, as seen in $[\text{Au}(\text{Tt}_2\text{Bi}_2)_2]^{4-}$ (also see the supertetrahedral Au/Ge/As cluster), but it can also lead to fragmentation and reorganization of the *pseudo*-tetrahedra to form larger clusters depending on the solvent used.

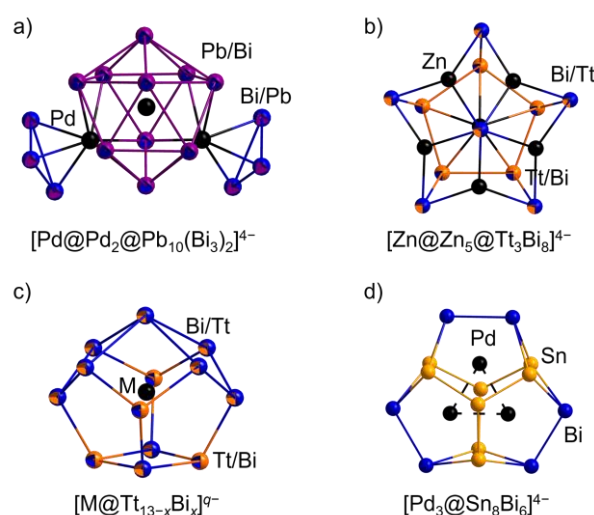


Figure 1.11: Molecular structures of $[\text{Pd}@\text{Pd}_2\text{Pb}_{10}(\text{Bi}_3)_2]^{4-}$ (a),^[219] $[\text{Zn}@\text{Zn}_5\text{Tt}_3\text{Bi}_8]^{4-}$ (Tt = Sn, Pb; b),^[89,95] and $[\text{M}@\text{Tt}_{13-x}\text{Bi}_x]^{q-}$ (M/Tt/x/q = La,Ce,Nd/Pb/10/3, La,Nd,Gd,Sm,Tb/Pb/9/4, U/Pb/9/4, La,Ce/Sn/9/4; c),^[215–217] and $[\text{Pd}_3@\text{Sn}_8\text{Bi}_6]^{4-}$ (d).^[221] Indistinguishable atom types are drawn in two-colored fashion, with the more probable atom being indicated by the dominate color. Considering intrinsic disorder problems, this also applies in the Sn/Bi based clusters, although Sn and Bi are generally distinguishable by SCXRD.

Therefore, in despite of the perceived differences in the atomic properties of the elements, $(\text{Sn}_2\text{Bi}_2)^{2-}$ and $(\text{Pb}_2\text{Bi}_2)^{2-}$ have rather similar chemistry. In the $(\text{TrBi}_3)^{2-}$ series of anions, “ $(\text{GaBi}_3)^{2-}$ ”, $(\text{InBi}_3)^{2-}$ and $(\text{TlBi}_3)^{2-}$, a different chemical behavior is observed. The covalent radii of In (1.42 Å), Tl (1.45 Å) and Bi (1.48 Å) are similar, yet that of Ga is smaller (1.22 Å). The electron affinity of the group 13 element is considerably smaller than that of Bi (Ga = 0.30 eV, In = 0.38 eV, Tl = 0.32 eV). Though it is not consistent to make a direct comparison between $(\text{TrBi}_3)^{2-}$ and $(\text{Tt}_2\text{Bi}_2)^{2-}$ anions in terms of their reactivity, most likely it is this difference in electron affinity that governs the chemistry of the $(\text{TrBi}_3)^{2-}$ system. This leads to the preference of element segregation in reactions involving group 13/Bi units, resulting in the formation of elemental group 13 metal and Bi-rich clusters. This is most pronounced for the Ga/Bi combination, while In/Bi and Tl/Bi show a higher possibility of being combined in ternary clusters owing to a better match of their atomic size.

For instance, in an en solution, $(\text{TlBi}_3)^{2-}$ (Figure 1.12a) reacts with $[\text{Ru}(\text{cod})(\text{H}_2\text{CC}(\text{Me})\text{CH}_2)_2]$ to afford $[\{(\text{codRu})_2\text{Bi}_9\}]^{3-}$ (Figure 1.12b), which can be regarded as two eclipsed $\{\text{Bi}_3\}$ triangles sandwiching a slightly corrugated $\{\text{Bi}_3\text{Ru}_2\}$ ring, or as a $\{\text{Bi}_4\}$ zig-zag chain capped by seven atoms forming an elongated $\{\text{Bi}_5\text{Ru}_2\}$ hexagonal pyramid.^[82] Tl is not included in this anion, however, if the mother liquor is concentrated and layered with toluene (tol), another ternary anion $[\{(\text{codRu})(\text{Tl}_2\text{Bi}_6)\}]^{2-}$ (Figure 1.12c) can be isolated as its $[\text{K}(\text{crypt-222})]^+$ salt.^[82]

Reactions of $(\text{TlBi}_3)^{2-}$ with $[\text{ZnPh}_2]$, and $[\text{CdPh}_2]$ lead to the formation of the heteroatomic clusters $[(\text{TlBi}_5)\text{Zn}_3\text{Bi}_6]^{4-}$ (Figure 1.12d), co-crystallizing with $(\text{Tl}_4\text{Bi}_5)^{3-}$ (Figure 1.12e), and $(\text{Bi}_7\text{CdBi}_7)^{4-}$ (Figure 1.12f), respectively.^[144] The former can be described as a truncated nortricyclane-type $\{\text{Bi}_7\}$ fragment, in which the top atom is replaced by three Zn atoms bonding to a $\{\text{TlBi}_5\}$ fragment. The other cluster consists of two $\{\text{Bi}_7\}$ fragments linked by a central Cd atom. A corresponding reaction with $[\text{HgPh}_2]$ yields the binary anion $(\text{Tl}_4\text{Bi}_5)^{3-}$ only. The investigation of $(\text{TlBi}_3)^{2-}$ reacting with group 12 complexes indicates the potential of binary Bi-containing anions to form large polybismuthide anions, like Bi_7^{3-} , in situ.

Reactions of $(\text{TlBi}_3)^{2-}$ with f-block complexes show a tendency of forming intermetalloid clusters. An example is $[\text{An}@\text{Tl}_2\text{Bi}_{11}]^{3-}$ (Figure 1.12g), prepared by reacting $(\text{TlBi}_3)^{2-}$ with $[\text{AnCp}^\#_3]$ (An = U, Th, $\text{Cp}^\# = \text{tetramethylcyclopentadienide}$).^[217,224] $[\text{An}@\text{Tl}_2\text{Bi}_{11}]^{3-}$ is isostructural to the 13-vertex Tt/Bi clusters mentioned above, upon isoelectronic replacement of $\{\text{Tt}_4\}$ with $\{\text{Tr}_2\text{Bi}_2\}$. This cluster can be viewed as a central U atom encapsulated by a $\{\text{Tl}_2\text{Bi}_{11}\}$ cage with a $\{\text{Bi}_5\}$ cap linked to four Bi atoms, which further bind to a $\{\text{Tl}_2\text{Bi}_2\}$ ring. These clusters are different from the cluster obtained with the lighter analogue “ $(\text{GaBi}_3)^{2-}$ ” and $[\text{U}(\text{C}_5\text{Me}_4\text{H})_3]$, which will be discussed in detail below.^[217] An intact $(\text{TlBi}_3)^{2-}$ unit has only been observed in a recent study using the less polar solvent THF instead of en, presenting a new synthetic approach towards the formation of silyl-decorated clusters, such as $[\{(\text{hmds})_2\text{Mn}\}_2(\text{TlBi}_3)]^{2-}$ (hmds = $\text{N}(\text{SiMe}_3)_2$, Figure 1.12h).^[225] This cluster, isolated from the reaction of $(\text{TlBi}_3)^{2-}$ with $[\text{Mn}(\text{hmds})_2]$, demonstrates that $[\text{Mn}(\text{hmds})_2]$ not only supports the dissolution of $(\text{TlBi}_3)^{2-}$ in THF, but also retains the tetrahedral $(\text{TlBi}_3)^{2-}$ unit in the center. $[\{(\text{hmds})_2\text{Mn}\}_2(\text{TlBi}_3)]^{2-}$ remains the only exception for all clusters obtained from binary $(\text{TrBi}_3)^{2-}$ units.

While $(\text{InBi}_3)^{2-}$ (Figure 1.12i) was shown to deliver both In and Bi atoms to product clusters, “ $(\text{GaBi}_3)^{2-}$ ” represents a “mismatch” case in binary *pseudo*-tetrahedral units. $[\text{Bi}@\text{In}_8\text{Bi}_{12}]^{3-/5-}$

(Figure 1.12j) was derived from the reaction of a solid with the nominal combination “K₅In₂Bi₄”, the source of (InBi₃)²⁻ anions, with [ZnMes₂] in pyridine at 60 °C.^[226] [Bi@In₈Bi₁₂]^{3-/5-} is an endohedral cluster, featuring a central Bi atom. In [Bi@In₈Bi₁₂]³⁻, the Bi atom is embedded by an In₈ cube, with each face capped by two connected Bi atoms. In a more reduced variant, [Bi@In₈Bi₁₂]⁵⁻, two adjacent In atoms from the In₈ cube are moved outwards, creating a planar In₂Bi₃ five-membered ring. Despite [ZnMes₂] not being incorporated into the cluster, it may facilitate the redox reaction, and further promote the formation of larger clusters through the assembly of subunits. [(La@In₂Bi₁₁)(μ-Bi)₂(La@In₂Bi₁₁)]⁶⁻ (Figure 1.12k) was obtained from the reaction of (InBi₃)²⁻ and [La(C₅Me₄H)₃].^[227] This cluster can be viewed as two hypothetical intermetalloid clusters, “[La@In₂Bi₁₁]⁴⁻”, connected by two μ-Bi⁺ bridges. DFT calculations suggest that the hypothetical “[La@In₂Bi₁₁]⁴⁻” is thermodynamically disfavored owing to a high charge density accumulated on the (formal) In²⁻ sites without bridging.

The “(GaBi₃)²⁻” precursor remains an arguable case. It is deemed to exist, like the other (TrBi₃)²⁻ anions, but it has never been isolated in a crystalline salt. The source of the “(GaBi₃)²⁻” salts, “K₅Ga₂Bi₄”, reacting with [Th(C₅Me₄H)₃] leads to the formation of the Bi-based cluster [Th@Bi₁₂]⁴⁻ (Figure 1.12l).^[224] Similarly, the extracted “(GaBi₃)²⁻” salts reacting with [U(C₅Me₄H)₃] yields the analogous cluster, [U@Bi₁₂]³⁻ (Figure 1.12l). The formation of these clusters was hypothesized as by replacement of three (C₅Me₄H)⁻ ligands with three Bi₄²⁻ rings. In the [Th@Bi₁₂]⁴⁻ cluster, an all-metal π-aromaticity was shown to exist, evidenced by the observation of π-delocalization of the respective two electrons in the 12-membered macrocycle {Bi₁₂} and a notable ring current that was identified by extensive quantum chemical calculations. In the case of [U@Bi₁₂]³⁻, a main group metal-actinide magnetic coupling is observed between the U⁵⁺ center and the Bi₁₂⁸⁻ shell. The only exceptions for a ternary cluster emerging from the Ga/Bi system have been the intermetalloid clusters [Sm@Ga_{3-x}H_{3-2x}Bi_{10+x}]³⁻ (x = 0, 1; Figures 1.12m, 1.12n), obtained from the reaction of “(GaBi₃)²⁻” with [Sm(C₅Me₄H)₃]. The result also served to indicate the presence of Ga in the “(GaBi₃)²⁻” precursor, yet in an unknown form.^[228] Different from the [An@Ti₂Bi₁₁]³⁻ cluster, the [Sm@Ga_{3-x}H_{3-2x}Bi_{10+x}]³⁻ (x = 0, 1) anion is the first protonated ternary intermetalloid cluster, while possessing a nearly identical architecture. Notably, in this cluster, protons serve to lower the charge overload at the formal “Tr²⁻” sites, while in the In/Bi analogue, μ-Bi⁺ bridges were used instead. The H atoms bonded to Ga atoms were detected by the Ga–H coupling in the ¹H NMR measurement of dissolved single crystals of [K(crypt-222)]₃[Sm@Ga_{3-x}H_{3-2x}Bi_{10+x}] (x = 0, 1) in d₇-DMF (DMF = N,N-dimethylformamide). The proposed source of the protonation reaction is the reaction solvent, en. The solvent was also involved in the formation of Bi₁₁³⁻ from “(GaBi₃)²⁻” in pyridine.^[229] [K₂Zn₂₀Bi₁₆]⁶⁻ (Figure 1.12o) that was obtained from the reaction of “K₅Ga₂Bi₄” with [ZnPh₂].^[230] Here, an inner {Zn₁₂} unit is embedded in a macrocycle consisting of eight Zn and sixteen Bi atoms. Both EDS measurements of the single crystals and DFT calculations ruled out the presence of Ga atoms in the compound.

As mentioned above, in the combination of group 13 elements with Bi, In and Tl tend to coexist with Bi in most clusters derived from (TlBi₃)²⁻ and (InBi₃)²⁻ anions mostly upon fragmentation and reorganization, whereas Ga in the “(GaBi₃)²⁻” shows a tendency to be released as elemental gallium, which leads to a preference of forming (larger) Bi-based clusters instead.

In summary, clusters derived from heavier *pseudo*-tetrahedral units (Sb- and Bi- based) show a tendency of forming more complicated structures which seem to be less predictable compared to those obtained from the lighter homologues. It seems that the tendency for the absence of the original *pseudo*-tetrahedral units in the final products is due to weaker covalent bonds. It is worth noting that the range of the products emerging from heavier $(\text{TrBi}_3)^{2-}$ and $(\text{Tt}_2\text{Pn}_2)^{2-}$ units exhibits distinct preferences: the former tends to form Bi-rich heteroatomic and intermetalloid clusters, whereas the latter prefers to form ternary intermetalloid, yet less Pn-rich clusters. This can be rationalized by the fact that, for favorable crystallization, the total charge of the anion, must not exceed a certain value. Hence, instead of accumulating more (highly charged) Tr^{2-} atoms in the cluster structure, their number is kept relatively low, while Bi^0 atoms replace these sites. For the Tt^- analogues, this is not as critical, so their relative atom content tends to be higher.

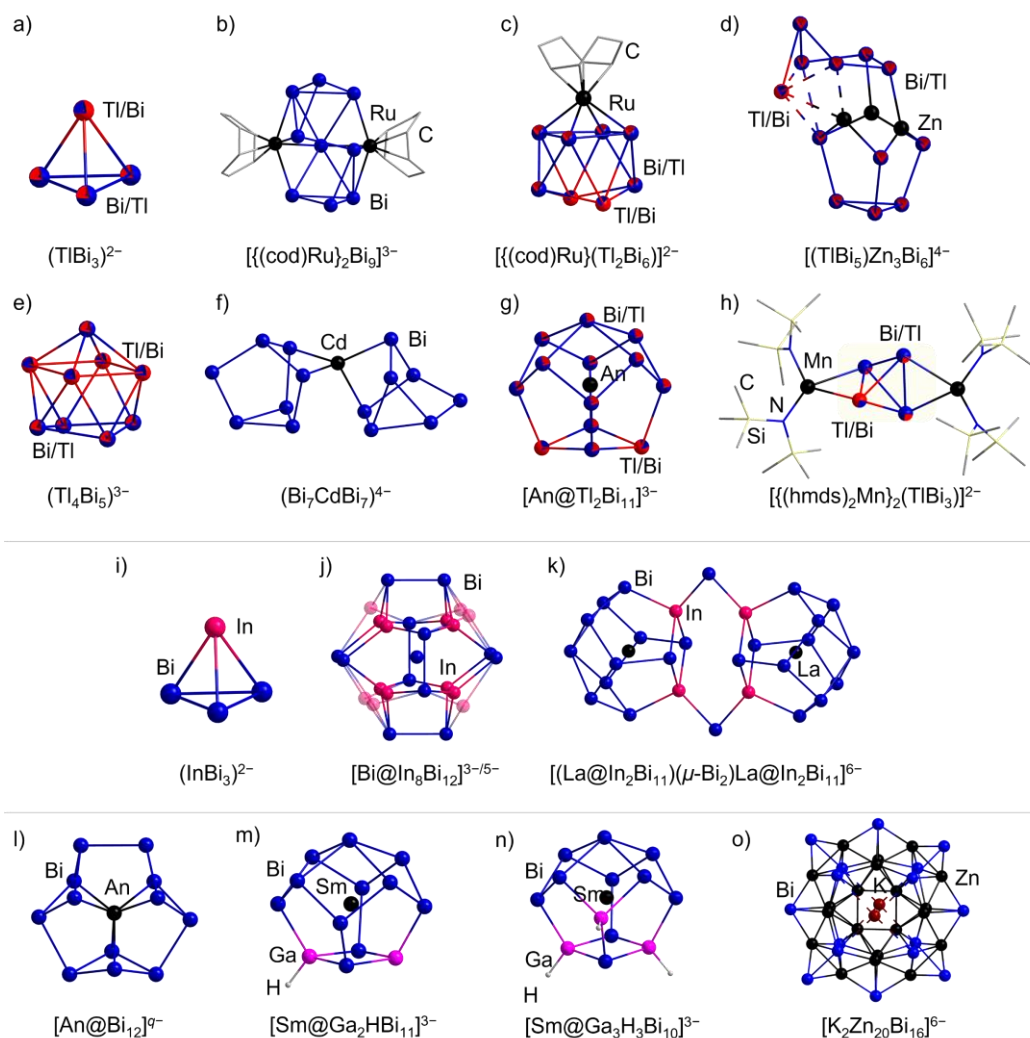


Figure 1.12: Molecular structures of $(\text{TlBi}_3)^{2-}$ (a),^[144] and of clusters prepared from $(\text{TlBi}_3)^{2-}$: $[(\text{cod})\text{Ru}]_2\text{Bi}_9]^{3-}$ (b),^[82] $[(\text{cod})\text{Ru}](\text{Tl}_2\text{Bi}_6)]^{2-}$ (c),^[82] $[(\text{TlBi}_5)\text{Zn}_3\text{Bi}_6]^{4-}$ (d),^[144] $(\text{Tl}_4\text{Bi}_5)^{3-}$ (e),^[144] $(\text{Bi}_7\text{CdBi}_7)^{4-}$ (f),^[144] $[\text{An}@\text{Tl}_2\text{Bi}_{11}]^{3-}$ (An = U, Th; g),^[217,224] and $[(\text{hmds})_2\text{Mn}]_2(\text{TlBi}_3)]^{2-}$ (h)^[225]. Since Tl and Bi are not distinguishable by SCXRD measurements, the corresponding atom types are drawn in two-colored fashion, with the more probable atom being indicated by the dominate color. Molecular structures of $(\text{InBi}_3)^{2-}$ (i)^[44], and of clusters that emerged from “ $\text{K}_5\text{In}_2\text{Bi}_4$ ” or $(\text{InBi}_3)^{2-}$: $[\text{Bi}@\text{In}_8\text{Bi}_{12}]^{3-/5-}$ (j),^[226] and $[(\text{La}@\text{In}_2\text{Bi}_{11})(\mu\text{-Bi}_2)\text{La}@\text{In}_2\text{Bi}_{11}]]^{6-}$ (k)^[227]. Molecular structures of clusters that have been prepared from either the ternary solid “ $\text{K}_5\text{Ga}_2\text{Bi}_4$ ” or “ $(\text{GaBi}_3)^{2-}$ ”: $[\text{An}@\text{Bi}_{12}]^q$ (An/q = Th/4, U/3; l),^[217,224] $[\text{Sm}@\text{Ga}_2\text{HBi}_{11}]^{3-}$ (m),^[228] $[\text{Sm}@\text{Ga}_3\text{H}_3\text{Bi}_{10}]^{3-}$ (n),^[228] and $[\text{K}_2\text{Zn}_{20}\text{Bi}_{16}]^{6-}$ (o)^[230]. Note that the $(\text{TlBi}_3)^{2-}$ units retained in the products are emphasized by light yellow background.

1.4.3 Synthesis of Zintl Clusters from Other Miscellaneous Units

Besides the precursor units discussed above, some more units with different motifs also appeared to serve as precursors. As briefly mentioned in Section 1.3, the homoatomic Bi_2^{2-} dumb-bell can be isolated in a $[\text{K}(\text{crypt-222})]^+$ salt by extracting K_5Bi_4 . Reactions of this salt with $[\text{CpRu}(\text{MeCN})_3][\text{PF}_6]$ (Cp = cyclopentadienide, MeCN = acetonitrile), and $[(\text{cod})\text{IrCl}_2]$, respectively, lead to the formation of the novel clusters, $[(\text{CpRu})_3\text{Bi}_6]^-$ (Figure 1.13a) and $[(\text{cod})\text{Ir}]_3\text{Bi}_6]^-$ (Figure 1.13b).^[96] Both clusters feature a $\{\text{Bi}_6\}$ prism coordinating three transi-

tion metal fragments, yet they are different in structural details. The $[\{\text{CpRu}\}_3\text{Bi}_6]^-$ cluster is based on a very regular $\{\text{Bi}_6\}$ prism, and displays a new type of aromatic property, ϕ -aromaticity, involving two coplanar $\{\text{Bi}_3\}$ triangles. The $[\{(\text{cod})\text{Ir}\}_3\text{Bi}_6]^-$ cluster possesses a more distorted $\{\text{Bi}_6\}$ prism which does not show ϕ -type aromaticity.

The extraction of “ K_2GeBi ” has afforded the binary $(\text{Ge}_4\text{Bi}_{14})^{4-}$ anion, which is isostructural to the $(\text{Ge}_4\text{Sb}_{14})^{4-}$ anion (Figure 1.10c).^[218] However, a “ $(\text{Ge}_2\text{Bi}_2)^{2-}$ ” anion has never been isolated, in agreement with no miscibility between Ge and Bi in well-defined binary solids.

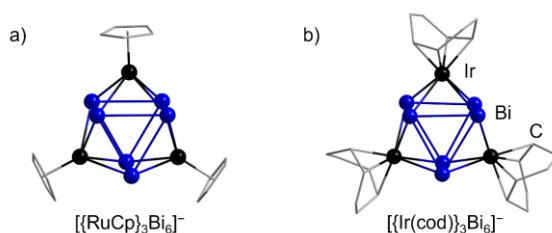


Figure 1.13: Molecular structures of $[\{\text{CpRu}\}_3\text{Bi}_6]^-$ (a), and $[\{(\text{cod})\text{Ir}\}_3\text{Bi}_6]^-$ (b), that were synthesized using Bi_2^{2-} salts. All the hydrogen atoms are omitted for clarity.^[96]

1.5 Electronic Situation and Structures of Zintl Clusters

In addition to exploring novel Zintl anions to form larger Zintl clusters, one of the keystones is to understand the bonding properties of these clusters. This requires the need of certain rules to analyze different types of clusters, which in many cases refers to the number of valence electrons.

1.5.1 Concept of Electron-Precise Zintl Anions and Clusters

In an electron-precise compound, all electrons can be localized into 2-center-2-electron (2c-2e) bonds and lone pairs (1c-2e). Such electron configuration results in the formation of $8-N$ bonds per atom, where N is the number of valence electrons of the respective atom or (charged) *pseudo*-atom. For heavier main group elements, electrons in s orbital typically manifest as lone pairs, whereas electrons in p orbital electrons tend to contribute to bonds with neighboring atoms.

In a neutral Pn_4 ($\text{Pn} = \text{P}, \text{As}$) unit, for instance, each pnictogen atom bonds to three other atoms, forming a tetrahedron with a total valence count of $5n$, where n is the number of the vertices. This also applies to derivatives of negatively charged homoatomic, and binary (*pseudo*-)tetrahedral units composed of group 13-15 elements. Group 15 atoms perfectly exhibit their five valence electrons, whereas group 13-14 atoms do not. The electron assignment for these atoms, is explained by the Zintl-Klemm-Busmann concept.^[53,231] For instance, in the structure of Ge_4^{4-} , a Ge^- anion is isoelectronic to an As^0 atom, therefore it behaves like a *pseudo*-group 15 atom; in the larger Bi_7^{3-} anion, four three-bonded Bi atoms maintain a formal charge of zero, while three two-bonded Bi atoms behave as *pseudo*-group 16 atoms, which therefore can be

viewed as monocharged Bi anions, corresponding to the overall 3[−] charge of Bi₇^{3−}.^[74] Also many more complicated structures, including ternary intermetallic clusters, can be electron-precise. Examples include [Ta@Ge₈As₄]^{3−}, and [Ln@Pb₇Bi₇]^{4−}, the p-block atom shells of which are isoelectronic to hypothesized neutral group 15 cages.^[84,216] These two clusters can be understood through the donation of valence electrons from the central atom (5e[−] for Ta, and 3e[−] for Ln) to the cluster shell, which leads to them being 5n clusters, as well.

1.5.2 Concept of Electron-Deficient Zintl Anions and Clusters

In contrast to the structures involving only 1c-2e or 2c-2e interactions, many species are known to exist that exhibit electron delocalization in multicenter bonds. Some of them can be described by the Wade-Mingos rules that were originally formulated to explain the structure and bonding of polyhedral boranes and their derivatives.^[232–234] Wade-Mingos rules can be extended to similar (semi-)metal cages, specifically electron-deficient Zintl anions and clusters.^[235–238]

Complete deltahedra with no missing vertexes are known as *closo*-type cages, and deltahedra missing one to three vertexes are described as *nido*, *arachno*, or *hypho* cages, respectively. Corresponding formula and examples are shown in Table 1.2. Note that odd numbers of valence electrons can also be found in electron-deficient cages, such as Ge₉^{3−}, which represent defective variants.^[159–161]

Table 1.2: Classification and examples of Zintl anions according to Wade-Mingos Rules.

Cluster type	Valence electrons	Examples
<i>closo</i>	2n+2	Pb ₁₀ ^{2−} [239]
<i>nido</i>	2n+4	Ge ₉ ^{4−} [58,64–67]
<i>arachno</i>	2n+6	Sn ₈ ^{6−} [240]
<i>hypho</i>	2n+8	Sn ₃ Bi ₃ ^{5−} [94]

In electron-deficient Zintl anions and clusters, a facile way of elucidating the electron configuration is to obtain the skeleton electron number (SEN), by summing up the valence electron number (VEN) and the overall charge of the cage. Wade postulated that each of the main group atoms has an exohedral electron pair and orbital pointing outward from the cage, with the remaining electrons and three orbitals used for the skeleton bonds. For transition metal atoms, correspondingly 12 electrons (in 6 orbitals) do not contribute to bonding within the cage, while all remaining electrons and 3 orbitals again contribute to the skeleton bonds. The SEN is calculated by subtracting 2 exo-electrons of each main group atom (with a total number of n) and 12 exo-electrons of each transition metal atom (with a total number of m) from the VEN. The relationship between VEN and SEN is presented in eq 1.9, illustrating the calculation of the SENs based on Wade-Mingos rules.

$$\text{SEN} = \text{VEN} - 2 \cdot n - 12 \cdot m \quad (1.9)$$

2 Research Objectives and Questions

As mentioned in Section 1, the relative size and electron affinity of the elements in binary p-block (semi-)metal *pseudo*-tetrahedra are crucial factors towards the formation of the Zintl clusters. Considering the size factor alone, most binary *pseudo*-tetrahedra would stay intact when reacting with metal complexes. In fact, only *pseudo*-tetrahedra consisting of atoms of the lighter elements of periods 3 and 4 tend to retain their original units, whereas *pseudo*-tetrahedra comprising heavier p-block element atoms usually undergo fragmentation and reorganization. One reason might be the nature of stronger covalent bonds in the lighter *pseudo*-tetrahedra. The influence of electron affinity is evident in the range of the products obtained from the group 13/15 and group 14/15 units. The group 13 elements, which have lower electron affinities, show a more distinct tendency to be oxidized and further released as the elements as compared to group 14 elements.

The addition of various transition metal complexes can modulate the reaction conditions, providing a more Lewis-acidic environment, which might result in different formation pathways and products. For instance, reactions of Zintl precursors with f-block metal complexes are known to yield preferably intermetalloid clusters, whereas reactions with d-block metal complexes result in both heteroatomic clusters and intermetalloid clusters with similar preference. In some cases, these metal complexes are not part of the cluster, yet are supposed to play a crucial role in the reaction, as the clusters do not form in their absence.

The nature of the transition metal also has an impact on the reaction path. As observed in reactions of $(\text{TlBi}_3)^{2-}$ with group 12 metal compounds $[\text{MPh}_2]$ ($\text{M} = \text{Zn}, \text{Cd}, \text{Hg}$), three different clusters were isolated, respectively.^[144] The subtle changes in the relative charge on the metal may play a significant part in this outcome. Additionally, the ligands on the metal complexes may have subtle effects on the transition metal electron density depending on the electron donation or withdrawal nature of the ligand, and the entire cluster, which also needs to be taken into consideration when choosing the transition metal complexes.

Taken all of these facts into account, the following research objectives arouse:

Two ternary Zintl solids, containing either the “match” elements, Ge and As, or the “mismatch” elements, Ga and Bi, will be applied as the precursors in reactions with different d- or f- block metal complexes in this thesis. The aim is to characterize and understand the novel clusters obtained from these two systems, and to further collect information about the reactivity and reaction pathways of these elemental combinations. Note that the terms “match” and “mismatch” refer to the relative size as well as the electron affinity of the elements in their respective combination. The research questions and hypotheses to be addressed in this project are listed below.

For the “match” Ge/As system:

-
- Do $(\text{Ge}_2\text{As}_2)^{2-}$ and $(\text{Ge}_3\text{As})^{3-}$ always tend to stay intact in the sphere of d^{10} metal fragments or is it possible to fragment $(\text{Ge}_2\text{As}_2)^{2-}$ or $(\text{Ge}_3\text{As})^{3-}$ and form novel clusters in corresponding redox reactions?

For the “mismatch” Ga/Bi system:

- Can an intact “ $(\text{GaBi}_3)^{2-}$ ” unit be found, and if not, can Ga and Bi be incorporated together in other structures?
- Is the tendency of reactions of group 13/Bi units with transition metal complexes to form large Bi-rich clusters a general feature that can be further expanded?

For both systems:

- How does the chemical behavior of the Ge/As and Ga/Bi systems differ from each other and from other systems?
- Can we get more insight into the cluster formation pathway?
- Is it possible to further functionalize these clusters, or do these systems provide any hints towards catalytic reactions?

Section 3 and 4 will demonstrate expansions of the Ge/As and Ga/Bi systems in corresponding reactions with d- and f-block metal complexes. Products are characterized by means of X-ray diffraction, spectroscopy and spectrometry. DFT calculations, which are carried out in cooperations, helped to answer these questions/hypotheses as detailed as possible.

3 Behavior of “K₂GeAs” Solids in the Formation of Ternary Ge/As-based Clusters

3.1 Introduction

Main group tetrahedra acting as ligands to transition metal atoms has a long tradition for P₄, and more recently realized for As₄ and also anionic group 14 tetrahedra, too. By the *pseudo*-element concept, exchanging the phosphorus atoms with other group 15 atoms and with (negatively charged) group 13 or group 14 atoms provided the foundation for the exploration of homoatomic and heteroatomic species.^[115–126] These tetrahedral species proved to be excellent building blocks for novel molecular architectures and for introducing new elemental combinations which are not otherwise accessible.

The use of d¹⁰ metal compounds has shown great promise in this regard, as these redox inert species ensure that the respective tetrahedron remains intact. Homoatomic examples without organic substituents bound to the metal atom demonstrated the ability of anionic tetrahedral molecules to function as terminal ligands to metal centers, affording complexes of the general formula [M(Tt₄)₂]^{q−}, such as [Zn(η³-Ge₄)₂]^{6−}, [Zn(η²-(Si/Ge)₄)₂]^{6−}, [Au(η²-Sn₄)₂]^{7−}, and [(η²-Sn₄)Zn(η³-Sn₄)]^{6−}, which were obtained as neat solids by solid state reactions, or as ammoniates of their alkali metal salts from extraction solutions of Zintl phases in liquid ammonia.^[132,135,136,241] The presence of metal-ligand fragments was accessed by using d¹⁰ metal atoms in the form of an organometallic complex, which reacts with different phases and solids in an appropriate solvent. The first examples were a series of [{MesCu}₂(μ,η^{3:3}-Tt₄)]^{4−} (Tt₄ = Si₄, Ge₄, Si_{3.3}Ge_{0.7}; Mes = mesityl) clusters with four-atom units bridging two {MesCu} fragments.^[138–140] A larger supertetrahedral cluster, [M₆(μ,η^{2:2:2}-Ge₄)₄]^{4−} built up from Ge₄^{4−} clusters and either Zn or Cd atoms was also achieved by reaction of corresponding binary solids with organometallic complexes.^[141]

Analogous heteronuclear *pseudo*-tetrahedral anions of Tt and Pn elements, i.e., (Tt₂Pn₂)^{2−}, have also been shown to coordinate to d¹⁰ metal atoms, namely in the examples of [Au(η²-Sn₂Sb₂)₂]^{3−}, and the recently reported [Au{η²-Tt₂Bi₂}₂]^{3−} (Tt = Sn, Pb).^[210,211,222,223] For the reactions of lighter *pseudo*-tetrahedral units, (Ge₂P₂)^{2−} and (Ge₂As₂)^{2−}, with other d¹⁰ metal complexes, a distinct change in the reaction outcome has been found. Coordination clusters such as the pin-wheel-like shaped [Cd₃(μ,η^{2:3}-Ge₃P)₃]^{3−}, and the supertetrahedral [Au₆(μ,η^{2:2:2}-Ge₃As)(μ,η^{2:2:2}-Ge₂As₂)₃]^{3−} clusters, both exhibit an exchange of the atomic composition in the parent *pseudo*-tetrahedron on cluster formation from a Ge/Pn ratio of 2:2 to 3:1.^[83,208] This exchange process appears to be a property inherent to the elements the tetrahedron is comprised of.

As mentioned in Section 1.4, the reaction pathway of heteronuclear clusters is related to the size and electron affinity of the elements involved. Oftentimes, the reactions of Sb- and Bi-based tetrahedra with transition metal complexes show a strong tendency to form clusters which are less predictable, usually accompanied by redox reactions, only a few retain the original tetrahedra as the ligands (see Section 1.4.2). In contrast, those *pseudo*-tetrahedral anions with lighter elements (Ge, P, As) predominantly maintain their *pseudo*-tetrahedral structures, as shown with the examples above. The balance of the reaction pathway not only lies with the cluster elements, but also with the organometallic reagent used, as observed in $[\text{Au}\{\eta^2\text{-(Sn}_2\text{Sb}_2)\}_2]^{3-}$, and $[\{\text{Cu}(\text{Sn}_5\text{Sb}_3)\}_2]^{4-}$.^[210,212] Understanding this balance is one of the keystones for the prediction of cluster formation pathways and remains as a significant challenge.

Over the past several years, both salts of binary *pseudo*-tetrahedral p-block anions and also ternary solids as in-situ sources for said anions have been used to discern their properties and follow-up chemistry. Elucidation of cluster growth steps remains an endeavor needed to be tackled, therefore the ternary solid, “K₂GeAs”, was selected as a source for stable 4-atom anions, reacting with d¹⁰ metal complexes as well as other group 7-12 metal complexes. The aim is to gain access to a diverse family of clusters, which enables investigation into the reactivity of the Ge/As system, as well.

3.2 Synthesis and Investigation of the Ternary “K₂GeAs” solids

The solids of the nominal composition “K₂GeAs” were synthesized via combining elements in a carbonized silica tube, which was placed into an oven for a defined temperature profile. The detailed synthesis information and the X-ray powder diffraction patterns are showed in Section 6.3.

Typically, the extraction and subsequent crystallization of ternary K/Tt/Pn solids with en and crypt-222 leads to the exclusive formation of salts of the composition $[\text{K}(\text{crypt-222})]_2(\text{Tt}_2\text{Pn}_2)$. This applies to “K₂GeAs”, too. A previous study has indicated that the energetically more favorable side lies to the right-hand side of a potential equilibrium between two equivalents of $(\text{Ge}_2\text{As}_2)^{2-}$ and one equivalent each of $(\text{Ge}_3\text{As})^{3-}$ and $(\text{GeAs}_3)^{-}$.^[208] To confirm a distribution of possible *pseudo*-tetrahedra during the extraction process, an in-situ electrospray ionization mass spectrometry (ESI-MS) measurement was recorded. The sample was prepared from a fresh en solution of “K₂GeAs” and crypt-222 after stirring for five minutes, filtration and dilution with toluene. The spectrum in Figure 3.1 indeed shows signals of $(\text{Ge}_3\text{As})^{-}$ at m/z 292.7, $(\text{Ge}_3\text{AsH}_2)^{-}$ at m/z 294.7, $(\text{Ge}_2\text{As}_2\text{H})^{-}$ at m/z 296.7, and $(\text{GeAs}_3)^{-}$ at m/z 298.7 (note that Zintl anions often undergo oxidation to a 1- charge under ESI-MS conditions). This clearly demonstrates the coexistence of these different binary species upon extraction of “K₂GeAs”. For the full spectrum and other species, see Section 7.3.1.

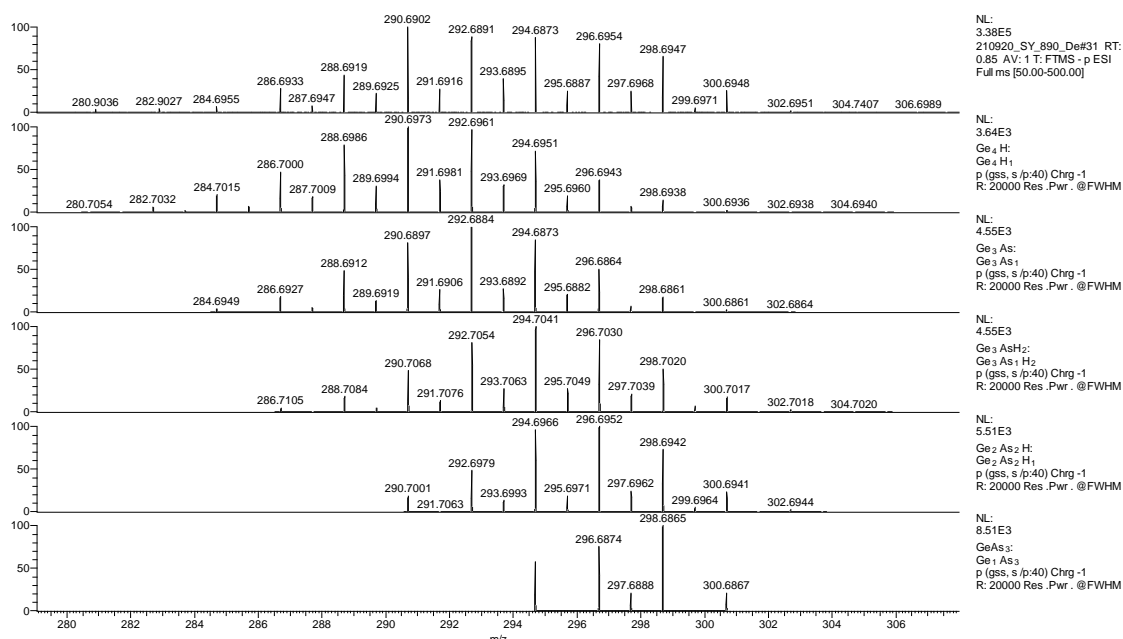


Figure 3.1: High-resolution electrospray-ionization mass spectrum in negative ion mode of a fresh solution of “K₂GeAs” in en/tol between 280 m/z and 305 m/z. Assignment of the peaks are written on the right-hand side of the spectrum. Topmost: measured isotope patterns, second from top down to bottom: simulated isotope patterns (from top in the order listed here).

Different from the in-situ mass spectrum of the “K₂GeAs” solid showed in Figure 3.1, the mass spectrum obtained upon directly dissolving the (Ge₂As₂)²⁻ salt in en showed only the predominant signal of (Ge₃As)⁻ at m/z 298.7 and the signal of (Ge₂As₂H)⁻ at m/z 296.7 with minor intensity (Figure 3.2). In fact, the species detected in ESI-MS (–) studies of Zintl anions do not necessarily reflect to their original charge, but, as a result of a rapid in-situ oxidation during the measurement, is usually less negative (typically 1–). It remains unclear as to why only (Ge₃As)⁻ was detected in the mass spectrum of the (Ge₂As₂)²⁻ salt in en. However, it is clear that the “K₂GeAs” solid can provide a wider variety of binary species compared to the (Ge₂As₂)²⁻ salt, and serves as a more reactive starting material. This was also observed for other systems, such as “K₅Ga₂Bi₄” and “(GaBi₃)²⁻”.^[230] This is the reason for selecting the ternary “K₂GeAs” solid rather than the (Ge₂As₂)²⁻ salt for the formation of Ge/As-based clusters.

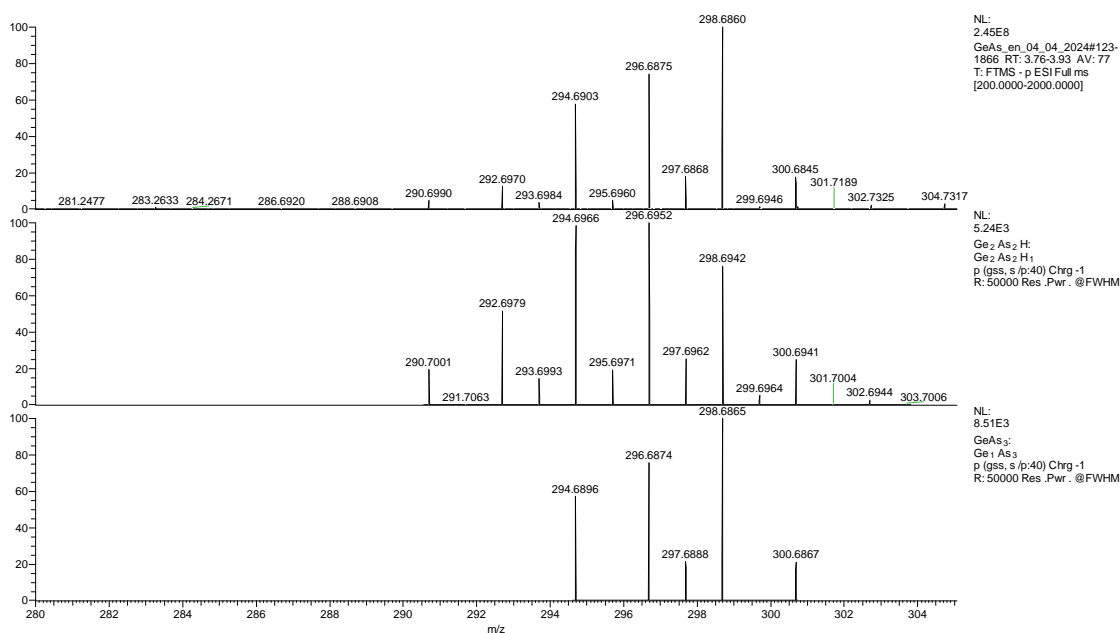


Figure 3.2: High-resolution electrospray-ionization mass spectrum in negative ion mode of a fresh solution of redissolving $(\text{Ge}_2\text{As}_2)^{2-}$ salts in en between 280 m/z and 305 m/z. Assignment of the peaks are written on the right-hand side of the spectrum. Topmost: measured isotope patterns, middle and bottom: simulated isotope patterns (from top in the order listed here).

3.3 *Pseudo-Tetrahedral* Ge/As Clusters as Ligands in the Coordination Sphere of d^{10} Metals

The results discussed in this section were published in:

S. Wei, B. Peerless, L. Guggolz, S. Mitzinger, S. Dehnen, *Angew. Chem. Int. Ed.* **2023**, e202303037.

3.3.1 Syntheses, Structures and Bonding

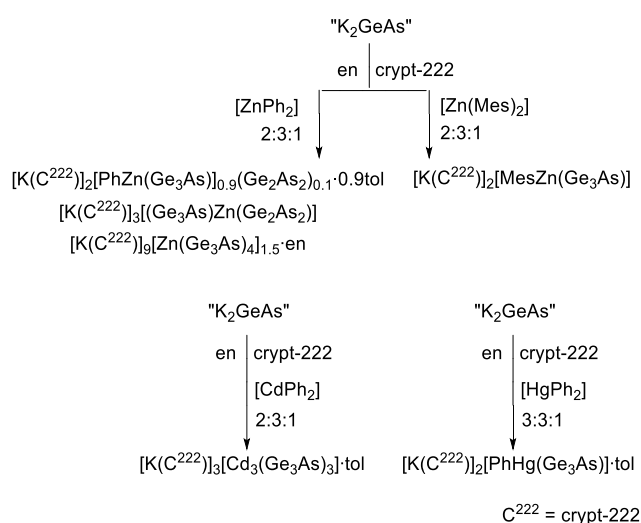
The reaction of “ K_2GeAs ”, $[\text{ZnPh}_2]$ and crypt-222 in a molar ratio of 2:1:3 in en solution enables the isolation of three types of crystals after different crystallization times. Filtration and layering the reaction solution with toluene, and subsequent storage at 5 °C for two days led to the formation of a large quantity of orange needle-shape crystals of compound $[\text{K}(\text{crypt-222})]_2[\text{PhZn}(\text{Ge}_3\text{As})]_{0.9}(\text{Ge}_2\text{As}_2)_{0.1} \cdot 0.9\text{tol}$ ($[\text{K}(\text{crypt-222})]_2(\mathbf{1})_{0.9}(\text{Ge}_2\text{As}_2)_{0.1} \cdot 0.9\text{tol}$). If the solution was stored for longer, the needle-shaped crystals started to redissolve after a few days, and two new crystalline products grew over 21 days. These were identified as $[\text{K}(\text{crypt-222})]_3[(\text{Ge}_3\text{As})\text{Zn}(\text{Ge}_2\text{As}_2)]$ ($[\text{K}(\text{crypt-222})]_2\mathbf{3}$) and $[\text{K}(\text{crypt-222})]_9[\text{Zn}_3(\text{Ge}_3\text{As})_4]_{1.5} \cdot \text{en}$ (with two different conformers of the anion, $\mathbf{5a}^{6-}$ and $\mathbf{5b}^{6-}$, in $[\text{K}(\text{crypt-222})]_9(\mathbf{5a})(\mathbf{5b})_{0.5} \cdot \text{en}$).

On changing from $[\text{ZnPh}_2]$ to $[\text{HgPh}_2]$, under slight variation of the reactant (molar) ratio to 3: 1: 3, the reaction appears to stop at $[\text{K}(\text{crypt-222})]_2[\text{PhHg}(\text{Ge}_3\text{As})] \cdot \text{tol}$ ($[\text{K}(\text{crypt-222})]_2\mathbf{2} \cdot \text{tol}$) and no further products were observed. With respect to $[\text{CdPh}_2]$, only the pinwheel-like struc-

ture [K(crypt-222)]₃[Cd₃(Ge₃As)₃]·tol ([K(crypt-222)]₃**4**·tol) was obtained upon reaction of a 2: 1: 3 (molar) mixture of “K₂GeAs”, [CdPh₂] and crypt-222.

Substitution of [ZnPh₂] with [ZnMes₂] afforded crystals that were identified as the analogous salt [K(crypt-222)]₂[MesZn(Ge₃As)] ([K(crypt-222)]₂**6**). Additionally, [Zn(C₆F₅)₂] and ZnCl₂ were also used, however led to inconclusive result and seemed to only decompose the cluster anions to metal powders. Scheme 3.1 summarizes the syntheses of compounds comprising anions **1**²⁻ – **6**²⁻.

Scheme 3.1: Syntheses of compounds [K(crypt-222)]₂(**1**)_{0.9}(Ge₂As₂)_{0.1}·0.9tol – [K(crypt-222)]₂**6** by treatment of “K₂GeAs” in en/crypt-222 in the presence of a series of d¹⁰ transition metal complexes and subsequent crystallizations by layering with toluene (for the detailed molar ratio, see text above).



As mentioned in Section 1.4.2.1, neither the ratio nor the exact atomic position of the Ge/As atoms in the compounds reported herein can be distinguished by X-ray diffraction alone. Therefore, within the structure models of all compounds reported, the positions of the Ge and As atoms have been statistically refined over all atom sites in the *pseudo*-tetrahedra. The atomic compositions were rationalized by means of the *pseudo*-element concept in accordance with the total charges of the product clusters and confirmed by μ -XFS studies, the combination of which also ruled out protonation of any of the clusters in the crystalline products. The most probable site occupancies were elucidated using DFT calculations, the results of which are illustrated in the structure figures by a predominance of the respective atom color (yellow = Ge, blue = As) in the two-colored thermal ellipsoids (see below).

Given that anions **1**²⁻, **2**²⁻, **6**²⁻ are related owing to their chemical compositions and similar structures, these three compounds are discussed together. Side views, and front views of the molecular structures of anion **1**²⁻, **2**²⁻ and **6**²⁻ are presented in Figure 3.3. Compounds [K(crypt-222)]₂(**1**)_{0.9}(Ge₂As₂)_{0.1}·0.9tol, [K(crypt-222)]₂**6**·tol both crystallize in the orthorhombic space group type *Pnma*, and compound [K(crypt-222)]₂**2** also crystallizes in another orthorhombic space group, *Pbnm*. All three compounds contain four formula units per unit cell. The unit cell of each compound is shown respectively in Figure 3.4. As seen from Figure 3.4, the anionic molecules are aligning between cations.

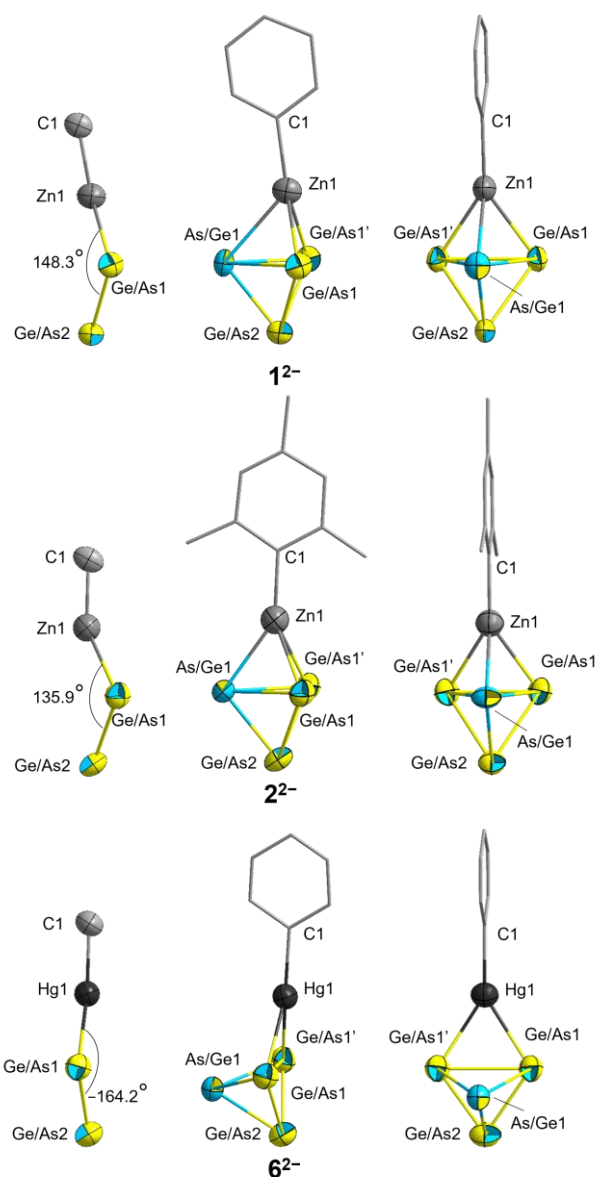


Figure 3.3: Side views (left and center) and front view (right) of the molecular structures of the anions $[\text{PhZn}(\text{Ge}_3\text{As})]^{2-}$ (1^{2-}) in compound $[\text{K}(\text{crypt-222})]_2(\mathbf{1})_{0.9} \cdot (\text{Ge}_2\text{As}_2)_{0.1} \cdot 0.9\text{tol}$, $[\text{PhHg}(\text{Ge}_3\text{As})]^{2-}$ (2^{2-}) in compound $[\text{K}(\text{crypt-222})]_2 \cdot \text{tol}$, and $[\text{MesZn}(\text{Ge}_3\text{As})]^{2-}$ (6^{2-}) in compound $[\text{K}(\text{crypt-222})]_2 \mathbf{6}$ with thermal ellipsoids drawn at 50% probability. Since Ge and As atoms cannot be distinguished, the corresponding atom types are drawn in two-colored fashion (yellow-blue), with the more probable atom according to quantum chemical calculations being indicated by the dominant color (see text).

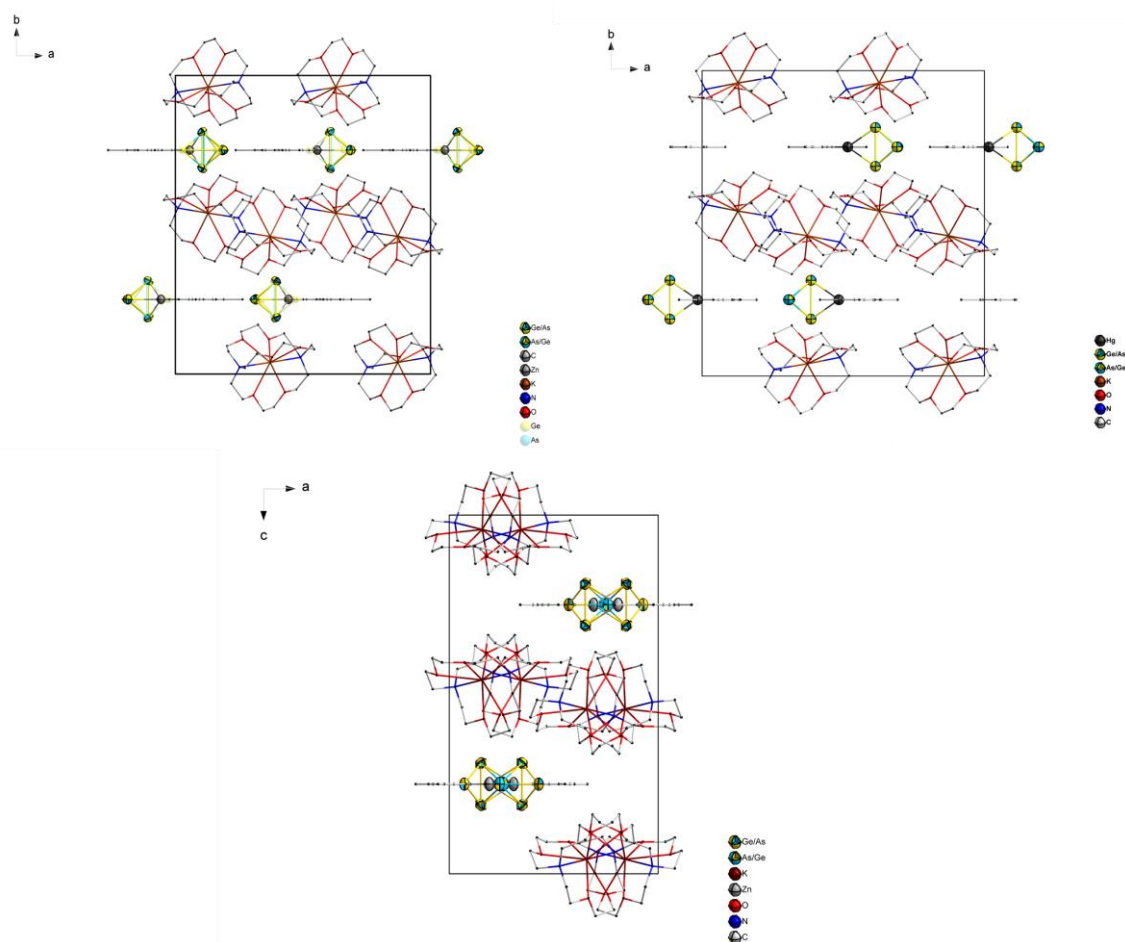


Figure 3.4: Top left: view of the (extended) unit cell of compound $[\text{K}(\text{crypt-222})]_2(\mathbf{1})_{0.9}(\text{Ge}_2\text{As}_2)_{0.1} \cdot 0.9\text{tol}$, viewed along the crystallographic c -axis. Top right: view of the (extended) unit cell of compound $[\text{K}(\text{crypt-222})]_2 \cdot \text{tol}$, viewed along the crystallographic c -axis. Bottom: view of the (extended) unit cell of compound $[\text{K}(\text{crypt-222})]_2 \mathbf{6}$, viewed along the crystallographic b -axis. H atoms are omitted for clarity.

The single crystal structure analyses of $[\text{K}(\text{crypt-222})]_2(\mathbf{1})_{0.9}(\text{Ge}_2\text{As}_2)_{0.1} \cdot 0.9\text{tol}$ and $[\text{K}(\text{crypt-222})]_2 \mathbf{2} \cdot \text{tol}$ show both anions with a general formula of $[\text{PhM}(\text{Ge}_{4-x}\text{As}_x)]^{2-}$ (for $\text{M} = \text{Zn}$ in combination with a 10% co-crystallization of the $(\text{Ge}_2\text{As}_2)^{2-}$ anion). However, the coordination mode of the *pseudo*-tetrahedron differs between the Zn and Hg compounds (Figure 3.3, top and center). The presence of two $[\text{K}(\text{crypt-222})]^+$ molecules observed in the structures indicate an anion possessing an overall charge of 2^- , and, consequently, the *pseudo*-tetrahedron therefore has a $3-$ charge and a composition of Ge:As of 3:1. In both molecules, the coordination of the tetrahedron to the metal atom was shown to have a preference for the Ge–Ge bond by DFT calculations (discussed in more detail below).^[242] The $(\text{PhZn})^+$ unit in $\mathbf{1}^{2-}$ is coordinated by the $(\text{Ge}_3\text{As})^{3-}$ tetrahedron in a $\eta^3\text{-Ge}_2\text{As}$ fashion, similar to complexes containing d^{10} transition metal fragments and Ge_4^{4-} , such as $[\{\text{EtZn}\}_2(\mu, \eta^{3:3}\text{-Ge}_4)]^{2-}$ ($\text{Et} = \text{ethyl}$) and $[\{\text{MesCu}\}_2(\mu, \eta^{3:3}\text{-Ge}_4)]^{4-}$.^[140,243] However, the Zn atom does not sit exactly above the center of the triangular face, but rather offset towards the Ge–Ge bond. In $\mathbf{2}^{2-}$, the coordination mode is only $\eta^2\text{-Ge}_2$ with no significant As contribution at all. The difference in the coordination mode can be seen clearly in

different dihedral angles between the Ge_3 faces and the Ge_2M planes of $\mathbf{1}^{2-}$ compared to $\mathbf{2}^{2-}$ (148.3° vs. -164.2°).

Similarly, the anion in $[\text{K}(\text{crypt-222})]_2\mathbf{6}$ has an analogous structure to $\mathbf{1}^{2-}$. The *pseudo*-tetrahedron is coordinated in an $\eta^3\text{-Ge}_2\text{As}$ fashion, however, the Zn atom is more aligned to the center of the Ge_2As triangle. The bond length range between Zn–Ge/As is narrower in $\mathbf{6}^{2-}$ than $\mathbf{1}^{2-}$ ($2.4920(15)$ Å, $2.5237(12)$ Å vs. $2.657(2)$ Å, $2.4525(17)$ Å respectively), and is equally reflected in the Ge/As–Zn–Ge/As bond angles. This, however, seems to be due to a steric effect within the packing of the crystal structure.

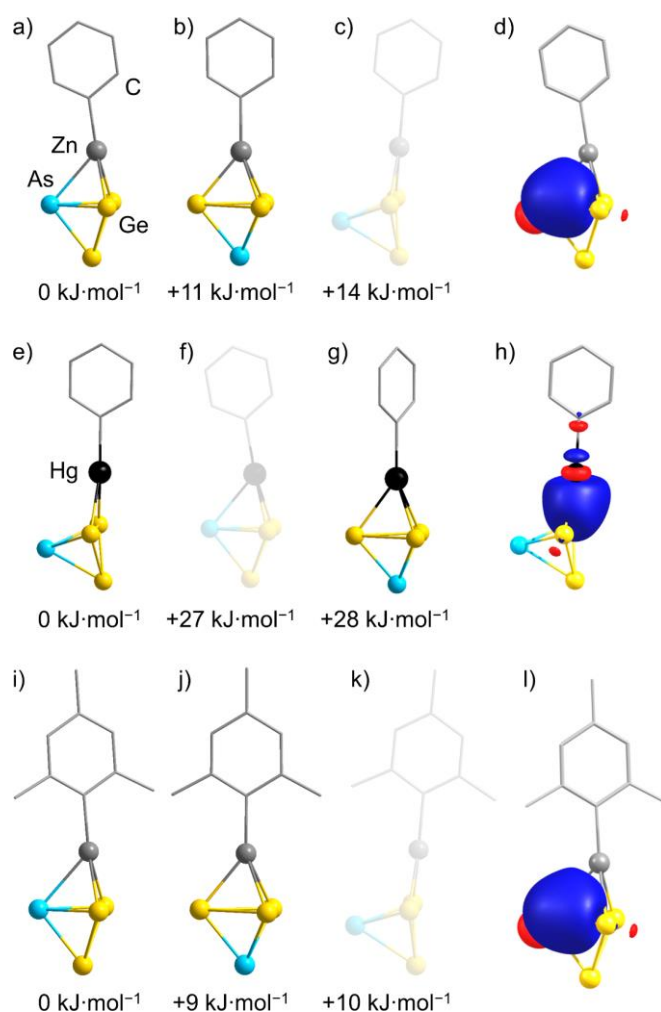


Figure 3.5: Computationally optimized minimum structures of the possible conformers of $\mathbf{1}^{2-}$ (a–c), $\mathbf{2}^{2-}$ (e–g), and $\mathbf{6}^{2-}$ (i–k), as well as LMOs of (d, l) one of two equivalent weak two-electron-three-center Zn–Ge–As interactions of the *pseudo*-tetrahedral moiety with the respective $(\text{RZn})^+$ fragment and (h) of the two-electron-three-center interaction of the *pseudo*-tetrahedral moiety with the $(\text{PhHg})^+$ fragment. H atoms are omitted in the images for clarity. Conformers that were computed with constrained dihedral angles for comparison are shown in semitransparent mode. Contour values are drawn at ± 0.05 a.u. The methods are detailed in Section 7.4.1.

DFT calculations served to determine the atom assignment. Capping of the Ge_2As face (Figure 3.5) instead of the Ge_3 face (Figure 3.5b) in $\mathbf{1}^{2-}$ seems counterintuitive at first. However, inspection of the canonical molecular orbitals (MOs) of the parent $(\text{Ge}_3\text{As})^{3-}$ *pseudo*-tetrahedron (see Figure 3.6)^[208] showed the doubly-degenerate highest occupied molecular orbital (HOMO) to mainly represent the Ge–Ge bond with a minor contribution of the As atom, while HOMO–1 is found in the center of the trigonal Ge_3 face. Thus, the experimentally found conformer of $\mathbf{1}^{2-}$ is energetically favored by $11 \text{ kJ}\cdot\text{mol}^{-1}$ over the conformer in which the $(\text{PhZn})^+$ fragment caps the Ge_3 face.

A complete neglect of the $\text{Zn}\cdots\text{As}$ interaction would be disadvantaged by $14 \text{ kJ}\cdot\text{mol}^{-1}$ (Figure 3.5c). However, localization of the molecular orbitals to form localized molecular orbitals (LMOs) and population analyses showed that the $\text{Zn}\cdots\text{As}$ interaction is weaker than the Zn–Ge bonds. This is the reason why the $(\text{PhZn})^+$ fragment is not situated centrally above the Ge_2As face (Figure 3.5d).

In contrast to the Zn atom in $\mathbf{1}^{2-}$, the Hg atom in $\mathbf{2}^{2-}$ has a trigonal coordination sphere (Figure 3.5e). So, the Ge–Ge bond of the *pseudo*-tetrahedral moiety coordinates to it in an $\eta^2\text{-Ge}_2$ fashion (Figure 3.5h), while an interaction with the Ge_2As or the Ge_3 faces (Figures 3.5f, 3.5g) would be disadvantaged by 27 or $28 \text{ kJ}\cdot\text{mol}^{-1}$, respectively. This can be explained in part by the calculated Mulliken partial charges of the respective metal atoms in the $(\text{PhM})^+$ fragment (+0.7 for Zn and +0.6 for Hg). The tendency to compensate for the higher positive charge by interacting with the more negatively polarized As atom of the parent $(\text{Ge}_3\text{As})^{3-}$ anion (-0.9 vs. -0.7 for the Ge Atom) is thus stronger for the Zn atom. A better compensation of the positive charges is probably also the reason why the $(\text{PhM})^+$ fragments – at least in this case – interact more readily with the $(\text{Ge}_3\text{As})^{3-}$ anions, than with the $(\text{Ge}_2\text{As}_2)^{2-}$ anions, due to the higher overall charge of the former, eventually leading to the formation of $\mathbf{1}^{2-}$ and $\mathbf{2}^{2-}$.

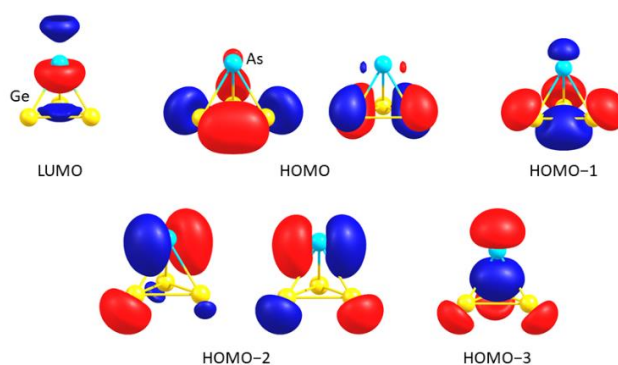


Figure 3.6: Canonical MOs of anion $(\text{Ge}_3\text{As})^{3-}$ (point group: C_{3v}). Contour values are drawn at ± 0.05 a.u. The methods are detailed in Section 7.4.1.

The computationally obtained minimum structure of $\mathbf{6}^{2-}$ exhibits the same elongation of the Zn–As bond, as found in $\mathbf{1}^{2-}$ (see Section 7.4.1). DFT calculations also show little difference in the Mulliken partial charges of the atoms in the molecules. Only the C atom bonded to the Zn atom has a slightly more negative value of -0.3 vs. -0.1 in the Mes and Ph groups, respectively.

Consequently, the Zn–C bond is slightly shorter in $\mathbf{6}^{2-}$. An interaction with the Ge_3 face (Figure 3.5j) of anion $\mathbf{6}^{2-}$ would be disadvantaged by $9 \text{ kJ}\cdot\text{mol}^{-1}$, and an $\eta^2\text{-Ge}_2$ fashion coordinates to the Ge–Ge bond of the *pseudo*-tetrahedral moiety would lead to a disadvantaged energy by $10 \text{ kJ}\cdot\text{mol}^{-1}$ (Figure 3.5k). It is not possible to draw any significant conclusions from the differences between $\mathbf{1}^{2-}$ and $\mathbf{2}^{2-}$ with regards to the overall reaction cascade and the influence of the ligand sphere of the starting material, though there are slight differences on the geometric parameters of the two structures.

Two different views of anion $[(\text{Ge}_3\text{As})\text{Zn}(\text{Ge}_2\text{As}_2)]^{3-}$ ($\mathbf{3}^{3-}$) as well as the unit cell of compound $[\text{K}(\text{crypt-222})]_3\mathbf{3}$ are shown in Figure 3.7 and 3.8, respectively. $[\text{K}(\text{crypt-222})]_3\mathbf{3}$ crystalized in the monoclinic space group type $C2/c$ with four formula units per unit cell. In $\mathbf{3}^{3-}$, the Zn atom is coordinated by two different *pseudo*-tetrahedral anions, one $(\text{Ge}_2\text{As}_2)^{2-}$ and one $(\text{Ge}_3\text{As})^{3-}$. This is derived from *pseudo*-element considerations again: for a total of three negative charges, the Zn^{2+} ion must be combined with anionic ligands of 5 charges altogether, which is congruent with the named composition. Both ligands are coordinated through the atoms of a Ge–Ge edge (η^2 -coordination mode), producing an overall distorted tetrahedral geometry around the Zn atom. However, the most interesting aspect of the anion $\mathbf{3}^{3-}$ is the occurrence of two different ligands. While it was reported that the same type of ligands can coordinate in different fashions to the same metal center in such assemblies, the occurrence of two differently charged *pseudo*-tetrahedra has not yet been realized. Assuming that the $(\text{ZnPh})^+$ unit could initially interact with both of them, hence leading to anion $\mathbf{1}^{2-}$ or a yet unidentified alternative with the formula $[\text{PhZn}(\text{Ge}_2\text{As}_2)]^-$, the next step is the replacement of the second phenyl substituent with the other binary anion.

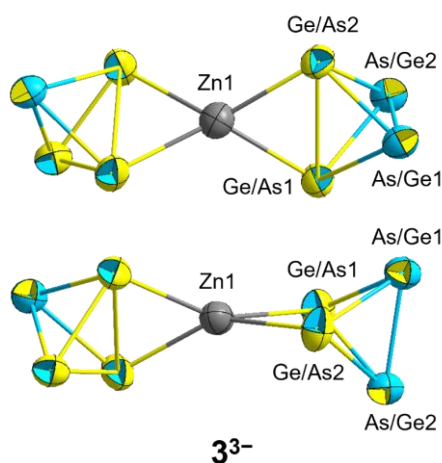


Figure 3.7: Two different views of the molecular structure of the anion $[(\text{Ge}_2\text{As}_2)\text{Zn}(\text{Ge}_3\text{As})]^{3-}$ ($\mathbf{3}^{3-}$) in compound $[\text{K}(\text{crypt-222})]_3\mathbf{3}$, with thermal ellipsoids drawn at 50% probability. Since Ge and As atoms cannot be distinguished, the corresponding atom types are drawn in two-colored fashion (yellow-blue), with the more probable atom according to quantum chemical calculations being indicated by the dominant color (see text).

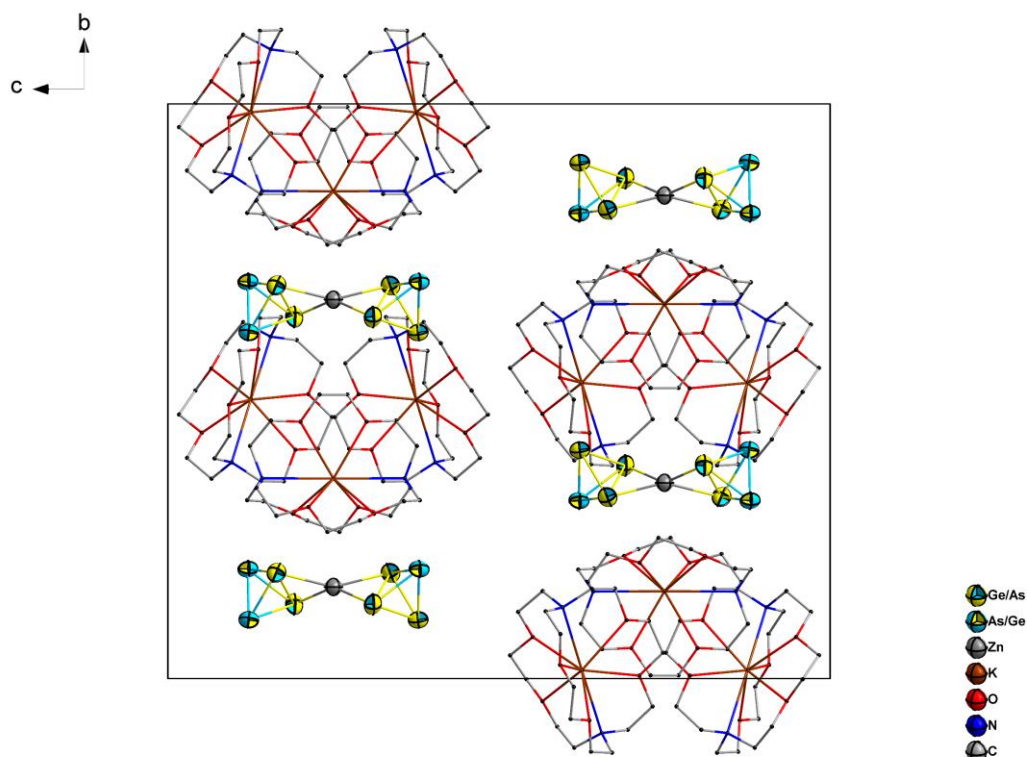


Figure 3.8: View of the (extended) unit cell of [K(crypt-222)]**33**, viewed along the crystallographic *a*-axis. H atoms are omitted for clarity.

It should be noted that the computational optimization of the geometry of the anion in **3**³⁻ without symmetry restrictions did not yield the structure depicted in Figure 3.7. Instead, the (Ge₃As)³⁻ ligand coordinates the Zn atom the same way as in **1**²⁻, hence in an η^3 -fashion. Fixation of the respective dihedral angles during the optimization, however, yielded the structure as found in **3**³⁻ (see Figure 3.9 below). The difference between the absolute energies of the global minimum and the local minimum under symmetry restrictions is not significant in context of the chosen DFT methods (5 kJ·mol⁻¹), which is plausible, considering the only weak interaction between the As and the Zn atom in **5**²⁻. The observation of the structure as shown in Figure 3.7 was ascribed to the energy differences in the lattice energy caused by the assumed different packing modes of cations and the different isomeric anions in the crystal structure.

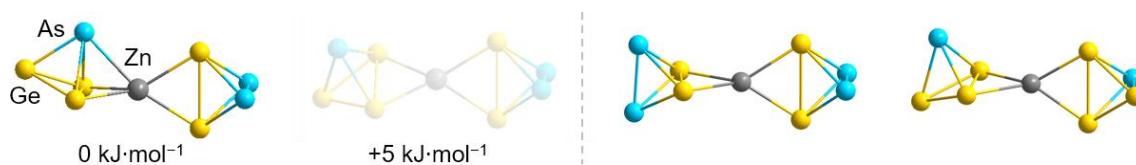


Figure 3.9: Calculated conformers of anion **3**³⁻ and relative energies ΔE with respect to the global minimum structure. The conformer that was computed with constrained dihedral angles for comparison is shown in semitransparent mode. The images to the right of the dashed gray line represent the hypothetical species ‘[(Ge₂As₂)Zn(Ge₂As₂)]²⁻’ and ‘[(Ge₃As)Zn(Ge₃As)]⁴⁻’ that were calculated for comparison (see also the energetic considerations in Scheme 3.4). The methods are detailed in Section 7.4.1.

Anion $\mathbf{4}^{3-}$ represents the heavier congener of the previously reported $[\text{Cd}_3(\text{Ge}_3\text{P})_3]^{3-}$ cluster anion, and also shows the same pinwheel-like structure (Figure 3.10).^[83] $[\text{K}(\text{crypt-222})]_3\mathbf{4}\cdot\text{tol}$ crystallizes in the hexagonal space group type $P6_5$, with six formula units per unit cell (see Figure 3.11 for the unit cell). The elemental composition was determined with the help of both the total charge/*pseudo*-element considerations and from energy-dispersive X-ray spectroscopy (EDS) (see Section 7.2). As corroborated by quantum chemistry, the assignment of As and Ge atoms is the same as for the lighter congener, all three *pseudo*-tetrahedra act as $\mu,\eta^{2:3}$ -bridging ligands, thereby using exclusively the Ge atoms for coordination. This observation is not only congruent with the formal assignment of negative charges to these atoms (which in fact is pretty much smeared over the whole *pseudo*-tetrahedron for the isolated species), but also with the nature of the HOMO (highest occupied molecular orbital) of all of these binary analogues of white phosphorous: the HOMO always comprises main contributions from Ge atoms, which are therefore the most Lewis-basic sites of the anions (see Figure 3.6).

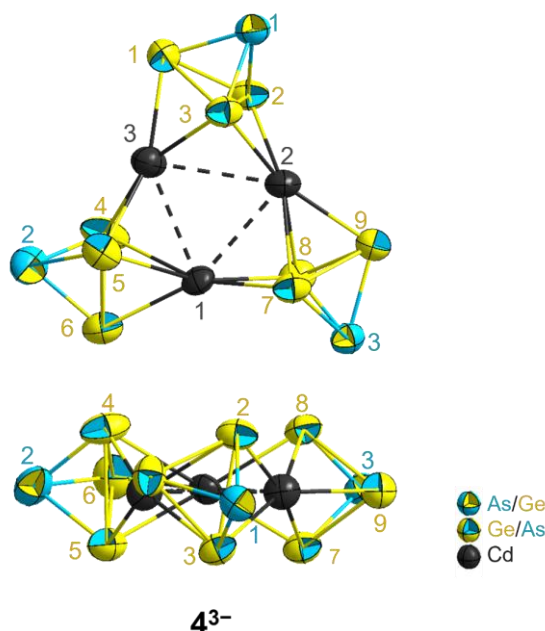


Figure 3.10: Top view (top) and side view (bottom) of the oblate molecular structure of the anion $[\text{Cd}_3(\text{Ge}_3\text{As})_3]^{3-}$ ($\mathbf{4}^{3-}$) in compound $[\text{K}(\text{crypt-222})]_3\mathbf{4}\cdot\text{tol}$, with thermal ellipsoids drawn at 50% probability. Since Ge and As atoms cannot be distinguished, the corresponding atom types are drawn in two-colored fashion (yellow-blue), with the more probable atom according to quantum chemical calculations being indicated by the dominant color; in addition, a corresponding color code was used for the atom labels (see bottom right).

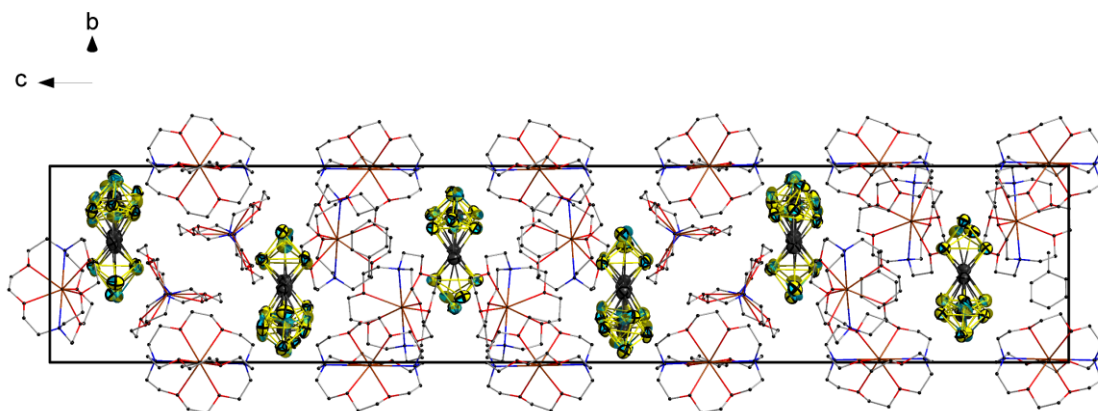


Figure 3.11: View of the (extended) unit cell of compound $[\text{K}(\text{crypt-222})]_3 \cdot 4\text{-tol}$, viewed along the crystallographic a -axis. H atoms are omitted for clarity.

A population analyses based on occupation numbers and the calculation of shared electron numbers confirmed the absence of significant $\text{Cd} \cdots \text{Cd}$ interactions, which is presented in Table 3.1 (also for the hypothetical Zn- and Hg- analogues). Moreover, the corresponding global minimum structures of both clusters (anion 4^{3-} and its hypothetical analogues) obtained from computation are presented in Figure 3.12.

Table 3.1: Calculated shared electron numbers for the respective $\text{M} \cdots \text{M}$ contacts in $[\text{Zn}_3(\text{Ge}_3\text{As})_3]^{3-}$, $[\text{Cd}_3(\text{Ge}_3\text{As})_3]^{3-}$ (4^{3-}), and $[\text{Hg}_3(\text{Ge}_3\text{As})_3]^{3-}$. The methods are detailed in Section 7.4.1.

	SEN
$\text{Zn} \cdots \text{Zn}$	0.10
$\text{Cd} \cdots \text{Cd}$	0.02
$\text{Hg} \cdots \text{Hg}$	---

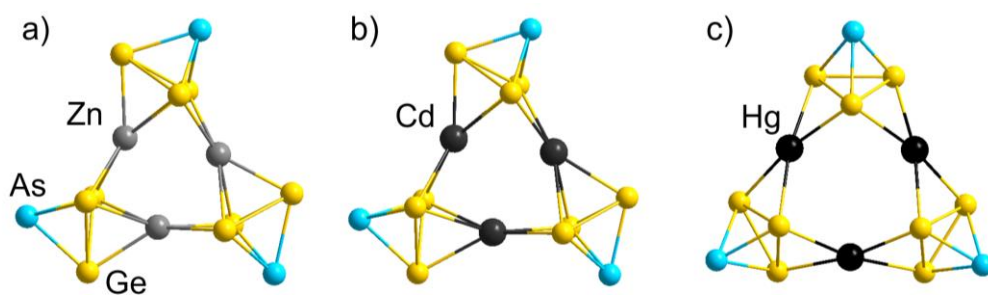


Figure 3.12: Computationally obtained global minimum structures of a) $[\text{Zn}_3(\text{Ge}_3\text{As})_3]^{3-}$, b) $[\text{Cd}_3(\text{Ge}_3\text{As})_3]^{3-}$ (4^{3-}), and c) $[\text{Hg}_3(\text{Ge}_3\text{As})_3]^{3-}$. The methods are detailed in Section 7.4.1.

In $[\text{K}(\text{crypt-222})]_9(\mathbf{5a})(\mathbf{5b})_{0.5} \cdot \text{en}$, three Zn^{2+} and a total of four $(\text{Ge}_3\text{As})^{3-}$ ligands form a chain-like coordination oligomer $[(\text{Ge}_3\text{As})\text{Zn}(\text{Ge}_3\text{As})\text{Zn}(\text{Ge}_3\text{As})\text{Zn}(\text{Ge}_3\text{As})]^{6-}$ (Figure 3.13), which nicely demonstrates the continuation of the coordination of *pseudo*-tetrahedral anions to group 12 metal ions. Two of the *pseudo*-tetrahedra act as $\mu, \eta^{2:2}$ -type bridges, and two terminal units represent η^2 -ligands.

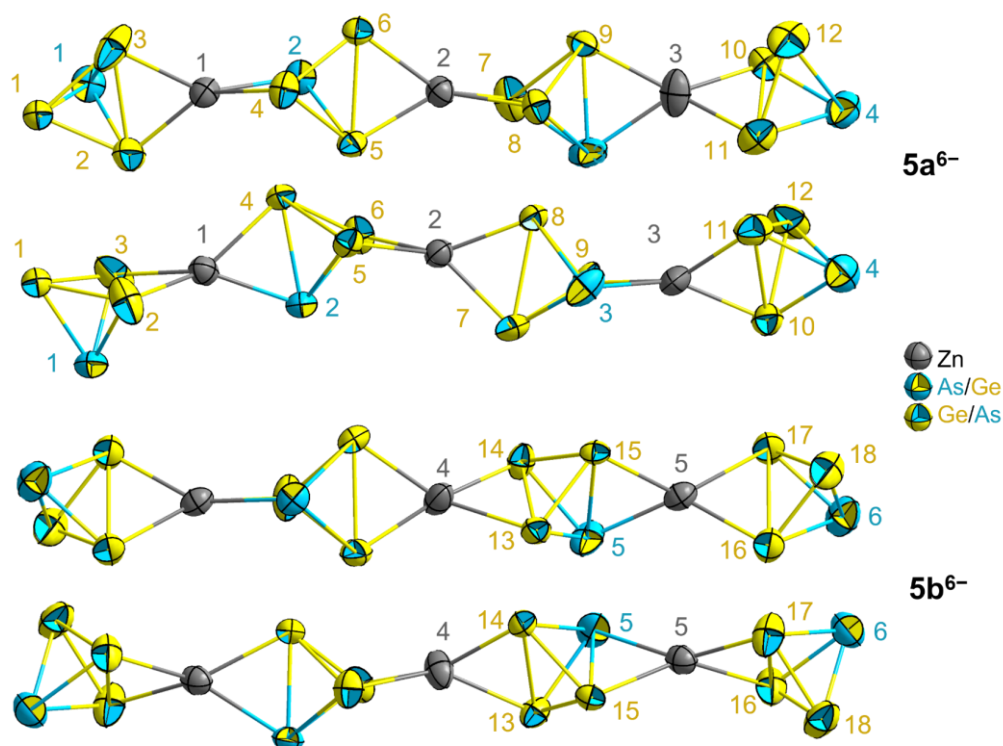


Figure 3.13: Two different views each of the molecular structures of the two crystallographically independent $[\text{Zn}_3(\text{Ge}_3\text{As})_4]^{6-}$ anions in compound $[\text{K}(\text{crypt-222})]_9(\mathbf{5a})(\mathbf{5b})_{0.5} \cdot \text{en}$, $\mathbf{5a}^{6-}$ (top) and $\mathbf{5b}^{6-}$ (bottom), with thermal ellipsoids drawn at 50% probability. Since Ge and As atoms cannot be distinguished, the corresponding atom types are drawn in two-colored fashion (yellow-blue), with the more probable atom type according to quantum chemical calculations being indicated by the dominant color; in addition, a corresponding color code was used for the atom labels (see center right). Note that within $\mathbf{5a}^{6-}$, Ge/As1, is isotropic.

$[\text{K}(\text{crypt-222})]_9(\mathbf{5a})(\mathbf{5b})_{0.5} \cdot \text{en}$ crystallizes in the triclinic space group type $P\bar{1}$, with two formula units per unit cell. The crystal structure comprises two conformers of the anion in a 1:0.5 ratio, $\mathbf{5a}^{6-}$ and $\mathbf{5b}^{6-}$, which apart from statistical disorder and structural details are very similar regarding the overall connection of Zn^{2+} ions and *pseudo*-tetrahedral units (Figure 3.14). In $\mathbf{5a}^{6-}$, all atoms are placed on general positions. However, anion $\mathbf{5b}^{6-}$ is located on an inversion center, thus producing a second set of split positions which requires all atoms to be refined as partly occupied (50% in most cases; for more details, see Section 7.1.3).

Owing to the role of the *pseudo*-tetrahedra acting as either $\mu, \eta^{2:2}$ -bridges or η^2 -type terminal ligands, the coordination environments of all Zn^{2+} ions represent (elongated) tetrahedra, as is typical for four-coordinate Zn^{2+} ions.

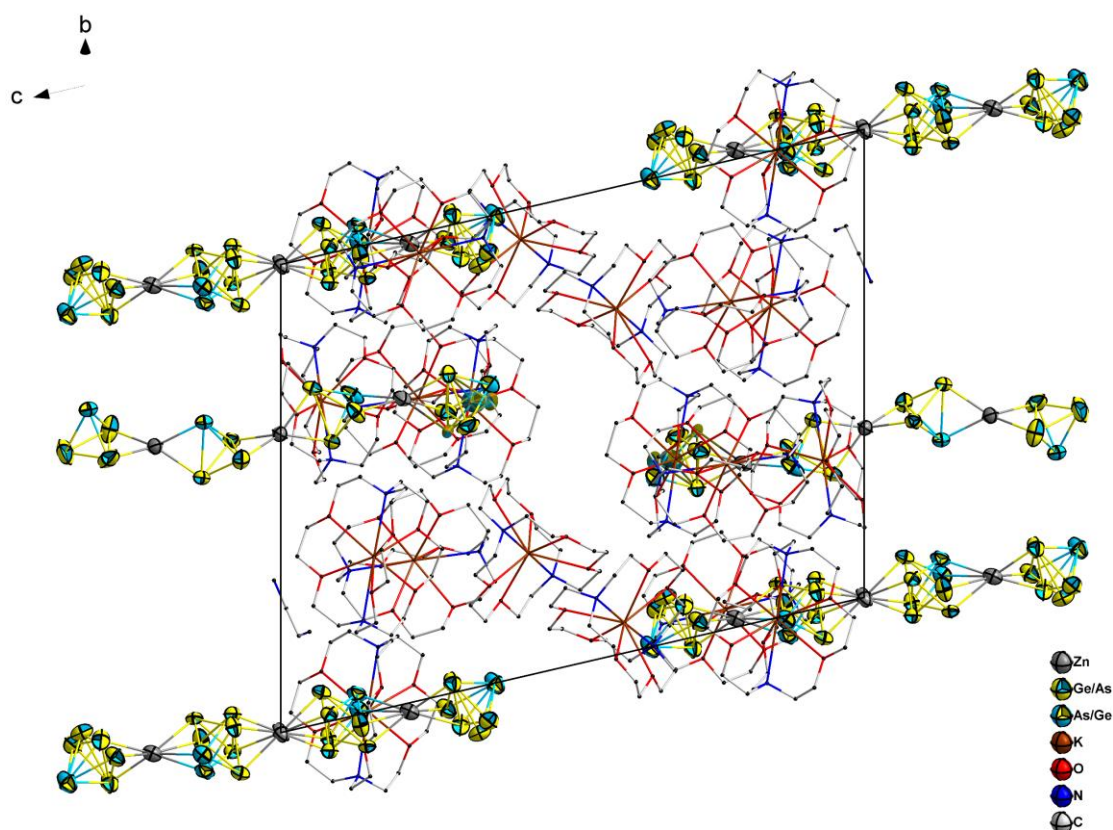


Figure 3.14: View of the (extended) unit cell of compound [K(crypt-222)]₉(**5a**)(**5b**)_{0.5}·en, viewed along the crystallographic *a*-axis. H atoms are omitted for clarity.

While the elemental composition of the anions **5**⁶⁻ is plausible based on the *pseudo*-element concept, as was confirmed by means of μ -XFS analyses, the assignment of Ge and As atoms along the chain-type anions remained an open question. The terminal *pseudo*-tetrahedra would again prefer Ge atoms for coordination, but the μ -bridging ones were forced to use all four atoms for coordination with no predictable preference for the position of the single As atom per *pseudo*-tetrahedron. Based on the relatively regular interatomic distances, a coexistence of three different types of binary anions (with three different charges), which would have been necessary if distributing the Ge and As atoms over the whole cluster in a different way than by assignment of a Ge: As ratio of 3:1 for all of the binary units, was ruled out.

For the most probable assignment of Ge and As atoms, quantum chemistry was employed once more. The DFT calculations converged into a structure exhibiting a distorted tetrahedral coordination environment around the central Zn atom. Assigning the As atoms on different positions in each *pseudo*-tetrahedral moiety led to six conformers within ~ 20 kJ·mol⁻¹ of relative energy (see Figure 3.15). Additionally, the absolute energy of a hypothetical conformer with a planar coordination sphere around the central Zn atom presenting in Figure 3.15 in semitransparent mode was found to be 18 kJ·mol⁻¹ higher than for the global minimum structure. In the presumed global minimum structure, it is shown that the central Zn atom solely coordinated by Ge

atoms and the two outer Zn atoms by no more than one As atom of the two inner $(\text{Ge}_3\text{As})^{3-}$ moieties. The bond lengths and angles are within the expected range (see Section 7.1.3).

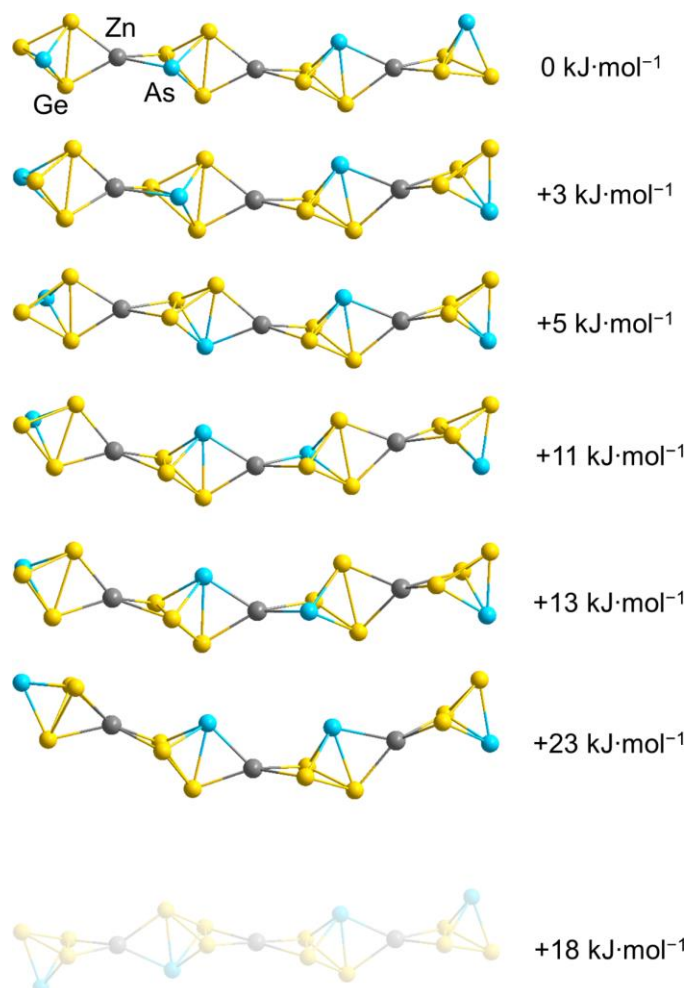
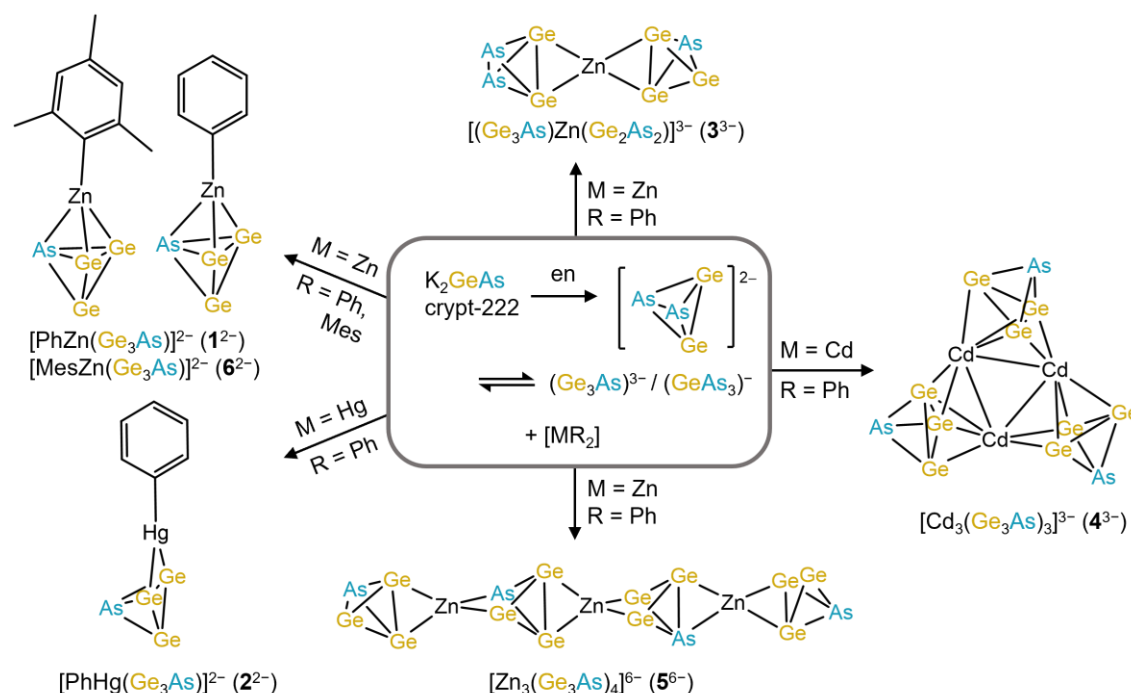


Figure 3.15: Calculated conformers of anion 5^{6-} and relative energies ΔE with respect to the global minimum structure. The conformer that was computed with constrained dihedral angles for comparison is shown in semitransparent mode. The methods are detailed in Section 7.4.1.

3.3.2 Assembly of One to Four Ge/As-based *pseudo*-Tetrahedra in the Coordination Sphere of d^{10} Metals

Group 12 organometallics seem to show a tendency to react with both the $(\text{Ge}_2\text{As}_2)^{2-}$ and the $(\text{Ge}_3\text{As})^{3-}$ anions owing to the relatively high Lewis acidity of both $(\text{MPh})^+$ and M^{2+} . The order of interaction with one or the other *pseudo*-tetrahedral species suggests a possible selectivity in the product spectrum: if $(\text{Ge}_2\text{As}_2)^{2-}$ is coordinated first, the only product to form will be 3^{3-} , while initial coordination of $(\text{Ge}_3\text{As})^{3-}$ can lead to any of the anions $1^{2-} - 6^{2-}$ (see Scheme 3.2). The order of interaction was ascribed to kinetic reasons, which includes relative concentrations of the anions. Note that other reactant stoichiometries than the ones used here did not alter the product spectrum in all cases.

Scheme 3.2: Summary of the reactions of an extraction solution of the solid ‘K₂GeAs’ in ethane-1,2-diamine (en) with [MPh₂] (M = Zn, Cd, Hg) and [ZnMes₂] yielding the complex anions **1**²⁻ – **6**²⁻.



Considering the reaction between “K₂GeAs” and [ZnPh₂] first, ESI-MS of the filtered reaction mixture showed several signals of which a number of Zn/Ge/As containing species could be assigned, the most relevant of which were [K₂Zn₃Ge₉As₃][−], [K₂(crypt-222)Zn₃Ge₉As₃][−] and [K₂(crypt-222)₂Zn₃Ge₉As₃][−].

Observation of these three compounds comprising **1**²⁻, **3**³⁻, and **5**⁶⁻ provides insight both into the coexistence of (Ge₂As₂)²⁻ and (Ge₃As)³⁻, and the stepwise growth (and crystallization) of the ternary assemblies using these species: exchange of one of the phenyl groups on the Zn atom with (Ge₃As)³⁻ affords anion **1**²⁻ as the first step; exchange of the second phenyl group with (Ge₂As₂)²⁻ yields anion **3**³⁻; if (Ge₃As)³⁻ were used in this step instead (with a hypothetical anion ‘[Zn(Ge₃As)₂]⁴⁻’ (**3'**) being produced), a continuation of the process with two further equivalents of both [ZnPh₂] and (Ge₃As)³⁻ allows anion **5**⁶⁻ to form and crystallize. The latter demonstrates the degree of freedom that is added to the reaction space by the two coexisting binary building units.

The successful isolation of **1**²⁻ led to the speculation that in the reaction that affords **3**³⁻, **1**²⁻ might form first before the Ph group is then substituted by a (Ge₂As₂)²⁻ anion in a second step. This is supported by the calculation of reaction energy of this second step being strongly exoenergetic (see Scheme 3.3 below). Typically, in Zintl cluster chemistry, several compounds coexist in solution, however, only the compounds that fit best with [K(crypt-222)]⁺ with regards to lattice enthalpies will crystallize. Therefore, most likely the main reason for anion **1**²⁻ to form an isolable salt instead of the mentioned alternative, and the reason for **3**³⁻ to crystallize, while the other possible variants with either two (Ge₂As₂)²⁻ ligands (**A**; two negative charges in total) or two (Ge₃As)³⁻ ligands (**B**; four negative charges in total) do not, is simply a matter of the resulting lattice energy. Obviously, the combination of one cluster anion of charge 3[−] with three

[K(crypt-222)]⁺ cations produces the lowest solubility under the given conditions (higher charges require K⁺ counterions in neat solids, see above). The reason of why the other species should generally not form (and mass spectra do give hints for other than the crystallized anions to exist) cannot be figured out, but in the absence of crystallographic data for them, this is mere speculation. However, the observation of potential follow-up products of variant **B** seems to underscore these thoughts, as discussed in the following.

The existence of anion **4**³⁻ indicates that the Cd analogue of a hypothetical **B**-type variant of compound '**3**⁴⁻' may have formed in solution, which could not crystallize along with [K(crypt-222)]⁺ cations unless being complemented by two more M²⁺ anions and another (Ge₃As)³⁻ unit. Although the Cd homologue of compound '**3**⁴⁻' has not yet been isolated, a similar start of the reaction cascade appears to be very plausible; ESI mass spectra of a fresh solution of single crystals of the compound comprising anion **4**³⁻ show the signal of a corresponding fragment (CdGe₅As₃C₇H₁₀)⁻ (see Figure 7.21), which is not a proof of the formation of **4**³⁻ from this species but indicates a chemical relationship. Notably, although a corresponding Zn compound was not isolated, a species with the elemental composition {Zn₃Ge₉As₃} was observed in the ESI mass spectrum (see above), which suggests that the same pinwheel-like structure can also form with the lightest group 12 metal. In fact, a poor-quality diffraction pattern was obtained of some crystals which appeared to show this anion. Therefore, the corresponding Zn homologue of **4**³⁻, '[Zn₃(Ge₃As)₃]³⁻', was synthesized as suggested from preliminary X-ray diffraction data and ESI-MS analyses of the reaction solution yielding compounds (see Section 7.3.3, Figures 7.28, 7.29). Again, three charges seem to fulfil the minimum precondition for crystallization of this anion with the available cations, although a lower crystal quality as compared to the compounds comprising anions **1**²⁻ – **3**³⁻ already indicates a deviation from an ideal fit.

Apparently, the oligomer growth was terminated at this stage with a total anionic charge of 6-. For the given size, any lower charge which could have been realized upon inclusion of (Ge₂As₂)²⁻ units instead of (Ge₃As)³⁻ seems to be more unfavorable. An anion of a similar topology but higher charge was reported to exist in the ternary solid K₆CdPb₈, [Pb₄CdPb₄CdPb₄CdPb₄]¹⁰⁻ (besides Pb₄⁴⁻ anions).^[133] Here, the Pb₄⁴⁻ ligands act as μ,η^{3:3}-ligands or η³-ligands, which results in near octahedral coordination of the Cd²⁺ cations and a zig-zag-type shape of the oligomer – hence markedly different from the anion **5**⁶⁻.

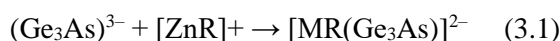
The low quantities of [K(crypt-222)]₂**2**-tol and [K(crypt-222)]₃**4**-tol obtained in these experiments gives rise to the question as to the fate of the rest of the reactants. In the mother liquor upon crystallization of both compounds, no meaningful signals were identifiable by ESI mass spectrometry owing to very low concentrations upon doubling the volume of solvent by layering. Inspection of the reaction solution by ESI-MS of the [HgPh₂] experiment, showed only anion **2**²⁻. Interestingly, on dissolution of [K(crypt-222)]₂**2**-tol in DMF, the ESI-MS measurement did not show a signal of **2**²⁻. Instead, a new anion with composition of [K(crypt-222)HgGe₅As₃H]⁻, hence an analogue of **3**³⁻, was observed (with a very low intensity though, and aggregated with one counterion and one proton in the gas phase). In the case of [CdPh₂], the in-situ ESI mass spectrum indicates the formation of transient species in very low concentrations containing Cd, Ge, and As (according to the isotope patterns); however, none of the compositions accords with any isolable anionic cluster, thus suggesting a relatively high reactivity of the (smaller) Cd-based species. Similarly to the Hg example, the ESI-MS measurement of

redissolved crystals of $[\text{K}(\text{crypt-222})]_3\mathbf{4}\cdot\text{tol}$ in DMF showed a signal for $(\text{CdGe}_5\text{As}_3\text{C}_7\text{H}_{10})^-$, indicating the formation of a Cd analogue of $\mathbf{3}^{3-}$. This can be understood as a reversion of the formation of $\mathbf{4}^{3-}$ from $\mathbf{3}^{3-}$, thus indicating the clusters' relationship. Although these spectra were of a rather low intensity, the findings shed light onto similar cluster formation processes to take place with Zn, Cd, and Hg complexes, yet with different reaction rates and yield.

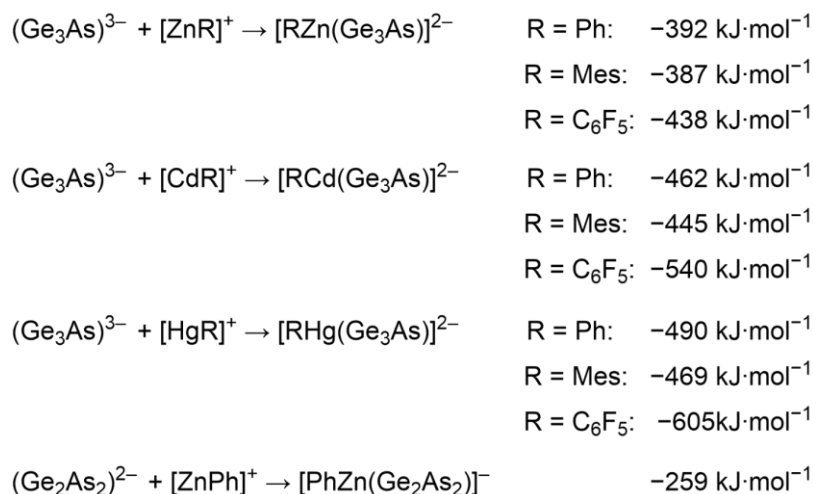
The range of products obtained from this series of organometallic complexes hints to the subtle effect the nature of the transition metal has on the reaction path. One possible explanation is the differing relative charge located at the respective metal atom in the starting material and products (also see the differing coordination modes observed in $\mathbf{1}^{2-}$ and $\mathbf{2}^{2-}$ in Figure 3.3).

Interestingly, despite the diverse product spectrum for $[\text{ZnPh}_2]$, $[\text{ZnMes}_2]$ only showed one product. This was also observed in the ESI-MS measurements of the reaction solution with only variations of one *pseudo*-tetrahedron per Zn atom (see Section 7, Figure 7.30) present. Additional signals at higher m/z ratios are present, however could not be assigned.

To corroborate the experimental studies, comprehensive quantum chemical calculations using density functional theory (DFT) methods were performed to investigate the different $[\text{MR}(\text{Ge}_3\text{As})]^{2-}$ ($M/\text{R} = \text{Zn}, \text{Cd}, \text{Hg}/\text{Ph}, \text{Mes}, \text{C}_6\text{F}_5$) combinations as well as their respective reaction energies towards exchange of the organic groups by Zintl anions. Calculations of the reaction energies for the formation of anions $\mathbf{1}^{2-}$, $\mathbf{2}^{2-}$, and $\mathbf{6}^{2-}$ in a first step according to eq 3.1 confirmed the expected trend (Scheme 3.3). The reactivity of the complex fragment with R being C_6F_5 causes the most exoenergetic reaction ($-438 \text{ kJ}\cdot\text{mol}^{-1}$), followed by the one with $\text{R} = \text{Ph}$ ($-392 \text{ kJ}\cdot\text{mol}^{-1}$) and finally the one with $\text{R} = \text{Mes}$ ($-387 \text{ kJ}\cdot\text{mol}^{-1}$). It could be shown, that all of these anions should in principle be stable. For the overview of the global minimum structure of all possible combinations with their calculated Mulliken and natural partial charges, see Section 7.4.1.2.

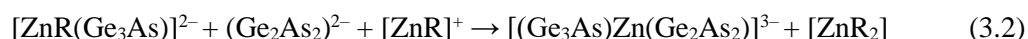


Scheme 3.3: Calculated reaction energies for the formation of the computationally obtained global minimum structures of all possible combinations of $[\text{MR}(\text{Ge}_3\text{As})]^{2-}$ ($M = \text{Zn}, \text{Cd}, \text{Hg}$; $\text{R} = \text{Ph}, \text{Mes}, \text{C}_6\text{F}_5$). The methods are detailed in Section 7.4.1.

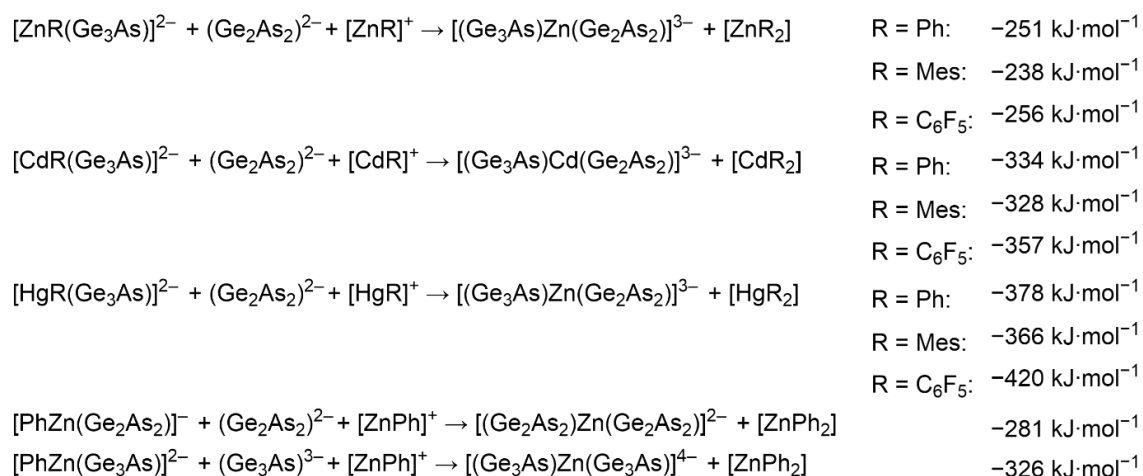


It has been noted in passing that the formation of this anion type is energetically preferred over a hypothetical $[\text{RM}(\text{Ge}_2\text{As}_2)]^-$ comprising a $(\text{Ge}_2\text{As}_2)^{2-}$ group (e.g., reaction energy for $\text{R}/\text{M} = \text{Ph}/\text{Zn}$ $-259 \text{ kJ}\cdot\text{mol}^{-1}$; Scheme 3.3). In accordance with the numbers shown in Figure 3.5, it is advantageous to avoid an As atom at the apex opposite the organic group, which is unlikely if $(\text{Ge}_2\text{As}_2)^{2-}$ is the coordinating species.

Regarding the second step to form anion $\mathbf{3}^{3-}$ (eq 3.2 and Scheme 3.4), the release and replacement of the C_6F_5 substituent is (again) the most exoenergetic ($-256 \text{ kJ}\cdot\text{mol}^{-1}$), followed by the process involving Ph ($-251 \text{ kJ}\cdot\text{mol}^{-1}$) and then the one involving Mes ($-238 \text{ kJ}\cdot\text{mol}^{-1}$). This may (in part) be ascribed to the fact that equation 3.2 formulates the recovery of $[\text{ZnR}_2]$, but also other possible fates of the substituents (like formation of RH upon deprotonation of the solvent en) show the same trend.



Scheme 3.4: Calculated reaction energies for the formation of the computationally obtained global minimum structures of all possible combinations of $[(\text{Ge}_3\text{As})\text{M}(\text{Ge}_2\text{As}_2)]^{3-}$ ($\text{M} = \text{Zn}, \text{Cd}, \text{Hg}$). An alternative (general) reaction scheme would be the following: $[\text{RM}(\text{Ge}_3\text{As})]^{2-} + (\text{Ge}_2\text{As}_2)^{2-} + \text{H}_2\text{NCH}_2\text{CH}_2\text{NH}_2 \rightarrow [(\text{Ge}_3\text{As})\text{M}(\text{Ge}_2\text{As}_2)]^{3-} + \text{RH} + (\text{H}_2\text{NCH}_2\text{CH}_2\text{NH})^-$; however, it leads to the same trends in energies according to the Born-Haber cycle, so the simpler set of reactants shown here for the discussion was used. The methods are detailed in Section 7.4.1.



Although the differences are not very large, the trend is in line with the experimental observation of a rather quick release of C_6F_5 (similar to Cl^- from ZnCl_2) from the reactant(s) and degradation of the reaction mixture, and also congruent with the tendency of the Ph compound to smoothly continue cluster growth, while the Mes compound reacts less readily.

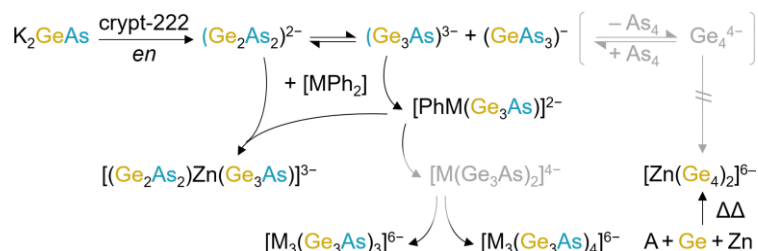
For comparison, reactions towards hypothetical alternatives, $[(\text{Ge}_2\text{As}_2)\text{Zn}(\text{Ge}_2\text{As}_2)]^{2-}$ or $[(\text{Ge}_3\text{As})\text{Zn}(\text{Ge}_3\text{As})]^{4-}$, from a hypothetical anion $[\text{PhZn}(\text{Ge}_2\text{As}_2)]^-$ or the anion $\mathbf{1}^{2-}$, have been studied respectively (Scheme 3.4). Interestingly, both would be energetically favorable, so they could form but do not crystallize owing to a mismatch of the cluster charge and size with

the required number of [K(crypt-222)]⁺ counterions, in contrast to a good match in case of anion **3**³⁻.

Similarly, as discussed above for the different substituents, comparison of the reaction energies involving Zn and Cd atoms helps to understand the direct formation of **4**³⁻ for M = Cd, while M = Zn allows for an observation of intermediate steps: for R being Ph, reaction energies are −392 kJ·mol^{−1} and −251 kJ·mol^{−1} (Zn) or −462 kJ·mol^{−1} and −334 kJ·mol^{−1} (Cd) for the first and second step, respectively, indicating a preference for continuous cluster growth with the heavier metal. The reaction energies obtained for M = Hg (−490 kJ·mol^{−1} and −378 kJ·mol^{−1}) would suggest an even higher reaction tendency toward cluster growth, in this regard, the crystallization of **2**²⁻ (and not a compound similar to **3**³⁻ or **4**³⁻) is somewhat surprising and lucky. The fact that the larger clusters are not obtained with M = Hg can be explained by the overall much higher sensitivity of the reaction solution that decomposes much more quickly than those of the Zn and Cd reactants.

As discussed within this section, it is believed that the anions **1**²⁻ – **5**⁶⁻ are, not only structurally, but also chemically related, and represent snapshots along a formation cascade. This, however, is not a straight line, but rather follows different ‘evolutionary branches’ of cluster formation. The fact that the extraction solution of “K₂GeAs” can provide (at least) two different binary *pseudo*-tetrahedral anions allows tracking these branches, while homoatomic anions would lead to other products with different charges. Scheme 3.5 summarizes the findings in this work, thereby including previous findings with Ge₄⁴⁻ anions for completeness.^[140] Note that the Scheme was drawn based on experimental observations (with R = Ph), as theoretical pathway studies that include small clusters of different (anionic) charges do not produce reliable reaction profiles. The computations of reaction energies discussed above, however, provided a rationale for the first steps to be feasible in the way shown here.

Scheme 3.5: Suggestion for the reaction branches that may occur for the combination of an extraction solution of ‘K₂GeAs’ in en/crypt-222 with [MPh₂], to afford cluster anions such as reported in this work (center and left) based on single crystal X-ray diffraction or mass spectrometry studies. Formulas given in grey shade refer to hypothetical species that have not (yet) been detected. Arrows with a black/grey color gradient indicate unproven, yet plausible steps towards and from such species, while unsubstantiated paths are crossed out for clarity. M = Zn, Cd, and/or Hg; A = K, Rb, or Cs.



more complicated multi-step exchange reactions to take place involving species with $(\text{Ge}_2\text{As}_2)^{2-}$ (and $(\text{Ge}_3\text{As})^{3-}$) anions as ligands, such as the one given on the left-hand side of Scheme 3.5, can be ruled out, but it would be much more difficult to argue for it.

Formally, the equilibrium shown in the top row could proceed towards the homoatomic tetrahedra, and ESI-MS gives hints for the occurrence of $\{\text{Ge}_4\}$ units, but no products have been isolated in crystalline form from such solutions comprising homoatomic Ge_4^{4-} anions. This part of the equilibrium is therefore given in grey characters, too, and the corresponding pathway towards related clusters comprising Ge_4^{4-} anions is crossed out. Such clusters were obtained by solid state reactions of the elements instead (right), hence in the Zintl phases $\text{A}_{14}\text{ZnGe}_{16}$ ($\text{A} = \text{K}, \text{Rb}$) or $\text{Cs}_6\text{Ge}_8\text{Zn}$, as the very high charge density requires the close proximity of alkali metal ions – and not the bulky $[\text{A}(\text{crypt-222})]^+$ complexes with their comparably low charge density.^[132,140] Noteworthy however, a related complex with a protonated $\{\text{Ge}_4\}$ unit, $[\text{Ph}_2\text{Zn}(\eta^2\text{-Ge}_4\text{H})]^{3-}$, was obtained from the reaction of the extraction solution of $\text{K}_6\text{Rb}_6\text{Ge}_{17}$ in en/crypt-222 with $[\text{ZnPh}_2]$. This indicates some flexibility of the reaction space including homoatomic units, too, by protonation.

3.4 Expansions of *pseudo*-Tetrahedral Ge/As Anions

As discussed in Section 3.3, the use of d^{10} metal complexes reacting with “ K_2GeAs ” has exclusively led to the formation of coordination compounds containing either $(\text{Ge}_2\text{As}_2)^{2-}$ and $(\text{Ge}_3\text{As})^{3-}$ *pseudo*-tetrahedra as ligands. To further investigate the reactivity of the “ K_2GeAs ” solid, a series of metal complexes containing the pentamethylcyclopentadienyl ligand (Cp^*) were selected for studying. Compared to the Ph and Mes group coordinating to metal atoms in an η^1 fashion, Cp^* usually combines with a transition metal in an η^5 fashion, providing greater electron donation to the metal center and potentially opening up new reaction pathways upon release of the ligand. Some previous publications have shown the successful isolation of Zintl clusters using Cp^* -based transition metal complexes in reactions with homoatomic Zintl units or neutral compounds, as seen in $[\{\text{Cp}^*\text{Ru}\}_2\text{Sb}_6]^{2-}$, $[\{\text{Cp}^*\text{Ru}\}\text{Pb}_{11}]^{3-}$, $[\text{Cu}@\text{Pb}_{11}\{\text{RuCp}^*\}]^{2-}$, $[(\text{Cp}^*\text{Ln})_2(\mu, \eta^{2:2}\text{-Bi}_2)]$ ($\text{Ln} = \text{Gd}, \text{Tb}, \text{Dy}, \text{Y}$), $[\{\text{Cp}^*\text{Ln}\}_2\text{Bi}_6]^{2-}$ ($\text{Ln} = \text{Tb}, \text{Dy}$), $[\{\text{Cp}^*\text{Fe}\}(\eta^5\text{-As}_5)]$, for instance. Inspired by these works, Cp^* complexes of group 7-10 metals have been employed, some of which are prominent metals in catalysis.^[244–248] These include the 3d metallocenes $[\text{MnCp}^*_2]$, $[\text{FeCp}^*_2]$, $[\text{CoCp}^*_2]$ and $[\text{NiCp}^*_2]$, and additionally $[\text{RuCp}^*(\text{cod})\text{Cl}]$ ($\text{cod} = \text{cyclooctadiene}$).

3.4.1 Syntheses, Structures and Bonding

The addition of en to a solid mixture of “ K_2GeAs ”, $[\text{NiCp}^*_2]$ and crypt-222 in a molar ratio of 2:1:3 afforded a green-brown suspension. Filtration and subsequent layering the solution with toluene led to the formation of brown plate crystals which were identified as the compound $[\text{K}(\text{crypt-222})]_2[\{\text{Cp}^*\text{Ni}\}_2(\text{Ge}_6\text{As}_2)] \cdot 2\text{en}$ ($[\text{K}(\text{crypt-222})]_2 \cdot 2\text{en}$).

The reaction of “ K_2GeAs ”, $[\text{MnCp}^*_2]$, and crypt-222 in an optimized molar ratio of 3:3:1 in an en solution yielded a greenish brown suspension, which led to the crystallization of dark brown

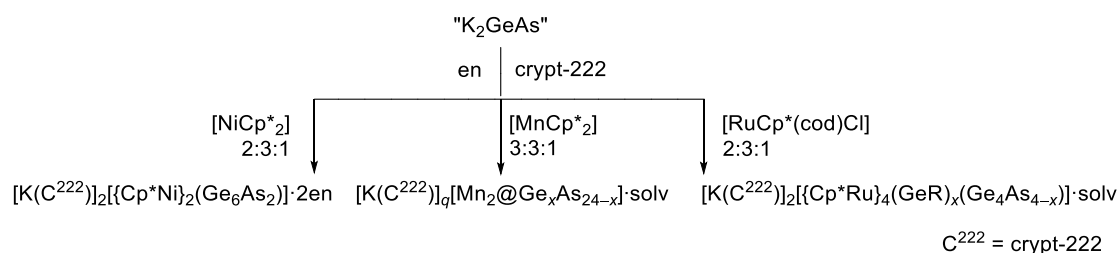
blocks of the compound $[\text{K}(\text{crypt-222})]_q[\text{Mn}_2\text{@Ge}_x\text{As}_{24-x}]\cdot\text{solv}$ ($[\text{K}(\text{crypt-222})]_q\mathbf{8}\cdot\text{solv}$). Note that the overall charge of the cluster and the ratio of the Ge and As could not be determined so far, owing to the a severe disorder problem of the cations.

$[\text{FeCp}^*_2]$ and $[\text{CoCp}^*_2]$ were also used in reactions with “K₂GeAs”, leading to the formation of $(\text{Ge}_2\text{As}_2)^{2-}$, but no crystals of other products.

Following the described success using 3d metallocenes, a survey of suitable 4d metallocenes was made. $[\text{RuCp}^*_2]$ was considered, however, it is not trivial to synthesize it, while several alternative Cp*-containing Ru compounds are commercially available. $[\text{RuCp}^*(\text{cod})\text{Cl}]$ proved to be suitable, and under the same reaction conditions as for the synthesis of $[\text{K}(\text{crypt-222})]_2\mathbf{7}\cdot 2\text{en}$, a dark red suspension was observed, from which the compound $[\text{K}(\text{crypt-222})]_2[\{\text{Cp}^*\text{Ru}\}_4(\text{GeR})_x(\text{Ge}_4\text{As}_{4-x})]\cdot\text{solv}$ ($[\text{K}(\text{crypt-222})]_2\mathbf{9}\cdot\text{solv}$, $x = 0$ or 2) was obtained as red plate crystals. Uncertainty remains in the presence, and (if no) identity, of the R group bonded to the Ge, as will be discussed in greater detail later in the section.

Scheme 3.6 summarizes the syntheses of compounds comprising anions $\mathbf{7}^{2-} - \mathbf{9}^{2-}$.

Scheme 3.6: Synthesis of $[\text{K}(\text{crypt-222})]_2\mathbf{7}\cdot 2\text{en}$, $[\text{K}(\text{crypt-222})]_q\mathbf{8}\cdot\text{solv}$, and $[\text{K}(\text{crypt-222})]_2\mathbf{9}\cdot\text{solv}$ by treatment of “K₂GeAs” in en/crypt-222 in the presence of various Cp*-based transition metal complexes and subsequent crystallizations by layering with toluene (for the detailed molar ratio, see text above).



The anion $[\{\text{Cp}^*\text{Ni}\}_2(\text{Ge}_6\text{As}_2)]^{2-}$ ($\mathbf{7}^{2-}$) can be viewed as a bicapped square antiprism where the central eight-atom Ge/As unit is capped by two $\{\text{NiCp}^*\}$ units. The structure of the cluster anion is shown in Figure 3.16. $[\text{K}(\text{crypt-222})]_2\mathbf{7}\cdot 2\text{en}$, crystallized in the triclinic space group type $P\bar{1}$, with four formula units per unit cell (see Figure 3.17).

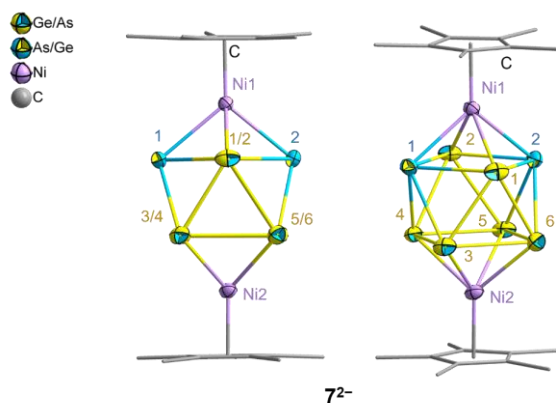


Figure 3.16: Two views of the molecular structure of the anion $[\{\text{Cp}^*\text{Ni}\}_2(\text{Ge}_6\text{As}_2)]^{2-}$ (7^{2-}) in $[\text{K}(\text{crypt-222})]_2 \cdot 7 \cdot 2\text{en}$ with thermal ellipsoids drawn at 50% probability. Since Ge and As atoms cannot be distinguished, the corresponding atom types are drawn in two-colored fashion (yellow-blue), with the more probable atom according to quantum chemical calculations being indicated by the dominant color (see top left); in addition, a corresponding color code was used for the atom labels. H atoms are omitted in the image for clarity.

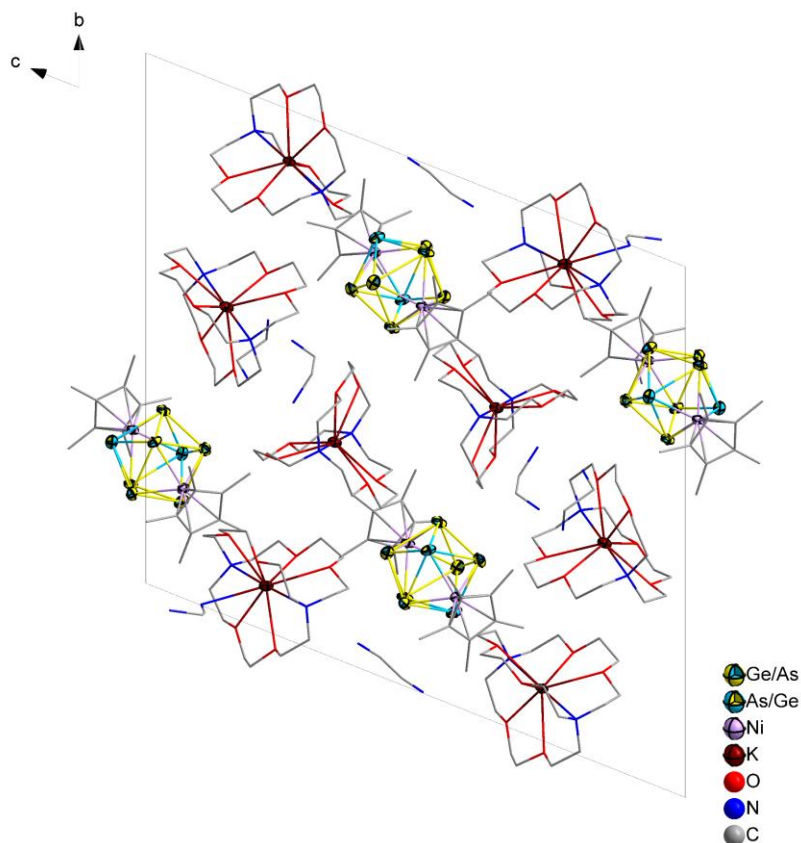


Figure 3.17: View of the (extended) unit cell of $[\text{K}(\text{crypt-222})]_2 \cdot 7 \cdot 2\text{en}$, viewed along the crystallographic a -axis. H atoms are omitted for clarity.

The presence of two [K(crypt-222)]⁺ indicates that the antiprism core carries a charge of 4[−], as the two {NiCp*} fragments contribute two positive charges. The central (Ge₆As₂)^{4−} square antiprism is isoelectronic with the homoatomic species Sn₈^{6−}, which is capped by two Li⁺ cations instead in the known compound A₄Li₂Sn₈ (A = K, Rb).^[240] The ratio of Ge and As atoms is supported by DFT calculations, which also reveal the preferred site arrangement of the Ge and As atoms in the cluster. As shown in Table 3.2, the atomic ratio of 6:2 for Ge and As atoms results in a HOMO-LUMO (highest occupied molecular orbital – lowest unoccupied molecular orbital) gap of 1.247 eV, which is larger than the ones obtained for cluster composition with a Ge:As ratio of 4:4 and 2:6 (at unchanged total charge). This is another clear hint towards the 6:2 composition to be the one present in **7**^{2−}.

Table 3.2: Calculated HOMO-LUMO gap of the anion **7**^{2−} with different atomic ratios of Ge and As atoms. The methods are detailed in Section 7.4.2.

[Cp*Ni] ₂ (Ge ₆ As ₂) ^{2−} (7 ^{2−})	
Ge:As	HOMO-LUMO gap [eV]
2:6	0.375
4:4	0.541
6:2	1.247

The computationally optimized conformers of anion **7**^{2−} are presented in Figure 3.18. In the optimized minimum conformer, two As atoms are positioned diagonally on the top face of the square antiprism (Figure 3.18a). Alternative arrangements, where the two As atoms are located at two different faces of the square antiprism, result in slight energy disadvantages of 1.31 kJ·mol^{−1} and 2.10 kJ·mol^{−1}, respectively (Figures 3.18b, 3.18c). It would be energetically disadvantaged by 10.50 kJ·mol^{−1}, and 17.59 kJ·mol^{−1} when the two As atoms are adjacent (Figures 3.18d, 3.18e). This is mainly caused by the larger electrostatic repulsion of the As atoms and the distortion of the cage.

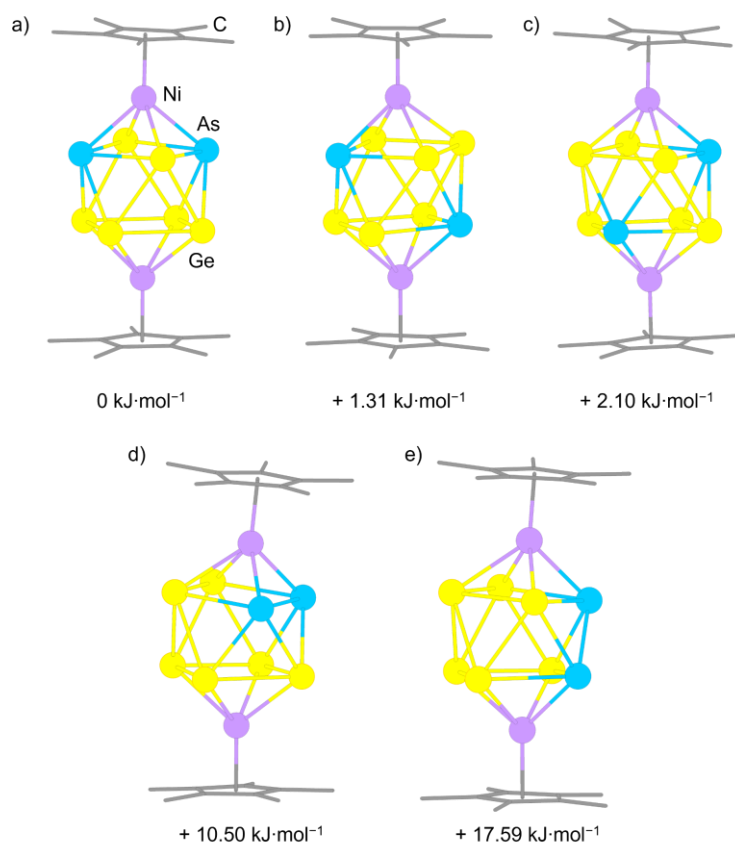


Figure 3.18: Computationally optimized minimum structures of the possible conformers of 7^{2-} . The methods are detailed in Section 7.4.2.

Two related peaks were observed at 973.48 m/z and 657.30 m/z in ESI mass spectra of redissolved single crystals of $[\text{K}(\text{crypt-222})]_2\mathbf{7}\cdot 2\text{en}$ in DMF. They are assigned to $(\{\text{Cp}^*\text{Ni}\}_2\text{Ge}_6\text{As}_2)^-$, and $(\text{Ge}_7\text{As}_2)^-$, respectively. The former species indicates that anion 7^{2-} can be transferred to the gas phase as a whole, accompanied by a one-electron oxidation (Figure 3.19, and see Section 7.3.2 for the full spectrum).

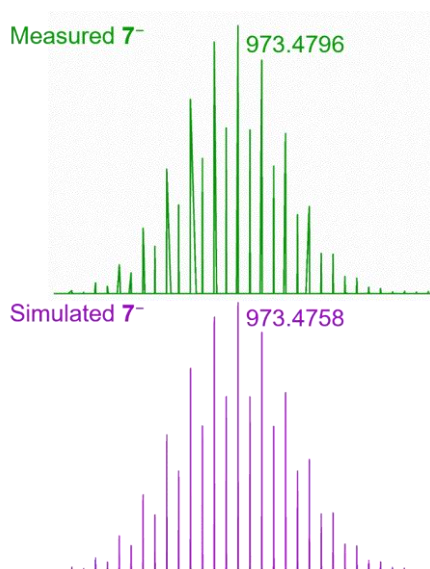


Figure 3.19: High-resolution electrospray-ionization mass spectrum of the anion 7^- at $m/z = 973.4796$, recorded immediately upon injection of a fresh solution of single-crystals of $[K(\text{crypt-222})]_2 7 \cdot 2\text{en}$ in DMF, with measured (top) and simulated (bottom) isotope patterns, obtained in negative-ion mode.

The bond lengths within the square antiprism are between 2.5621(10) Å and 2.7334(9) Å, which are similar to those found in anions $1^{2-} - 6^{2-}$ (see Table 3.5). Each Ge and As atoms bond directly to either the top or bottom Ni atom at similar bond lengths (2.42–2.49 Å), which are within the range of the lengths within reported species, such as $[(\eta^3\text{-Ge}_9)_2(\text{Ge}\{\text{Ni}(\text{CO})_2\}_3)]^{4-}$ (2.40–2.42 Å), $[\{(\text{CO})\text{Ni}\}\text{Ge}_9]^{3-}$ (2.38–2.52 Å) and $[\text{Ni}@_{\text{Ge}_9}\{\text{NiCO}\}]^{2-}$ (2.33–2.45 Å), $[\{\text{L}^1\text{Ni}\}_2(\mu\text{-}\eta^2, \kappa^1:\eta^2, \kappa^1\text{-As}_4)]$ (2.31–2.46 Å) and $[\{\text{L}^1\text{Ni}\}_2(\mu, \eta^{3:3}\text{-As}_3)]$ (2.35–2.42 Å), where $\text{L}^1 = \text{nacnac}$, though shorter than that of $[\{(\text{CO})_3\text{Ni}_2\}\text{Ge}_5]^{2-}$ (2.50–2.58 Å), and slightly longer than those reported for $[\{\text{Cp}^*\text{Ni}\}_3\{\text{Ni}(\mu\text{-Br})\}(\mu^3\text{-As})_4]_2$ (2.31–2.37 Å) and $[\{\text{Cp}^*\text{Ni}\}_3(\mu^3\text{-As})(\text{As}_4)]$ (2.32–2.35 Å), where $\text{Cp}^* = 1,2,4\text{-tri-tert-butyl-cyclopentadienide}$.^[179,249–252]

Owing to its bicapped square antiprismatic geometry, anion 7^{2-} resembles a *closo*-type cluster as a whole. Similar 10-vertex motifs have been found, for instance, the only known homoatomic example, Pb_{10}^{2-} , and some other clusters with one vertex or two vertexes exchanged by transition metal fragments, like $[\{(\text{CO})_3\text{M}\}\text{Tt}_9]^{3-}$ ($\text{M/Tt} = \text{Cr, Mo, W/Sn, Cr, Mo, W/Pb}$), $[\{\text{R}_3\text{Cu}\}\text{Ge}_9]^{3-}$ ($\text{R} = \text{PiPr, PCy}$), $[\{(\text{cod})\text{Ir}\}\text{Tt}_9]^{3-}$ ($\text{Tt} = \text{Sn, Pb}$), and $[\{(\text{CO})_3\text{Mo}\}_2\text{Ge}_8]^{4-}$.^[172–176,194,239,253–255] However, upon applying the Wade-Mingos rules, the 26-electron count of the cluster implies an *arachno*-structure type with a total valence electron count of $(2n+6)$ that is not structurally observed in this case. The overall slightly longer Ge/As–Ge/As distance in 7^{2-} actually suggest that the cage is less electron-deficient than a *closo*-cluster. The fact that it still adopts a “closed” shape might be attributed to the preference of a more regular cluster structure, and it also demonstrates the larger tolerance of Zintl clusters for slight variations in total electron counts.

Different from anion 7^{2-} , the product obtained upon using $[\text{MnCp}^*_2]$ was the intermetalloid cluster $[\text{Mn}_2@_{\text{Ge}_x\text{As}_{24-x}}]^{q-}$ (8^{q-}), which can be viewed as the oxidative coupling of two monomeric 12-vertex clusters incorporating an endohedral Mn atom each. Due to difficulties in solving the crystal structure from SCXRD, q is used to represent the still disputable overall

charge of the anion. The structure of anion $\mathbf{8}^{q-}$ is shown in Figure 3.20, and two views of the unit cell of $[\text{K}(\text{crypt-222})]_q\mathbf{8}\cdot\text{solv}$ are presented in Figure 3.21. Compound $[\text{K}(\text{crypt-222})]_q\mathbf{8}\cdot\text{solv}$ crystallizes in the trigonal space group type $R\bar{3}c$ with eighteen formula units per unit cell.

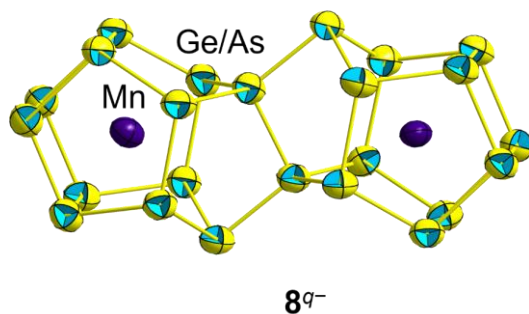


Figure 3.20: Molecular structure of the anion $[\text{Mn}_2@\text{Ge}_x\text{As}_{24-x}]^{q-}$ ($\mathbf{8}^{q-}$) in compound $[\text{K}(\text{crypt-222})]_q\mathbf{8}\cdot\text{solv}$, with thermal ellipsoids drawn at 50% probability. All the Ge and As atoms are drawn in yellow-blue fashion, as the ratio and the position of these atoms remain unknown.

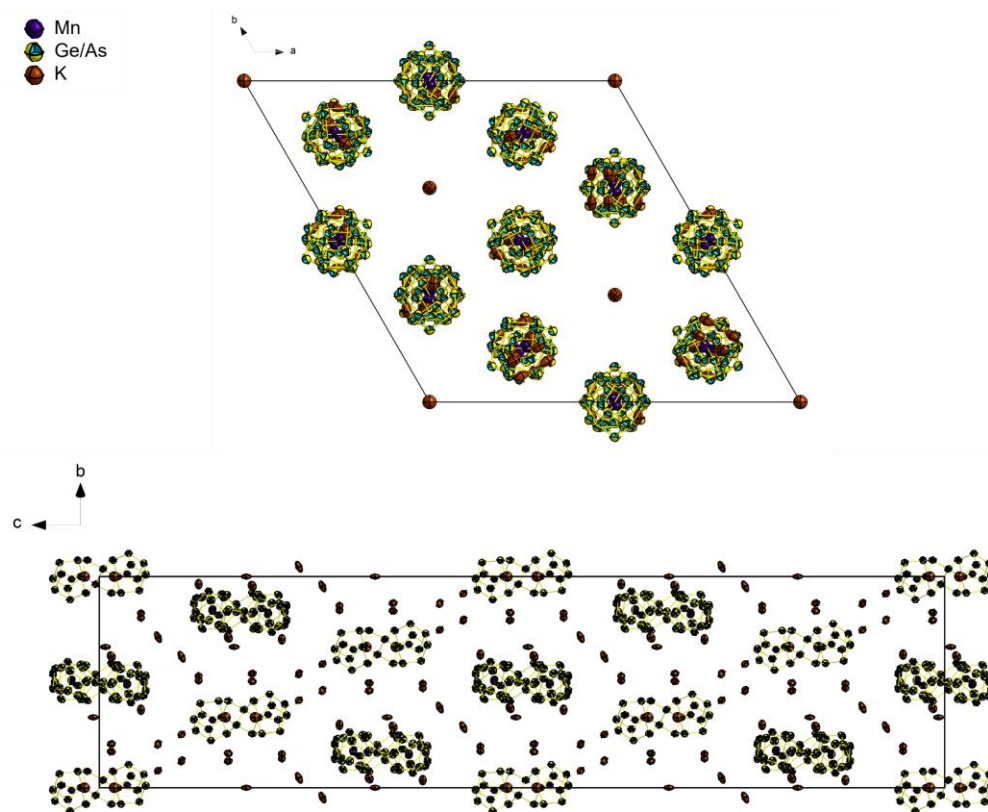


Figure 3.21: Views of the (extended) unit cell of $[\text{K}(\text{crypt-222})]_q\mathbf{8}\cdot\text{solv}$, viewed along the crystallographic c - and a -axis. All Ge and As atoms are drawn in yellow-blue fashion, owing to uncertain amount of Ge and As atoms in the cluster. The overall charge of the anion $\mathbf{8}^{q-}$ is unknown, due to the high symmetry space group, as well as the intrinsic disorder of $[\text{K}(\text{crypt-222})]^+$ cations. Note that the figure only indicates the position of the K atoms, the occupancy of which remains unknown. H, C, N, and O atoms are omitted for clarity.

As written in the formula, the exact ratio of Ge and As atoms in the anion 8^q could not be determined thus far, which is correlated to the overall charge of the anion. The overall charge of 8^q , however, remains unknown owing to the heavy disorder of cations, and the high-symmetry space group of the structure. Some preliminary calculations have been performed to gain some insight into the possible cluster configurations. For this, an average nuclear charge ranging from 32 (Ge) to 33 (As) was assigned to all atoms of the structure obtained by SCXRD to check the HOMO-LUMO gap for such species with an overall charge of either 4[−] or 6[−] (even numbers were anticipated to be more likely given the inversion symmetry of the cluster). It can be seen in Figure 3.22, that some species exhibit open-shell electron configurations (red column), while the clusters with compositions of $[\text{Mn}_2@ \text{Ge}_{18}\text{As}_6]^{6-}$, $[\text{Mn}_2@ \text{Ge}_{16}\text{As}_8]^{4-}$, $[\text{Mn}_2@ \text{Ge}_{10}\text{As}_{14}]^{6-}$, and $[\text{Mn}_2@ \text{Ge}_8\text{As}_{16}]^{4-}$ have closed-shell electron configuration (green column), which is more likely for heavier main-group elements compounds. A larger HOMO-LUMO gap, in addition, points to a more stable and, thus, more likely composition.

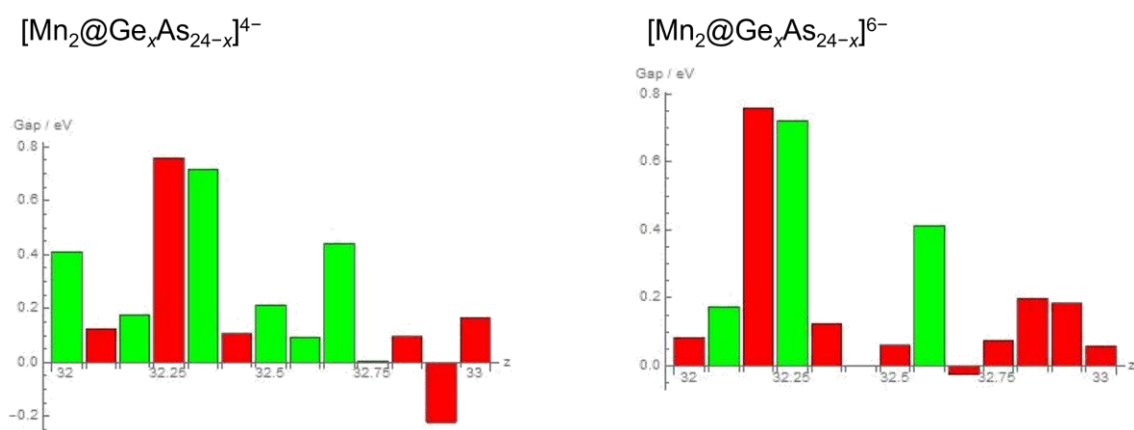


Figure 3.22: Calculated HOMO-LUMO gaps of $[\text{Mn}_2@ \text{Ge}_x\text{As}_{24-x}]^{q-}$ ($q = 4$, or 6) upon stepwise adjustment of the average nuclear charge ranging from 32 (Ge) to 33 (As). Green columns: close-shell electron configurations, red columns: open-shell electron configurations. The methods are detailed in Section 7.4.2.

The next step involves calculating the electrostatic potential at each site to assign the position of Ge and As atoms using first-order perturbation theory. Structural optimization (see Section 7.4.2) will be subsequently used in comparison with the SCXRD measurement data. The first calculation shows only one conformer, $[\text{Mn}_2@ \text{Ge}_{16}\text{As}_8]^{4-}$ (Figure 3.23a). In addition, a related composition with “average total charge” (5[−]), $[\text{Mn}_2@ \text{Ge}_{17}\text{As}_7]^{5-}$, was taken into consideration, and the corresponding conformers are shown in Figures 3.23b and 3.23c. All these conformers exhibited reasonable HOMO-LUMO gap, with + 0.94 eV, + 0.76 eV, and + 0.65 eV, respectively.

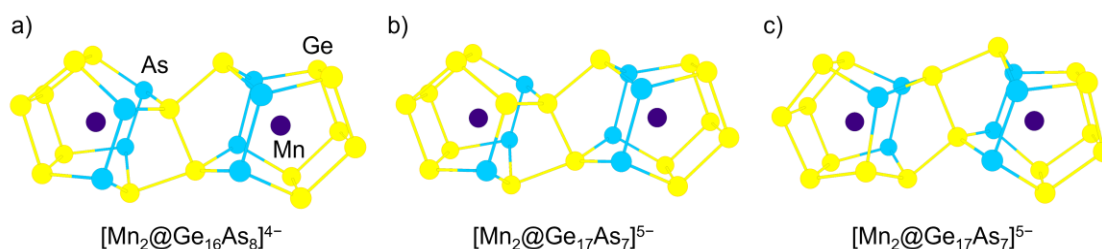


Figure 3.23: Computationally optimized minimum structures of the possible conformers of $\mathbf{8}^{q-}$, with a): $[\text{Mn}_2@Ge_{16}As_8]^{4-}$, b) and c): $[\text{Mn}_2@Ge_{17}As_7]^{5-}$. The methods are detailed in Section 7.4.2.

Based on the calculations above, it seems that in anion $\mathbf{8}^{q-}$, the most stable situation is with the maximum amount of 18 Ge atoms. This is also in consistent with the μ -XFS measurement of the single crystal of $[\text{K}(\text{crypt-222})]_q\mathbf{8}\cdot\text{solv}$, indicating that the ratio of Ge and As is approximately 17.6:6.4, which lies between Ge:As ratios of 17:7 and 18:6 obtained from the DFT calculations. However, the motif of anion $\mathbf{8}^{q-}$ suggests an electron-precise cluster, where the number of electrons involved in electron bonding is equal to the number of the nearest neighbors ($8-N = 3$ for 22 of the cluster shell atoms, and $8-N = 4$ for the two bridging atoms), and also to the number of valence atomic orbitals involved in the bonding, except for the two endohedral atoms. To fulfill a total requirement of $5n$ valence electrons (n is the number of vertexes), Mn atoms would need to contribute their 3d, and 4s electrons to the cluster shell. This will be analyzed by natural population analysis in the future. In addition to understanding the electron configuration of the anion $\mathbf{8}^{q-}$, ongoing and further efforts will focus on determining the actual ratio, the positions of the Ge and As atoms in $\mathbf{8}^{q-}$, as well as the overall charge.

Anion $\mathbf{9}^{2-}$, in general, has a distorted icosahedral structure, enveloped by four sterically demanding Cp^* groups situated on the Ru atoms, and (potentially) two unknown substituents bonded to two Ge atoms (see Figure 3.24 for two views of anion $\mathbf{9}^{2-}$). Compound $[\text{K}(\text{crypt-222})]_2\mathbf{9}\cdot\text{solv}$ crystalized in the monoclinic space group type $C2$, with eight formula units with per unit cell (Figure 3.25).

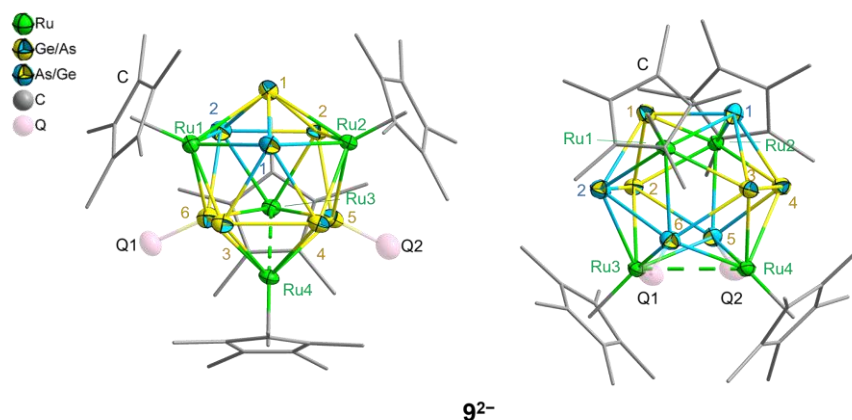


Figure 3.24: Two views of the molecular structure of the anion $[\{\text{Cp}^*\text{Ru}\}_4(\text{GeR})_x(\text{Ge}_4\text{As}_{4-x})]^{2-}$ (**9²⁻**) in compound $[\text{K}(\text{crypt-222})]_2\textbf{9}\cdot\text{solv}$, with thermal ellipsoids drawn at 50% probability. Since Ge and As atoms cannot be distinguished, the corresponding atom types are drawn in two-colored fashion (yellow-blue), with the more probable atom according to quantum chemical calculations being indicated by the dominant color (see top left); in addition, a corresponding color code was used for the atom labels. H atoms are omitted in the image for clarity.

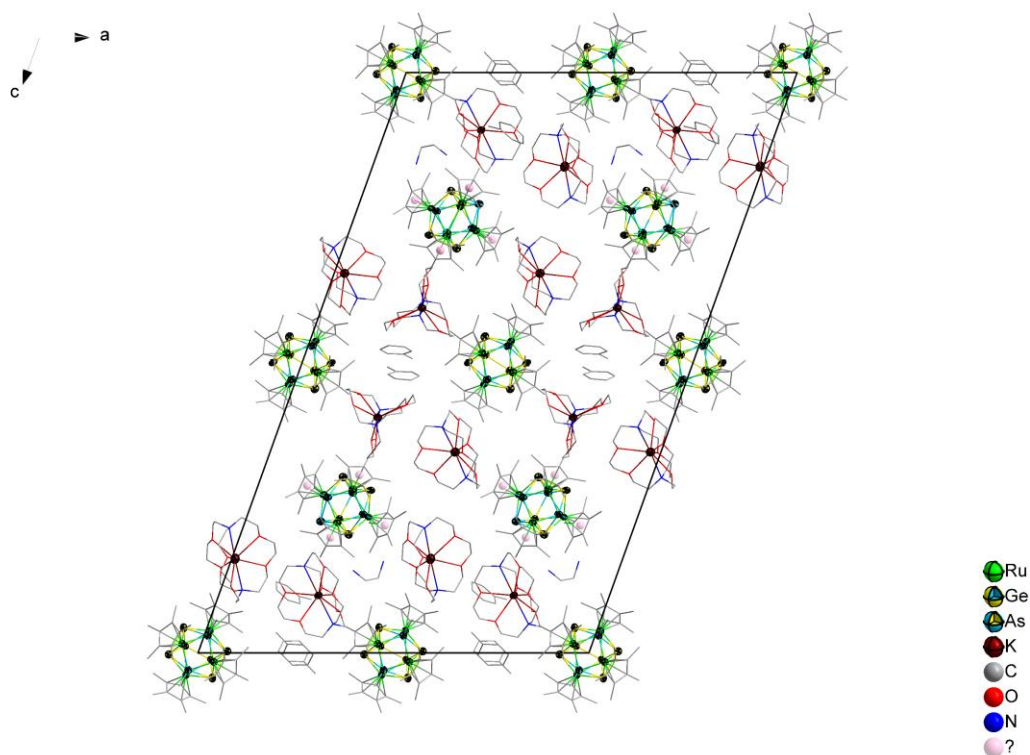


Figure 3.25: View of the (extended) unit cell of compound $[\text{K}(\text{crypt-222})]_2\textbf{9}\cdot\text{solv}$, viewed along the crystallographic *b*-axis. H atoms are omitted for clarity.

The icosahedral motif of anion **9²⁻** suggests a (near) *closo*-type cluster, and the overall 2-charge of anion **9²⁻** implies that the number of Ge and As atoms are even, therefore the ratio of

Ge:As should be 2:6, 4:4, or 6:2, with 4:4 being most likely according to DFT calculations (see below). However, this ratio will shift to 6:2 if an extra R group is added on a Ge⁻ atom as it would then be isoelectronic with to an As atom. A μ -XFS measurement of compound [K(crypt-222)]₂**9**·solv] presents a Ge:As ratio of 5.03:2.97 (based on 4 Ru atoms, see Section 7.2), which is in the middle of the 4:4 and the 6:2 ratio. However, it is worth noting that the accuracy of μ -XFS measurements on Zintl anions, especially, containing relatively light elements are not too reliable, hence could be general aligned with both of these compositions.

The distribution of Ru–Ge/As and Ru–As/Ge distances in anion **9**²⁻ varies between 2.4759(14) Å and 2.6632(13) Å. The length of Ge/As–As/Ge bond ranges between 2.5199(16) and 2.6301(13) Å, and that of Ge/As–Ge/As bonds is in the range of 2.5639(15) – 2.6420(13) Å (see Table 3.5 for comparison with anions **1**²⁻ – **8**²⁻). All As atoms are found to only bind to Ge and Ru atoms in anion **9**²⁻. Note that the distance between two adjacent Ru atoms (Ru3 and Ru4) is very large, 3.1988(15) Å, which is presumably caused by the sterically demanding Cp* ligands.

The presence and (if no) identity of the two substituents is still uncertain. Observation of ~ 4 e/Å for the highest residual electron peak from the SCXRD measurement suggests a single atom, either C, N or O. Given that this value would be too low for a (fully occupied site of a) metal atom, and as the four sterically demanding Cp* groups prohibit the presence of any other larger substituents, potential candidates for the R group include –CH₃, –NH₂, –OH, =CH₂, =NH, and =O (see below for detailed discussion) with respect to the chemicals present in this procedure: ethane-1,2-diamine and [RuCp*(cod)Cl].

Moreover, the ESI-MS measurement of redissolved single crystals of [K(crypt-222)]₂**9**·solv in DMF has showed several signals, the most intense one of which refers to the **9**²⁻ anion. The dominant signals represent three overlapping signals of three species differing by ~15 m/z, which likely correspond to clusters without a R group, with one R group, and with two R groups, respectively. Attempt to finally assign these signals to possible species was not successful, however, as there would be numerous possible combinations that could account for the m/z differences. For example, replacing a Ge atom with an As atom would increase the m/z by ~2.3, but this can be compensated by replacing the substituent with another, related one (see above), and protonation/deprotonation owing to the ionization process of ESI-MS measurement.

DFT calculations were thus employed to provide insight into the Ge:As ratio in the presence or absence of various R groups. The calculations indicate that the ratio for Ge and As atoms should be 4:4 when R groups are absent, supported by a HOMO-LUMO gap of 1.039 eV (see Table 3.3). When R groups are attached to the Ge atoms (–CH₃ as an example), a 6:2 ratio for Ge and As atoms is more likely, as this composition exhibits a significant HOMO-LUMO gap of 1.247 eV and in accordance with the fact that a Ge–R group is isoelectronic to an As atom. For all other variants, the gaps are too narrow (see Table 3.3).

Table 3.3: Calculated HOMO-LUMO gap of the anion $\mathbf{9}^{2-}$ with different atomic ratios of Ge and As atoms in the case of R = none, and R = $-\text{CH}_3$, respectively. The methods are detailed in Section 7.4.2.

$[\{\text{Cp}^*\text{Ru}\}_4(\text{GeR})_x(\text{Ge}_4\text{As}_{4-x})]^{2-} (\mathbf{9}^{2-})$			
R = none		R = $-\text{CH}_3$	
Ge:As	HOMO-LUMO gap [eV]	Ge:As	HOMO-LUMO gap [eV]
2:6	0.186	2:6	0.375
4:4	1.039	4:4	0.541
6:2	0.137	6:2	1.247

Based on the calculations of the HOMO-LUMO gap, the optimized conformers (without R group, and with R = $-\text{Me}$, $-\text{NH}_2$, $-\text{CH}_2$, $-\text{NH}$) are shown in Figure 3.26. Figure 3.26a shows the global minimum structure of $[\{\text{Cp}^*\text{Ru}\}_4(\text{Ge}_4\text{As}_4)]^{2-}$. Conformers of $[\{\text{Cp}^*\text{Ru}\}_4(\text{GeR})_2(\text{Ge}_4\text{As}_2)]^{2-}$, where R = $-\text{Me}$ and $-\text{NH}_2$, are given in Figures 3.26b–3.26g, demonstrating that 1) the ratio between Ge and As is 6:2 when the Ge–R bond exhibits a single-bond character; 2) the conformers are energetically disfavored by approximately 8 $\text{kJ}\cdot\text{mol}^{-1}$ when two As atoms are adjacent, similar to the case of anion $\mathbf{7}^{2-}$. Figures 3.26h–3.26k depict the conformers of $[\{\text{Cp}^*\text{Ru}\}_4(\text{GeR})_2(\text{Ge}_2\text{As}_4)]^{2-}$ where R is assigned as $-\text{CH}_2$ and $-\text{NH}$. In these conformers, the Ge–R bond exhibits a double-bond character, resulting in a 4:4 ratio of Ge and As atoms in order to match the total charge of the anion. Similar to the conformer in Figure 3.26a, an As–As connection cannot be avoided in such cases. In all possible conformers, the Ge atom is prone to bind the R group. The conformers will be energetically disadvantaged by more than 50 $\text{kJ}\cdot\text{mol}^{-1}$ when As atoms bind the R groups, and the whole cluster would also distort notably, as seen in Figures 3.26l, 3.26m, which is not in agreement with the experimental findings.

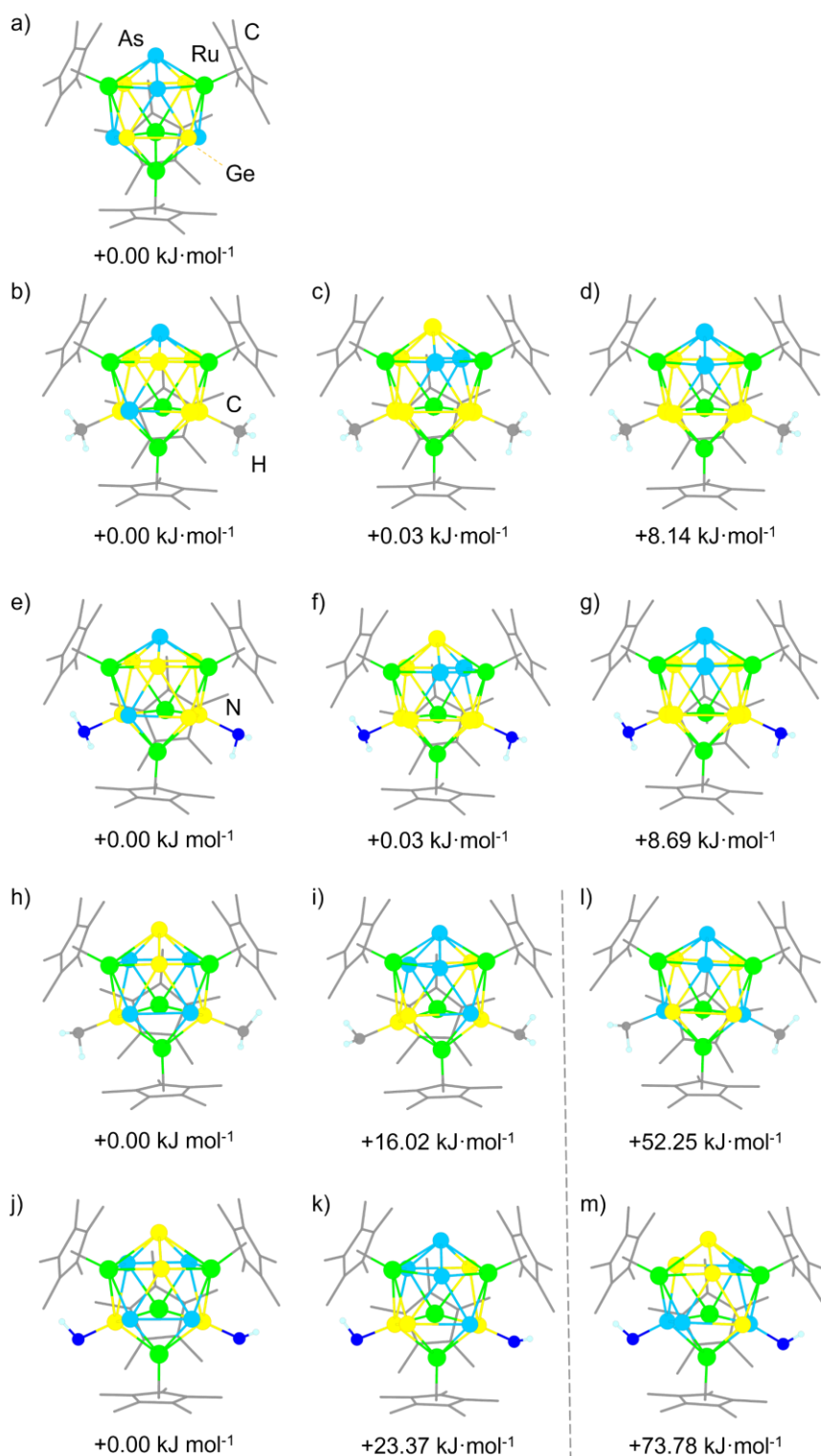


Figure 3.26: Computationally optimized minimum structures of the possible conformers of $\mathbf{9}^{2-}$: $[\{\text{Cp}^*\text{Ru}\}_4\text{Ge}_4\text{As}_4]^{2-}$ (a), $[\{\text{Cp}^*\text{Ru}\}_4(\text{GeMe})_2(\text{Ge}_4\text{As}_2)]^{2-}$ (b–d), $[\{\text{Cp}^*\text{Ru}\}_4(\text{GeNH}_2)_2(\text{Ge}_4\text{As}_2)]^{2-}$ (e–g), $[\{\text{Cp}^*\text{Ru}\}_4(\text{GeCH}_2)_2(\text{Ge}_2\text{As}_4)]^{2-}$ (h–i), $[\{\text{Cp}^*\text{Ru}\}_4(\text{GeNH})_2(\text{Ge}_2\text{As}_4)]^{2-}$ (j–k), as well as the conformers of $[\{\text{Cp}^*\text{Ru}\}_4(\text{AsCH}_2)_2(\text{Ge}_4\text{As}_2)]^{2-}$ (l), $[\{\text{Cp}^*\text{Ru}\}_4(\text{AsCH}_2)_2(\text{Ge}_4\text{As}_2)]^{2-}$ (m), for comparison. The methods are detailed in Section 7.4.2.

In an effort to identify the possible presence, and if no, the composition of the R groups, infrared (IR) spectroscopy was employed first. In Figure 3.27, three IR transmittance spectra from top to bottom are shown, top, a solid obtained by evaporation of all liquids from the reaction solution; middle, [K(crypt-222)]Cl·nH₂O (undried); bottom, [RuCp*(cod)Cl]. The last two spectra were recorded as reference spectra. Given that the band stretching and bending modes of Ge–C bonds appear in a region between $\sim 600\text{--}900\text{ cm}^{-1}$, this would be similar to those of the Ge–N bonds.^[256] However, these peaks are additionally likely to overlap with the bands of crypt-222, and Cp*, as seen in Figure 3.27, top. Bands of C–H or N–H bonds of the R groups will also overlap with the signals of crypt-222, Cp* (C–H bond stretching at $2800\text{--}3200\text{ cm}^{-1}$, bending at $700\text{--}900\text{ cm}^{-1}$) or en (N–H bond stretching at $3250\text{--}3400\text{ cm}^{-1}$, bending at $1580\text{--}1650\text{ cm}^{-1}$). As a N–H bond would give rise to a strong signal in the IR spectrum, the very small signals seen in the region of N–H bonds might be a hint for the exclusion of an –NH₂ group bound to the cluster anion.

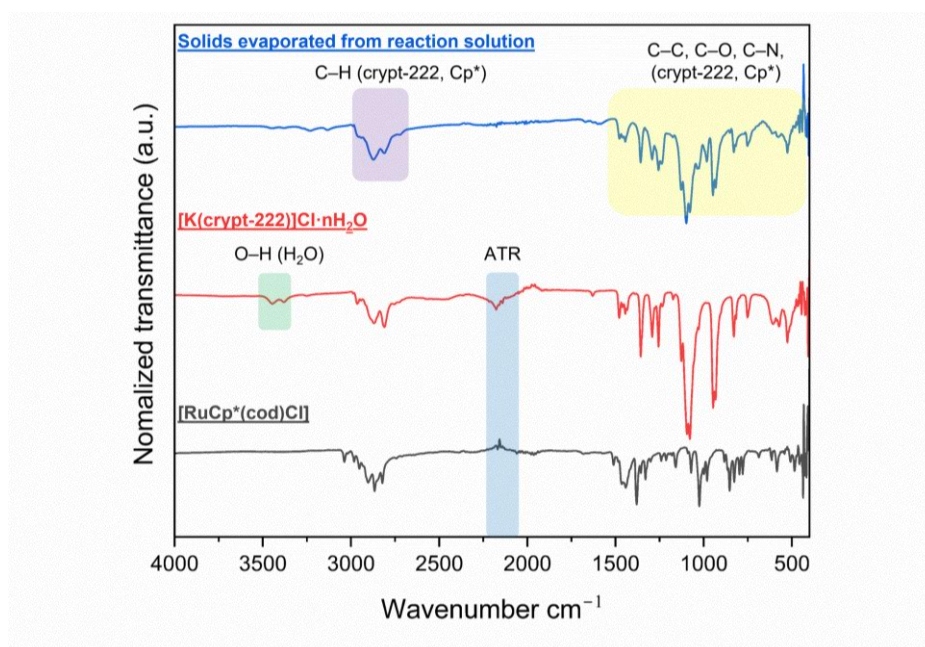


Figure 3.27: Top: Transmittance IR spectrum of the solid obtained by evaporation of all liquids from the reaction solution; middle: transmittance IR spectrum of [K(crypt-222)]Cl·nH₂O; bottom: transmittance IR spectrum of [RuCp*(cod)Cl].

Deuteration experiments were additionally conducted with the aim to gain further information. If the R group was –CH₃ or =CH₂, it would most likely originate from the methyl group of the Cp* ligand, though it cannot be ruled out that it could arise from the –C₂H₄– moiety in en. Therefore, the initial attempt was to synthesize d₁₅-[RuCp*(cod)Cl] which is an unknown compound so far. The synthesis was based on a similar procedure for a Rh analogue, however, was unfortunately unsuccessful, for more details, see Section 6.1. Alternatively, d₄-en was prepared following a slightly optimized literature procedure (see Section 6.1), to investigate if –NH₂ or =NH could be released and form the R group. Replacement of the reaction solvent with d₄-en (98.5%) resulted in a brown suspension, the color of which is identical to the color of the reac-

tion solution obtained in the original non-deuterated experiment, indicating that the reagents did not decompose in the presence of d_4 -en. An in-situ mass spectrum of the reaction solution was recorded after stirring for 3h, which, however, did not show any insightful signals that could correspond with a deuterated species. No crystals could be obtained from this solution, but the solid formed upon evaporation of the reaction solvent was analyzed by NMR spectroscopy. The ^2H NMR measurement in 0.6 mL of d_7 -DMF/DMF showed only solvent peaks (see Figure 3.28 below). While the lack of a crystalline product can hardly be used as an additional clue of excluding the possibility that R is an $-\text{NH}_2$ or $=\text{NH}$ group, we can at least not confirm this group to be present in $\mathbf{9}^{2-}$. None of these experiments could disclose $-\text{OH}$ or $=\text{O}$ from water trace in the solvent en as possibilities.

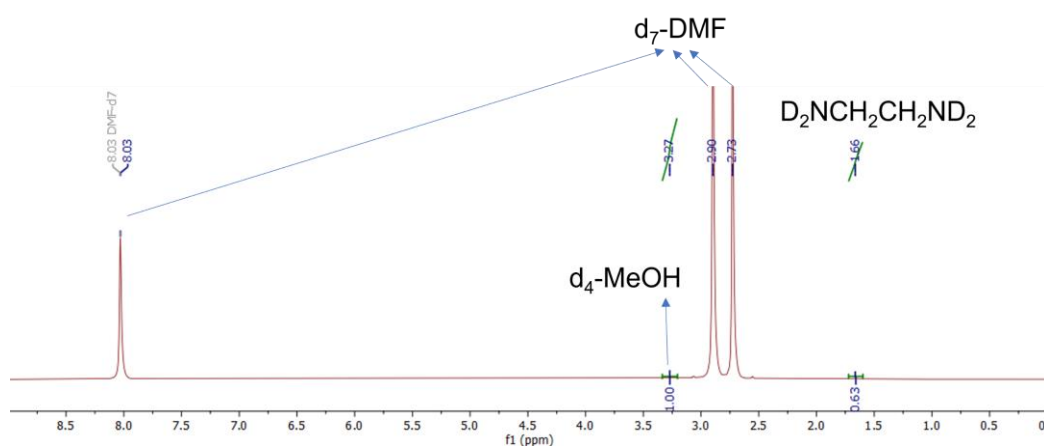


Figure 3.28: ^2H -NMR spectrum of the solids obtained by evaporation of the reaction solution in the attempted preparation of deuterated $\mathbf{9}^{2-}$ in d_7 -DMF/DMF (with a ratio of 10%:90%).

Despite the performance of a series of NMR and IR measurements, as mentioned above, no conclusion could be drawn so far about the identity of the R groups bonded to the Ge atoms and on their presence at all. This is mainly ascribed to the following facts: a) the number of H atoms in the R groups is negligible (a maximum of six), as compared to the large number of H atoms present in the cations (with two cations per cluster), solvent molecules, and Cp^* ligands, leading to the neglect of the signals in terms of their intensity; b) the signals for the R groups are likely to appear in the same chemical shift and wavenumber regions; c) the full removal of impurities or excess starting reagents is not feasible.

Zintl clusters that contain carbon-based R-groups bonded to Ge atoms of the cluster shell have been reported though. In these cases, the Ge–C bond lengths range between 1.927 and 2.045 Å.^[171,257–262] In this regard, the bond lengths in $\mathbf{9}^{2-}$ are way too short to represent a Ge–CH₃ moiety. Calculations confirmed this, as the Ge–R bond distance observed in anion $\mathbf{9}^{2-}$ does not correspond well with any possible bonds deduced from DFT calculations (see Table 3.4). At this point, it might be reasonable to consider, in addition, the possibility that the residual electron density found close to the cluster shell might even be an artifact. It is notable though that is found in several SCXRD analyses performed on compound $[\text{K}(\text{crypt-222})]_2\mathbf{9}\cdot\text{solv}$. The clarification of the identity and presence of R groups will be an objective to be tackled in the near future.

Table 3.4: Calculated bond lengths (Å) of different possible R group attached to the Ge atom, as well as the experimental bond lengths from SCXRD measurements. The methods are detailed in Section 7.4.2.

Possible R group	Calculated bond length [Å]
–CH ₃	2.02
–CH ₂	1.90
–NH ₂	1.95
–NH	1.77
Experimental bond lengths: 1.78 Å, 1.80 Å	

3.5 Conclusion

This section has demonstrated that a series of novel clusters emerged from the reactions of “K₂GeAs” with group 7-12 metal complexes. These investigations provided insight into the processes occurring in the solution. By mass spectrometry, it has been shown that the extraction of “K₂GeAs” in en/crypt-222 leads to the formation of different species analogous to As₄, including (Ge₄H)[–], (Ge₃As)[–], (Ge₃AsH₂)[–], (Ge₂As₂H)[–], and (GeAs₃)[–]. (Ge₂As₂)^{2–} remains the only species that could be transferred into a crystalline product upon the extraction process, whereas both (Ge₃As)^{3–} and (Ge₂As₂)^{2–} were observed as part of the products upon reaction with d¹⁰ metal complexes.

By reacting “K₂GeAs” with [MPh₂] (M = Zn, Cd, Hg) in en/crypt-222, the *pseudo*-tetrahedra served to coordinate M²⁺ cations or (MPh)⁺ fragments, thereby forming clusters with various architectures (anions **1**^{2–} – **5**^{6–}). These vary from the attachment of a (PhM)⁺ unit to one (Ge₃As)^{3–} anion, to a chain-type structure comprising four of such anions beside three M²⁺ cations. Anion **6**^{2–}, an analogue of anion **1**^{2–}, was formed in a similar reaction using [ZnMes₂].

Comprehensive studies combining X-ray diffraction analyses, mass-spectrometry, and quantum chemical calculations show that 1) there are notable differences in the reactivity and stability of the Zn-, Cd-, or Hg-based reactants and products, but 2) that many analogous species in all sets of reactions can be generally found. The different reactivities/stabilities (and possibly also solubilities) do not allow for the crystallization of them all, though.

Indeed, d¹⁰ metals seem to be inert enough to allow for a combination with the *pseudo*-tetrahedra under various coordination modes, which has been also observed previously for the clusters [Au₆(Ge₃As)(Ge₂As₂)₃]^{3–}, and [Cd₃(Ge₃P)₃]^{3–}.^[83,208] The range of the formed clusters is influenced by the subtle impacts of 1) the nature (especially the Lewis acidity) of the transition metal itself, and 2) the ligands with their different tendency to be released. The product spectrum of the coordination clusters described herein provides valuable insight into potential formation pathways (see Section 3.3).

Despite the tendency of forming coordination clusters, expansions upon fragmentation and reorganization of the anions are possible by using group 7, 8, and 10 metal complexes, as seen in anions **7**^{2–} – **9**^{2–}. At first glance, the three transition metal complexes employed herein are similar, as all of them contained the Cp* ligand. However, they behave differently when combined with “K₂GeAs”. In **7**^{2–} and **9**^{2–}, the Cp* ligands remain attached to the Ni and Ru atoms,

respectively. The transition metal fragments are part of the deltahedral cluster shell, which are electron-deficient. One reason of forming deltahedral clusters might be the electron configuration of the transition metal. It was already shown that in anion $\mathbf{1}^{2-} - \mathbf{6}^{2-}$, the electron-rich d^{10} metals tend to retain their electrons rather than transfer them to the cluster shell thus not “helping” the group 14 element to get more electron-rich. This is similar with the cases involving $[\text{NiCp}^*_2]$ and $[\text{RuCp}^*(\text{cod})\text{Cl}]$, which afford (different) electron-deficient products. A further difference is found in anion $\mathbf{8}^{q-}$, an intermetalloid cluster. The Mn atom in $[\text{MnCp}^*_2]$, in stark contrast, is obviously able to donate all of its 7 s- and d-electrons to the cluster shell. In this case, all the Cp^* ligands are released during the formation of anion $\mathbf{9}^{q-}$. The latter can be regarded as the oxidative coupling of two endohedral shells incorporating two Mn atoms which is a very unique finding.

Table 3.5 summarizes the Ge/As–Ge/As and Ge/As–As/Ge bond length range in anion $\mathbf{1}^{2-} - \mathbf{9}^{2-}$ for facilitating their comparison.

Table 3.5: Overview of the Ge/As–Ge/As and Ge/As–As/Ge bond length range (in Å) in the experimental structure in the cluster anion $\mathbf{1}^{2-} - \mathbf{9}^{2-}$.

Anion	Ge/As–Ge/As bond lengths [Å]	Ge/As–As/Ge bond length [Å]
$[\text{PhZn}(\text{Ge}_3\text{As})]^{2-} (\mathbf{1}^{2-})$	2.4673(15), 2.758(3)	2.4576(19), 2.5983(15)
$[\text{PhHg}(\text{Ge}_3\text{As})]^{2-} (\mathbf{2}^{2-})$	2.4899(18), 2.830(2)	2.4804(15), 2.541(2)
$[(\text{Ge}_3\text{As})\text{Zn}(\text{Ge}_2\text{As}_2)]^{3-} (\mathbf{3}^{3-})$	2.7360(10)	2.4595(12) – 2.4771(10)
$[\text{Cd}_3(\text{Ge}_3\text{As})_3]^{3-} (\mathbf{4}^{3-})$	2.552(13) – 2.922(10)	2.385(11) – 2.459(11)
$[\text{Zn}_3(\text{Ge}_3\text{As})_4]^{6-} (\mathbf{5a}^{6-}, \mathbf{5b}^{6-})$	2.416(6) – 2.769(2)	2.431(3) – 2.6752(19)
$[\text{MesZn}(\text{Ge}_3\text{As})]^{2-} (\mathbf{6}^{2-})$	2.4821(11), 2.6377(14)	2.4672(13), 2.6538(10)
$[\{\text{Cp}^*\text{Ni}\}_2(\text{Ge}_6\text{As}_2)]^{2-} (\mathbf{7}^{2-})$	2.5786(11) – 2.7285(12)	2.5631(9) – 2.7396(12)
$[\text{Mn}_2@\text{Ge}_x\text{As}_{24-x}]^{q-} (\mathbf{8}^{q-})$	2.438(3) – 2.585(2)	
$[\{\text{Cp}^*\text{Ru}\}_4(\text{GeR})_x(\text{Ge}_4\text{As}_{4-x})]^{2-} (\mathbf{9}^{2-})$	2.510(2) – 2.6426(14)	

4 Behavior of “K₅Ga₂Bi₄” in the Formation of Bi-based Anionic Clusters

4.1 Introduction

On a molecular scale, assemblies of Bi polycations such as the first isolation of tricapped prismatic Bi₉⁵⁺ from Bi₁₂Cl₁₄, as well as Bi₅⁺, Bi₅³⁺, Bi₆²⁺, Bi₈²⁺ that were isolated from Bi₁₁Cl₁₂Ir, Bi₅[GaCl₄]₃, Bi₁₁ClRh, and Bi₈[AlCl₄]₂, respectively, are known to exist.^[263–267] Further expansions like [CuBi₈]³⁺, [Au₂Bi₁₀]⁶⁺, [(Bi₈)Au(Bi₈)]⁵⁺, [Ni₂Bi₁₂]⁴⁺, [Rh@Bi₉]⁴⁺, [M@Bi₁₀]^{q+} (M/q = Pd/4, Pt/4, Au/5), [Rh₂@Bi₁₂]⁴⁺, and [(Bi₈)Ru(Bi₈)]⁶⁺, were typically approached by melting BiX₃ (X = Cl, Br) and/or Bi powders with metal powders/metal halides under ionothermal conditions, or by heating ternary or quaternary compounds in the presence of Lewis-acidic ionic liquids.^[268–277] These studies indicate that Bi polycations can further cooperate and be part of heteroatomic and intermetalloid clusters cations.

In addition to forming bismuth polycations, recent research has shown that Bi atoms are equally capable of forming polyanionic molecular assemblies: homoatomic, or heteroatomic in combination with other (semi)metal(s), similar to group 14 polyanions. The synthetic access to Bi-based polyanionic molecules was achieved through reactions of binary Zintl phases comprising homoatomic anions, K₃Bi₂ or K₅Bi₄,^[278,279] or by employing [K(crypt-222)]⁺ salts of binary anions, (Tt₂Bi₂)²⁻ (Tt = Sn, Pb),^[50,87,89,92] (TrBi₃)²⁻ (Tr = Ga, In, Tl)^[44,82] in reactions with transition metal, lanthanide, or actinide complexes.^[43,74,144,217,224,227,228,230,280–287]

As mentioned in Section 1.4.2.3, reactions of (Tt₂Bi₂)²⁻ (Tt = Sn, Pb) with metal complexes usually lead to ternary, yet usually less Bi-rich, intermetalloid clusters, in which the heteroatomic bonds usually seem to be strong enough to prevent the need for more Bi–Bi bonding in the cluster.^[215,219–221,288] A combination of K, Ge, and Bi, despite the immiscibility of Ge and Bi in the solid, which led to the formation of the hitherto most Bi-rich polyanion, (Ge₄Bi₁₄)⁴⁻, remains the only exception.^[218]

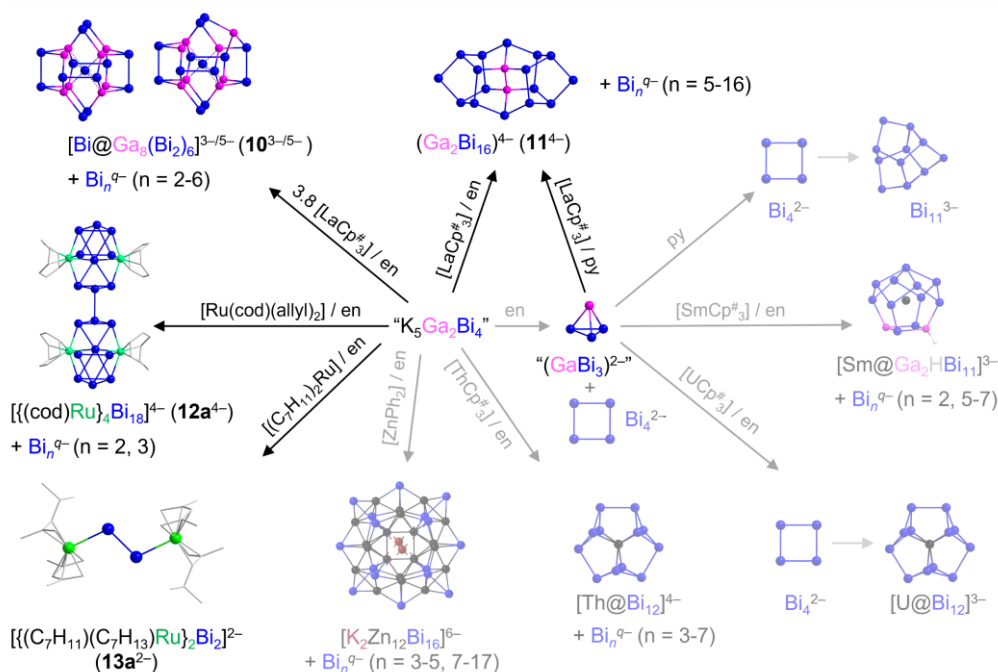
In a significant amount of reactions with the binary anions (TrBi₃)²⁻, the products turned out to comprise Bi atoms as the only main group component, as these anions tend to decompose under release of elemental group 13 metal. Indeed, elemental combinations that exhibit a significant size mismatch or do not reach sufficiently high bond energies tend to, but not always prefer element segregation, which may be terminated at the stage of Bi anionic clusters before finally forming the bulk phase of Bi metal. By introduction of further organometallic d-block or f-block compounds into solutions of (TrBi₃)²⁻ anions (Tr = Ga, In, Tl), which yielded binary or ternary anions [Bi@In₈(Bi₂)₆]^{3-/5-}, [(cod)Ru}Tl₂Bi₆]²⁻, [(TlBi₅)Zn₃(Bi₆)]⁴⁻, [Bi₇CdBi₇]⁴⁻, [(cod)Ru}Bi₉]³⁻, [Sm@Ga_{3-x}H_{3-2x}Bi_{10+x}]³⁻ (x = 0, 1), [U@Tl₂Bi₁₁]³⁻, or [(La@In₂Bi₁₁)](μ-

$\text{Bi})_2(\text{La}@\text{In}_2\text{Bi}_{11})]^{6-}$, $[\text{An}@\text{Bi}_{12}]^{q-}$ ($\text{An}/q = \text{Th}/4, \text{U}/3$), all of which except $[\text{Bi}@\text{In}_8(\text{Bi}_2)_6]^{3-/5-}$ comprise polybismuthide moieties, thus may be understood as intermediates on the way toward larger polybismuthide clusters^[82,144,217,224,226–228]

In regard to this behavior of compounds with binary group 13/Bi precursors with relatively poor tendency to form heteroatomic bonds, finding out more about the processes in solutions, in particular in the presence of Lewis-acidic metal ions, is meaningful. For this, the ternary solid “ $\text{K}_5\text{Ga}_2\text{Bi}_4$ ”, which was previously used as a source for salts of the “ $(\text{GaBi}_3)^{2-}$ ” anion, is employed as a precursor to investigate its reactivity. It has been recently showed that this solid yields not only said binary anion but also Bi-based cluster species, which might be attributed to the relatively different size and electron affinity of Ga and Bi compared to other known main group/Bi combinations. To expand these studies, different Lewis-acidic metal complexes, $[\text{La}(\text{C}_5\text{Me}_4\text{H})_3]$, $[\text{Ru}(\text{cod})(\text{H}_2\text{CC}(\text{Me})\text{CH}_2)_2]$, and $[(\text{C}_7\text{H}_{11})_2\text{Ru}]$ which were considered suitable for assisting in the assembly of $\{\text{Bi}_n\}$ building units, as the anticipated interaction with the anionic precursor are neither purely ionic nor too strongly covalent, were selected to react with the “ $\text{K}_5\text{Ga}_2\text{Bi}_4$ ”.

Scheme 4.1 summarizes the new findings, which will be discussed in detail below, and all related findings based on the K/Ga/Bi system that were reported previously.

Scheme 4.1: Overview of all known (gray arrows) and new (black arrows) homoatomic, binary, and ternary anions that were obtained directly or indirectly from the ternary K/Ga/Bi system. Clusters that were reported previously are shown in semitransparent mode.^[44,217,224,228–230]



4.2 Understanding and Elucidating the Formation and Relationship of Bi-Rich Nanostructures

The results discussed in this section were published in:

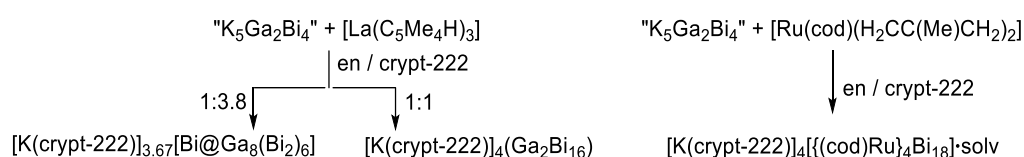
Fuxing Pan,[‡] Shangxin Wei,[‡] Lukas Guggolz, Armin R. Eulenstein, Frank Tambornino, and Stefanie Dehnen*, *J. Am. Chem. Soc.* **2021**, *143*, 7176–7188.

[[‡]] Equal authorship

4.2.1 Syntheses, Structures, and Bonding

By varying the molar ratios of the reactants “K₅Ga₂Bi₄”, [La(C₅Me₄H)₃], and crypt-222 (1:3.8:1.5 and 1:1:5) in en solutions, it was able to isolate two different compounds comprising different binary anions, [K(crypt-222)]_{3.67}[Bi@Ga₈(Bi₂)₆] ([K(crypt-222)]_{3.67}**10**) and [K(crypt-222)]₄(Ga₂Bi₁₆)·solv ([K(crypt-222)]₄**11**·solv, solv = none, the filtrate was layered with toluene, [K(crypt-222)]₄**11a**; solv = 4py, the solid mixtures were reacted in pyridine, [K(crypt-222)]₄**11b**·4py). For a variation in Lewis acidity, the d-block metal complex, [Ru(cod)(H₂CC(Me)CH₂)₂] was chosen to react with “K₅Ga₂Bi₄”, and crypt-222 in a ratio 1:1:5 in 4 mL of en. The reaction afforded another compounds, [K(crypt-222)]₄[(cod)Ru]₄Bi₁₈]·solv ([K(crypt-222)]₄**12**·solv, solv = 4.63THF·2en, [K(crypt-222)]₄**12a**·4.63THF·2en; solv = none, [K(crypt-222)]₄**12b**). Scheme 4.2 summarizes the syntheses information of both anions (**12a**^{4−} as a representative).

Scheme 4.2: Left: Syntheses of [K(crypt-222)]_{3.67}**10** and [K(crypt-222)]₄**11a** by treatment of “K₅Ga₂Bi₄” in en/crypt-222 in the presence of [La(C₅Me₄H)₃] and subsequent crystallizations by layering with Toluene. Right: Synthesis of [K(crypt-222)]₄**12**·solv by reaction of “K₅Ga₂Bi₄” with [Ru(cod)(H₂CC(Me)CH₂)₂] in en/crypt-222 and subsequent crystallizations by layering with THF.



Compound [K(crypt-222)]_{3.67}**10** crystallizes in the triclinic space group type $P\bar{1}$ with one formula unit per unit cell and the [Bi@Ga₈(Bi₂)₆]^{3−/5−} anions being positioned around a crystallographic inversion center, of which the central Bi atom (Bi1) sits on the symmetric axis (see Figure 4.1 for view of anion **10**^{3−/5−}, Figure 4.2 for view of unit cell of compound [K(crypt-222)]_{3.67}**1**). The structure of anion **10**^{3−/5−} is related to the one reported recently for [Pn@In₈(Pn₂)₆]^{3−/5−} (Pn = Sb, Bi), with varied bond lengths owing to the new elemental combination and another isomer preferred for the pentaanion.^[226,289] In anion **10**^{3−/5−}, two differently charged anions in a ratio of 2:1(3− versus 5−) are found, which is varied from the 1:1 ratio within the reported In/Bi anion. This is in agreement with the observation of a slight under-occupation of the cationic sites, refining to 3.67 instead of 4.00 in the sum, according to the single-crystal X-ray diffraction and μ -XRF studies (detailed measurement data is shown in Section 7.1, 7.2).

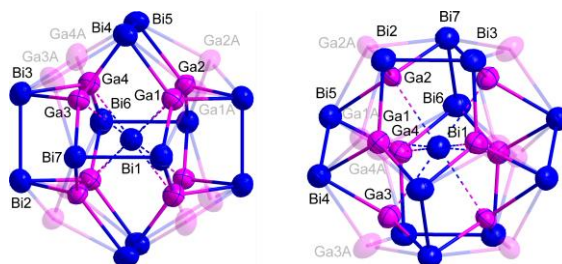


Figure 4.1: Molecular structure of the $[\text{Bi}@\text{Ga}_8(\text{Bi}_2)_6]^{3-/5-}$ (anion $10^{3-/5-}$) in two different orientations, emphasizing the (idealized) T_h symmetry of the 3- anion (left) and the pentagon-dodecahedral C_{20} fullerene topology if regarding all possible external Ga positions in the 5- anion (right). The external (minority) positions of the Ga atoms are drawn in semitransparent mode (displacement ellipsoids of heavy atoms set at 50% probability). Relevant structural parameters are mentioned in the text.

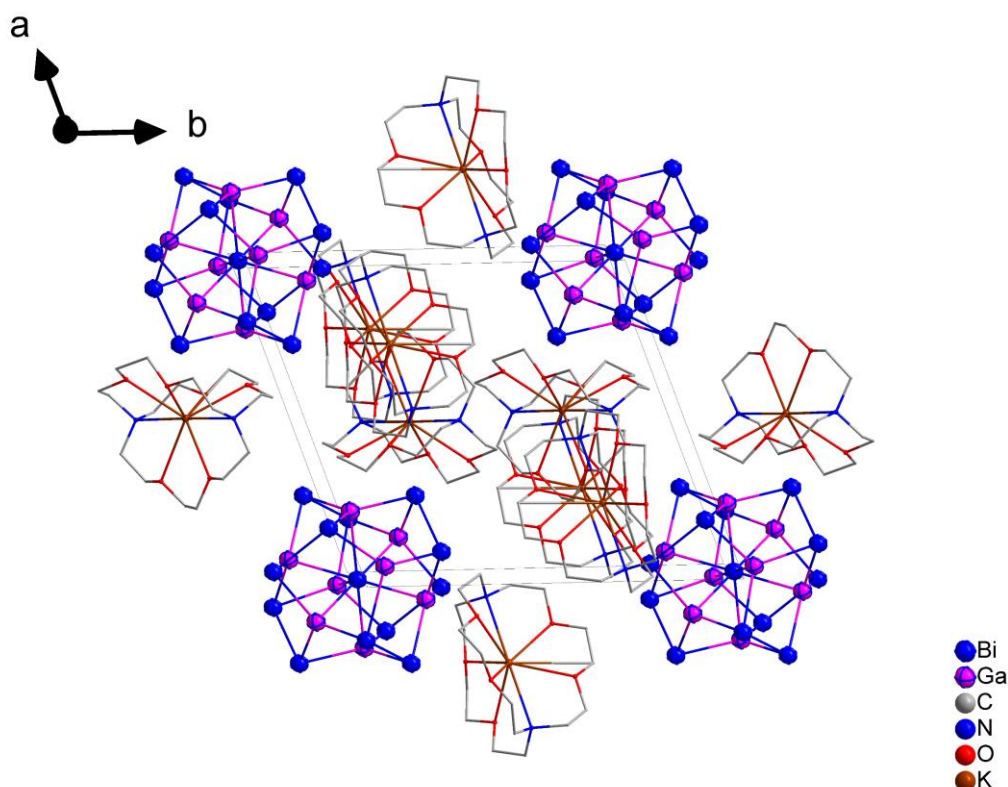


Figure 4.2: View of the (extended) unit cell of $[\text{K}(\text{crypt-222})]_{3.67}10$, viewed along the crystallographic c -axis. The disorder of the Ga atoms that is detailed in Figure 4.1 is omitted here for clarity. H atoms are omitted for clarity.

Figure 4.1 depicts both anion 10^{3-} (without transparent models) and anion 10^{5-} (Ga atoms are with semitransparent modes) as a whole, that shared all Bi atoms on the site. Figure 4.2 shows anion $10^{3-/5-}$ sitting on the edge of the axis surrounded by $[\text{K}(\text{crypt-222})]^+$ cations. The two molecules in terms of their charges within compound $[\text{K}(\text{crypt-222})]_{3.67}10$ are distinguished by the relative positions of the Ga atoms. As predicted by a *pseudo*-element consideration, the atoms in $[\text{Bi}@\text{Ga}_8(\text{Bi}_2)_6]^{3-}$ can be viewed as an inner “ Bi^{3-} ” ion (Bi1) being surrounded (at

relatively long Bi1...Ga distances, 2.823(4)–2.886(4) Å) by eight formally uncharged “Ga⁰” atoms. These Ga atoms are further bonded to three neighboring Bi atoms each (Ga–Bi 2.698(4)–2.780(3) Å) in a nearly planar trigonal fashion (disregarding the nearly perpendicular, weaker interaction to the central Bi atom). The outer Bi atoms are arranged in Bi₂ dumbbells, yet they behave like uncharged “Bi⁰” atoms and correspondingly show a pyramidal coordination environment with two bonds to adjacent Ga atoms and one Bi–Bi bond (2.9867(18)–3.0249(14) Å). Anions in compound [K(crypt-222)]_{3.67}**10** represents the overall largest binary main group cluster containing Ga and Bi atoms.

By addition of two charges to one of the Ga atoms, the formally resulting “Ga²⁻” site becomes isoelectronic to a group 15 atom. Such atoms are pushed outward and, if all eight Ga atoms were involved, would ultimately generate a pentagon-dodecahedral 20-atom polyhedron. A corresponding “[Bi@Ga₈(Bi₂)₆]¹⁹⁻” would thus be isoelectronic with a hypothetical “[Bi@Bi₂₀]³⁻” fullerane and the known [20]silafullerane [Cl@Si₂₀(SiCl₃)₁₂Cl₈]⁻.^[290,291] However, an anion of such an extremely high charge (19-) is not likely to form in solution. Instead, only one of the Ga atoms is shifted to an outward position while the overall charge is increased to 5- in [Bi@Ga₈(Bi₂)₆]⁵⁻. The respective Ga atom is statistically disordered over all eight possible positions, with an average site occupancy factor of 0.33. Correspondingly, this anion contributes to the overall sum formula with a weight of 0.33, while the contribution of the anion with charge 3- is 0.67. It is also worth noting here that in both of the recently reported clusters [Pn@In₈(Pn₂)₆]^{3-/5-} (Pn = Sb, Bi), two In atoms were moved to an outward position in the 5- species instead of only one in the cluster reported herein. As a consequence of two atoms being displaced, the respective structural change per atom was smaller. This difference is attributed to the presence of (smaller) Ga atoms in the case of compound [K(crypt-222)]_{3.67}**10** and its corresponding consequences for structures and relative stabilities. However, the general, intrinsic observation of the crystallization of such clusters as double salts with anions of different charges on the same crystallographic position indicates the relatively high flexibility of such clusters regarding their charge, which allows them to respond to the needs of an optimal packing of anions and cations in the crystal. Disordered models of anion **10**^{3-/5-} are detailed in Figure 4.3.

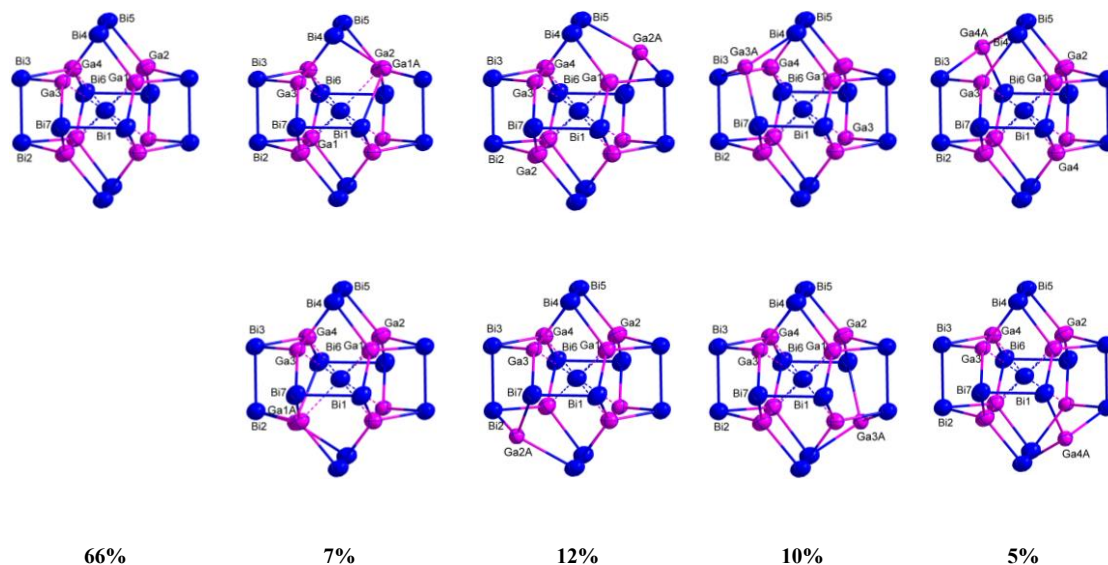
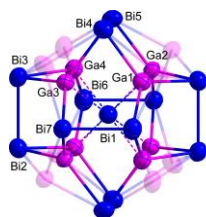


Figure 4.3: Disorder model illustrated by superposition of different compositions in $10^{3-/5-}$. Top: The entire model with disorder positions given in semi-transparent mode. Center and bottom: Different components along with their significance. Note that the structures shown in the middle and the bottom row are produced by the molecular inversion symmetry. The methods are detailed in Section 7.4.3.

The effect of different charges on the cluster structures was corroborated by quantum chemical investigations using DFT methods. In anion $10^{3-/5-}$ the preference for the formation of a 5– anion (12% in 34%, see Figure 4.3) with one single Ga atom moved outwards is more distinct than for the homologous In compounds. This might be explained by the fact that in the In/Bi case, a smaller shift of two In atoms serves to form a nearly perfectly planar five-membered Bi–In–Bi–Bi–In ring, in which the two In atoms occupy positions of the dodecahedral cluster architecture, which seems to be preferential. In the Ga/Bi case, however, a corresponding five-membered ring would still be folded. Here, a “dodecahedral position” of a Ga atom is only reached by a more significant structural change, such as performed by one atom alone.

Consequently, in the global minimum isomer of the anion $10^{3-/5-}$ one Ga atom (e.g., Ga2) is moved to an outward position (Figure 4.4, A). Furthermore, it possesses the largest HOMO–LUMO gap of all isomers (E_{gap} 1.1 eV, see Table 4.1), and represents a closed-shell molecule. The alternative versions, in which two Ga atoms at a time are shifted less pronouncedly to an outward position, hence not reaching the fullerene-related positions (e.g., Ga1/Ga2, Ga1'/Ga2, or Ga2/Ga2', respectively) are higher in energy (by +35, +73, +80 kJ/mol, respectively). Fur-

thermore, they possess smaller HOMO-LUMO gaps throughout (E_{gap} 0.54, 0.35, 0.23 eV), and the second least stable case converges in an open-shell configuration.

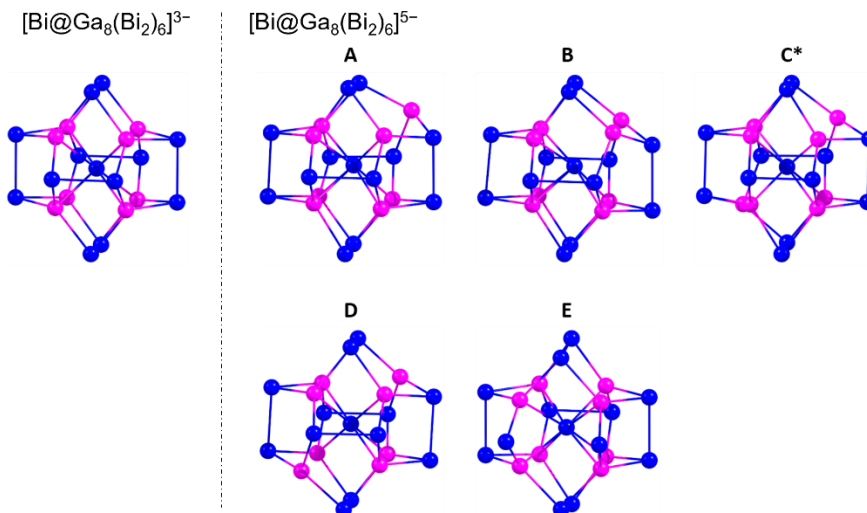


Figure 4.4: Calculated structures of the four isomers of the anions $[\text{Bi}@\text{Ga}_8(\text{Bi}_2)_6]^{3-}$ and $[\text{Bi}@\text{Ga}_8(\text{Bi}_2)_6]^{5-}$ in compound $[\text{K}(\text{crypt-222})]_{3.67} \mathbf{11}$ with one Ga atom shifted outwards (A) or two Ga atoms shifted outwards that occupy one edge (B), one face diagonal (C), or one space diagonal (D) of the originally cubic arrangement of the eight Ga atoms. A second isomer upon simultaneous shift of two directly neighboring Ga atoms (see B) bears a break of one Bi–Bi bond. For clarity, only one of the two enantiomers for each of the isomers is shown (Ga: pink, Bi: blue). Isomer C (marked with an asterisk) possesses a triplet ground state. The methods are detailed in Section 7.4.3.

For comparison of the anion $\mathbf{10}^{3-/5-}$ with the reported homologues possessing In/Bi or In/Sb elemental compositions, and also the yet unknown variant with a Ga/Sb combination of atoms, the structures of their corresponding isomers using the very same methods as for the anion in $\mathbf{10}^{3-/5-}$, which proved to be suitable for such clusters in many cases, were calculated. It is worth noting that we find not identical, but similar numbers to those reported for $[\text{Pn}@\text{In}_8(\text{Pn}_2)_6]^{3-/5-}$ (Pn = Sb, Bi), with slight deviations being likely due to the application of slightly different methods. The results of the new calculations are summarized in Table 4.1.

In all cases, the isomer with one group 13 element shifted to an outward position represents the global minimum structure. The energy difference, between the global minimum and the most stable isomers with two group 13 atoms moved outwards, is +21 kJ/mol for the In/Bi homologue, +35 kJ/mol for the Ga/Bi anion in $\mathbf{10}^{3-/5-}$ (see above), +37 kJ/mol for the In/Sb homologue, and +53 kJ/mol for the (hypothetical) Ga/Sb homologue, which nicely follows a trend of increasing energy differences with decreasing sum of the atomic numbers of the involved elements. Thus, for the In/Bi and In/Sb clusters, the minimum structure is apparently not the one that was reported to crystallize.^[226,289]

Table 4.1: Calculated relative energies (ΔE in $\text{kJ}\cdot\text{mol}^{-1}$) and HOMO-LUMO gaps (E_{gap} in eV) of the five isomers of the following anions, optimized with the same quantum chemical methods: $[\text{Sb}@Ga_8(\text{Sb}_2)_6]^{5-}$ (hypothetical), $[\text{Sb}@In_8(\text{Sb}_2)_6]^{5-}$, $[\text{Bi}@Ga_8(\text{Bi}_2)_6]^{5-}$ (this work, anion **10**⁵⁻), and $[\text{Bi}@In_8(\text{Bi}_2)_6]^{5-}$. The methods are detailed in Section 7.4.3.

Species (sum of Tr + Pn atomic numbers)	A ΔE	E_{gap}	B ΔE	E_{gap}	C ΔE	E_{gap}	D ΔE	E_{gap}	E ΔE	E_{gap}
$[\text{Sb}@Ga_8(\text{Sb}_2)_6]^{5-}$ (31 + 51 = 82)	0	+1.37	+53	+0.56	+63 ^b	+0.53 ^b	+86	+0.30	+12	+1.05
$[\text{Sb}@In_8(\text{Sb}_2)_6]^{5-}$ (49 + 51 = 90)	0	+1.21	+37	+0.82	^a	^a	+71	+0.12	+19	+1.11
$[\text{Bi}@Ga_8(\text{Bi}_2)_6]^{5-}$ (31 + 83 = 114)	0	+1.13	+35	+0.54	+73 ^b	+0.35 ^b	+80	+0.23	+24	+0.92
$[\text{Bi}@In_8(\text{Bi}_2)_6]^{5-}$ (49 + 83 = 132)	0	+0.98	+21	+0.53	+38	+0.37	^a	^a	+29	+0.82

^a The isomers with the indicated starting structures converge into isomer **E** during the geometry optimization process.

^b Isomer **C** possesses a triplet ground state for the elemental combinations Ga/Sb and Ga/Bi, while the elemental combination In/Bi leads to convergence into a closed-shell molecule, and the cluster with the elemental combination In/Sb undergoes a structural change to isomer **E**.

Noteworthy, an isomer that was not yet considered nor discussed, represents the second best isomer for all four elemental combinations. (+24 kJ/mol for **10**^{3-/5-}; E_{gap} 0.92 eV) in the studies shown in Table 4.1. In two cases, higher energy isomers created by shifting two of the group 13 atoms outwards even converge into this isomer during the geometry optimization cycles. Here, all eight Ga atoms are finally shifted inwards, thereby accumulating charge density in the cluster center, while one of the Bi–Bi bonds (e.g., Bi6–Bi7') is cleaved. Interestingly, the order of energy differences with regard to the global minimum structure develops in the opposite direction with the atomic number sums than for the isomers discussed above: +12 kJ/mol for Ga/Sb, +19 kJ/mol for In/Sb, +24 kJ/mol for Ga/Bi, and +29 kJ/mol for In/Bi. The fact that there is no indication whatsoever for the existence of such isomers in the experimentally determined crystal structures can only be explained in terms of the shift of the charge density towards the cluster center in these cases, and thus a less preferred situation for crystallization along with cations.

Overall, the calculations of the full series of homologous cluster isomers is in full agreement with experimental findings, while the reported coexistence of the 3– with 5– isomers that possess two In atoms on outer positions was rendered unlikely. Consequently, the hypothesis of a crystallization of nonminimum structures in the case of clusters with In/Sb and In/Bi elemental combinations owing to overcompensation of the energy difference by effects caused by the crystalline environment appears to be reasonable.

Through an ESI(–) mass spectrometry study, $(\text{Ga}_8\text{Bi}_{13})^-$, $(\text{KGa}_8\text{Bi}_{13})^-$ and $(\text{K}_2\text{Ga}_8\text{Bi}_{13})^-$ were assigned from a solution of freshly dissolved crystals of compound $[\text{K}(\text{crypt-222})]_{3.67}\text{10}$ (see Figure 4.5). The three species that are relevant to the unchanged cluster composition represent the original 3–, 2–, and 1– charge, respectively. However, the changed charge of anions found in ESI(–) mass spectrometry are attributed to a rapid in-situ oxidation effect during the meas-

urement. Further signals comprise additional crypt-222 ligands and the full spectrum is shown in Section 7.3.2.

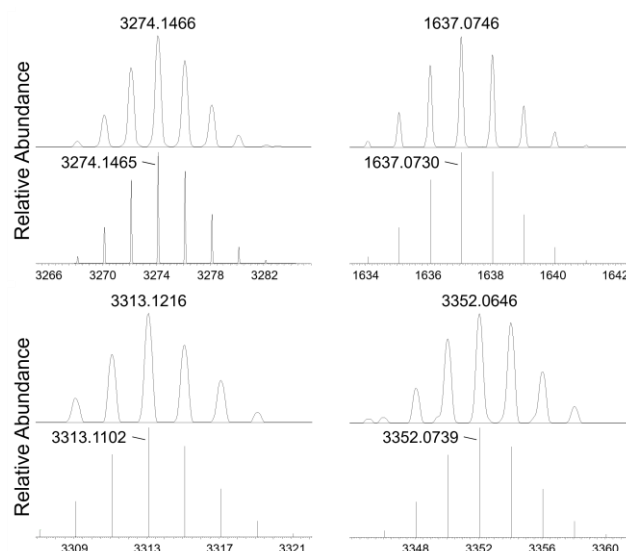


Figure 4.5: High-resolution electrospray-ionization mass spectra of a fresh solution of single-crystals of compound [K(crypt-222)]_{3.67}**10** in DMF, indicating four variations of the mass peak in the measured (upper part of each panel) and simulated isotope patterns (lower part of each panel), obtained in negative-ion mode. Top left: (Ga₈Bi₁₃)⁻, centered at *m/z* 3274.1466 (calc. 3274.1465). Top right: (Ga₈Bi₁₃)²⁻, centered at *m/z* 1637.0746 (calc. 1637.0730). Bottom left: (KGa₈Bi₁₃)⁻, centered at *m/z* 3313.1216 (calc. 3313.1102). Bottom right: (K₂Ga₈Bi₁₃)⁻, centered at *m/z* 3352.0646 (calc. 3352.0739).

Compound [K(crypt-222)]₄**11a** crystallizes in the orthorhombic space group type *Pbca* with four formula units per unit cell, in which the anionic moiety possesses crystallographic inversion symmetry (see Figure 4.6 for anion **11a**⁴⁻, and Figure 4.7 for viewing of unit cell of compound [K(crypt-222)]₄**11a**). The solvate [K(crypt-222)]₄**11b**·4py that was obtained from py instead of en as solvent crystallizes in the monoclinic space group type *P2₁/n* with two formula units per unit cell. The anions in both compounds show only minor deviations of structural parameters, for which only the structure of the anion **11a**⁴⁻ is discussed here in detail (for **11b**⁴⁻, see Section 7.1.3).

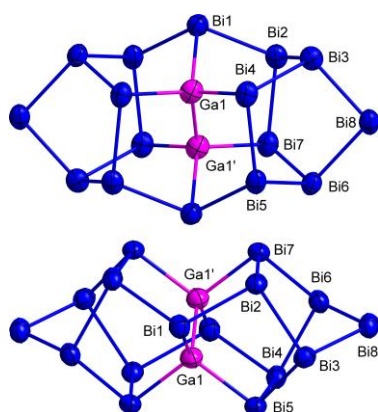


Figure 4.6: Perpendicular views of the molecular structure of the $(\text{Ga}_2\text{Bi}_{16})^{4-}$ anion, as found in the single-crystal structures of $\mathbf{11a}^{4-}$ as an example of compound $[\text{K}(\text{crypt-222})]_4\mathbf{11} \cdot \text{solv}$ (displacement ellipsoids of heavy atoms set at 50% probability). Relevant structural parameters are mentioned in the text.

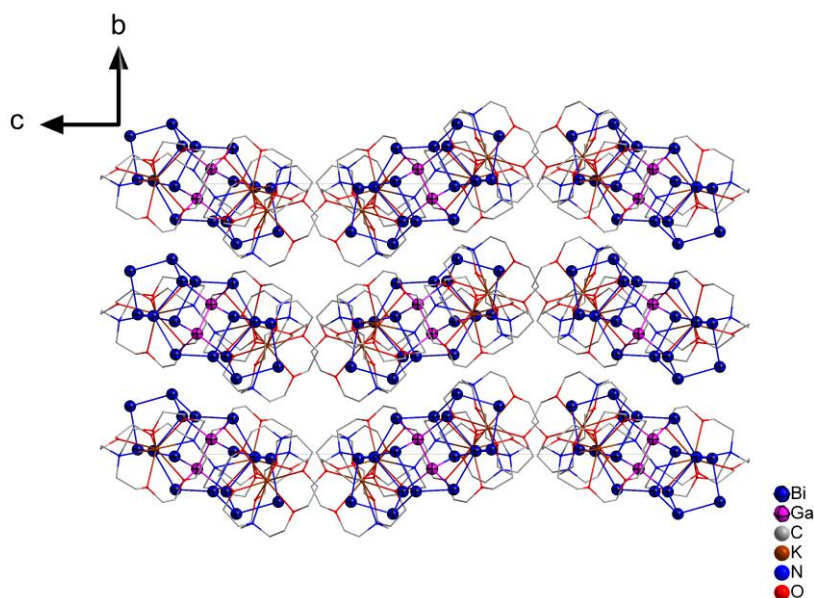


Figure 4.7: View of the (extended) unit cell of $[\text{K}(\text{crypt-222})]_4\mathbf{11a}$, viewed along the crystallographic a -axis. H atoms are omitted for clarity.

The cluster anion $\mathbf{11}^{4-}$ can be transferred to the gas phase as a whole, as confirmed by ESI mass spectrometry (Figure 4.8). This is accompanied by a two-electron oxidation, which is obviously tolerated for the time of the measurement. The relatively low sensitivity for such oxidations during ESI mass spectrometry of $[\text{K}(\text{crypt-222})]_4\mathbf{11a}$, which was also observed for $[\text{K}(\text{crypt-222})]_{3.67}\mathbf{10}$, is clearly different from the Ge–Bi system, where only fragments of the anion were observed in the ESI(–) mass spectrum.

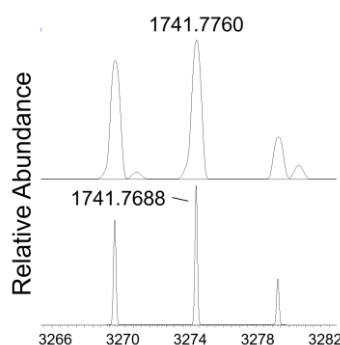


Figure 4.8: High-resolution electrospray-ionization mass spectrum of a fresh solution of single crystals of compound $[K(\text{crypt-222})]_4\mathbf{11a}$ in DMF, showing the mass peak of $(\text{Ga}_2\text{Bi}_{16})^{2-}$ (upon two-electron oxidation under ESI-MS conditions) centered at m/z 1741.7760 (top; calc. 1741.7688, bottom), obtained in negative-ion mode.

The motif of the $(\text{Ga}_2\text{Bi}_{16})^{4-}$ cluster anion as a whole, and with respect to the tendency for element segregation, is reminiscent of the isoelectronic anion $(\text{Ge}_4\text{Bi}_{14})^{4-}$, yet obviously different in detail.^[218] While $(\text{Ge}_4\text{Bi}_{14})^{4-}$ may be viewed as two $\{\text{Bi}_7\}$ units being linked through a $\{\text{Ge}_4\}$ chain, a $\{\text{Ga}_2\}$ dumbbell is “embedded” in a $\{\text{Bi}_{16}\}$ framework in the structure of $(\text{Ga}_2\text{Bi}_{16})^{4-}$. Anion $\mathbf{11}^{4-}$ thus possesses the largest number of Bi atoms included and consecutively linked in a binary main group cluster to date. As another difference from $(\text{Ge}_4\text{Bi}_{14})^{4-}$, any disorder of the Ga atoms on positions that are indicated as Bi atoms in the anion $\mathbf{11}^{4-}$ was observed.

According to *pseudo*-element considerations, the four-bonded Ga (*pseudo*-group 14) may be viewed as formally “ Ga^- ”, and the two-bonded Bi atoms (*pseudo*-group 16) as “ Bi^- ”, which correlates with the total charge of 4^- . Accordingly, the three-bonded Bi atoms are formally neutral. Localized molecular orbitals (LMOs, Figure 4.9) that were obtained from the Kohn–Sham orbitals by the method of Boys confirm a fully localized bonding structure here, indicating the high relationship of this architecture with the bonding situation in elemental Bi.^[292]

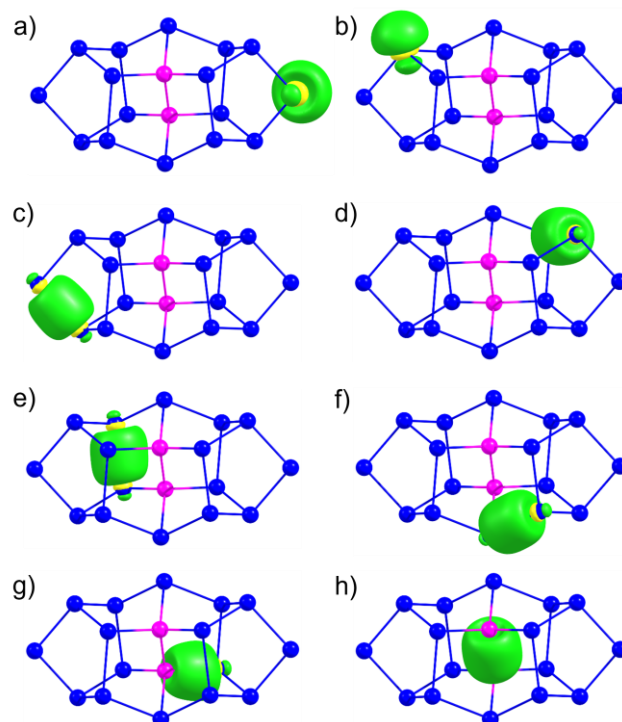


Figure 4.9: Selected localized molecular orbitals (LMOs) of the $(\text{Ga}_2\text{Bi}_{16})^{4-}$ anion in compound $[\text{K}(\text{crypt-222})]_4\mathbf{11a}$ upon simultaneous optimization of the electronic and geometric structure using density functional theory (DFT) methods and localization of the Kohn-Sham orbitals by the Boys method. The panels show LMOs representing Bi lone pairs (a and b), one of each types of homopolar Bi–Bi bonds (c, d, e, f), one of the six Ga–Bi bonds, all of which are slightly polarized towards the Bi atoms (g), and the Ga–Ga bond (h). The color code is the same as in Figure 4.6. For a full selection of representative LMOs, see Section 7.4.3.

The Ga–Ga bond in $\mathbf{11a}^{4-}$ (2.4703(40) Å) is significantly shorter than the bonds reported for the deltahedral Ga_{11}^{7-} cluster in $\text{Cs}_8\text{Ga}_{11}$ or $\text{Cs}_8\text{Ga}_{11}\text{Cl}$ (2.6421(7)–2.913(1) Å), thus indicating the presence of a strong Ga–Ga single bond.^[293] The same holds for the Ga–Bi distances in $\mathbf{11a}^{4-}$ (2.6940(30)–2.7106(29) Å), which are slightly shorter than the shortest contact in $[\text{Sm}@\text{Ga}_{3-x}\text{H}_{3-2x}\text{Bi}_{10+x}]^{3-}$ ($x = 0, 1$; 2.750(4) Å) and thus represent strong single bonds. Bi–Bi bond lengths in $\mathbf{11a}^{4-}$ are 2.9469(16)–3.0303(15) Å, which compares well with the corresponding bond lengths in $(\text{Ge}_4\text{Bi}_{14})^{4-}$ and Bi_{11}^{3-} (2.9464(7)–3.0304(15) and 2.917(1)–3.029(1) Å, respectively).^[218,228,229] They are also very similar to those observed in compound $[\text{K}(\text{crypt-222})]_{3.67}\mathbf{10}$, as another indication for the electron-precise situation in both Bi-rich anions.

Two related compounds from $[\text{K}(\text{crypt-222})]_4\mathbf{12}$ ·solv both crystallize in the triclinic space group $P\bar{1}$, with one $\mathbf{12a}^{4-}$ or two $\mathbf{12b}^{4-}$ formula units per unit cell. The molecular structures of the anions $\mathbf{12a}^{4-}$ and $\mathbf{12b}^{4-}$ differ mainly by the relative position of two $\{[(\text{cod})\text{Ru}]_2\text{Bi}_9\}$ units: in $\mathbf{12a}^{4-}$ two units align well; yet in $\mathbf{12b}^{4-}$ one of them bends (see Figure 4.10, and detail information see below). Under the effect of different solvate together with slightly varied structure of both anions, compound $[\text{K}(\text{crypt-222})]_4\mathbf{12a} \cdot 4.63\text{THF} \cdot 2\text{en}$ and $[\text{K}(\text{crypt-222})]_4\mathbf{12b}$ also show different packing patterns in the unit cell (see Figure 4.11). $\{[(\text{cod})\text{Ru}]_4\text{Bi}_{18}\}^{4-}$ ($\mathbf{12}^{4-}$) may be viewed as a dimer of the $\{[(\text{cod})\text{Ru}]_2\text{Bi}_9\}^{3-}$ cluster cousin upon oxidative coupling, where $\{[(\text{cod})\text{Ru}]_2\text{Bi}_9\}^{3-}$ was produced by reactions of $[\text{Ru}(\text{cod})(\text{H}_2\text{CC}(\text{Me})\text{CH}_2)_2]$ with $(\text{TlBi}_3)^{2-}$.^[82]

12a^{4−} and **12b**^{4−} thus comprise the largest number of directly connected Bi atoms in any molecular system reported so far and may pave a way for the stepwise formation of new nanoarchitectures with Bi-rich polyanions as building blocks.

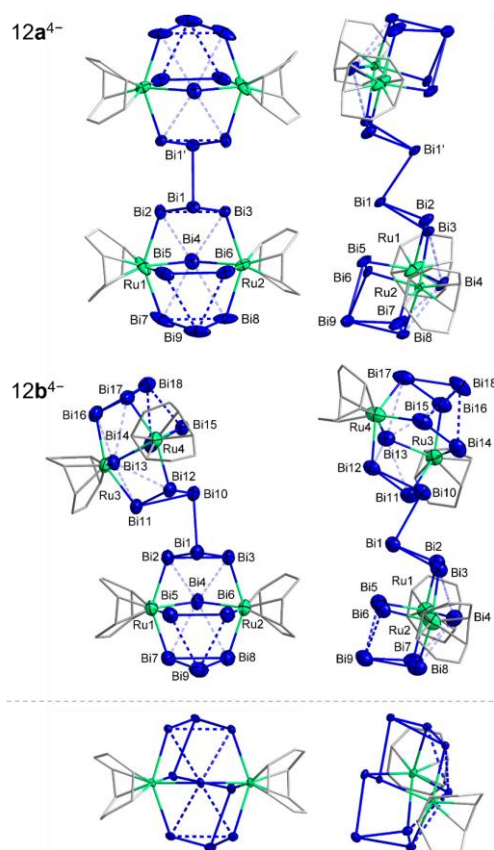


Figure 4.10: Molecular structures of the $[(\text{cod})\text{Ru}]_4\text{Bi}_{18}]^{4-}$ anions in compounds $[\text{K}(\text{crypt-222})]_4\mathbf{12a} \cdot 4.63\text{THF} \cdot 2\text{en}$ (top), $[\text{K}(\text{crypt-222})]_4\mathbf{12b}$ (center), and the related monomeric $[(\text{cod})\text{Ru}]_2\text{Bi}_9]^{3-}$ anion (bottom, beneath grey dash line) for comparison, in two perpendicular views each (displacement ellipsoids of heavy atoms set at 50% probability; cod ligands shown in wire representation). Multicenter bonds are represented by dashed lines. Very weak interactions between Bi4 (**12a**^{4−}, **12b**^{4−}), Bi4' (**12a**^{4−}), or Bi13 (**12b**^{4−}) and adjacent Bi atoms are indicated by semi-transparent, dashed lines. Relevant structural parameters are mentioned in the text.

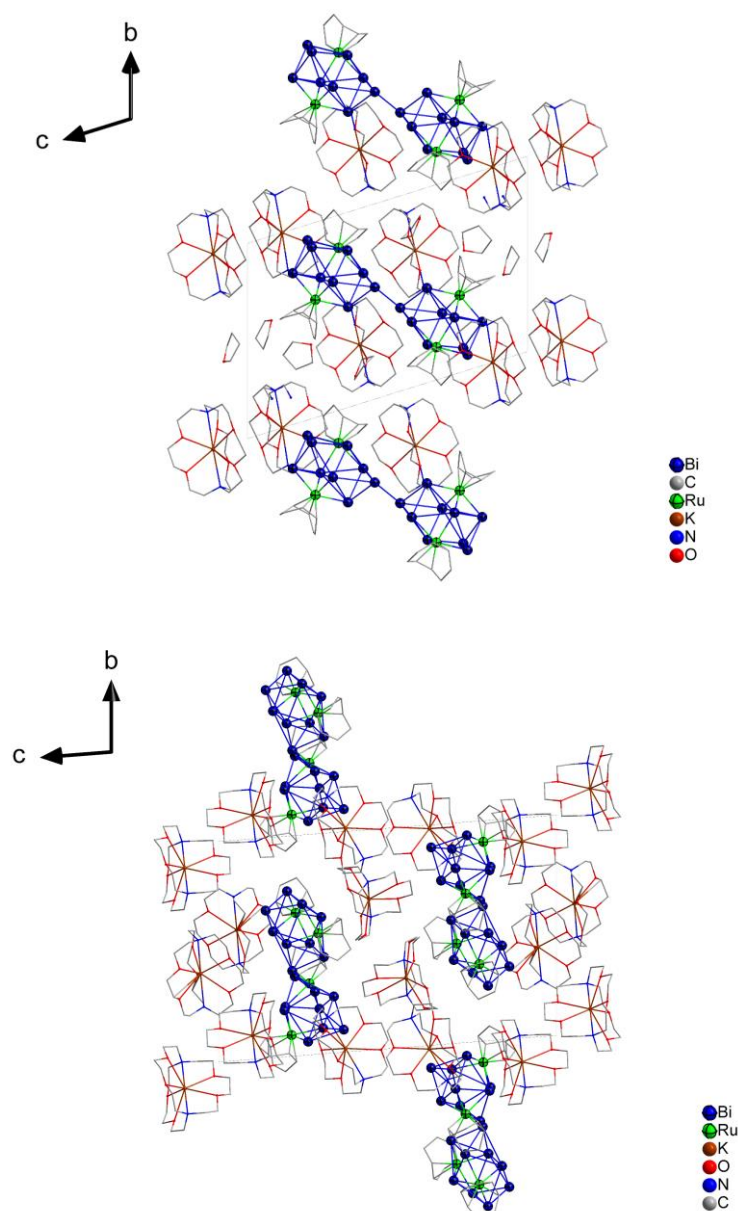


Figure 4.11: Top: view of the (extended) unit cell of $[\text{K}(\text{crypt-222})]_4\mathbf{12a} \cdot 4.63\text{THF} \cdot 2\text{en}$, viewed along the crystallographic a -axis; bottom: view of the (extended) unit cell of $[\text{K}(\text{crypt-222})]_4\mathbf{12b}$, viewed along the crystallographic a -axis. H atoms are omitted for clarity.

The connection of the two cluster subunits is realized via a Bi–Bi bond, which in the case of compound $[\text{K}(\text{crypt-222})]_4\mathbf{12a} \cdot 4.63\text{THF} \cdot 2\text{en}$ is placed on a crystallographic inversion center. The oxidative linkage of the cluster units causes the overall charge of the dimer “[$\{(\text{cod})\text{Ru}\}_4\text{Bi}_{18}\}^{6-}$ ” to be decreased by two, hence [$\{(\text{cod})\text{Ru}\}_4\text{Bi}_{18}\}^{4-}$. However, this is not the only difference of the cluster in compound $[\text{K}(\text{crypt-222})]_4\mathbf{12a} \cdot 4.63\text{THF} \cdot 2\text{en}$ from the structure of the reported monomer [$\{(\text{cod})\text{Ru}\}_2\text{Bi}_9\}^{3-}$: the monomeric half of $\mathbf{12a}^{4-}$ can be described as a sandwich structure, the middle plane of which contains a nearly perfectly planar five-atom ring $\{\text{Ru}_2\text{Bi}_3\}$ between two Bi_3 triangles that are slightly inclined against each other, with the mean planes including an angle of $\sim 18^\circ$. In [$\{(\text{cod})\text{Ru}\}_2\text{Bi}_9\}^{3-}$ in contrast, the $\{\text{Ru}_2\text{Bi}_3\}$ ring is puck-

ered: the two Bi_3 triangles are perfectly coplanar. This also affects the bonding situation of the monomeric versus dimeric clusters. While the monomeric cluster shows a combination of two-center bonding (Ru-Bi , Bi-Bi) and three-center bonding (Bi-Bi-Bi), the dimeric cluster shows a much lower tendency for three-center bonding according to DFT calculations, with Bi5-Bi9-Bi6 exhibiting the only (open) three-center bond besides a rather localized two-center bond, Bi5-Bi6 (and equivalent bonds); see Figure 4.12, right. Bi5 (and equivalent atoms) are mostly bonded to the Ru atoms, with little or no polarization of the bonds to adjacent Bi atoms. Furthermore, while the cluster comprised a chain Bi1-Bi5-Bi6-Bi9 with Bi-Bi two-center bonds in the monomeric version $[(\text{cod})\text{Ru}_2\text{Bi}_9]^{3-}$, besides two very long $\text{Bi}\cdots\text{Bi}$ distances of ~ 3.9 Å ($\text{Bi1}\cdots\text{Bi6}$, $\text{Bi5}\cdots\text{Bi9}$; not shown in Figure 4.10), the Bi1-Bi5 connection is mostly replaced in the dimeric cluster $[(\text{cod})\text{Ru}_4\text{Bi}_{18}]^{4-}$ by the intercluster Bi1-Bi1' bond, while Bi5 , Bi9 , and Bi6 (and equivalent bonds) form an approximately isosceles triangle with said three-center bonding. This structural rearrangement clearly shows the fluxionality of these bonds during the growth of polybismuthide subunits.

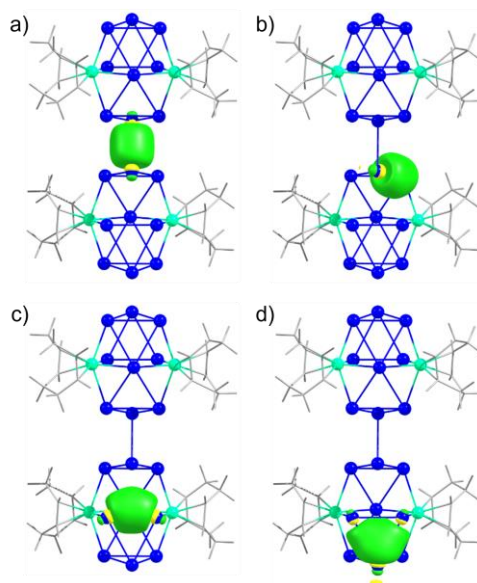


Figure 4.12: Selected localized molecular orbitals (LMOs) of the $[(\text{cod})\text{Ru}]_4\text{Bi}_{18}]^{4-}$ anions in $[\text{K}(\text{crypt-222})]_4\mathbf{12a} \cdot 4.63\text{THF} \cdot 2\text{en}$ upon simultaneous optimization of the electronic and geometric structure using density functional theory (DFT) methods and localization of the Kohn-Sham orbitals by the Boys method: a) LMO representing the Bi-Bi bond between the two cluster subunits, b) one of the LMOs representing the bonds from Bi1 to the adjacent Bi atoms, c) and d) two LMOs representing the bond within the Bi5-Bi6-Bi9 triangle, which is best described as three-center-two-electron bond with highest contribution from Bi9' plus one two center Bi5-Bi6 bond polarized towards Bi1 . The color code is the same as for Figure 4.10. For a full selection of representative LMOs, see Section 7.4.3.

As mentioned above, the monomeric cluster units in $\mathbf{12b}^{4-}$ are very similar to the ones observed in $\mathbf{12a}^{4-}$, yet the cluster is missing inversion symmetry, as the two subunits are rotated against each other about the intercluster Bi1-Bi10 bond by $\sim 121^\circ$, and the cluster units are additionally inclined against each other, such that the $\{\text{Ru}_2\text{Bi}_3\}$ rings are no longer coplanar, but are tilted by $\sim 27^\circ$. The observation of two conformers of the $[(\text{cod})\text{Ru}]_4\text{Bi}_{18}]^{4-}$ cluster dimer as a conse-

quence of a different solvent found in the crystal content suggests that the connection between the two subunits allows for rather free rotation about the Bi–Bi bonds (Bi1–Bi1' 3.0536(14) Å in **12a**^{4–}, Bi1–Bi10 3.101(3) Å in **12b**^{4–}) in a certain angle range. This is supported by DFT calculations, which showed only nonsignificant total energy differences between conformers **12a**^{4–} and **12b**^{4–} that were within the error of the chosen method. This is also consistent with a relatively high mobility of the atoms (visible in relatively large displacement ellipsoids) in the crystal.

In agreement with the bonding analysis, experimentally determined Bi–Bi distances in **12a**^{4–} and **12b**^{4–}, illustrated by solid lines in Figure 4.10, are indicative of single bonds (2.9569(13)–3.0822(17), 3.1228(10) Å in **12a**^{4–}; 2.962(3)–3.068(3), 3.135(2), 3.145(2) Å in **12b**^{4–}), yet with two bonds each that are notably longer than in anions **10**^{3–/5–} and **11**^{4–} (LMO examples in Figure 4.12, left).

The very weak interactions between Bi4 (**12a**^{4–}, **12b**^{4–}), Bi4' (**12a**^{4–}), or Bi13 (**12b**^{4–}) and the adjacent Bi atoms (indicated by semitransparent, dashed lines in Figure 4.10) are found to be 3.3460(11)–3.3596(13) Å in **12a**^{4–} and 3.227(2)–3.479(3) Å in **12b**^{4–}, which are a bit longer on average than the corresponding distances in the monomeric cluster (3.266–3.394 Å).

The Ru–Bi bond lengths amount to 2.713(2)–2.7806(19) Å in **12a**^{4–} and 2.713(4)–2.795(4) Å in **12b**^{4–}, indicating regular single bonds, which allow the [Ru(cod)]²⁺ units to adopt an 18-electron situation. The three-center bonds extending along the sides of the approximately isosceles triangle (Bi5–Bi9–Bi6 and equivalent atoms) are elongated relative to the other Bi–Bi bonds, with Bi5–Bi9 and Bi6–Bi9 (and equivalent distances) of 3.1695(13) and 3.2143(14) Å in **12a**^{4–} and 3.180(3)–3.219(4) Å in **12b**^{4–}. An apparently equivalent triangle, Bi7–Bi9–Bi8, exhibits shorter bonds, with Bi7–Bi9 and Bi8–Bi9 (and equivalent distances) of 3.0719(18) and 3.0458(12) Å in **12a**^{4–} and 3.056(3)–3.088(3) Å in **12b**^{4–}, and hence shows almost no sign of multicenter bonding. In the monomeric cluster, the corresponding triangle is opened to form a chain of regularly bonded Bi atoms instead (see above; Bi–Bi 2.947–3.006 Å).

In summary, despite the discussed differences, the overall average interatomic distances do not seem to change upon oxidative coupling of the monomeric cluster [$\{(\text{cod})\text{Ru}\}_2\text{Bi}_9\}^{3-}$ to give the two dimeric versions, [$\{(\text{cod})\text{Ru}\}_4\text{Bi}_{18}\}^{4-}$].^[82] Under consideration of all next interatomic distances (including Bi1...Bi5, Bi2...Bi5, Bi1...Bi6, Bi2...Bi6, and equivalents) for all structures, the following average values are found: Bi–Bi 3.341 Å (monomer), 3.285 Å (**12a**^{4–}), and 3.297 Å (**12b**^{4–}); Ru–Bi being 2.775 Å (monomer), 2.744 (**12a**^{4–}), and 2.750 Å (**12b**^{4–}).

4.2.2 Understanding and Elucidating the Formation of Bismuth-rich Nanoclusters

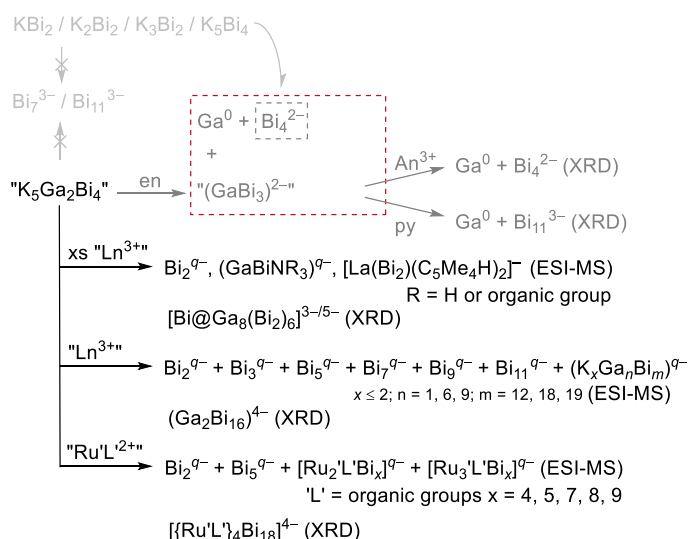
Only little is known in the field of cluster formation, including the generation and growth of Zintl polyanions.^[112] This is particularly valid for bismuth-based nanoarchitectures, as Bi atoms do not provide any spectroscopic handle for tracking the processes in solution. ²⁰⁹Bi has an abundance of 100%, but a nuclear spin of 9/2 that inhibits NMR investigation beyond highest-symmetry species. ESI mass spectrometry is so far the only way to gain information, yet inves-

tigations in real time are difficult, too, as the ESI-MS conditions largely affect the abundances of the detected species.

Solid state compounds comprising Bi₂^{q-} and Bi₄^{q-} motifs in nonstoichiometric phases K₃Bi₂ and K₅Bi₄, or in stoichiometric compounds [K(crypt-222)]₂Bi₄ and K₆(Bi₄)(NH₃)₈, and to cluster compounds comprising triangular or chain-like Bi₃^{q-} units: [{(CO)₆Ni₄}Bi₃]³⁻, [{(CO)₉Ni₆}Bi₃]³⁻, [Bi₁₂Ni₇(CO)₄]⁴⁻, [{M₂(CO)₆}Bi₃]³⁻ (M = Cr, Mo), [{(CO)₃M}Bi₃]²⁻ (M = Cr, Mo), [Pd@Pd₂Bi₁₀@(Bi₃)₂]⁴⁻, indicate the formation of small {Bi_n} moieties to take place with a certain preference under the given, sometimes harsh, reaction conditions.^[99,219,278,281,285–287,294] Referring to this knowledge, the information collected from means of single-crystal data from isolated species in combination with mass spectrometric investigations at various steps of a reaction and different reaction conditions allows some insight to share herein.

In addition to ESI-MS experiments of re-dissolved single crystals, ESI-MS studies of extraction solutions of “K₅Ga₂Bi₄” in en/crypt-222 and of solutions in which reactions between “K₅Ga₂Bi₄” in en/crypt-222 and [LaCp[#]₃] or [Ru(cod)(H₂CC(Me)CH₂)₂] were performed (All spectra are shown in Section 7.3.3). These time-dependent mass spectra of the reaction solutions during the synthesis of compounds [K(crypt-222)]_{3.67}**10** (5 min, 1 h, 3 h, and 1 d; Figures 7.31–7.34; Tables 7.54–7.57), [K(crypt-222)]₄**11a** (10 min, 1 d, and 7 d; Figures 7.35–7.37; Tables 7.58–7.60), and [K(crypt-222)]₄**12a**·4.63THF·2en (10 min, 1 h, and 7 d; Figures 7.38–7.40; Tables 7.61–7.63) indicated different initial species form under the slightly varied reaction conditions. The major findings of this study and previous investigations are summarized in Scheme 4.3.

Scheme 4.3: Transformations of “K₅Ga₂Bi₄” and known binary potassium bismuthides under different conditions, as verified by means of X-ray diffraction (XRD) or electrospray ionization mass spectrometry (ESI-MS). Previous findings are depicted in grey scale,^[44,74,229,278,280,281,286,294] findings from this work are given in black (An = actinide; Ln = lanthanide, py = pyridine; en = ethane-1,2-diamine; xs = excess). Only most relevant species detected by ESI-MS are given. Note that metal polyanions detected by ESI-MS generally carry one or two negative charges irrespective of their original charge; hence the charges were indicated as “q-” here.



Three major processes are assigned to possibly take place in solutions of “K₅Ga₂Bi₄” or “(GaBi₃)²⁻” formed in situ from the latter, upon addition of a Lewis-acidic d-block or f-block metal compound:

First, the Lewis acid seems to support the formation of {Bi₂}, {GaBi}, and {Bi₃} units, as indicated by the early presence of these species in time-dependent ESI-MS. Bi₂^{q-} and Bi₃^{q-} also form in the absence of a Lewis acid and occur beside (GaBi₃)^{q-} in the mass spectra of extraction solutions of the raw solid “K₅Ga₂Bi₄” (see above). However, they seem to form more quickly and in larger relative amounts upon addition of the metal complexes.

Second, further linkage of the di- and tribismuthide units into chain-type or monocyclic Bi_n^{q-} units with four and five atoms is likely to happen in the coordination sphere of the d-block or f-block metal. This is corroborated by the fact that free Bi_n^{q-} with n > 3 has never been observed in extraction solutions of “K₅Ga₂Bi₄” in the absence of Lewis acids. As a hint toward the interaction of the {Bi_n} species with the Lewis-acidic metal ions, metal complexes with {Bi₂} units besides some of the original ligands, such as [LaCp[#]₂(Bi₂)]⁻ after some time in solution was detected (see Figure 4.13).

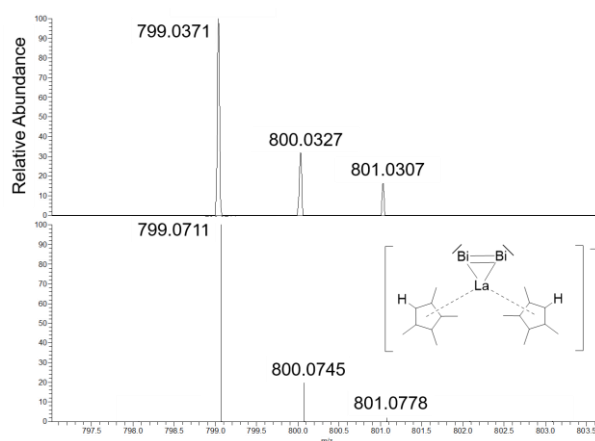


Figure 4.13: High-resolution electrospray-ionization mass spectrum of [LaCp[#]₂Bi₂]⁻ detected in the reaction solution over the course of the formation of compound [K(crypt-222)]_{3,67}**10** after 1 day reaction time, obtained in negative-ion mode. The species might be viewed as an intermediate upon replacement of one of the three (C₅Me₄H)⁻ ligands of the precursor [La^{III}(C₅Me₄H)₃] with a Bi₂²⁻ unit, which also explains the negative charge.

As the third role of the Lewis-acidic metal ions seem to assist the oxidative coupling of small chain-type or monocyclic polybismuthide units with up to five atoms to form larger homoatomic or heteroatomic aggregates, under overall reductive reaction conditions. This is also confirmed by the time-dependent ESI-MS studies, in which larger aggregates of the involved elemental combinations can be found over time. Figure 4.14 gives an impression of the development of the reactive solutions during the formation of compound [K(crypt-222)]₄**11a**. The time dependent mass spectra indicate the predominant formation of Bi_n^{q-} during the first hours, followed by the involvement of Ga, along with the formation of organic fragments that are attached to the cluster species. This not only reflects the temporal progress of the cluster

formation but also informs about the high reactivity of the metallic species toward the organic solvent.

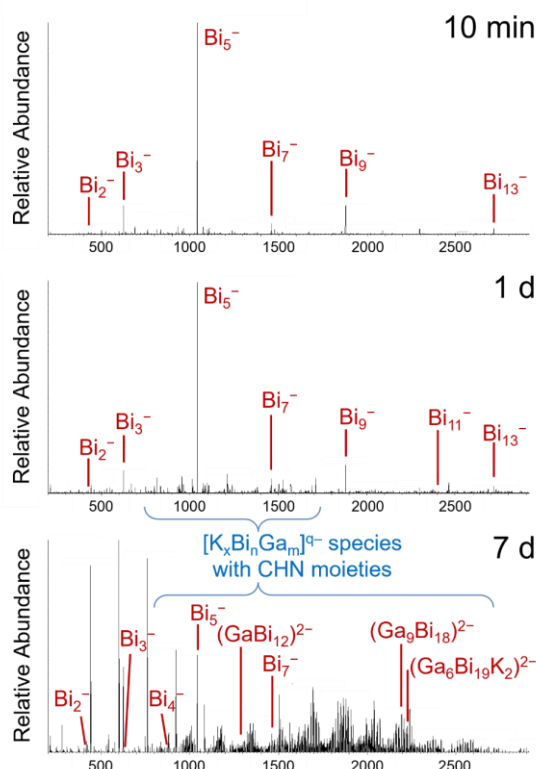


Figure 4.14: Overview electrospray-ionization mass spectra from a time-dependent study of the formation of compound $[K(\text{crypt-222})]_4\mathbf{11a}$, recorded after 10 min (top), 1 day (center), and 7 days (bottom) reaction time. The appearance of multinary clusters—mostly involving organic moieties—can be initially recognized after 1 day, yet much more pronouncedly after a week at the expense of the Bi_x^{q-} units. The most prominent peaks that could be assigned are indicated; charges are given as detected, which for the larger units do not necessarily represent the original charges in solution. The separate spectra with all details are shown in Section 7.3.3.

In many cases, the involvement of the d-block or f-block metal in the cluster formation can lead to its incorporation into the cluster molecule (“trapped catalyst”), but does not necessarily mean that this heteroatom is included. For compounds $[K(\text{crypt-222})]_{3.67}\mathbf{10}$ and $[K(\text{crypt-222})]_4\mathbf{11}\cdot\text{solv}$, the La complex is not maintained in the product, yet its role is obvious, as the clusters are not obtained without it. The active role of the Lewis acid is even more pronounced in the case of compound $[K(\text{crypt-222})]_4\mathbf{12}\cdot\text{solv}$. According to the time-dependent studies (detail spectra see Section 7.3.3), the reaction rate seems to be larger here, as the picture does not change a lot between several minutes and days upon the start of the reaction. Yet, in contrast to the results observed for compounds $[K(\text{crypt-222})]_{3.67}\mathbf{10}$ and $[K(\text{crypt-222})]_4\mathbf{11}\cdot\text{solv}$, the Ru complex fragments are not only immediately involved in the cluster formation but also are retained on the polybismuthide units, with $[\text{Ru}_2(\text{cod})_2\text{Bi}_7]^-$ being a predominant intermediate (see Figure 4.15). This observation is consistent with the crystallization of clusters comprising

{Ru(cod)} units from such solutions. Hence, the different Lewis acidities are key to the course of the cluster formation.

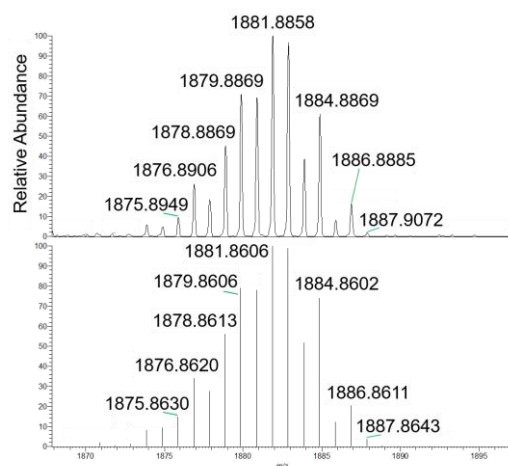


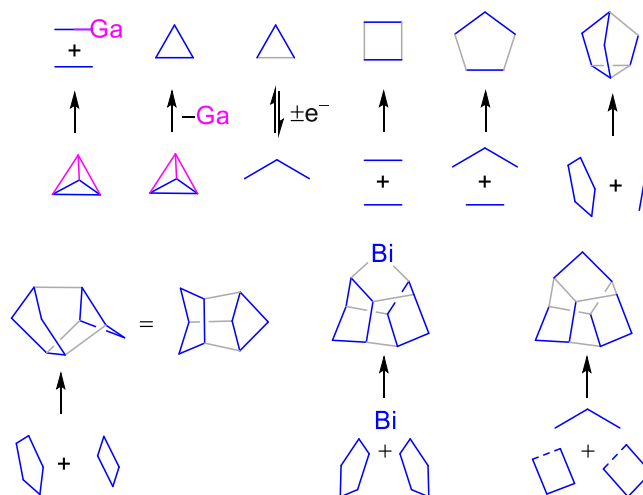
Figure 4.15: High-resolution electrospray-ionization mass spectrum of $[\text{Ru}_2(\text{cod})_2\text{Bi}_7]^-$ detected in the reaction solution over the course of the formation of compound after 10 minutes reaction time, after 1 hour and 7 days, obtained in negative-ion mode. The early occurrence of this and other $\{\text{Ru}_x\text{Bi}_y\}$ species reflects the pronounced affinity of Ru^{2+} to medium-size Bi_n^{q-} subunits. As $[\text{Ru}_2(\text{cod})_2\text{Bi}_7]^-$ is also detectable in ESI mass spectra of re-dissolved single crystals of $[\text{K}(\text{crypt-222})]_4\mathbf{12a} \cdot 4.63\text{THF} \cdot 2\text{en}$ (for a full spectrum see Section x), it is considered a key intermediate to the cluster anion $\mathbf{12}^{4-}$. Note that the charge is given here as detected, which does not necessarily represent the original charge of the polybismuthide species in solution.

The anions of the final compounds were not detected in these time-dependent studies owing to their low concentrations, which require a shift of the equilibrium by layering and crystallization. The existence of such equilibria are supported by the fact that a reduced species with the composition of the anion $\mathbf{10}^{3-/5-}$, $(\text{Ga}_8\text{Bi}_{13})^{2-}$, was detected in the ESI mass spectrum of a fresh solution of redissolved single crystals of $[\text{K}(\text{crypt-222})]_4\mathbf{11}$ in DMF, though with low intensity (The full spectrum is shown in Section 7.3.2).

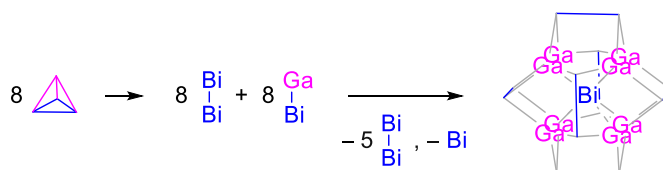
On the basis of spectrometric findings and the resulting polybismuthide substructures of the crystalline compounds presented in this work, the following processes to occur during cluster formation are proposed in the following sequence: $\{\text{Bi}_2\}$ and $\{\text{Bi}_3\}$ form initially. From these, $\{\text{Bi}_4\}$ and $\{\text{Bi}_5\}$ units form in a subsequent step. All larger homoatomic, binary, or ternary clusters based on polybismuthide units can be formed by linkage of these small chains or rings, as illustrated in Schemes 4.4–4.7, with the intensity of the involvement of the d-block or f-block metal complex being characteristic for each system. The following schemes summarize potential consecutive steps on the way from binary $\{\text{GaBi}_3\}$ or small homoatomic $\{\text{Bi}_2\}$ or $\{\text{Bi}_3\}$ units to larger polybismuthide units (Scheme 4.4) and, upon addition of Lewis-acidic d-block or f-block metal complexes, binary clusters (Schemes 4.5, 4.6, and 4.7) that are reported in this work; side-reactions that involve the f-block ions are not given. Indications for the occurrence of the corresponding species were obtained by means of ESI mass spectrometry (see Sections 7.3.2, 7.3.3) or X-ray diffraction studies of final products. It is emphasized herein that the following suggestion make no claims of being complete or the only possible ways of the clusters to

form. They just provide the readers with some ideas for atomically balanced ways of composing Bi-rich architectures, which follow the findings in this section, as a basis of further discussion.

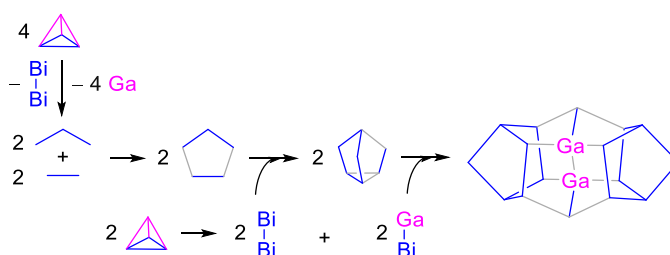
Scheme 4.4: Consecutive linkage of smallest polybismuthide units $\{\text{Bi}_2\}$ and $\{\text{Bi}_3\}$ along the atomically balanced formation of larger polybismuthide units in homoatomic architectures (with two options given for the formation of Bi_{11}^{3-}). Newly formed bonds are drawn in grey. The (negative) charges of the involved species are not indicated, as this information is not provided by ESI mass spectrometry.



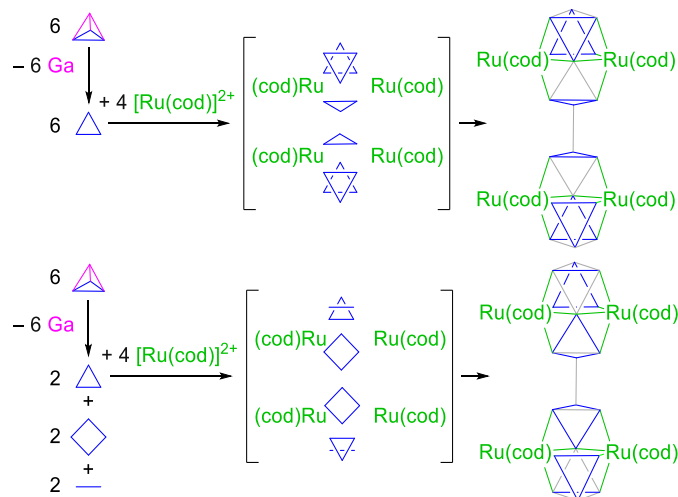
Scheme 4.5: Suggestion for the atomically balanced formation of the cluster anion $\mathbf{10}^{3-/5-}$, starting out from binary $\{\text{GaBi}_3\}$ units and species obtained in time-dependent mass spectrometric studies of the reactive solutions. Newly formed bonds are drawn in grey. The (negative) charges of the involved species are not indicated, as this information is not provided by ESI mass spectrometry. Note that side-reactions that involve the f-block ions are not given.



Scheme 4.6: Suggestion for the atomically balanced formation of the cluster anion $\mathbf{11}^{4-}$, starting out from binary $\{\text{GaBi}_3\}$ units and species obtained in time-dependent mass spectrometric studies of the reactive solutions. Newly formed bonds are drawn in grey. The (negative) charges of the involved species are not indicated, as this information is not provided by ESI mass spectrometry. Note that side-reactions that involve the f-block ions are not given.



Scheme 4.7: Two suggestions for the atomically balanced formation of the cluster anion $\mathbf{12}^{4-}$, starting out from binary $\{\text{GaBi}_3\}$ units and key species observed in time dependent mass spectrometric studies of the reactive solutions. Newly formed bonds are drawn in grey. While the upper reaction path is based on the general stability of $\{\text{Bi}_3\}$ units, the suggestion shown at the bottom seems to be more likely, as it is consistent with the occurrence of the $\{\text{Bi}_4\}$ moiety in the most predominant quasi-binary species $[\text{Ru}_2(\text{cod})_2\text{HBi}_4]^{q-}$, and with the occurrence of the $\{\text{Bi}_7\}$ moiety in the species $[\text{Ru}_2(\text{cod})_y\text{Bi}_7]^{q-}$ ($y = 0, 1, 2$) as well as in $[\text{Ru}_3(\text{cod})\text{Bi}_7]^{q-}$ in the reactive solutions. The charges of the involved species are not indicated, as this information is not provided by ESI mass spectrometry. Note that side-reactions that involve organic molecules are not given.



Note that most of the sketched steps come along with redox processes, which are obviously possible under the given experimental conditions in solution; the suggestion here includes the fact that the subsequent steps do not require multiple electron redox processes. At the same time, these redox processes inhibit parallel quantum chemical studies of the reaction pathway, in which the loss or addition of (free) electrons would lead to unreliable reaction energies; corresponding studies would thus require the knowledge of the respective redox partner, which at this stage still concerns too many unknown parameters as being reasonable.

4.3 Inducing In-Situ Hydrogenation in the Coordination Sphere of Ru^{2+} Ions with Bi_2^{2-}

4.3.1 Syntheses, Structures and Bonding

“ $\text{K}_5\text{Ga}_2\text{Bi}_4$ ”, $[(\text{C}_7\text{H}_{11})_2\text{Ru}]$, and crypt-222 were combined in a molar ratio of 1:0.73:5 in 3 mL of en, which led to the formation of the novel anionic complex $[(\text{C}_7\text{H}_{11})(\text{C}_7\text{H}_{13})\text{Ru}]_2\text{Bi}_2^{2-}$ ($\mathbf{13}^{2-}$) in the form of a $[\text{K}(\text{crypt-222})]^+$ salt. Layering with different solvents allows the formation of compounds with different degrees of solvation: with THF (3 mL) for $[\text{K}(\text{crypt-222})]_2[(\text{C}_7\text{H}_{11})(\text{C}_7\text{H}_{13})\text{Ru}]_2\text{Bi}_2$ ($[\text{K}(\text{crypt-222})]_2\mathbf{13a}$) or toluene (3 mL) for $[\text{K}(\text{crypt-222})]_2[(\text{C}_7\text{H}_{11})(\text{C}_7\text{H}_{13})\text{Ru}]_2\text{Bi}_2 \cdot 2\text{tol}$ ($[\text{K}(\text{crypt-222})]_2\mathbf{13b} \cdot 2\text{tol}$ and $[\text{K}(\text{crypt-222})]_2\mathbf{13c} \cdot 2\text{tol}$), respectively. Note that $[\text{K}(\text{crypt-222})]_2\mathbf{13c} \cdot 2\text{tol}$ was obtained by replacing “ $\text{K}_5\text{Ga}_2\text{Bi}_4$ ” with “ $\text{K}_5\text{In}_2\text{Bi}_4$ ” while keeping the reaction condition unchanged. The reaction of the salt $[\text{K}(\text{crypt-222})]$

222)]₂Bi₂ with [(C₇H₁₁)₂Ru] in en also yields the compounds comprising anionic complex **13**²⁻, but in a much lower yield. Interestingly, in this complex molecule, a partial hydrogenation of the π -system on one of the ligands has occurred.

All three compounds crystallize in the triclinic space group type $P\bar{1}$ with one formula unit per unit cell, and complex anion **13**²⁻ is situated around a crystallographic inversion center. The three salts differ in the exact arrangement of cations, anions, and solvent molecules (if present), and in structural details of the anionic complexes in them. The molecular structure of [{(C₇H₁₁)(C₇H₁₃)Ru}₂Bi₂]²⁻ (**13a**²⁻) and the view of the unit cell of [K(crypt-222)]**13a** are shown in Figure 4.16, and Figure 4.17, respectively (for detailed information of **13b**²⁻, and **13c**²⁻ see Sections 7.1.2 and 7.1.3). Compared to the cluster motifs introduced in Section 4.2, the structure of complex anion **13**²⁻ is not a cluster, but rather, a {Bi₂} dumbbell linking by two {(C₇H₁₁)(C₇H₁₃)Ru} units. A four-membered Ru–Bi–Bi–Ru zigzag chain is thus formed, with further ligation at the Ru center by one partially hydrogenated allyl ligand and one pentadienide ligand.

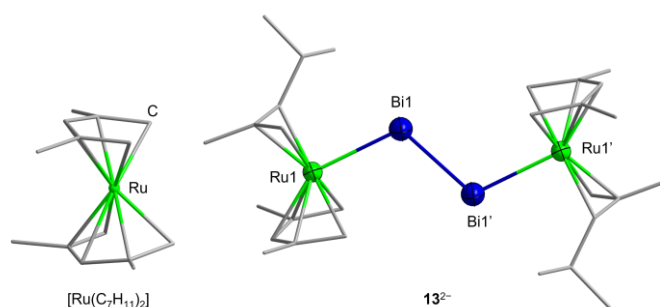


Figure 4.16: Molecular structures of [(η^5 -C₇H₁₁)₂Ru] (left) and the anionic complex [{(C₇H₁₁)(C₇H₁₃)Ru}₂Bi₂]²⁻ (**13a**²⁻) (right) in compound [K(crypt-222)]**13a** (displacement ellipsoids of heavy atoms drawn at 50% probability).

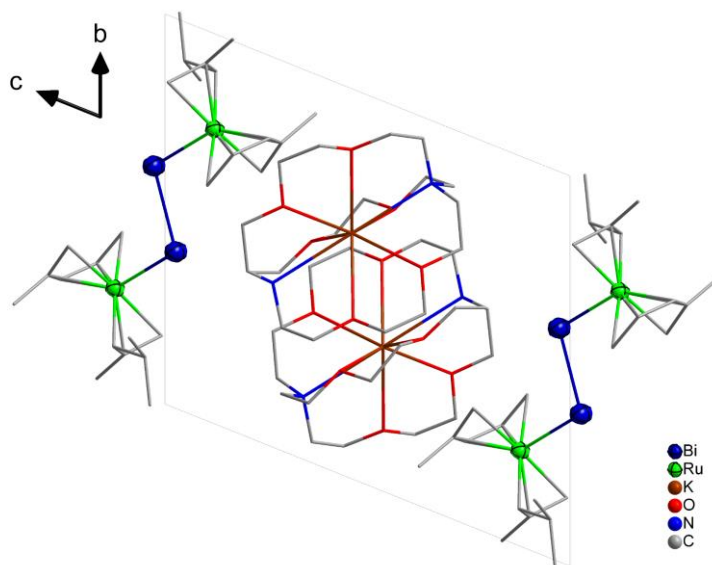


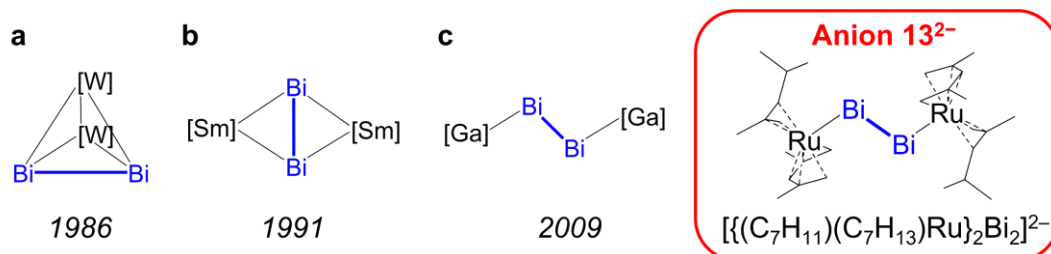
Figure 4.17: View of the (extended) unit cell of compound $[\text{K}(\text{crypt-222})]_2\mathbf{13a}$, viewed along the crystallographic a -axis. H atoms are omitted for clarity.

The bond lengths of Ru–Bi in anionic complex $\mathbf{13}^{2-}$ are 2.7512(15) Å ($\mathbf{13a}^{2-}$), 2.7498(6) Å ($\mathbf{13b}^{2-}$), and 2.7678(9) Å ($\mathbf{13c}^{2-}$), respectively, which are similar to those seen in $\mathbf{12}^{4-}$ (2.713(2)–2.7806(19) Å), $[\{(\text{cod})\text{Ru}\}_2\text{Bi}_9]^{3-}$ (2.7518(9)–2.800(1) Å), $[\{(\text{cod})\text{Ru}\}(\text{Ti}_2\text{Bi}_6)]^{2-}$ (2.7915(7)–2.8019(5) Å), and $[\{\text{CpRu}\}_3\text{Bi}_6]^-$ (2.7620(18)–2.8121(16) Å).^[82,96]

The distances between the two Bi atoms in the salts $[\text{K}(\text{crypt-222})]\mathbf{13a}$, $[\text{K}(\text{crypt-222})]\mathbf{13b} \cdot 2\text{tol}$, and $[\text{K}(\text{crypt-222})]\mathbf{13c} \cdot 2\text{tol}$ (2.8318(12) Å, 2.8578(3) Å, 2.8623(19) Å, respectively) compare well with the ones reported for the uncoordinated Bi_2^{2-} anion as well as $\text{RBi}=\text{BiR}$ with either organic or inorganic functionalities. The corresponding compounds are $[\text{K}(\text{crypt-222})]_2\text{Bi}_2$, $[\text{K}(\text{crypt-222})]_2\text{Bi}_2 \cdot \text{NH}_3)_4$, or $[\text{Cs}(18\text{-crown-6})]_2\text{Bi}_2 \cdot 7\text{NH}_3$ ($d_{\text{Bi}=\text{Bi}} = 2.8377(7)$ Å, 2.875 Å. or 2.8635(4), respectively), and 2,6-Mes₂-H₃C₆Bi=BiC₆H₃-2,6-Mes₂, $[\{\text{L}(\text{Et}_2\text{N})\text{Ga}\}_2\text{Bi}_2]$ ($d_{\text{Bi}=\text{Bi}} = 2.833$ Å, 2.813 Å; $\text{L} = \text{HC}[\text{C}(\text{Me})\text{N}(2,6\text{-iPr}_2\text{C}_6\text{H}_3)]_2$).^[98–100,295–297] The Bi–Bi bonds in $[\text{Th}@\text{Bi}_{12}]^{4-}$, Bi_{11}^{3-} , and $\mathbf{10}^{3-/5-}$ – $\mathbf{12}^{4-}$ are significantly longer (3.0420(14)–3.132(1) Å or 2.9164(14)–3.0292(15) Å, 2.9469(16)–3.145(2) Å, respectively), pointing to a lower bond order.^[224,229]

As shown in Scheme 4.8, coordination of the $\{\text{Bi}_2\}$ unit with different metals can be realized as in a *pseudo*-tetrahedral mode, in a side-on, and in an end-on mode. $\mathbf{13}^{2-}$ represents the first example of a $\{\text{Bi}_2\}$ dumbbell linking between two d-block metal atoms in a zig-zag end-on fashion, similar to the known compounds $[\{\text{L}^1\text{L}^2\text{Ga}\}_2(\text{Bi}_2)]$ ($\text{L}^1 = \text{nacnac}$; $\text{L}^2 = \text{OSO}_2\text{CF}_3$, OC_6F_5 , NEt_2 , Cl ; note that when $\text{L}^2 = \text{NEt}_2$, radical anions $[\{\text{L}^1\text{L}^2\text{Ga}\}_2(\text{Bi}_2)]^{\bullet-}$ are formed).^[296–299] However, despite the overall structural similarities, there are remarkable differences of the electronic structures between $[\{\text{L}^1\text{L}^2\text{Ga}\}_2(\text{Bi}_2)]^{0/\bullet-}$ and $[\{(\text{C}_7\text{H}_{11})(\text{C}_7\text{H}_{13})\text{Ru}\}_2\text{Bi}_2]^{2-}$ ($\mathbf{13}^{2-}$).

Scheme 4.8: Structural diagrams of the first published examples of dinuclear d-, f-, or p-block metal complexes with one {Bi₂} unit acting as bridging ligand, a) in an overall *pseudo*-tetrahedral shape ([W] = [W(CO)₄]), b) in a planar side-on-bridging mode ([Sm] = [Sm(C₅Me₅)₂]), c) in a zig-zag end-on mode of the {Bi₂} unit ([Ga] = {L¹L²Ga}; L¹ = nacnac; L² = OSO₂CF₃, OC₆F₅, NEt₂, Cl), and anionic complex **13**²⁻ (right).^[296–301]



To further investigate the electronic structure and the bonding situation in the complex anion **13**²⁻, DFT studies were performed (a full list of methods and procedures are given in Section 7.4.4). Although the calculations were started without any symmetry restrictions, the molecular structure converged into the *C_i* point group during the optimization cycles. Figure 4.18 shows the computationally optimized minimum structure of the complex anion **13**²⁻ along with the relevant localized molecular orbitals (LMOs) representing the respective Bi–Bi and Ru–Bi bonds. The distance between the two Bi atoms was calculated to be 2.84 Å, hence in perfect agreement with the experimentally observed distance (2.8318(12) Å). Together with the inspection of the LMOs, this confirms the double-bond character between the two Bi atoms.

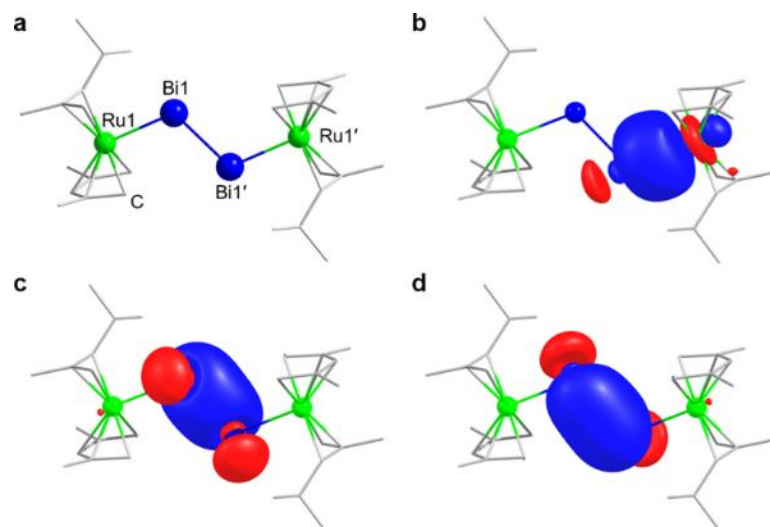


Figure 4.18: Computationally obtained minimum structure of complex anion **13**²⁻ (a) and representative localized molecular orbitals (LMOs) for one of the two equivalent Ru–Bi bonds (b) and the Bi=Bi double bond (c, d). H atoms are omitted for clarity. Contour values are drawn at ± 0.03 a.u. The methods are detailed in Section 7.4.4.

Figure 4.19 gives a comprehensive overview of the molecular orbital (MO) diagrams of the following calculated species: The Bi₂²⁻ anion (left), the (hypothetical) heteroleptic complex [(C₇H₁₁)(C₇H₁₃)Ru] (right), and the anion in **13**²⁻ (center). Clearly, the lone pair-like extensions

of MOs $5a_{1g}$ and $3e_{1u}$ of the Bi_2^{2-} unit at the Bi atoms are mainly responsible for the Ru–Bi interaction (MOs $69a_u$ and $72a_g$, as well as $71a_u$, respectively). Additional contributions come from a combination of the lowest unoccupied molecular orbital (LUMO) of $[(\text{C}_7\text{H}_{11})(\text{C}_7\text{H}_{13})\text{Ru}]$ with the singly occupied doubly degenerated molecular orbital (SOMO; MO $3e_{1g}$) of the Bi_2^{2-} anion (MOs $72a_u$ and $74a_g$). While the SOMO is antibonding along the Bi=Bi axis in Bi_2^{2-} , the zig-zag-type arrangement in $\mathbf{13}^{2-}$ allows for bonding interactions along Bi–Bi in the HOMO (MO $74a_g$); only MO $72a_u$ has a slightly antibonding character along Bi–Bi, rationalizing altogether no change in the Bi–Bi bond order and length. A full overview of the significant MOs of $\mathbf{13}^{2-}$ is given in the Section 7.4.4.

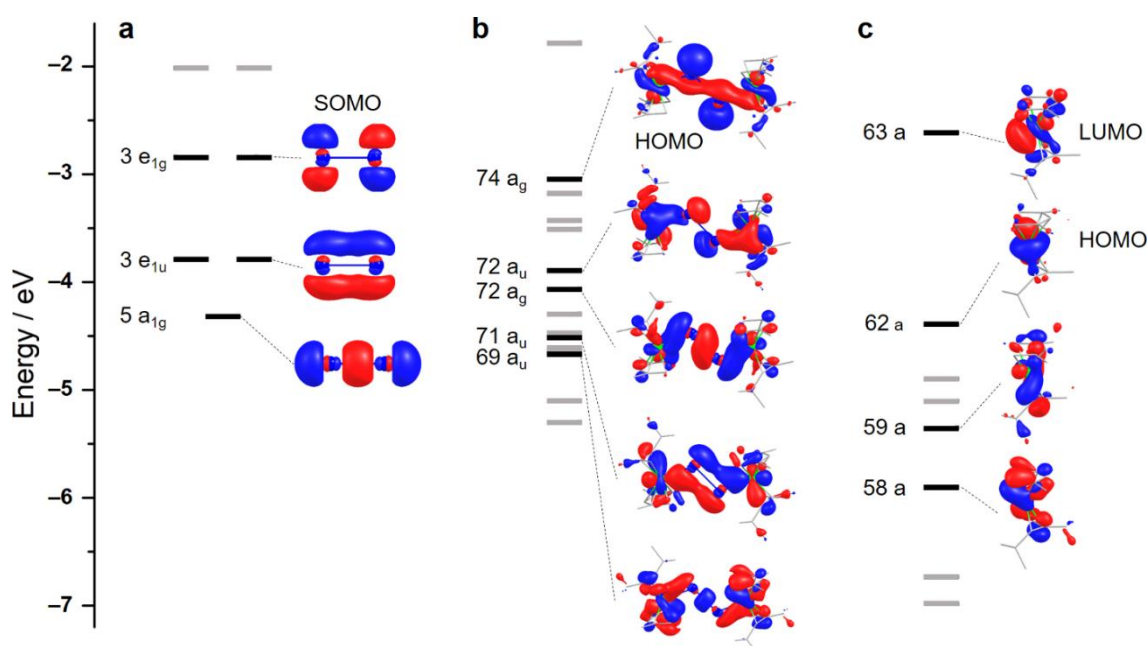


Figure 4.19: MO diagrams for of the Bi_2^{2-} anion (a), of complex anion $\mathbf{13}^{2-}$ (b), and of the (hypothetical) heteroleptic complex $[(\text{C}_7\text{H}_{11})(\text{C}_7\text{H}_{13})\text{Ru}]$ (c). Important canonical MOs are additionally shown for each molecule, with only one of two energetically degenerate MOs plotted. H atoms are omitted for clarity. Contour values are plotted at ± 0.05 a.u. for Bi_2^{2-} and $[(\text{C}_7\text{H}_{11})(\text{C}_7\text{H}_{13})\text{Ru}]$, and at ± 0.03 a.u. for $\mathbf{13}^{2-}$ for clarity. The methods are detailed in Section 7.4.4.

4.3.2 Hydrogenation Study of $[(\text{C}_7\text{H}_{11})(\text{C}_7\text{H}_{13})\text{Ru}]_2\text{Bi}_2^{2-}$

In $[\text{K}(\text{crypt-222})]_2\mathbf{13a}$, $[\text{K}(\text{crypt-222})]_2\mathbf{13b} \cdot 2\text{tol}$, and $[\text{K}(\text{crypt-222})]_2\mathbf{13c} \cdot 2\text{tol}$, one of the $\{\text{C}_7\text{H}_{11}\}$ ligands attached to the Ru atom in the precursor complex $[(\text{C}_7\text{H}_{11})_2\text{Ru}]$ was partially hydrogenated to $\{\text{C}_7\text{H}_{13}\}$ during the formation of the final compounds. The detection of $[(\text{C}_7\text{H}_{11})\text{Ru}]\text{Bi}_2\{\text{Ru}(\text{C}_7\text{H}_{11})(\text{C}_7\text{H}_{13})\}]^-$ ($m/z = 909.0433$, Figure 4.20) in the ESI-MS measurement of a freshly prepared solution of $[\text{K}(\text{crypt-222})]_2\mathbf{13a}$ in DMF indicates the existence of the different ligands by a species representing the complex anion $\mathbf{13}^{2-}$ upon release of one $\{\text{C}_7\text{H}_{13}\}$ ligand and the typical one-electron oxidation. Further fragment that were observed in the ESI mass spectrum are $[(\text{C}_7\text{H}_{11})(\text{C}_7\text{H}_{13})\text{Ru}]\text{Bi}]^-$ and Bi_x^- ($x = 2 - 9, 11$; Figure 7.27, Table 7.50, see Section 7), indicating the relatively low stability of the anion $\mathbf{13}^{2-}$ at least under ESI-MS conditions.

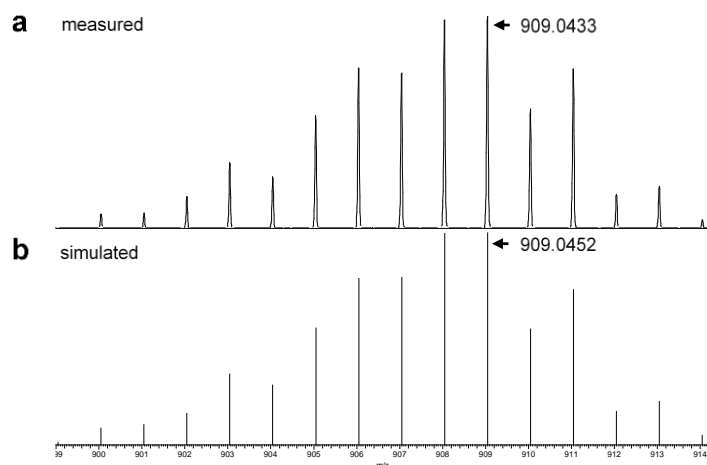


Figure 4.20: High-resolution electrospray-ionization mass spectrum of $[(\text{C}_7\text{H}_{11})\text{Ru}\}_2\text{Bi}_2\{\text{Ru}(\text{C}_7\text{H}_{11})(\text{C}_7\text{H}_{13})\}]^-$ at $m/z = 909.0433$, recorded immediately upon injection of a fresh solution of single-crystals of $[\text{K}(\text{crypt-222})]_2\mathbf{13a}$ in DMF, with measured (top) and simulated (bottom) isotope patterns, obtained in negative-ion mode.

Quantum chemical studies confirm that a change of the 6-electron-donor behavior of the ligands is a necessary precondition for the complex anion $\mathbf{13}^{2-}$ to form, as the two electrons coming in from the Bi_2^{2-} unit require one of the organic ligands to change into a 4-electron donor. This way, each of the Ru^{2+} ions retain their preferred $18 = 6(\text{Ru}^{2+}) + 6(\text{C}_7\text{H}_{11}) + 4(\text{C}_7\text{H}_{13}) + 2(\text{Bi}_2)$ electron count.

To verify the assumption that the hydrogenation of one of the ligands per Ru atom and the modified coordination mode is associated with the replacement of this part of the allyl ligand with the donor electrons from the Bi_2^{2-} unit, an additional geometry optimization for the hypothetical anion “ $[(\text{C}_7\text{H}_{11})_2\text{Ru}\}_2\text{Bi}_2]^{2-}$ ” was performed. As expected, a stable minimum structure was not obtained – a corresponding calculation failed to converge in a minimum structure and underwent Bi–Bi bond cleavage. This proves that the heteroleptic coordination at the Ru atoms, is indeed crucial for the formation of $\mathbf{13}^{2-}$.

Considering the hydrogen source during the formation of the three compounds, the reaction solution, en, stands as the only plausible source, which in the context of heterometallic Zintl cluster chemistry was previously reported both as a protonation agent and as a source of H_2 . The assumption is that either H_2 formed in situ in the mother liquor or that protons and electrons from en were transferred towards one of the double bonds in the ligand. The consistent observation of the same anionic complex $\mathbf{13}^{2-}$ from three independent reactions in en strongly supports this assumption to be an important process. To further validate this, the reaction solvent was changed from en to pyridine, DMF and acetonitrile, respectively. In pyridine, only Bi_{11}^{3-} can be isolated, which results from the oxidation of the Bi_2^{2-} anion, a common effect of using pyridine

as a solvent with Zintl anions. No reactions were observed in DMF or acetonitrile, confirming the requirement of a hydrogen source from the solvent in this case.

Based on the observed structure of **13**²⁻ and the quantum chemical investigations, Bi₂²⁻ then seems to initiate the hydrogenation of the allyl ligand. Therefore, a series of experiments (mainly using NMR spectrometry) were performed to prove this finding and to verify en as a source of the H atoms. The first attempt was to obtain in-situ NMR spectra of the reaction solution and of redissolved single crystals in d₇-DMF. However, too many unknown chemical shifts were found in both spectra which prohibited the identification of any hydrogenated signal, likely due to reactions of (unknown) reactants stemming from the “K₅Ga₂Bi₄” solid with the transition metal complex. To address this issue, “K₅Ga₂Bi₄” (0.0085 mmol), crypt-222 (0.04 mmol), [(C₇H₁₁)₂Ru] (0.068 mmol), the same ratio as in Section 4.3.1, were dissolved in 0.6 mL of d₄-en, which was then stirred for 3h and filtered for recording a ²H-NMR measurement. From the spectrum in Figure 4.21, it can be seen that besides the signal from the locking solvent, C₆D₆, only the signals corresponding to d₄-en (1.66 ppm) and d₄-MeOH (3.38 ppm) are present. Note that d₄-MeOH cannot be removed completely after the deuteration of en, although the amount of which does not appear to affect the reaction. Despite the absence of the hydrogenated species in the spectrum, en cannot be excluded as the hydrogen source, owing to the fact that it stands for the only hydrogen donor in the reaction. The reason of any signal observed from the ²H-NMR spectrum might be that the concentration of the hydrogenated species is too low compared to the massive amount of the d₄-en.

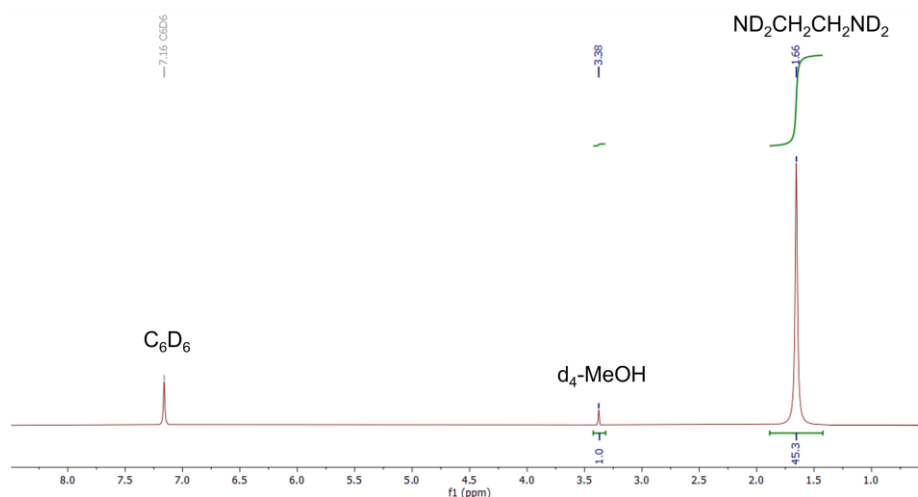


Figure 4.21: ²H-NMR spectrum of in-situ reaction solution of “K₅Ga₂Bi₄”, crypt-222, and [(C₇H₁₁)₂Ru] in d₄-en, with C₆D₆ as locking solvent.

The second set of experiments was carried out in the absence of the “K₅Ga₂Bi₄” solid. An en solution (1 mL) of [(C₇H₁₁)₂Ru] (~ 5mg) was stirred for about 15 minutes. Thereafter, the solvent was evaporated, and the remaining solid was dissolved in 0.6 mL of CD₃CN for ¹H-NMR analysis. As shown in Figure 4.22, the ¹H-NMR spectrum of [(C₇H₁₁)₂Ru] (~ 5mg) dissolved in 0.6 mL of CD₃CN (top) is identical to that of [(C₇H₁₁)₂Ru] in en (bottom), indicating that the hydrogenation does not occur without the addition of “K₅Ga₂Bi₄”. This is consistent with the

DFT studies, which suggested that the lone pair from Bi₂²⁻ is needed for valence-saturation of the Ru²⁺ ion with 18 electrons when one ligand turns from a six-electron donor to a four-electron donor due to hydrogenation.

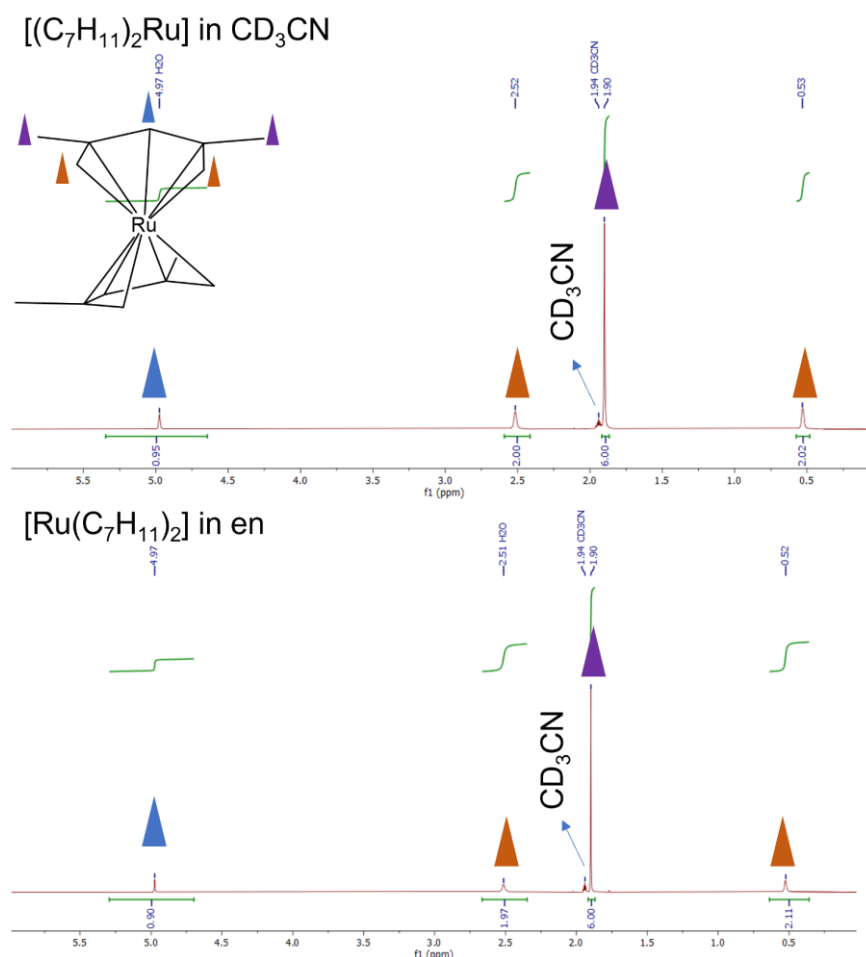


Figure 4.22: Top: ¹H-NMR spectrum of [(C₇H₁₁)₂Ru] dissolved in CD₃CN; bottom: ¹H-NMR spectrum of [(C₇H₁₁)₂Ru] first dissolved in en, then evaporated to dryness and redissolved in CD₃CN.

To further investigate the pathway of the hydrogenation process, BH₃NH₃ was selected as a potential hydrogen source. In this set of studies, CD₃CN, which shows great solubility for the starting materials, was chosen as the reaction solution to minimize any overlapping chemical shifts in the ¹H-NMR spectrum. In addition, the Bi₂²⁻ salt instead of “K₅Ga₂Bi₄” was employed, as the “K₅Ga₂Bi₄” solid is a strong reducing agent and could lead to the further unwanted side reactions.

Time-dependent ¹H-NMR spectra were performed via the following sequence: 1) 0.05 mmol of [(C₇H₁₁)₂Ru] was dissolved in 0.6 mL of CD₃CN and stirred until no solid remained; 2) an excess amount of BH₃NH₃ (0.25 mmol), due to low mass quantities involved and the very large molecular mass of [K(crypt-222)]₂Bi₂, was then added to the solution of 1), and stirred for 30 minutes; 3) 0.025 mmol of Bi₂²⁻ was added into the solution of 2), followed by another 30

minutes of stirring. All the spectra are shown in Figure 4.23. No additional peaks are observed after adding BH_3NH_3 and Bi_2^{2-} , except for the reagents themselves, though the integration of their peaks shows minor changes only. Heating the solution of 3) led to a colorless solution implying decomposition of the Bi_2^{2-} anion and indicating that no hydrogenation reaction occurred upon addition of BH_3NH_3 to Bi_2^{2-} in CD_3CN .

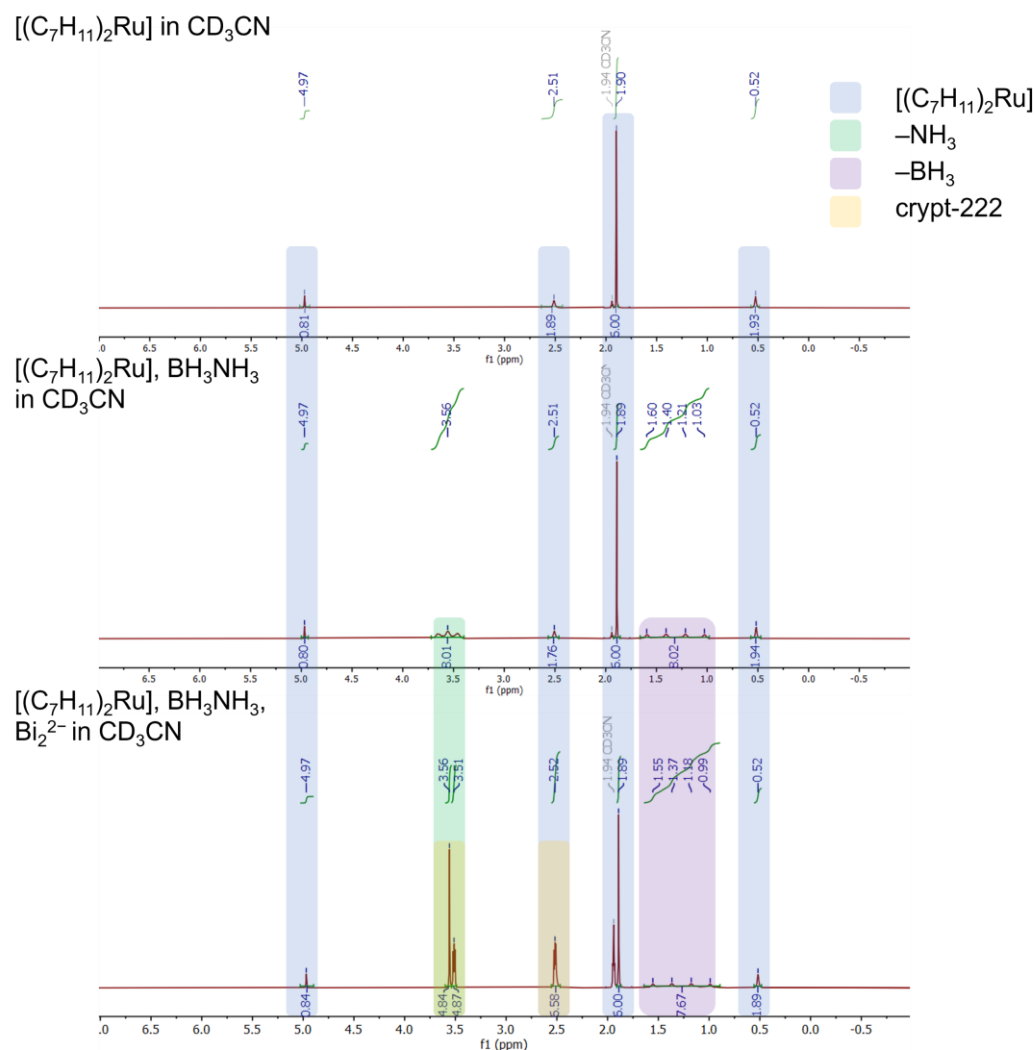


Figure 4.23: Top: ^1H -NMR spectrum of $[(\text{C}_7\text{H}_{11})_2\text{Ru}]$ dissolved in CD_3CN (1.94 ppm); center: ^1H -NMR spectrum of $[(\text{C}_7\text{H}_{11})_2\text{Ru}]$, and BH_3NH_3 dissolved in CD_3CN ; bottom: ^1H -NMR spectrum of $[(\text{C}_7\text{H}_{11})_2\text{Ru}]$, BH_3NH_3 , and the Bi_2^{2-} salt dissolved in CD_3CN .

So far, the reaction pathway of the hydrogenation process remains unclear. However, there is no doubt that 1) one of the unsaturated $\text{C}=\text{C}$ bonds in the ligand has been hydrogenated and that 2) anion $\mathbf{13}^{2-}$ will not form in the absence of Bi_2^{2-} anions or en.

4.4 Conclusions

In this section, three Lewis-acidic complexes [La(C₅Me₄H)₃], [Ru(cod)(H₂CC(Me)CH₂)₂], and [(C₇H₁₁)₂Ru] were reacted with the ternary solid “K₅Ga₂Bi₄”, which afforded four novel Bi-based clusters or complexes anions.

Cluster anions **10**^{3-/5-} and **11**⁴⁻ both were formed in reactions involving “K₅Ga₂Bi₄”, [La(C₅Me₄H)₃], and crypt-222 in different molar ratios. Interestingly, despite the involvement of the Ln³⁺ atoms, the latter are not part of the crystalline products. This is in contrast to reactions using other elemental combinations, such as Sn/Sb, Sb/Bi, Pb/Bi, In/Bi, and Tl/Bi, where the Ln³⁺ atoms were retained within the cluster structure.^[90,215,216,227,288] Here, the role of [La(C₅Me₄H)₃] can obviously be put down to the Lewis acidity of Ln³⁺, which may serve to stabilize intermediately formed Bi_x^{q-} moieties that are more easily oxidatively coupled while coordinating the Ln³⁺ ion. A similar observation was made for the linkage of intermediately formed Bi₄²⁻ units that replaced the Cp[#] ligands of a corresponding U³⁺ complex, to form the [U@Bi₁₂]³⁻ anion in the end.^[217] In the present case, however, the Ln⋯Bi interaction does not seem to end up with the encapsulation of the metal ion, but leads to the aggregation of anionic units only, with subsequent release of Ln³⁺ (or a complex comprising Ln³⁺).

“K₅Ga₂Bi₄” and crypt-222 were combined with the Lewis-acidic d-block complex [Ru(cod)(H₂CC(Me)CH₂)₂] in an en solution, affording the isolation of anion **12**⁴⁻ which represents the most Bi-rich architecture reported to date. In this system, the role of [Ru(cod)(H₂CC(Me)CH₂)₂] is not only stabilizing of the Bi_x^{q-} units, but it also provides mildly Lewis-acidic conditions for in-situ oxidative coupling. Notably, such observations have not been made in the case of (TlBi₃)²⁻, which seems to be less reactive.

A detailed mass spectrometric study, including time-dependent measurements, provided some insight into the initial steps of the formation of these unusual and complex polybismuthide structures, in an exclusive way, as bismuth does not possess suitable NMR nuclei. The intention is to illustrate possible ways of the construction of Bi-rich nanostructures from smaller units. Finally, the studies discussed above and the conclusions drawn from them are based on the fact that the smaller units seem to be ubiquitous and that their structural patterns reoccur in the final structures, but represent no means of final proofs for the formation of these species.

Additionally, Bi₂²⁻ can be effectively trapped by transition metal fragments. Anionic complex **13**²⁻ was obtained from the reaction of “K₅Ga₂Bi₄”, [(C₇H₁₁)₂Ru], and crypt-222, where [(C₇H₁₁)₂Ru] is not only coordinated by Bi₂²⁻ dumbbell, but is partially hydrogenated at one of its ligands. Complex anion **13**²⁻ represents the first example of a {Bi₂} unit in a zig-zag end-on coordination mode. Formation of this molecule is achieved through hydrogenation of one ligand in [(C₇H₁₁)₂Ru], which retains an 18-electron count while being coordinated by the {Bi₂} unit. Solvent en was assumed to serve as the hydrogen source in this reaction, which has not been directly proven so far. However, there is some indirect evidence, for instance, replacing the solvents to aprotic ones will not lead to the formation of anionic complex **13**²⁻. Furthermore, no hydrogenation occurs in [(C₇H₁₁)₂Ru] without the addition of the “K₅Ga₂Bi₄”, indicating the crucial role of Bi₂²⁻ in this reaction sequence. Future research will explore alternative reagents to replace en in order to investigate the pathway of the hydrogenation process.

Overall, the novel compounds introduced herein are very different from known species regarding the molecular architectures and bonding properties. Furthermore, the relative mismatch of the size and electron affinity of the Ga and Bi atoms was underscored once more: though **10**^{3-/5-} and **11**⁴⁻ contain both Ga and Bi atoms, none of the clusters retained the {GaBi₃} unit but rather underwent an elemental segregation process.

5 Summary

In this thesis, the reactivity of two ternary Zintl solids, “K₂GeAs” and “K₅Ga₂Bi₄”, were explored with the aim to form new binary and ternary Zintl clusters. According to the relative covalent radii and electron affinities of the two p-block elements, “K₂GeAs” exemplifies a “match” combination (Ge and As), whereas “K₅Ga₂Bi₄” represents a “mismatch” case (Ga and Bi). A glance at the product range of these two systems shows a different tendency when these two solids were reacted with different metal complexes.

The study in section 3 is grounded on the fact that extraction of the “K₂GeAs” solid with en in the presence of crypt-222 in en affords a mixture of coexisting *pseudo*-tetrahedral (Ge₂As₂)²⁻ and (Ge₃As)³⁻ units in solution.

1) Inspired by the work using d¹⁰ metal complexes along with Tt₉⁴⁻ (Tt = Ge, Sn) and (Ge₂Pn₂)²⁻ (Pn = P, As) Zintl anions, “K₂GeAs” was treated with d¹⁰ metal complexes first, aiming to expand the class of coordination-type clusters, as well as to elucidate cluster formation pathways. Reactions between “K₂GeAs” and [ZnPh₂] in en, in the presence of crypt-222, yielded three [K(crypt-222)]⁺ salts of anions comprising one, two and four *pseudo*-tetrahedral units in the coordination sphere of Zn²⁺, or (ZnPh)⁺ in [PhZn(Ge₃As)]²⁻, [(Ge₃As)Zn(Ge₂As₂)]³⁻, and [Zn₃(Ge₃As)₄]⁶⁻. Subsequent reactions with heavier homologues [MPh₂] (M = Cd, Hg) afforded species with three cadmium atoms arranged in a triangle and three (Ge₃As)³⁻ units linking the Cd atoms in [Cd₃(Ge₃As)₃]³⁻, or with one (HgPh)⁺ and one (Ge₃As)³⁻ unit in [PhHg(Ge₃As)]²⁻, respectively. The subtle impact of different [MR₂] reactants was additionally studied by corresponding reactions using [ZnMes₂], which showed success in selectively crystallizing [MesZn(Ge₃As)]²⁻. Based on these findings, a suggestion of the underlying reaction cascade was derived.

2) Upon combining extraction solutions of “K₂GeAs” with group 7, 8, and 10 metal complexes [NiCp*₂], [MnCp*₂], and [RuCp*(cod)Cl], respectively, the (Ge₂As₂)²⁻ and (Ge₃As)³⁻ units underwent fragmentation and reorganization processes, which was observed for the first time in this reaction system. [{Cp*Ni}₂(Ge₆As₂)]²⁻, [Mn₂@Ge_xAs_{24-x}]^{q-}, and [{Cp*Ru}₄(GeR)_x(Ge₄As_{4-x})]²⁻ (x = 0, 2) were formed through the expansion of the parent units. [{Cp*Ni}₂(Ge₆As₂)]²⁻ and [{Cp*Ru}₄(GeR)_x(Ge₄As_{4-x})]²⁻ (x = 0, 2) represent 10-vertex and 12-vertex electron-deficient clusters with deltahedral motifs. The [Mn₂@Ge_xAs_{24-x}]^{q-} cluster, formed upon reactions with [MnCp*₂], is an endohedral intermetalloid cluster, possessing an electron-precise configuration instead. The electron configuration of the transition metals has an impact on the type of the formed cluster, which is modulated by the number of electrons donated from transition metal towards the cluster shell.

Metals with fewer d electrons tend to donate more electrons towards the cluster shell while being turned into highly-charged cations themselves, leading to the formation of electron-precise clusters like observed in [Mn₂@Ge_xAs_{24-x}]^{q-}. In contrast, metals comprising more d electrons prefer to retain their electrons, thus resulting in electron-deficient clusters, as observed

for all other clusters reported herein. $[\{\text{Cp}^*\text{Ru}\}_4(\text{GeR})_x(\text{Ge}_4\text{As}_{4-x})]^{2-}$ cluster may comprise so far unidentified groups on two of the germanium atoms, which would represent a rare example of an intermetallic cluster functionalization; however, this remains to be confirmed.

In Section 4, the chemical behavior of “ $\text{K}_5\text{Ga}_2\text{Bi}_4$ ” was explored by treatment with lanthanide complexes, as well as transition metal complexes. The said solid is considered as a source of “ $(\text{GaBi}_3)^{2-}$ ”, which has not been isolated as a definite solid so far, however. As proven by previously reported clusters, both Ga and Bi are incorporated in “ $\text{K}_5\text{Ga}_2\text{Bi}_4$ ”, in a yet unknown form. In fact, binary 13/15 units tend to decompose under release of elemental group 13 metal, which applies to the Ga/Bi combination in particular. Compared to clusters obtained from group 14/Bi units, clusters emerging from the Ga/Bi combination show a tendency of forming binary Bi-based clusters, with the presence of few or no Ga atoms.

1) The range of products is influenced by the selection of the Lewis-acidic complexes, with regard to the amount used in the reaction, and the Lewis acidity of the metal ion involved. The use of $[\text{La}(\text{C}_5\text{Me}_4\text{H})_3]$ in reactions with “ $\text{K}_5\text{Ga}_2\text{Bi}_4$ ” and crypt-222 in en at different molar ratios led to the formation of two $[\text{K}(\text{crypt-222})]^+$ salts comprising $[\text{Bi}@\text{Ga}_8(\text{Bi}_2)_6]^{3-/5-}$, and $(\text{Ga}_2\text{Bi}_{16})^{4-}$ anions, respectively. In these two clusters, Ga and Bi coexist, whereas the Ln^{3+} atoms are not part of the crystalline products. It was proposed that in the presence of the Lewis-acidic metal complexes, the Bi_x^{q-} moieties would coordinate to the Ln^{3+} ion to form an intermediate at the first step, which is then oxidized in situ to form larger Bi-based aggregates under the release of the Ln^{3+} fragment.

2) By varying the Lewis acidity, two more novel anions were isolated in the compounds, $[\{(\text{cod})\text{Ru}\}_4\text{Bi}_{18}]^{4-}$ and $[\{(\text{C}_7\text{H}_{11})(\text{C}_7\text{H}_{13})\text{Ru}\}_2\text{Bi}_2]^{2-}$, upon reactions with $[\text{Ru}(\text{cod})(\text{H}_2\text{CC}(\text{Me})\text{CH}_2)_2]$, and $[(\text{C}_7\text{H}_{11})_2\text{Ru}]$, respectively. Ga is absent in both structures, supporting the mismatch of Ga and Bi atoms. The role of $[\text{Ru}(\text{cod})(\text{H}_2\text{CC}(\text{Me})\text{CH}_2)_2]$ is twofold. On one hand, it appears to stabilize and interact with Bi_x^{q-} units, and on the other hand, it might provide mild conditions for in-situ oxidation coupling of two monomeric $[\{(\text{cod})\text{Ru}\}_2\text{Bi}_9]^{3-}$ units.

3) In addition to forming larger Bi-based aggregates, the Bi_2^{2-} dumbbell was trapped in the coordination sphere of two Ru^{2+} ions linked by a $\mu\text{-Bi}_2$ bridge. The process induced in-situ hydrogenation of an olefin employing amine protons and electrons from the Zintl compound, as observed for the formation of $[\{(\text{C}_7\text{H}_{11})(\text{C}_7\text{H}_{13})\text{Ru}\}_2\text{Bi}_2]^{2-}$, in which 50% of the ligands on the Ru^{2+} ion has been hydrogenated.

The findings reported in this thesis highlight the complex interplay between the nature of the p-block element anions, and the nature of the metal complexes, including their ligands and the Lewis acidity of the metal ion, which ultimately influences the formation and properties of Zintl clusters.

6 Experimental Section

6.1 General

All manipulations and reactions were performed under dry Ar atmosphere by using standard Schlenk technique or working in a glovebox. Ethane-1,2-diamine (en) (Aldrich, 99.8%) was distilled from CaH_2 and stored over 3 Å molecular sieves. Toluene (Acros Organics, 99%) was distilled from a sodium-potassium alloy and stored over 3 Å molecular sieves. Crypt-222 (Merck) was dried in vacuo for at least 18 hours. $[\text{MPh}_2]$ ($\text{M} = \text{Zn}, \text{Cd}$) were prepared by a previous co-worker in the group and stored in the glovebox for use. $[\text{ZnMes}_2]$ were prepared according to the literature procedures.^[302] $[\text{MPh}_2]$ ($\text{M} = \text{Zn}, \text{Cd}$), $[\text{HgPh}_2]$ (Merck), $[\text{ZnMes}_2]$, and $[\text{Zn}(\text{C}_6\text{F}_5)_2]$ (Merck) were stored in the glovebox. $[\text{Ni}(\text{C}_5\text{Me}_5)_2]$ (Thermo Fisher Scientific), $[\text{RuCp}^*(\text{cod})\text{Cl}]$ (abcr GmbH) and $[\text{MnCp}^*_2]$ (Merck) were stored in the glovebox. $[\text{La}(\text{C}_5\text{Me}_4\text{H})_3]$, $[\text{Ru}(\text{cod})(\text{H}_2\text{CC}(\text{Me})\text{CH}_2)_2]$, and $[(\text{C}_7\text{H}_{11})_2\text{Ru}]$ were both purchased from Aldrich, and were stored in the glovebox.

According to the literature, $[\text{RuCp}^*(\text{cod})\text{Cl}]$ could be synthesized using $[\text{RuCp}^*\text{Cl}_2]$.^[303] Following this approach, the first step was to synthesize d_{15} - $[\text{RuCp}^*\text{Cl}_2]$ based on the literature procedures for d_{15} - $[\text{RhCp}^*\text{Cl}_2]$.^[304] However, this synthesis has failed, as no signal has been observed in the ^2H -NMR spectrum of the formed solids, except for the solvent peak (Figure 6.1).

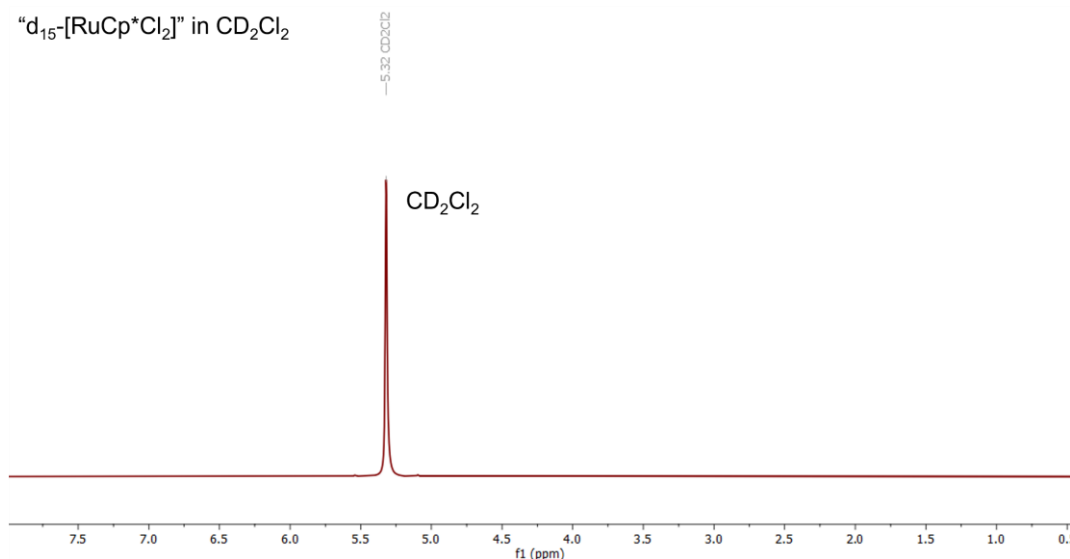


Figure 6.1: ^2H -NMR spectrum of solids of synthesized " d_{15} - $[\text{RuCp}^*\text{Cl}_2]$ " dissolved in CD_2Cl_2 , indicating the solvent peak only.

As mentioned in Section 3.4, d₄-en was synthesized as an alternative by exchanging deuterium atoms with d₄-MeOH according to slight modification of the literature.^[305] 7.00 mL of ethylenediamine (6.29 g, 105 mmol) was mixed with 40 mL of d₄-methanol and heated under reflux for 6 days under an argon atmosphere before the excess methanol was removed by distillation. The obtained partially deuterated ethane-1,2-diamine was again treated with d₄-methanol and the process repeated. Small pieces of Na were then added to the flask containing the distilled solution until no more Na dissolved. The solution was filtered and fractionally distilled. Small pieces of Na were added into the obtained solution again, which were heated till refluxing for overnight. The solution was filtered and fractionally distilled again before use. Figure 6.2 shows the NMR spectrum of deuterated en dissolved in C₆D₆, confirming that the solution contains 98.5% of d₄-en, and 1.5% of d₄-MeOH.

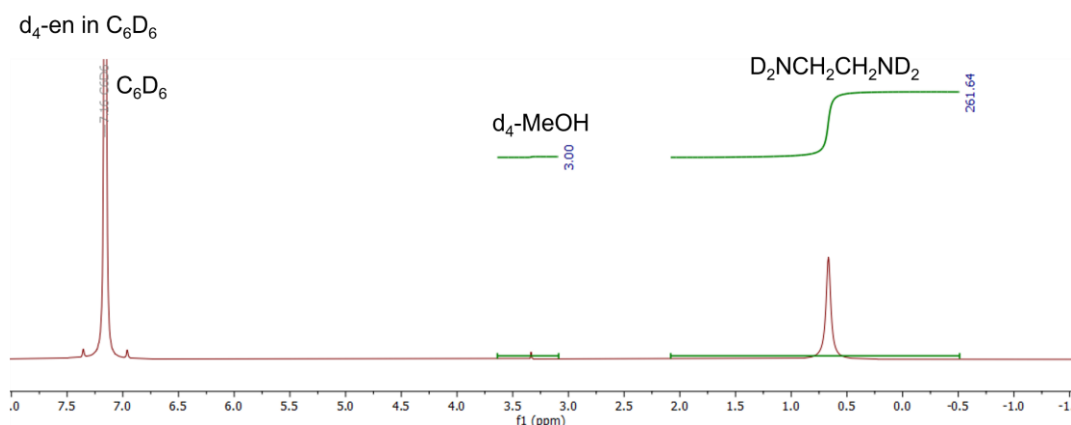


Figure 6.2: ²H-NMR spectrum of solids of synthesized d⁴-en dissolved in C₆D₆/C₆H₆ (with a ratio of 10%:90%), indicating that d₄-en is 98.5% pure.

6.2 General Methods

Optical Microscope Light microscopic investigation of crystals was performed on the stereo light microscope SteREO Discovery.V8 by Carl Zeiss. The microscope was equipped with a high-intensive cold-light source CL 1500 ECO, an Achromat S 0.63x objective (FWD 107 mm), a PL 10x/21 Br ocular, and the microscope camera AxioCam MRc 5 with the camera adapter 60N-C 2/3'' 0,63x. The raw photo material was examined by the AxioVision40x64 4.9.1 SP1 software.

Powder X-ray Diffraction (PXRD) The data were obtained with Cu-K α radiation in transmission mode on a Stoe StadiMP diffractometer using a Mythen detector system. The data were examined by using WinXPOW.

Micro-X-ray Fluorescence Spectroscopy (μ -XFS) The measurements were performed with a Bruker M4 Tornado, equipped with an Rh-target X-ray tube and a Si drift detector. The emitted fluorescence photons are detected with an acquisition time of 180 s. Quantification of the elements is achieved through deconvolution of the spectra. The μ -XFS measurements were performed by the colleagues: Dr. Bastian Weinert, Katrin Beuthert, and Mirko Tallu.

Energy Dispersive X-ray Spectroscopy (EDS) The analyses of single crystals were carried out using an EDS-device Voyager 4.0 of Noran Instruments coupled with an electron microscope CamScan CS 4DV. Data acquisition was performed with an acceleration voltage of 25 kV and 100 s accumulation time. The EDS measurements were performed by Michael Hellwig from physics department at Philipps University of Marburg.

Electrospray Ionization Mass Spectrometry (ESI-MS) All spectra of were recorded with a Thermo Fischer Scientific Finnigan LTQ-FT spectrometer in negative ion mode. The solutions were injected into the spectrometer with gastight 250 μ L Hamilton syringes by syringe pump infusion. All capillaries within the system were washed with dry solvents for 2 hours before and at least 10 minutes in between measurements to avoid decomposition reactions and consequent clogging. The ESI parameters were used: spray voltage: 3.6 kV, capillary temp: 290 $^{\circ}$ C, capillary voltage: -20 , tube lens voltage: -121.75 , sheath gas: 45, sweep gas: 0, auxiliary gas: 40. The ESI-MS measurements were performed by the mass spectrometry service team of the chemistry department at Philipps University of Marburg, as well as the colleagues Dr. Bastian Weinert and Franziska Ganslmaier.

Nuclear Magnetic Resonance (NMR) Spectrometry ^1H -NMR spectra were recorded either on a Bruker Avance III 500 console with Ultrashield Plus 500 magnet spectrometer or a Bruker Avance Neo console with Ascend 400 magnet spectrometer employing deuterated solvents. ^2H -NMR spectra were recorded on a Bruker AVANCE III 600 MHz spectrometer. Part of the NMR spectra was measured by the NMR service team of the chemistry department at Philipps University of Marburg, as well as Dr. Andreas Rapp from organic department at Karlsruhe Institute of Technology.

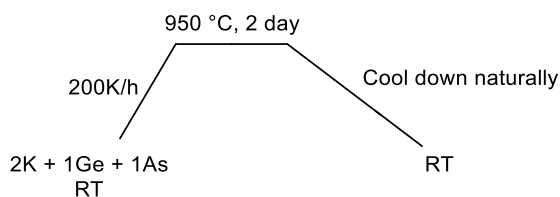
Infrared (IR) Spectrometry The spectra were recorded in the region $4000\text{--}400\text{ cm}^{-1}$ on a Bruker Tensor 37 FTIR spectrometer equipped with a room temperature DLaTGS detector, a diamond attenuated total reflection (ATR) unit in an argon filled glovebox.

Detailed information of single crystal X-ray diffraction measurements and density functional theory methods for each cluster is listed in Section 7.

6.3 Syntheses of Ternary Zintl Solids

A ternary solid with the nominal composition “ K_2GeAs ” was synthesized by combining K, Ge and As by stoichiometric fusion of the elements at $950\text{ }^{\circ}\text{C}$ for 48 hours in a quartz tube (see Scheme 6.1). The tube was coated with graphite beforehand to inhibit the reaction between silicon and arsenic.

Scheme 6.1: Synthesis profiles of the “K₂GeAs” solids.



The “K₂GeAs” solids were then analyzed by powder X-ray diffractions, and the patterns is shown in Figure 6.3. It can be seen from Figure 6.3 that the major component of “K₂GeAs” solids is the “K₂GeAs₂” phase, and the pattern labelled with a red triangle is unknown from literature.^[306]

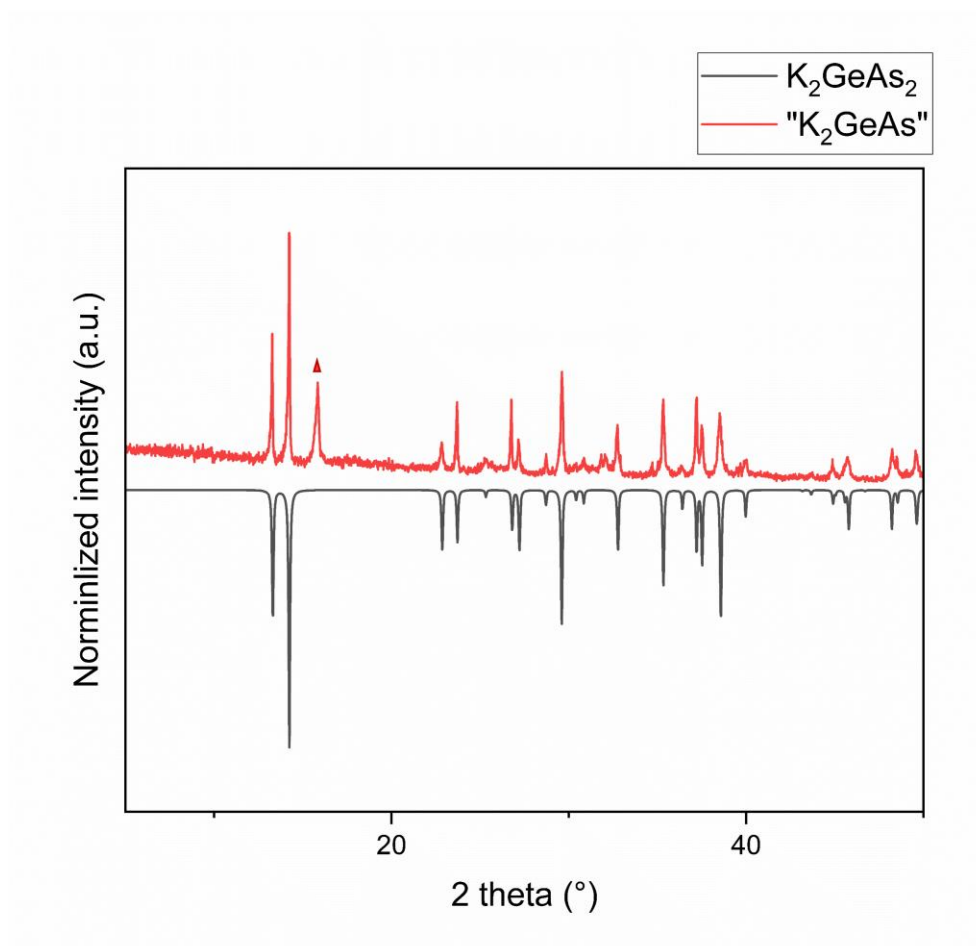
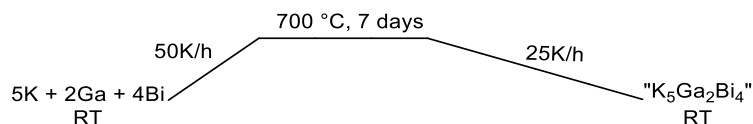


Figure 6.3: Powder X-ray diffractogram of the starting material “K₂GeAs”. The powder was investigated as used in the subsequent reactions.

A ternary solid with the nominal composition “K₅Ga₂Bi₄” was synthesized by combining K, Ga and Bi by stoichiometric amounts of element in a niobium ampoule. The ampoule was sealed by

arc-welding, then placed in an oven for a certain heating process (Scheme 6.2), which is slightly modified from the literature.^[44]

Scheme 6.2: Synthesis profiles of the “ $\text{K}_5\text{Ga}_2\text{Bi}_4$ ” solids.



The “ $\text{K}_5\text{Ga}_2\text{Bi}_4$ ” solids were then analyzed by powder X-ray diffractions, and the patterns is shown in Figure 6.4. It can be seen from Figure 6.4 that the “ $\text{K}_5\text{Ga}_2\text{Bi}_4$ ” solids are composed of the known $\text{K}_{10}\text{Ga}_3\text{Bi}_{6.65}$ phases, excess Bi, and patterns that were not identifiable (blue triangles).^[307]

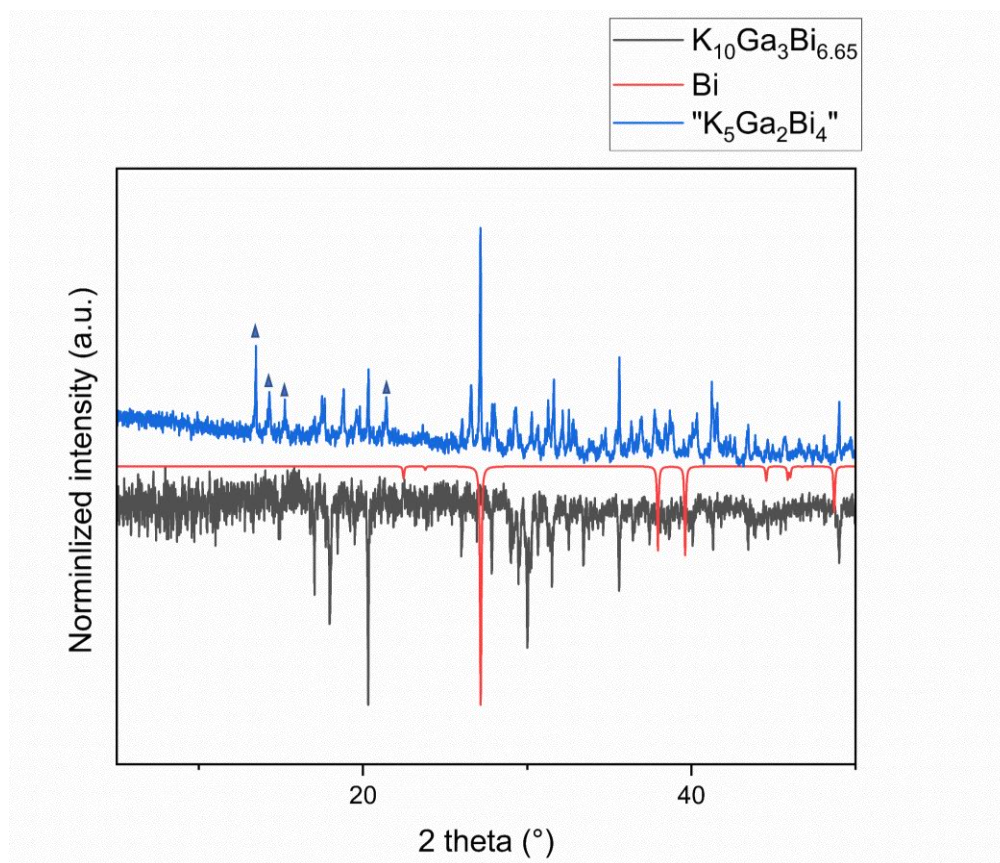


Figure 6.4: Powder X-ray diffractogram of the starting material “ $\text{K}_5\text{Ga}_2\text{Bi}_4$ ”. The powder was investigated as used in the subsequent reactions.

6.4 Syntheses of Zintl Compounds

Syntheses of $[\text{K}(\text{crypt-222})]_2[\text{PhZn}(\text{Ge}_3\text{As})]_{0.9}(\text{Ge}_2\text{As}_2)_{0.1} \cdot 0.9\text{tol}$ ($[\text{K}(\text{crypt-222})]_2[\text{1}_{0.9}(\text{Ge}_2\text{As}_2)_{0.1} \cdot 0.9\text{tol}]$); $[\text{K}(\text{crypt-222})]_3[(\text{Ge}_2\text{As}_2)\text{Zn}(\text{Ge}_3\text{As})]$ ($[\text{K}(\text{crypt-222})]_3\text{3}$); $[\text{K}(\text{crypt-222})]_9[\text{Zn}_3(\text{Ge}_3\text{As})_4]_{1.5} \cdot \text{en}$ ($[\text{K}(\text{crypt-222})]_9(\text{5a})(\text{5b})_{0.5} \cdot \text{en}$)

“ K_2GeAs ” (60 mg, 0.23 mmol), $[\text{ZnPh}_2]$ (23 mg, 0.10 mmol) and crypt-222 (100 mg, 0.27 mmol) were combined in a Schlenk tube and suspended in en (3 mL). The reaction mixture was stirred for 3 hours. The resultant orange yellow suspension was filtered through a $0.45 \mu\text{m}$ PTFE syringe filter, carefully layered with toluene (5 mL), and stored for crystallization at 5°C . After one day, needle-like crystals of compound $[\text{K}(\text{crypt-222})]_2(\text{1})_{0.9}(\text{Ge}_2\text{As}_2)_{0.1} \cdot 0.9\text{tol}$ formed at the wall of the Schlenk tube. In the same tube compound $[\text{K}(\text{crypt-222})]_3\text{3}$ and compound $[\text{K}(\text{crypt-222})]_9(\text{5a})(\text{5b})_{0.5} \cdot \text{en}$ appeared respectively within 21 days (Figure 6.5). The yield of each compound can only be estimated by macroscopic estimation. Together, they were obtained in 75 mg (crystalline) yield, with approximate relative contributions of 25% by compound $[\text{K}(\text{crypt-222})]_2(\text{1})_{0.9}(\text{Ge}_2\text{As}_2)_{0.1} \cdot 0.9\text{tol}$, 65% by compound $[\text{K}(\text{crypt-222})]_3\text{3}$, and 10% by compound $[\text{K}(\text{crypt-222})]_9(\text{5a})(\text{5b})_{0.5} \cdot \text{en}$.

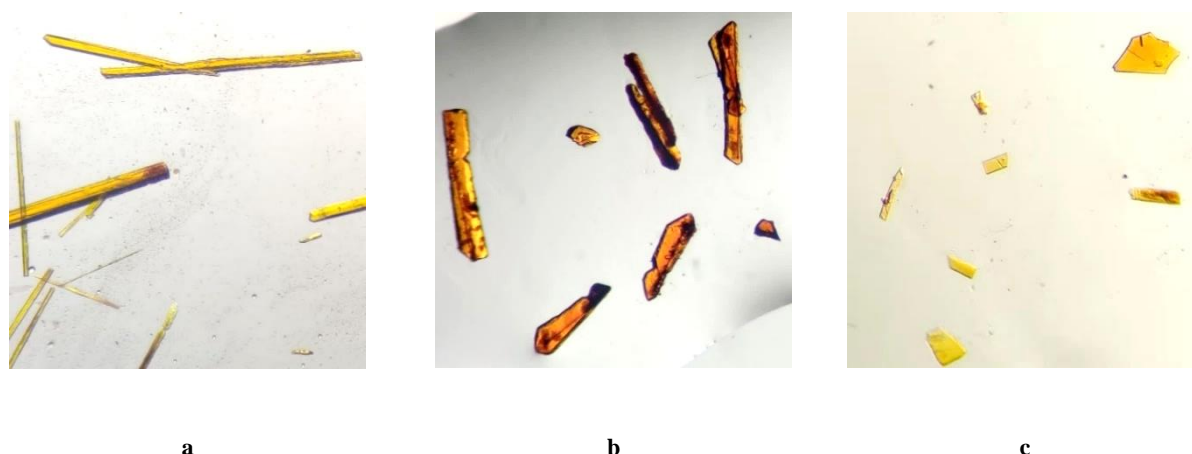


Figure 6.5: Crystal photographs of a) of $[\text{K}(\text{crypt-222})]_2(\text{1})_{0.9}(\text{Ge}_2\text{As}_2)_{0.1} \cdot 0.9\text{tol}$, b) $[\text{K}(\text{crypt-222})]_3\text{3}$, c) $[\text{K}(\text{crypt-222})]_9(\text{5a})(\text{5b})_{0.5} \cdot \text{en}$ taken under a light microscope.

Synthesis of $[\text{K}(\text{crypt-222})]_2[\text{PhHg}(\text{Ge}_3\text{As})] \cdot \text{tol}$ ($[\text{K}(\text{crypt-222})]_2\text{2} \cdot \text{tol}$)

“ K_2GeAs ” (28 mg, 0.12 mmol), $[\text{HgPh}_2]$ (15 mg, 0.04 mmol) and crypt-222 (47 mg, 0.13 mmol) were combined in a Schlenk tube and suspended in en (3 mL). The reaction mixture was stirred for 3 hours. The resultant dark red suspension was filtered through a $0.45 \mu\text{m}$ PTFE syringe filter, carefully layered with toluene (5 mL), and stored for crystallization at 5°C for 2 days, which afforded red needle crystals of $[\text{K}(\text{crypt-222})]_3\text{2} \cdot \text{tol}$ (Figure 6.6) at the wall of the Schlenk tube in 7 mg (crystalline) yield.

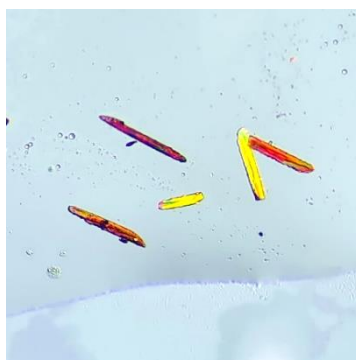


Figure 6.6: Crystal photograph of $[\text{K}(\text{crypt-222})]_2\cdot\text{tol}$ taken under a light microscope.

Synthesis of $[\text{K}(\text{crypt-222})]_3[\text{Cd}_3(\text{Ge}_3\text{As})_3]\cdot\text{tol}$ ($[\text{K}(\text{crypt-222})]_3\mathbf{4}\cdot\text{tol}$)

“ K_2GeAs ” (60 mg, 0.23 mmol), $[\text{CdPh}_2]$ (26 mg, 0.10 mmol) and crypt-222 (100 mg, 0.27 mmol) were combined in a Schlenk tube and suspended in en (3 mL). The reaction mixture was stirred for 3 hours. The resultant red solution was filtered through a $0.45\ \mu\text{m}$ PTFE syringe filter, carefully layered with toluene (5 mL), and stored for crystallization at $5\ ^\circ\text{C}$ for 21 days, which afforded red block crystals of $[\text{K}(\text{crypt-222})]_3\mathbf{4}\cdot\text{tol}$ (Figure 6.7) at the wall of the Schlenk tube in 8 mg (crystalline) yield.

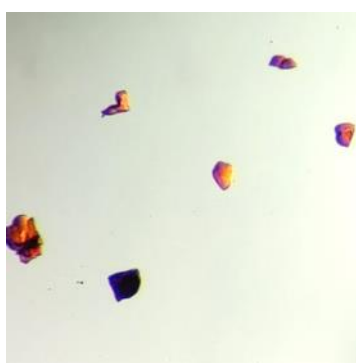


Figure 6.7: Crystal photograph of $[\text{K}(\text{crypt-222})]_3\mathbf{4}\cdot\text{tol}$ taken under a light microscope.

Synthesis of $[\text{K}(\text{crypt-222})]_2[\text{MesZn}(\text{Ge}_3\text{As})]$ ($[\text{K}(\text{crypt-222})]_2\mathbf{6}$)

“ K_2GeAs ” (60 mg, 0.23 mmol), $[\text{ZnMes}_2]$ (30 mg, 0.10 mmol) and crypt-222 (100 mg, 0.27 mmol) were combined in a Schlenk tube and suspended in en (3 mL). The reaction mixture was stirred for 3 hours. The resultant orange yellow solution was filtered through a $0.45\ \mu\text{m}$ PTFE syringe filter, carefully layered with toluene (5 mL), and stored for crystallization at $5\ ^\circ\text{C}$ for 2 days, which afforded yellow needle-like crystals of $[\text{K}(\text{crypt-222})]_2\mathbf{6}$ (Figure 6.8) at the wall of the Schlenk tube in 8 mg (crystalline) yield.

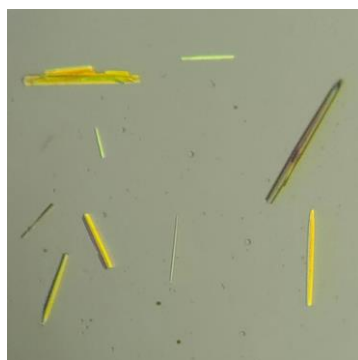


Figure 6.8: Crystal photograph of $[\text{K}(\text{crypt-222})]_{26}$ taken under a light microscope.

Synthesis of $[\text{K}(\text{crypt-222})]_2[\{\text{Cp}^*\text{Ni}\}_2(\text{Ge}_6\text{As}_2)] \cdot 2\text{en}$ ($[\text{K}(\text{crypt-222})]_2 \cdot 2\text{en}$)

“ K_2GeAs ” (60 mg, 0.23 mmol), $[\text{NiCp}^*_2]$ (33 mg, 0.10 mmol) and crypt-222 (100 mg, 0.27 mmol) were combined in a Schlenk tube and suspended in en (3 mL). The reaction mixture was stirred for 3 hours. The resultant green-brown suspension was filtered through a 0.7 μm PTFE syringe filter, carefully layered with toluene (5 mL), and stored for crystallization at 5 $^\circ\text{C}$. After three weeks, brown crystals of compound $[\text{K}(\text{crypt-222})]_2 \cdot 2\text{en}$ (Figure 6.9) formed at the wall of the Schlenk tube in the estimation of 8 mg yield.

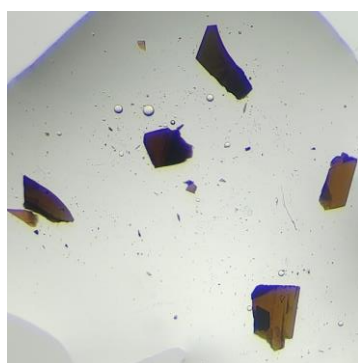


Figure 6.9: Crystal photograph of $[\text{K}(\text{crypt-222})]_{27} \cdot 2\text{en}$ taken under a light microscope.

Synthesis of $[\text{K}(\text{crypt-222})]_q[\text{Mn}_2@\text{Ge}_x\text{As}_{24-x}] \cdot \text{solv}$ ($[\text{K}(\text{crypt-222})]_q \cdot \text{solv}$)

“ K_2GeAs ” (68 mg, 0.3 mmol), $[\text{MnCp}^*_2]$ (33 mg, 0.10 mmol) and crypt-222 (100 mg, 0.27 mmol) were combined in a Schlenk tube and suspended in en (3 mL). The reaction mixture was stirred for 3 hours. The resultant olive-green suspension was filtered through a 0.7 μm PTFE syringe filter, carefully layered with toluene (5 mL), and stored for crystallization at 5 $^\circ\text{C}$ for 21 days, which afforded dark brown block crystals of $[\text{K}(\text{crypt-222})]_q \cdot \text{solv}$ (Figure 6.10) at the wall of the Schlenk tube in the estimation of 5 mg yield.

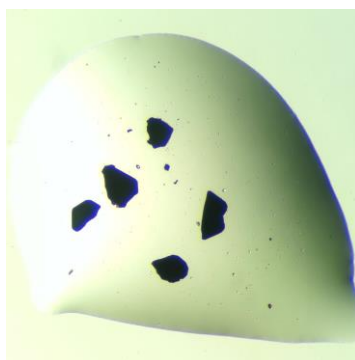


Figure 6.10: Crystal photograph of $[\text{K}(\text{crypt-222})]_2[\mathbf{8}] \cdot \text{solv}$ taken under a light microscope.

Synthesis of $[\text{K}(\text{crypt-222})]_2[\{\text{Cp}^*\text{Ru}\}_4\{\text{GeR}\}_x(\text{Ge}_4\text{As}_{4-x})] \cdot \text{solv}$ ($[\text{K}(\text{crypt-222})]_2\mathbf{9} \cdot \text{solv}$)

“ K_2GeAs ” (60 mg, 0.23 mmol), $[\text{RuCp}^*(\text{cod})\text{Cl}]$ (38 mg, 0.10 mmol) and crypt-222 (100 mg, 0.27 mmol) were combined in a Schlenk tube and suspended in en (3 mL). The reaction mixture was stirred for 3 hours. The resultant dark red suspension was filtered through a 0.7 μm PTFE syringe filter, carefully layered with toluene (5 mL), and stored for crystallization at 5 $^\circ\text{C}$ for 2 days, which afforded red needle crystals of $[\text{K}(\text{crypt-222})]_2\mathbf{9} \cdot \text{solv}$ (Figure 6.11) at the wall of the Schlenk tube in the estimation of 10 mg yield.



Figure 6.11: Crystal photograph of $[\text{K}(\text{crypt-222})]_2\mathbf{9} \cdot \text{solv}$ taken under a light microscope.

Attempted synthesis of $[\{\text{Cp}^*\text{Ru}\}_4\{\text{GeND}_2\}_2\text{Ge}_4\text{As}_2]^{2-} \cdot$

“ K_2GeAs ” (17 mg, 0.075 mmol), $[\text{RuCp}^*(\text{cod})\text{Cl}]$ (9.5 mg, 0.025 mmol) and crypt-222 (28 mg, 0.075 mmol) were combined in a Schlenk tube and suspended in $\text{d}_4\text{-en}$ (1 mL). The reaction mixture was stirred for 3 hours. The resultant dark red suspension was filtered through a 0.7 μm PTFE syringe filter, afterwards the solution was evaporated under vacuum. The solids obtained from evaporation were redissolved in 0.6 mL of $\text{d}^7\text{-DMF/DMF}$ (~10%:90%) for a ^2H -NMR measurement, the spectrum is shown in Figure 3.28.

Reactions of “ K_2GeAs ” with different metallocenes

Reactions of “K₂GeAs”, crypt-222 with [FeCp*₂], and [CoCp*₂] were respectively prepared using the same stoichiometric ratio as in the synthesis of compound [K(crypt-222)]₂·2en. No products or meaningful spectrometric data was obtained.

Synthesis of [K(crypt-222)]_{3.67}[Bi@Ga₈(Bi₂)₆] ([K(crypt-222)]_{3.67}**10**)

The combination of “K₅Ga₂Bi₄” (80 mg, 0.068 mmol), [La(C₅Me₄H)₃] (110 mg, 0.22 mmol), and crypt-222 (129 mg, 0.34 mmol) in en solutions (3 mL) in a Schlenk tube has led to an emerald green solution initially. The reaction mixtures were stirring for 3 h, and the color of the reaction solution turned to dark brown. The resulting solution was filtered through a standard glass frit, and carefully layered with toluene (3 mL), and stored for crystallization at 5°C. After 15 days, plate-like crystals of [K(crypt-222)]_{3.67}[Bi@Ga₈(Bi₂)₆] (compound [K(crypt-222)]_{3.67}**10**) formed at the wall of the Schlenk tube in ~8% yield (Figure 6.12).

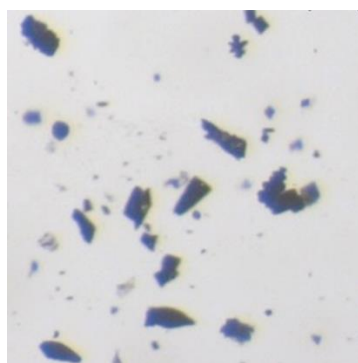


Figure 6.12: Crystal photograph of [K(crypt-222)]_{3.67}**10** taken under a light microscope.

Syntheses of [K(crypt-222)]₄(Ga₂Bi₁₆) ([K(crypt-222)]₄**11a**) and [K(crypt-222)]₄(Ga₂Bi₁₆)·4py ([K(crypt-222)]₄**11b**·4py)

A slight variation of the molar ratio of the reactants, with 117 mg (0.1 mmol) amount of “K₅Ga₂Bi₄”, 186 mg of crypt-222 (0.5 mmol), and 50 mg (0.1 mmol) of [La(C₅Me₄H)₃], respectively, yielded another compound. The reactants were combined in a Schlenk tube, and dissolved in 4 mL of en. After stirring overnight, the emerald green solution remained the same color, the was filtered by a glass microfiber filter, carefully layered with 4 mL of toluene, and then placed carefully in the refrigerator (5 °C). After about a week, needle-shaped crystals of [K(crypt-222)]₄(Ga₂Bi₁₆)·solv ([K(crypt-222)]₄**11**·solv, solv = none, the filtrate was layered with toluene, [K(crypt-222)]₄**11a**; solv = 4py, the solid mixtures were reacted in pyridine, [K(crypt-222)]₄**11b**·4py) appeared on the wall of the tube (Figure 6.13). Yields of both compounds are ~12%, and ~10%, respectively.

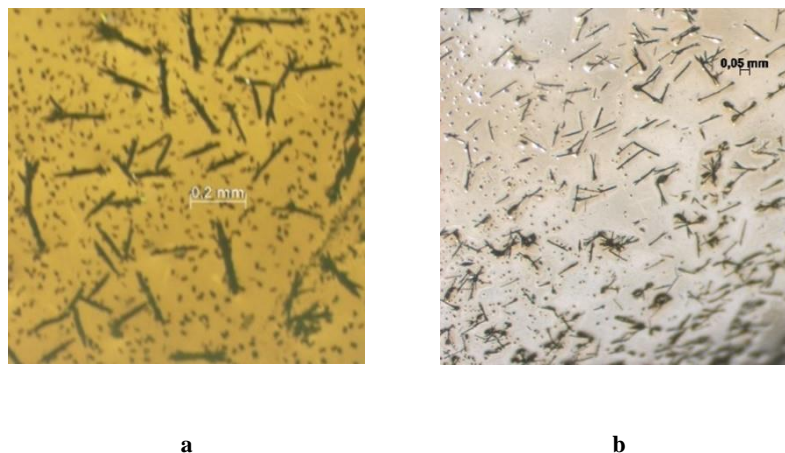


Figure 6.13: Crystal photographs of $[\text{K}(\text{crypt-222})]_4\mathbf{11a}$ (a) and $[\text{K}(\text{crypt-222})]_4\mathbf{11b}\cdot 4\text{py}$ (b) taken under a light microscope.

Syntheses of $[\text{K}(\text{crypt-222})]_4\{[(\text{cod})\text{Ru}]_4\text{Bi}_{18}\}_2\cdot 4.63\text{THF}\cdot 2\text{en}$ ($[\text{K}(\text{crypt-222})]_4\mathbf{12a}\cdot 4.63\text{THF}\cdot 2\text{en}$) and $[\text{K}(\text{crypt-222})]_4\{[(\text{cod})\text{Ru}]_4\text{Bi}_{18}\}_2$ ($[\text{K}(\text{crypt-222})]_4\mathbf{12b}$)

“ $\text{K}_5\text{Ga}_2\text{Bi}_4$ ” (117 mg, 0.1 mmol), crypt-222 (186 mg, 0.5 mmol), and $[\text{Ru}(\text{cod})(\text{H}_2\text{CC}(\text{Me})\text{CH}_2)_2]$ (32 mg, 0.1 mmol) were combined in 4 mL of en in a brown vial in a glovebox. After stirring for two hours, the emerald green solution was filtered through a PTFE membrane filter and carefully layered with 4 mL of THF before carefully placing the mixture in the refrigerator (5 °C). After about 2 weeks, needle-shaped crystals of compound $[\text{K}(\text{crypt-222})]_4\{[(\text{cod})\text{Ru}]_4\text{Bi}_{18}\}_2\cdot \text{solv}$ (compound $[\text{K}(\text{crypt-222})]_4\mathbf{12}\cdot \text{solv}$, solv = 4.63THF·2en, $[\text{K}(\text{crypt-222})]_4\mathbf{12a}\cdot 4.63\text{THF}\cdot 2\text{en}$; solv = none, $[\text{K}(\text{crypt-222})]_4\mathbf{12b}$) were obtained in the same reaction room in ~23% yield, and they are not distinguishable via microscopy (Figure 6.14).

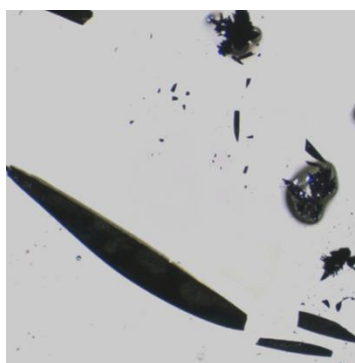


Figure 6.14: Crystal photographs of $[\text{K}(\text{crypt-222})]_4\mathbf{12a}$ taken under a light microscope.

Syntheses of $[\text{K}(\text{crypt-222})]_2\{[(\text{C}_7\text{H}_{11})(\text{C}_7\text{H}_{13})\text{Ru}]_2\text{Bi}_2\}\cdot \text{solv}$ (solv = none, $[\text{K}(\text{crypt-222})]_2\mathbf{13a}$; solv = 2tol, $[\text{K}(\text{crypt-222})]_2\mathbf{13b}$ and $[\text{K}(\text{crypt-222})]_2\mathbf{13c}$, tol = toluene)

80 mg (0.068 mmol) of the ternary solid “K₅Ga₂Bi₄”, 129 mg (0.34 mmol) crypt-222 and 15 mg (0.05 mmol) of [(C₇H₁₁)₂Ru] were combined in a Schlenk tube and dissolved in en (3 mL). The reaction mixture was stirred for 3 hours at room temperature. The resulting dark brown solution was filtered into another Schlenk tube through a standard glass frit, carefully layered with THF for [K(crypt-222)]₂**13a** (3 mL) or toluene for [K(crypt-222)]₂**13b**·2tol (3 mL), respectively. The Schlenk tube was then stored for crystallization at 5 °C. After 15 days, plate-like crystals of compounds [K(crypt-222)]₂**13a** or [K(crypt-222)]₂**13b**·2tol formed at the wall of the Schlenk tube in ~25% or ~30% yield, respectively.

[K(crypt-222)]₂**13c**·2tol was obtained in a similar way: 86 mg (0.068 mmol) of K₅In₂Bi₄,^{ref} 129 mg (0.34 mmol) of crypt-222 and 15 mg (0.05 mmol) of [(C₇H₁₁)₂Ru] were combined in a Schlenk tube and dissolved in en (3 mL). The reaction mixture was stirred for 3 hours at room temperature. The resulting dark brown solution was filtered into another Schlenk tube through a standard glass frit, carefully layered with toluene (3 mL). The Schlenk tube was then stored for crystallization at 5 °C. After 15 days, red plate-like crystals of compound [K(crypt-222)]₂**13c**·2tol formed at the wall of the Schlenk tube in ~20% yield (Figure 6.15).

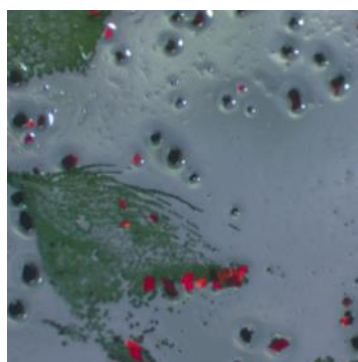


Figure 6.15: Crystal photographs of a) [K(crypt-222)]₂**13a** ([K(crypt-222)]₂**13b**·2tol and [K(crypt-222)]₂**13c**·2tol show similar shape and color as [K(crypt-222)]₂**13a**) were taken under a light microscope. The greenish solid beside [K(crypt-222)]₂**13a** formed from the corresponding mother liquor.

Attempted synthesis of [{(C₇H₁₁)(C₇H₁₁D₂)Ru}₂Bi₂]²⁻·

10 mg (0.0085 mmol) of the ternary solid “K₅Ga₂Bi₄”, 15 mg (0.04mmol) crypt-222 and 3 mg (0.068 mmol) of [(C₇H₁₁)₂Ru] were combined in a Schlenk tube and dissolved in d₄-en (0.6 mL). The reaction mixture was stirred for 3 hours at room temperature. The resulting emerald green solution was filtered through a 0.7 μm PTFE syringe filter, afterwards the solution was transferred into a J Young NMR tube. A sealed capillary of C₆D₆ solvent was carefully added into the J Young NMR tube for locking the sample. The sample then was used for the measurement of a ²H-NMR spectrum, which is shown in Figure 4.21.

7 Appendix

7.1 Crystal Structure Measurements and Data

7.1.1 Data Collection and Refinement

The X-ray structural analyses were collected at T = 100.0 K with CuK α -radiation ($\lambda = 1.54186$ Å) or with Mo-K α -radiation ($\lambda = 0.71073$ Å) on area detector system Stoe StadiVari, or on a Bruker D8Quest with a CMOS detector, or at T= 150.0 K with GaK α -radiation ($\lambda = 1.34143$ Å) on a dectris pilatus detector Stoe StadiVari. The structures were solved by methods of SHELXT from SHELXL-2018/136,^[308] and refined by full matrix least-squares methods against F^2 with the SHELXL program.^[309] All hydrogen atoms were kept riding on calculated positions with isotropic displacement parameters U = 1.2 Ueq of the bonding partners. Measurement, structure solution, and refinement results, as well as details on the back Fourier transform procedure using the SQUEEZE algorithm in the PLATON program package, are detailed in corresponding Tables below. Specific comments for each data set are given below. All crystallographic figures were created with Diamond 4.^[310]

7.1.2 Crystal Data and Details of the Structure Determinations

7.1.2.1 Crystal Data and Details of the Structure Determinations of [K(crypt-222)]₂(1)_{0.9}(Ge₂As₂)_{0.1}·0.9tol

Compound	[K(crypt-222)] ₂ (1) _{0.9} (Ge ₂ As ₂) _{0.1} ·0.9tol
Chemical formula	C _{47.7} H _{83.7} As _{1.1} Ge _{2.9} K ₂ N ₄ O ₁₂ Zn _{0.9}
Empirical formula	C _{47.7} H _{83.7} As _{1.1} Ge _{2.9} K ₂ N ₄ O ₁₂ Zn _{0.9}
Formula weight / [g mol ⁻¹]	1335.24
Temperature /K	100
Crystal system	orthorhombic
Space group	<i>Pnma</i>
<i>a</i> /Å	20.481(4)
<i>b</i> /Å	22.302(5)
<i>c</i> /Å	13.241(3)
α /°	90
β /°	90
γ /°	90
Volume /Å ³ , <i>Z</i>	6048(2), 4
ρ_{calc} /g cm ⁻³ , μ /mm ⁻¹	1.466, 4.439
F(000)	2752.0
Radiation	CuK α (λ 1.54186)
2 θ range for data collection /°	7.776 to 129.996
Index ranges	-21 \leq h \leq 24, -25 \leq k \leq 26, -15 \leq l \leq 12
Reflections collected	101660
Independent reflections	5299 [<i>R</i> _{int} = 0.0421, <i>R</i> _{sigma} = 0.0132]
LS-data/restraints/parameters	5296/166/363
Goodness-of-fit on F ²	1.128
Final R indexes [<i>I</i> \geq 2 σ (<i>I</i>)]	<i>R</i> _I = 0.0699, <i>wR</i> ₂ = 0.2042
Final R indexes [all data]	<i>R</i> _I = 0.0745, <i>wR</i> ₂ = 0.2070
Largest diff. peak/hole /e Å ⁻³	2.17/-1.15
CCDC deposition number	2195385

7.1.2.2 Crystal Data and Details of the Structure Determinations of [K(crypt-222)]₂·tol

Compound	[K(crypt-222)] ₂ ·tol
Chemical formula	C ₄₉ H ₈₅ As ₁ Ge ₃ Hg ₁ K ₂ N ₄ O ₁₂
Empirical formula	C ₄₉ H ₈₅ As ₁ Ge ₃ Hg ₁ K ₂ N ₄ O ₁₂
Formula weight / [g mol ⁻¹]	1493.75
Temperature /K	100
Crystal system	Orthorhombic
Space group	<i>Pnma</i>
<i>a</i> /Å	20.579(4)
<i>b</i> /Å	22.260(4)
<i>c</i> /Å	13.280(3)
α /°	90
β /°	90
γ /°	90
Volume /Å ³ , <i>Z</i>	6084(2), 4
ρ_{calc} /g cm ⁻³ , μ /mm ⁻¹	1.631, 8.433
<i>F</i> (000)	3000
Radiation	CuK α (λ 1.54186)
2θ range for data collection /°	7.752 to 119.986
Index ranges	$-23 \leq h \leq 23$, $-25 \leq k \leq 25$, $-6 \leq l \leq 14$
Reflections collected	34419
Independent reflections	4639 [$R_{\text{int}} = 0.0524$, $R_{\text{sigma}} = 0.0264$]
LS-data/restraints/parameters	4507/0/350
Goodness-of-fit on F^2	1.036
Final <i>R</i> indexes [$I \geq 2\sigma(I)$]	$R_I = 0.0795$, $wR_2 = 0.2192$
Final <i>R</i> indexes [all data]	$R_I = 0.0853$, $wR_2 = 0.2265$
Largest diff. peak/hole /e Å ⁻³	5.33/-1.49
CCDC deposition number	2195386

7.1.2.3 Crystal Data and Details of the Structure Determinations of [K(crypt-222)]₃3

Compound	[K(crypt-222)] ₃ 3
Chemical formula	C ₅₄ H ₁₀₈ As ₃ Ge ₅ K ₃ N ₆ O ₁₈ Zn ₁
Empirical formula	C ₅₄ H ₁₀₈ As ₃ Ge ₅ K ₃ N ₆ O ₁₈ Zn ₁ *
Formula weight / [g mol ⁻¹]	1899.84
Temperature /K	100
Crystal system	Monoclinic
Space group	C2/c
<i>a</i> /Å	13.270(3)
<i>b</i> /Å	24.360(5)
<i>c</i> /Å	28.380(6)
<i>α</i> /°	90
<i>β</i> /°	98.56(3)
<i>γ</i> /°	90
Volume /Å ³ , <i>Z</i>	9072(3), 4
<i>ρ</i> _{calc} /g cm ⁻³ , <i>μ</i> /mm ⁻¹	1.391, 5.059
F(000)	3856.0
Radiation	CuKα (λ 1.54186)
2θ range for data collection /°	7.258 to 152.504
Index ranges	-16 ≤ <i>h</i> ≤ 16, -30 ≤ <i>k</i> ≤ 18, -35 ≤ <i>l</i> ≤ 33
Reflections collected	50909
Independent reflections	9402, [<i>R</i> _{int} = 0.0535, <i>R</i> _{sigma} = 0.0651]
LS-data/restraints/parameters	9402/2/407
Goodness-of-fit on <i>F</i> ²	0.850
Final <i>R</i> indexes [<i>I</i> ≥ 2σ(<i>I</i>)]	<i>R</i> _I = 0.0477, <i>wR</i> ₂ = 0.1175
Final <i>R</i> indexes [all data]	<i>R</i> _I = 0.0789, <i>wR</i> ₂ = 0.1282
Largest diff. peak/hole /e Å ⁻³	0.73/-0.74
CCDC deposition number	2195387

* Owing to heavy disorder of the solvent molecules they could not be fully localized from the difference Fourier map. In order to avoid impairment of the refinement of the anionic substructures by an incomplete model, the influence of the electron density of some of the solvent atoms, which could not be localized, was detracted from the data by application of the back Fourier transform method using the SQUEEZE routine in PLATON.^[311] The number of electrons withdrawn by the solvent mask is 514 e⁻ in one void per unit cell, 400 of which can be assigned to the 8 additional toluene molecules per unit cell (à 50 e⁻) that could not be localized and are therefore not indicated in the formula of [K(crypt-222)]₃3. The residual number of withdrawn electrons per unit cell (141 e⁻) might, in theory, stem from (up to) four heavily disordered en molecules (C₂N₂H₈, 37 e⁻) per unit cell. This is not indicated in the formula, however, as it could not be verified by means of experimental techniques.

7.1.2.4 Crystal Data and Details of the Structure Determinations of [K(crypt-222)]₃4·tol

Compound	[K(crypt-222)] ₃ 4·tol
Chemical formula	C ₆₁ H ₁₁₆ As ₃ Cd ₃ Ge ₉ K ₃ N ₆ O ₁₈
Empirical formula	C ₆₁ H ₁₁₆ As ₃ Cd ₃ Ge ₉ K ₃ N ₆ O ₁₈
Formula weight / [g mol ⁻¹]	2554.16
Temperature / K	100
Crystal system	hexagonal
Space group	<i>P</i> 6 ₅
<i>a</i> / Å	15.3012(2)
<i>b</i> / Å	15.3012(2)
<i>c</i> / Å	69.9915(13)
α / °	90
β / °	90
γ / °	120
Volume / Å ³ , <i>Z</i>	13988.7(5), 6
ρ_{calc} / g cm ⁻³ , μ / mm ⁻¹	1.819, 11.424
<i>F</i> (000)	7536
Radiation	CuK α (λ 1.54186)
2 θ range for data collection / °	6.67 to 89.992
Index ranges	$-12 \leq h \leq 13$, $-13 \leq k \leq 12$, $-62 \leq l \leq 61$
Reflections collected	44947
Independent reflections	7505, [<i>R</i> _{int} = 0.0953, <i>R</i> _{sigma} = 0.0593]
LS-data/restraints/parameters	7229/1851/1065
Goodness-of-fit on <i>F</i> ²	1.051
Final <i>R</i> indexes [<i>I</i> ≥ 2 σ (<i>I</i>)]	<i>R</i> _I = 0.0533, <i>wR</i> ₂ = 0.1278
Final <i>R</i> indexes [all data]	<i>R</i> _I = 0.0768, <i>wR</i> ₂ = 0.1372
Largest diff. peak/hole / e Å ⁻³	0.56/−0.30
CCDC deposition number	2195388

7.1.2.5 Crystal Data and Details of the Structure Determinations of [K(crypt-222)]₉(5a)(5b)_{0.5}·en

Compound	[K(crypt-222)] ₉ (5a)(5b) _{0.5} ·en
Chemical formula	C ₁₆₄ H ₃₃₂ As ₆ Ge ₁₈ K ₉ N ₂₀ O ₅₄ Zn _{4.5}
Empirical formula	C ₁₆₄ H ₃₃₂ As ₆ Ge ₁₈ K ₉ N ₂₀ O ₅₄ Zn _{4.5} **
Formula weight / [g mol ⁻¹]	5516.04
Temperature /K	100
Crystal system	Triclinic
Space group	<i>P</i> $\bar{1}$
<i>a</i> /Å	22.9608(10)
<i>b</i> /Å	24.2487(9)
<i>c</i> /Å	27.3404(11)
α /°	101.474(3)
β /°	89.976(3)
γ /°	118.243(3)
Volume /Å ³ , <i>Z</i>	13064.4(10), 2
ρ_{calc} /g cm ⁻³ , μ /mm ⁻¹	1.402, 5.369
F(000)	5272
Radiation	CuK α (λ 1.54186)
2 θ range for data collection /°	7.444 to 140.676
Index ranges	$-27 \leq h \leq 19$, $-29 \leq k \leq 29$, $-30 \leq l \leq 33$
Reflections collected	183660
Independent reflections	49866, [<i>R</i> _{int} = 0.1466, <i>R</i> _{sigma} = 0.1391]
LS-data/restraints/parameters	46784/1242/2270
Goodness-of-fit on <i>F</i> ²	0.901
Final <i>R</i> indexes [<i>I</i> ≥ 2σ(<i>I</i>)]	<i>R</i> _I = 0.0927, <i>wR</i> ₂ = 0.2255
Final <i>R</i> indexes [all data]	<i>R</i> _I = 0.1528, <i>wR</i> ₂ = 0.2532
Largest diff. peak/hole /e Å ⁻³	1.44/−0.77
CCDC deposition number	2195389

** The empirical formula of compound [K(crypt-222)]₉(5a)(5b)_{0.5}·en deviates from the chemical formula as heavy disorder of the cations did not allow for H atoms to be added to the organic molecules without problems.

7.1.2.6 Crystal Data and Details of the Structure Determinations of [K(crypt-222)]₂6

Compound	[K(crypt-222)] ₂ 6
Chemical formula	C ₄₅ H ₈₃ AsGe ₃ K ₂ N ₄ O ₁₂ Zn ₁
Empirical formula	C ₄₅ H ₇₂ AsGe ₃ K ₂ N ₄ O ₁₂ Zn ₁ ***
Formula weight / [g mol ⁻¹]	1297.32
Temperature / K	100
Crystal system	orthorhombic
Space group	<i>Pbnm</i>
<i>a</i> / Å	22.6415(12)
<i>b</i> / Å	20.6177(15)
<i>c</i> / Å	13.1852(7)
α / °	90
β / °	90
γ / °	90
Volume / Å ³ , <i>Z</i>	6155.1(6), 4
ρ_{calc} / g cm ⁻³ , μ / mm ⁻¹	1.400, 4.379
<i>F</i> (000)	2652.0
Radiation	CuK α (λ 1.54186)
2 θ range for data collection / °	7.76 to 139.93
Index ranges	$-15 \leq h \leq 14$, $-24 \leq k \leq 24$, $-18 \leq l \leq 27$
Reflections collected	42460
Independent reflections	5906, [<i>R</i> _{int} = 0.0762, <i>R</i> _{sigma} = 0.0600]
LS-data/restraints/parameters	5906/147/301
Goodness-of-fit on <i>F</i> ²	0.977
Final <i>R</i> indexes [<i>I</i> ≥ 2 σ (<i>I</i>)]	<i>R</i> ₁ = 0.0581, <i>wR</i> ₂ = 0.1504
Final <i>R</i> indexes [all data]	<i>R</i> ₁ = 0.0977, <i>wR</i> ₂ = 0.1626
Largest diff. peak/hole / e Å ⁻³	0.87/−0.96
CCDC deposition number	2233616

*** The empirical formula of compound [K(crypt-222)]₂6 deviates from the chemical formula as the limited data quality did not allow for H atoms to be added to the mesityl groups without problems. Furthermore, heavy disorder of the solvent molecules did not allow for a full localization of them from the difference Fourier map. In order to avoid impairment of the refinement of the anionic substructures by an incomplete model, the influence of the electron density of some of the counterions' atoms, which could not be localized, was detracted from the data by application of the back Fourier transform method using the SQUEEZE routine in PLATON.^[311] The number of electrons withdrawn by the solvent mask is 20 e[−] in one void per unit cell, which can be assigned to the 0.5 additional en molecule (C₂N₂H₈, 37 e[−]) per unit cell. This is not indicated in the formula of [K(crypt-222)]₂6, however, as it could not be verified by means of other experimental techniques.

7.1.2.7 Crystal Data and Details of the Structure Determinations of [K(crypt-222)]₂·2en

Compound	[K(crypt-222)] ₂ ·2en
Chemical formula	C ₆₀ H ₁₁₈ As ₂ Ge ₆ K ₂ N ₈ Ni ₂ O ₁₂
Empirical formula	C ₆₀ H ₁₁₈ As ₂ Ge ₆ K ₂ N ₈ Ni ₂ O ₁₂
Formula weight / [g mol ⁻¹]	1924.615
Temperature /K	100
Crystal system	triclinic
Space group	<i>P</i> $\bar{1}$
<i>a</i> /Å	26.2981(11)
<i>b</i> /Å	23.6043(9)
<i>c</i> /Å	14.1013(5)
α /°	68.194(3)
β /°	78.820(3)
γ /°	86.977(3)
Volume /Å ³ , <i>Z</i>	7971.0(6), 2
ρ_{calc} /g cm ⁻³ , μ /mm ⁻¹	1.604, 5.347
F(000)	3928.0
Radiation	CuK α (λ 1.54186)
2 θ range for data collection /°	6.39 to 139.794
Index ranges	$-16 \leq h \leq 10$, $-28 \leq k \leq 28$, $-31 \leq l \leq 29$
Reflections collected	102478
Independent reflections	29234 [$R_{\text{int}} = 0.0450$, $R_{\text{sigma}} = 0.0372$]
LS-data/restraints/parameters	29234/62/1617
Goodness-of-fit on F^2	1.016
Final <i>R</i> indexes [$I \geq 2\sigma(I)$]	$R_1 = 0.0556$, $wR_2 = 0.1361$
Final <i>R</i> indexes [all data]	$R_1 = 0.0791$, $wR_2 = 0.1527$
Largest diff. peak/hole /e Å ⁻³	2.58/−1.68
CCDC deposition number	

7.1.2.8 Crystal Data and Details of the Structure Determinations of [K(crypt-222)]₂·8·solv

Compound	[K(crypt-222)] ₂ ·8·solv
Chemical formula	
Empirical formula	
Formula weight / [g mol ⁻¹]	
Temperature / K	150
Crystal system	monoclinic
Space group	C2
<i>a</i> / Å	53.0849
<i>b</i> / Å	13.1083
<i>c</i> / Å	33.6787
α / °	90
β / °	109.749
γ / °	90
Volume / Å ³ , <i>Z</i>	22057.0, 2
ρ_{calc} / g cm ⁻³ , μ / mm ⁻¹	
F(000)	10260.0
Radiation	GaK α (λ 1.34143)
2 θ range for data collection / °	6.336 to 125.258
Index ranges	$-44 \leq h \leq 42$, $-17 \leq k \leq 14$, $-70 \leq l \leq 59$
Reflections collected	
Independent reflections	[R_{int} = , R_{sigma} =]
LS-data/restraints/parameters	
Goodness-of-fit on F^2	
Final R indexes [$I \geq 2\sigma(I)$]	R_1 = , wR_2 =
Final R indexes [all data]	R_1 = , wR_2 =
Largest diff. peak/hole / e Å ⁻³	/
CCDC deposition number	

7.1.2.9 Crystal Data and Details of the Structure Determinations of [K(crypt-222)]_q9·solv

Compound	[K(crypt-222)] _q 9·solv
Chemical formula	
Empirical formula	
Formula weight / [g mol ⁻¹]	
Temperature /K	100
Crystal system	trigonal
Space group	$R\bar{3}c$
a /Å	30.965(4)
b /Å	30.965(4)
c /Å	107.36(2)
α /°	90
β /°	90
γ /°	120
Volume /Å ³ , Z	89150, 36
ρ_{calc} /g cm ⁻³ , μ /mm ⁻¹	1.371, 6.890
$F(000)$	36064.0
Radiation	CuK α (λ 1.54186)
2θ range for data collection /°	5.272 to 125.236
Index ranges	$-31 \leq h \leq 22$, $-31 \leq k \leq 35$, $-121 \leq l \leq 123$
Reflections collected	294641
Independent reflections	$[R_{\text{int}} = , R_{\text{sigma}} =]$
LS-data/restraints/parameters	
Goodness-of-fit on F^2	
Final R indexes [$I \geq 2\sigma(I)$]	$R_1 = , wR_2 =$
Final R indexes [all data]	$R_1 = , wR_2 =$
Largest diff. peak/hole /e Å ⁻³	/
CCDC deposition number	

7.1.2.10 Crystal Data and Details of the Structure Determinations of [K(crypt-222)]_{3.67}10

Compound	[K(crypt-222)] _{3.67} 10
Chemical formula	C ₆₆ H _{132.12} Bi ₁₃ Ga ₈ K _{3.67} N _{7.33} O ₂₂
Empirical formula	C ₆₆ H _{132.12} Bi ₁₃ Ga ₈ K _{3.67} N _{7.33} O ₂₂
Formula weight / [g mol ⁻¹]	4792.85
Temperature / K	100.0
Crystal system	triclinic
Space group	<i>P</i> $\bar{1}$
<i>a</i> / Å	15.495(3)
<i>b</i> / Å	15.905(3)
<i>c</i> / Å	17.157(3)
α / °	111.36(3)
β / °	115.78(3)
γ / °	96.96(3)
Volume / Å ³ , <i>Z</i>	3343.2(15), 1
ρ_{calc} / g cm ⁻³ , μ / mm ⁻¹	2.381, 18.777
<i>F</i> (000)	2147.0
Radiation	MoK α (λ = 0.71073)
2 θ range for data collection / °	2.916 to 53.376
Index ranges	$-19 \leq h \leq 19$, $-15 \leq k \leq 20$, $-20 \leq l \leq 21$
Reflections collected	80307
Independent reflections	13693 [<i>R</i> _{int} = 0.0785, <i>R</i> _{sigma} = 0.0550]
LS-data/restraints/parameters	13693/1092/619
Goodness-of-fit on <i>F</i> ²	0.954
Final <i>R</i> indexes [<i>I</i> ≥ 2 σ (<i>I</i>)]	<i>R</i> ₁ = 0.0752, <i>wR</i> ₂ = 0.2128
Final <i>R</i> indexes [all data]	<i>R</i> ₁ = 0.1154, <i>wR</i> ₂ = 0.2443
Largest diff. peak/hole / e Å ⁻³	2.57/−4.59
CCDC deposition number	2052900

7.1.2.11 Crystal Data and Details of the Structure Determinations of [K(crypt-222)]₄11·solv

Compound	[K(crypt-222)] ₄ 11a	[K(crypt-222)] ₄ 11b·4py
Chemical formula	C ₇₂ H ₁₄₄ Bi ₁₆ Ga ₂ K ₄ N ₈ O ₂₄	C ₉₂ H ₁₆₄ Bi ₁₆ Ga ₂ K ₄ N ₁₂ O ₂₄
Empirical formula	C ₇₂ H ₁₄₄ Bi ₁₆ Ga ₂ K ₄ N ₈ O ₂₄	C ₉₂ H ₁₆₄ Bi ₁₆ Ga ₂ K ₄ N ₁₂ O ₂₄
Formula weight / [g mol ⁻¹]	5145.46	5457.83
Temperature /K	100.0	100.0
Crystal system	orthorhombic	monoclinic
Space group	<i>Pbca</i>	<i>P2₁/n</i>
a /Å	25.2502(13)	17.640(4)
b /Å	17.9333(9)	17.630(4)
c /Å	29.3548(15)	22.040(4)
α /°	90	90
β /°	90	95.26(3)
γ /°	90	90
Volume /Å ³ , Z	13292.4(12), 4	6825(2), 2
ρ _{calc} /g cm ⁻³ , μ /mm ⁻¹	2.571, 21.668	2.656, 21.109
F(000)	9160.0	4908.0
Radiation	MoKα (λ = 0.71073)	MoKα (λ = 0.71073)
2θ range for data collection /°	4.256 to 49.488	2.834 to 53.302
Index ranges	-29 ≤ h ≤ 29, -21 ≤ k ≤ 21, -34 ≤ l ≤ 34	-18 ≤ h ≤ 22, -17 ≤ k ≤ 22, -27 ≤ l ≤ 27
Reflections collected	111440	95259
Independent reflections	11352 [<i>R</i> _{int} = 0.1384, <i>R</i> _{sigma} = 0.0763]	14174 [<i>R</i> _{int} = 0.0584, <i>R</i> _{sigma} = 0.0307]
LS-data/restraints/parameters	11352/1182/568	14174/1182/676
Goodness-of-fit on F ²	1.176	1.090
Final R indexes [<i>I</i> ≥ 2σ(<i>I</i>)]	<i>R</i> ₁ = 0.0802, <i>wR</i> ₂ = 0.1735	<i>R</i> ₁ = 0.0831, <i>wR</i> ₂ = 0.2410
Final R indexes [all data]	<i>R</i> ₁ = 0.1166, <i>wR</i> ₂ = 0.1859	<i>R</i> ₁ = 0.1024, <i>wR</i> ₂ = 0.2620
Largest diff. peak/hole /e Å ⁻³	3.36/-1.68	5.65/-2.74
CCDC deposition number	2052901	2052902

7.1.2.12 Crystal Data and Details of the Structure Determinations of [K(crypt-222)]₄12·solv

Compound	[K(crypt222)] ₄ 12a·4.63THF·2en	[K(crypt-222)] ₄ 12b
Chemical formula	C _{126.51} H _{245.04} Bi ₁₈ K ₄ N ₁₂ O _{28.63} Ru ₄	C ₁₀₄ H ₁₉₂ Bi ₁₈ K ₄ N ₈ O ₂₄ Ru ₄
Empirical formula	C _{126.51} H _{245.04} Bi ₁₈ K ₄ N ₁₂ O _{28.63} Ru ₄	C ₁₀₄ H ₁₉₂ Bi ₁₈ K ₄ N ₈ O ₂₄ Ru ₄
Formula weight / [g mol ⁻¹]	6706.82	5457.83
Temperature / K	100.0	100.0
Crystal system	triclinic	triclinic
Space group	<i>P</i> $\bar{1}$	<i>P</i> $\bar{1}$
a / Å	13.5587(18)	17.470(4)
b / Å	16.249(2)	17.820(4)
c / Å	23.165(3)	27.680(6)
α / °	102.957(4)	94.31(3)
β / °	98.683(4)	98.60(3)
γ / °	110.025(4)	90.90(3)
Volume / Å ³ , Z	4526.1(10), 1	8493(3), 2
ρ_{calc} / g cm ⁻³ , μ / mm ⁻¹	2.461, 17.894	2.448, 39.824
F(000)	3055.0	5620.0
Radiation	MoK α (λ = 0.71073)	CuK α (λ = 1.54186)
2 θ range for data collection / °	4.32 to 46.79	6.146 to 130
Index ranges	-15 \leq h \leq 15, -18 \leq k \leq 18, -25 \leq l \leq 25	-20 \leq h \leq 19, -20 \leq k \leq 14, -32 \leq l \leq 32
Reflections collected	78145	60316
Independent reflections	13152 [R_{int} = 0.1086, R_{sigma} = 0.0721]	17229 [R_{int} = 0.0987, R_{sigma} = 0.1057]
LS-data/restraints/parameters	13152/339/902	17229/2406/1454
Goodness-of-fit on F ²	1.037	0.927
Final R indexes [$I \geq 2\sigma(I)$]	R_1 = 0.0514, wR_2 = 0.1064	R_1 = 0.1009, wR_2 = 0.2611
Final R indexes [all data]	R_1 = 0.0991, wR_2 = 0.1284	R_1 = 0.1409, wR_2 = 0.2825
Largest diff. peak/hole / e Å ⁻³	2.92/-3.56	3.22/-3.58
CCDC deposition number	2052903	2052904

7.1.2.13 Crystal Data and Details of the Structure Determinations of [K(crypt-222)]₂13·solv

Compound	[K(crypt-222)] ₂ 13a	[K(crypt-222)] ₂ 13b·2tol
Chemical formula	C ₆₄ H ₁₂₀ Bi ₂ K ₂ N ₄ O ₁₂ Ru ₂	C ₇₈ H ₁₃₆ Bi ₂ K ₂ N ₄ O ₁₂ Ru ₂
Empirical formula	C ₆₄ H ₁₂₀ Bi ₂ K ₂ N ₄ O ₁₂ Ru ₂	C ₇₈ H ₁₃₆ Bi ₂ K ₂ N ₄ O ₁₂ Ru ₂
Formula weight /[g mol ⁻¹]	1835.93	2018.18
Temperature /K	100	100
Crystal system	triclinic	triclinic
Space group	<i>P</i> $\bar{1}$	<i>P</i> $\bar{1}$
a /Å	11.950(2)	12.8125(7)
b /Å	13.710(3)	13.0855(7)
c /Å	14.360(3)	15.1540(8)
α /°	64.16(3)	94.441(2)
β /°	74.85(3)	112.035(2)
γ /°	64.52(3)	109.909(2)
Volume /Å ³ , Z	1903.6(9), 1	2152.1(2), 1
ρ_{calc} /g cm ⁻³ , μ /mm ⁻¹	1.602, 5.162	1.557, 4.574
F(000)	920.0	1018.0
Radiation	MoK α (λ = 0.71073)	MoK α (λ = 0.71073)
2 Θ range for data collection /°	3.164 to 53.218	5.03 to 52.14
Index ranges	-13 \leq h \leq 15, -7 \leq k \leq 16, -17 \leq l \leq 17	-15 \leq h \leq 15, -16 \leq k \leq 16, -18 \leq l \leq 18
Reflections collected	33256	90209
Independent reflections	7455 [R_{int} = 0.0671, R_{sigma} = 0.0904]	8381 [R_{int} = 0.0295, R_{sigma} = 0.0135]
LS-data/restraints/parameters	7455/0/393	8381/9/457
Goodness-of-fit on F ²	0.929	1.060
Final R indexes [$I \geq 2\sigma(I)$]	R_1 = 0.0606, wR_2 = 0.1486	R_1 = 0.0285, wR_2 = 0.0669
Final R indexes [all data]	R_1 = 0.1142, wR_2 = 0.1770	R_1 = 0.0306, wR_2 = 0.0683
Largest diff. peak/hole /e Å ⁻³	2.96/-2.07	2.41/-1.90
CCDC deposition number	2131134	2131135

Compound	[K(crypt-222)] ₂ 13c ·2tol
Chemical formula	C ₇₈ H ₁₃₆ Bi ₂ K ₂ N ₄ O ₁₂ Ru ₂
Empirical formula	C ₇₈ H ₁₃₆ Bi ₂ K ₂ N ₄ O ₁₂ Ru ₂
Formula weight /[g mol ⁻¹]	2020.20
Temperature /K	100
Crystal system	triclinic
Space group	<i>P</i> $\bar{1}$
<i>a</i> /Å	12.820(3)
<i>b</i> /Å	13.110(3)
<i>c</i> /Å	15.160(3)
α /°	94.56(3)
β /°	111.90(3)
γ /°	109.96(3)
Volume /Å ³ , <i>Z</i>	2158.7(9), 1
ρ_{calc} /g cm ⁻³ , μ /mm ⁻¹	1.554, 4.560
<i>F</i> (000)	1020.0
Radiation	MoK α (λ = 0.71073)
2 θ range for data collection /°	3.652 to 53.18
Index ranges	-16 ≤ <i>h</i> ≤ 14, -16 ≤ <i>k</i> ≤ 14, -17 ≤ <i>l</i> ≤ 19
Reflections collected	46015
Independent reflections	8434 [<i>R</i> _{int} = 0.0338, <i>R</i> _{sigma} = 0.0236]
LS-data/restraints/parameters	8434/1/457
Goodness-of-fit on <i>F</i> ²	1.037
Final <i>R</i> indexes [<i>I</i> ≥ 2 σ (<i>I</i>)]	<i>R</i> ₁ = 0.0455, <i>wR</i> ₂ = 0.1168
Final <i>R</i> indexes [all data]	<i>R</i> ₁ = 0.0503, <i>wR</i> ₂ = 0.1216
Largest diff. peak/hole /e Å ⁻³	2.01/-2.56
CCDC deposition number	2131136

7.1.3 Structural Details

Table 7.1: Selected interatomic distances (in Å) of the experimental and optimized structures in the cluster anion $[\text{PhZn}(\text{Ge}_3\text{As})]^{2-}$ in compound $[\text{K}(\text{crypt-222})]_2(\mathbf{1})_{0.9}(\text{Ge}_2\text{As}_2)_{0.1} \cdot 0.9\text{tol}$.

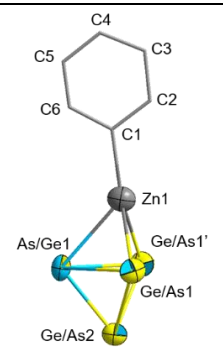
Atom1–Atom2	Bond length (exp)	Bond length (calc)	
Zn1–As/Ge1	2.657(2)	2.66	
Zn1–Ge/As1	2.4525(17)	2.49	
As/Ge1–Ge/As1	2.5983(15)	2.61	
As/Ge1–Ge/As2	2.4576(19)	2.51	
Ge/As1–Ge/As2	2.4673(15)	2.50	
Ge/As1–Ge/As1'	2.758(3)	2.77	
C1–Zn1	2.037(11)	2.00	

Table 7.2: Selected bond angles (in degrees) of the experimental and optimized structures in the cluster anion $[\text{PhZn}(\text{Ge}_3\text{As})]^{2-}$ in compound $[\text{K}(\text{crypt-222})]_2(\mathbf{1})_{0.9}(\text{Ge}_2\text{As}_2)_{0.1} \cdot 0.9\text{tol}$.

Atom1–Atom2–Atom3	Bond angle range (exp)	Bond angle range (calc)
Ge/As–As/Ge–Ge/As	58.34(4), 64.10(7)	58.40, 64.02
Ge/As–As/Ge–Zn	55.63(4)	56.41
Ge/As–Zn–Ge/As	68.41(7)	67.43
Ge/As–Zn–As/Ge	60.98(5)	60.72
Ge/As–Ge/As–Ge/As	56.03(3), 67.95(7)	56.40, 67.18
Ge/As–Ge/As–As/Ge	57.98(5), 57.95(3), 63.68(5)	58.89, 58.00, 62.72
C–C–Zn	119.6(9), 125.0(8)	122.0, 122.34
C–C–C	115.4(10) – 125.0(11)	115.65 – 122.57
C–Zn–Ge/As	145.45(6)	145.97
C–Zn–As/Ge	131.3(3)	131.19
Zn–Ge/As–Ge/As	55.78(4), 105.61(6)	56.28, 106.39
Zn–Ge/As–As/Ge	63.39(5)	62.87

Table 7.3: Selected interatomic distances (in Å) of the experimental and optimized structures in the cluster anion $[\text{PhHg}(\text{Ge}_3\text{As})]^{2-}$ in compound $[\text{K}(\text{crypt-222})]_2\mathbf{2} \cdot \text{tol}$.

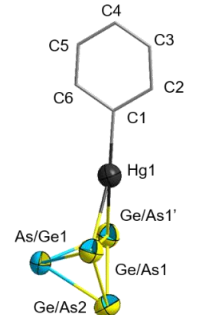
Atom1–Atom2	Bond length (exp)	Bond length (calc)	
Hg1–Ge/As1	2.6394(13)	2.66	
As/Ge1–Ge/As1	2.4804(15)	2.51	
As/Ge1–Ge/As2	2.541(2)	2.57	
Ge/As1–Ge/As2	2.4899(18)	2.50	
Ge/As1–Ge/As1'	2.830(2)	2.83	
C1–Hg1	2.123(16)	2.20	

Table 7.4: Selected bond angles (in degrees) of the experimental and optimized structures in the cluster anion $[\text{PhHg}(\text{Ge}_3\text{As})]^{2-}$ in compound $[\text{K}(\text{crypt-222})]_2\cdot\text{tol}$.

Atom1–Atom2–Atom3	Bond angle range (exp)	Bond angle range (calc)
Ge/As–As/Ge–Ge/As	59.44(5), 69.57(7)	58.95, 68.80
Ge/As–Hg–Ge/As	64.84(5)	64.27
Ge/As–Ge/As–Ge/As	55.37(3), 69.26(7)	55.49, 69.03
Ge/As–Ge/As–As/Ge	55.22(3) – 61.49(6)	55.60 – 61.80
C–C–Hg	121.0(11), 125.1(12)	121.86, 121.47
C–C–C	113.9(15) – 124.1(15)	116.67 – 121.95
C–Hg–Ge/As	147.18(7)	147.36
Hg–Ge/As–Ge/As	57.58(3), 111.34(5)	57.85, 111.92
Hg–Ge/As–As/Ge	91.62(5)	91.37

Table 7.5: Selected interatomic distances (in Å) of the experimental and optimized structures in the cluster anion $[(\text{Ge}_2\text{As}_2)\text{Zn}(\text{Ge}_3\text{As})]^{3-}$ in compound $[\text{K}(\text{crypt-222})]_3\cdot\mathbf{3}$.

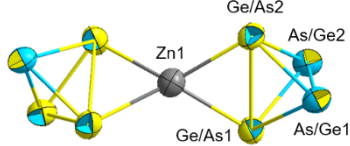
Atom1–Atom2	Bond length (exp)	Bond length (calc)	
As/Ge1–As/Ge2	2.4968(10)	2.48	
As/Ge1–Ge/As1	2.4671(10)	2.49	
As/Ge1–Ge/As2	2.4705(11)	2.50	
As/Ge2–Ge/As1	2.4595(12)	2.49	
As/Ge2–Ge/As2	2.4771(10)	2.49	
Ge/As1–Ge/As2	2.7360(10)	2.78	
Ge/As1–Zn1	2.5240(9)	2.57	
Ge/As2–Zn1	2.5439(9)	2.56	

Table 7.6: Selected bond angles (in degrees) of the experimental and optimized structures in the cluster anion $[(\text{Ge}_2\text{As}_2)\text{Zn}(\text{Ge}_3\text{As})]^{3-}$ in compound $[\text{K}(\text{crypt-222})]_3\cdot\mathbf{3}$.

Atom1–Atom2–Atom3	Bond angle range (exp)	Bond angle range (calc)
within Ge/As <i>Pseudo</i> -tetrahedra	56.04(3) – 67.31(3)	56.18 – 67.74
Ge/As–Ge/As–Zn	56.98(3)	57.38
Zn–Ge/As–As/Ge	100.76(4) – 108.38(4)	104.62 – 105.06

Table 7.7: Selected interatomic distances (in Å) of the experimental and optimized structures in the cluster anion $[\text{Cd}_3(\text{Ge}_3\text{As})_3]^{3-}$ in compound $[\text{K}(\text{crypt-222})]_3\cdot\mathbf{4}\cdot\text{tol}$.

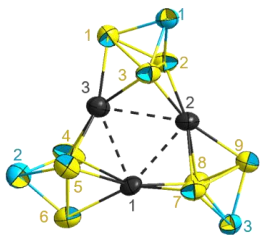
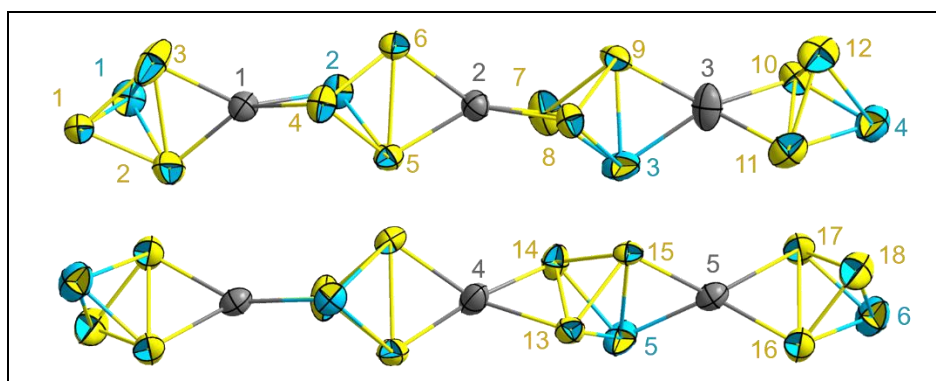
Atom1–Atom2	Bond length (exp)	Bond length (calc)	
Cd...Cd	3.23(3) – 3.403(9)	3.22	
Cd–Ge/As	2.697(12) – 3.02(3)	2.74 – 2.92	
Ge/As–Ge/As	2.552(13) – 2.922(10)	2.64 – 2.93	
Ge/As–As/Ge	2.385(11) – 2.459(11)	2.45 – 2.51	

Table 7.8: Selected bond angles (in degrees) of the experimental structures of the anion in the cluster anion $[\text{Cd}_3(\text{Ge}_3\text{As})_3]^{3-}$ in compound $[\text{K}(\text{crypt-222})]_3\text{4-tol}$.

Atom1–Atom2–Atom3	Bond angle range (exp)	Bond angle range (calc)
Within Ge/As <i>Pseudo</i> -tetrahedra	52.2(3) – 74.2(3)	53.39 – 73.25
$\text{Cd}\cdots\text{Cd}\cdots\text{Cd}$	58.1(5) – 63.6(6)	59.96 – 60.03
$\text{Cd}\cdots\text{Cd}\cdots\text{Ge/As}$	52.0(2) – 62.8(2), 91.3(3) – 111.1(6), 148.4(5) – 157.2(11)	53.38 – 57.70, 96.03 – 107.64, 155.82 – 156.09
$\text{Cd}\cdots\text{Ge/As}\cdots\text{Cd}$	68.0(6) – 75.8(3)	68.90 – 69.19
$\text{Cd}\cdots\text{Ge/As}\cdots\text{Ge/As}$	57.3(2) – 76.2(4), 106.3(4) – 112.9(3)	56.25 – 65.68, 109.81 – 110.06
$\text{Cd}\cdots\text{Ge/As}\cdots\text{As/Ge}$	98.5(6) – 111.6(5)	98.27 – 108.93
$\text{Ge/As}\cdots\text{Cd}\cdots\text{Ge/As}$	53.1(6) – 63.5(2), 113.9(3) – 165.0(3)	55.52 – 63.87, 113.40 – 160.69

Table 7.9: Selected interatomic distances (in Å) of the experimental and optimized structures in the cluster anion $[\text{Zn}_3(\text{Ge}_3\text{As})_4]^{6-}$ in compound $[\text{K}(\text{crypt-222})]_9(\mathbf{5a})(\mathbf{5b})_{0.5}\text{en}$.



Atom1–Atom2	Bond length (exp)	Bond length (calc)
Zn–Ge/As	2.332(10) – 2.658(7)	2.52 – 2.59
Zn–As/Ge	2.535(2) – 2.589(3)	2.49 – 2.68
Ge/As–Ge/As	2.416(6) – 2.769(2)	2.49 – 2.79
Ge/As–As/Ge	2.431(3) – 2.6752(19)	2.57 – 2.58

Table 7.10: Selected bond angles (in degrees) of the experimental structures of the anion in the cluster anion $[\text{Zn}_3(\text{Ge}_3\text{As})_4]^{6-}$ in compound $[\text{K}(\text{crypt-222})]_9(\mathbf{5a})(\mathbf{5b})_{0.5}\text{en}$

Atom1–Atom2–Atom3	Bond angle range (exp)	Bond angle range (calc)
within Ge/As <i>Pseudo</i> -tetrahedra	55.29(6) – 68.94(11)	55.89 – 68.09
$\text{Zn}\cdots\text{Ge/As}\cdots\text{Ge/As}$	56.00(6) – 59.30(8), 93.84(14) – 112.29(14)	56.55 – 57.00 104.96 – 110.65
$\text{Ge/As}\cdots\text{Zn}\cdots\text{Ge/As}$	63.37(8) – 66.68(9), 127.95(11) – 144.15(11)	66.37 – 66.77, 129.90 – 137.29
$\text{Ge/As}\cdots\text{Zn}\cdots\text{As/Ge}$	62.32(10) – 62.70(6), 116.41(13) – 150.11(16)	62.49 – 62.53, 134.74 – 137.89

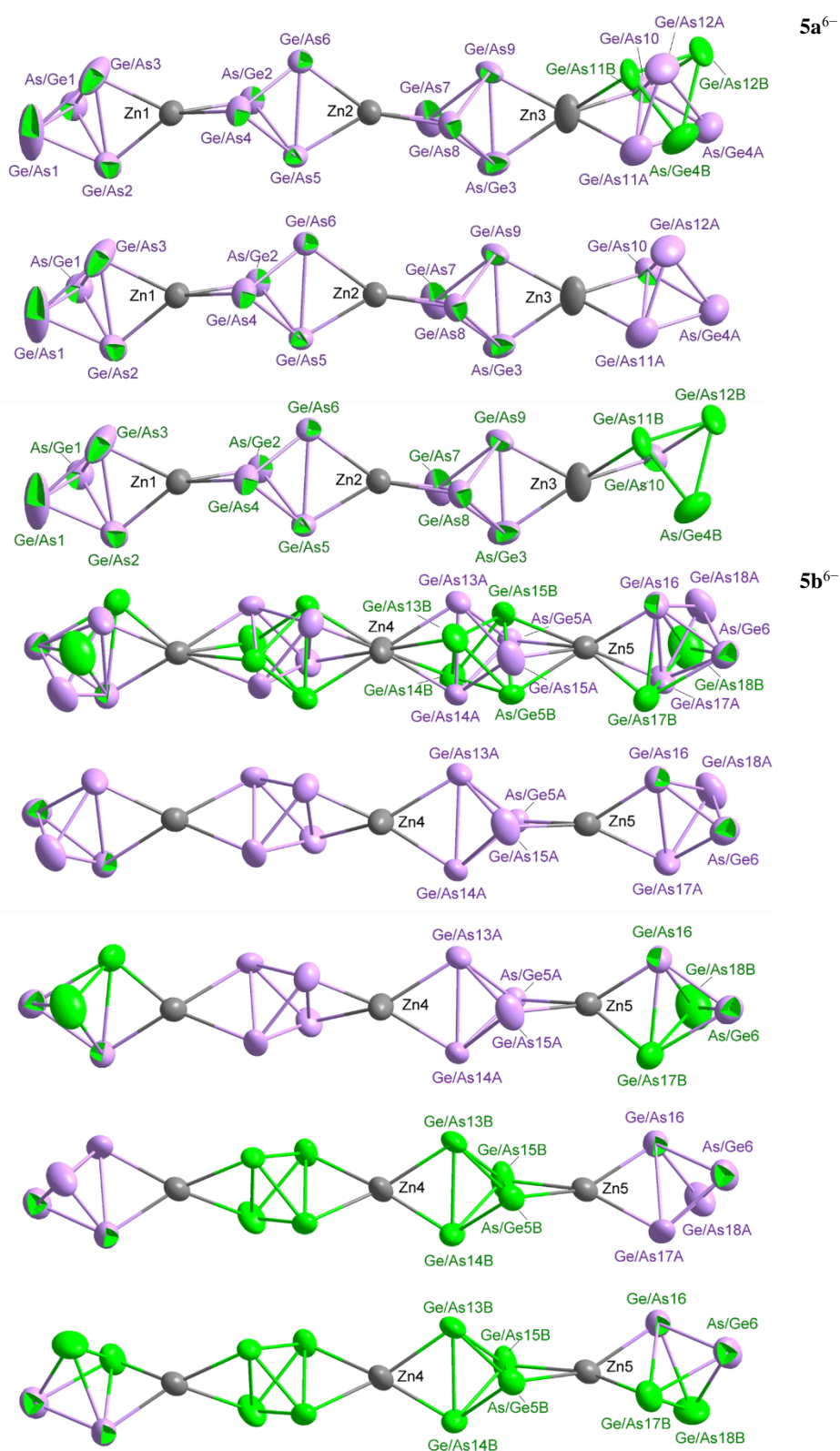


Figure 7.1: Representation of the different conformers of the anions 5^{6-} (top and second from top: $5a^{6-}$, third from top to bottom: $5b^{6-}$), the disordered positions of which are overlaid in $5b^{6-}$ owing to this anion's location on a crystallographic inversion center.

Table 7.11: Selected interatomic distances (in Å) of the experimental and optimized structures in the cluster anion [MesZn(Ge₃As)]²⁻ in compound [K(crypt-222)]₂6.

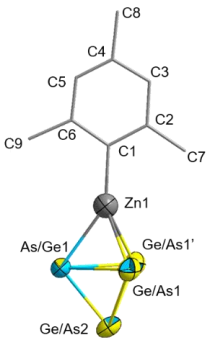
Atom1–Atom2	Bond length (exp)	Bond length (calc)	
Zn1–As/Ge1	2.4920(15)	2.70	
Zn1–Ge/As1	2.5237(12)	2.49	
As/Ge1–Ge/As1	2.6538(10)	2.60	
As/Ge1–Ge/As2	2.4672(13)	2.51	
Ge/As1–Ge/As2	2.4821(11)	2.50	
Ge/As1–Ge/As1'	2.6377(14)	2.75	
C1–Zn1	1.970(9)	2.01	

Table 7.12: Selected bond angles (in degrees) of the experimental and optimized structures in the cluster anion [MesZn(Ge₃As)]²⁻ in compound [K(crypt-222)]₂6.

Atom1–Atom2–Atom3	Bond angle range (exp)	Bond angle range (calc)
Ge/As–As/Ge–Ge/As	57.85(3), 59.60(4)	58.86, 63.81
Ge/As–Zn–Ge/As	63.01(4)	67.11
Ge/As–Zn–As/Ge	63.89(4)	59.96
Ge/As–Ge/As–Ge/As	57.90(2), 64.19(4)	56.40, 66.70
Ge/As–Ge/As–As/Ge	57.30(3), 60.202(18), 64.85(3)	58.83, 58.34, 62.31
C–C–Zn	120.7(8), 121.9(7)	119.86, 123.09
C–C–C	114.7(11) – 123.3(12)	117.05 – 121.75
C–Zn–Ge/As	140.00(17)	148.23
C–Zn–As/Ge	147.1(3)	134.25
Zn–Ge/As–Ge/As	58.49(2), 103.93(3)	56.59, 58.83
Zn–Ge/As–As/Ge	57.48(3)	64.09
Zn–As/Ge–Ge/As	58.64(3), 105.32(5)	55.95, 100.90

Table 7.13: Selected interatomic distances (in Å) of the experimental structures in the cluster anion [{Cp*Ni}₂(Ge₆As₂)]²⁻ in compound [K(crypt-222)]₂7·2en.

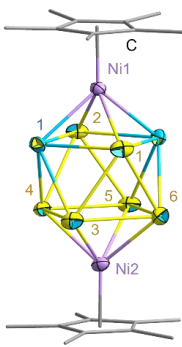
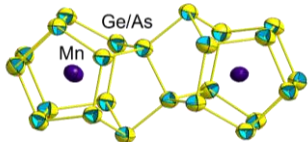
Atom1–Atom2	Bond length (exp)	
Ni–As/Ge	2.4200(11), 2.4329(14)	
Ni–Ge/As	2.4303(12) – 2.4855(12)	
As/Ge–Ge/As	2.5631(9) – 2.7396(12)	
Ge/As–Ge/As	2.5786(11) – 2.7285(12)	

Table 7.14: Selected bond angles (in degrees) of the experimental structures in the cluster anion $[(\text{Cp}^*\text{Ni})_2(\text{Ge}_6\text{As}_2)]^{2-}$ in compound $[\text{K}(\text{crypt-222})]_2 \cdot 2\text{en}$.

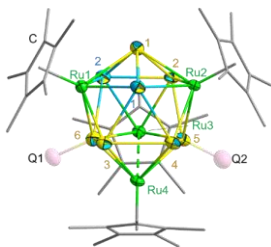
Atom1–Atom2–Atom3	Bond angle range (exp)
within Ge/As square antiprism	57.78(3) – 64.22(3), 86.98(3) – 106.02(3)
Ni–Ge/As–Ge/As	55.80(3) – 57.76(3), 108.59(3) – 112.60(4)
Ni–Ge/As–As/Ge	55.28(3) – 56.16(3), 107.88(4) – 110.59(4)
Ni–As/Ge–Ge/As	56.95(3) – 57.90(3), 110.23(3) – 113.67(4)
C–Ni–C	37.3(3) – 38.5(2), 63.1(2) – 63.9(2)
C–Ni–As/Ge	95.74(14) – 162.92(14)
C–Ni–Ge/As	95.59(15) – 160.40(16)
Ge/As–Ni–Ge/As	66.44(3) – 67.75(3), 102.46(4) – 104.03(4)
Ge/As–Ni–As/Ge	65.93(3) – 67.76(3)
As/Ge–Ni–As/Ge	100.79(4)

Table 7.15: Selected interatomic distances (in Å) of the experimental structures in the cluster anion $[\text{Mn}_2@\text{Ge}_x\text{As}_{24-x}]^{q-}$ in compound $[\text{K}(\text{crypt-222})]_4 \cdot 9\text{solv}$.

Atom1–Atom2	Bond length (exp)	
Mn··As/Ge and Mn··Ge/As	2.585(2) – 2.743(3)	
As/Ge–Ge/As and Ge/As–Ge/As	2.438(3) – 2.585(2)	

Since the exact structure of $[\text{Mn}_2@\text{Ge}_x\text{As}_{24-x}]^{q-}$ has not been determined yet, selected bond angles (in degrees) of the experimental structures cannot be provided and classified here.

Table 7.16: Selected interatomic distances (in Å) of the experimental structures in the cluster anion $[(\text{Cp}^*\text{Ru})_4(\text{GeR})_x(\text{Ge}_4\text{As}_{4-x})]^{2-}$ in compound $[\text{K}(\text{crypt-222})]_2 \cdot 8\text{solv}$.

Atom1–Atom2	Bond length (exp)	
Ru–As/Ge and Ru–Ge/As	2.4747(11) – 2.6638(12)	
As/Ge–Ge/As and Ge/As–Ge/As	2.510(2) – 2.6426(14)	

Since the exact structure of $[(\text{Cp}^*\text{Ru})_4(\text{GeR})_x(\text{Ge}_4\text{As}_{4-x})]^{2-}$ has not been determined yet, selected bond angles (in degrees) of the experimental structures cannot be provided and classified here.

Table 7.17: Selected interatomic distances (in Å) of the experimental and optimized structures in the cluster anion $[\text{Bi}@\text{Ga}_8(\text{Bi}_2)_6]^{3-/5-}$ in compound $[\text{K}(\text{crypt-222})]_{3.67}\mathbf{10}$.

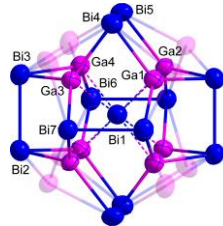
Atom1–Atom2	Bond length (exp)	Bond length (calc)	
Ga–Bi	2.698(4) – 3.036(4)	2.774 – 2.936	
Bi–Bi	2.9667(18) – 3.0249(14)	3.015	

Table 7.18: Selected bond angles (in degrees) of the experimental and optimized structures in the cluster anion $[\text{Bi}@\text{Ga}_8(\text{Bi}_2)_6]^{3-/5-}$ in compound $[\text{K}(\text{crypt-222})]_{3.67}\mathbf{10}$.

Atom1–Atom2–Atom3	Bond angle range (exp)
Ga–Bi–Ga	69.57(10) – 74.43(10), 91.46(17) – 110.43(10), 180.00 – 180.00(15)
Ga–Bi–Bi	92.03(8) – 94.87(9), 102.3(2) – 110.3(2)
Bi–Ga–Bi	93.76(11) – 95.91(11), 104.46(13) – 121.31(13)
Bi–Bi–Ga	106.38(19) – 109.58(9)

Table 7.19: Selected interatomic distances (in Å) of the experimental and optimized structures in the cluster anion $(\text{Ga}_2\text{Bi}_{16})^{4-}$ in compound $[\text{K}(\text{crypt-222})]_4\mathbf{11}\cdot\text{solv}$.

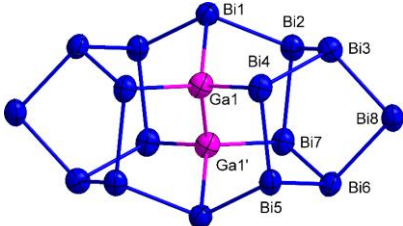
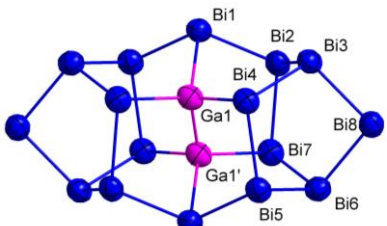
<div style="display: flex; justify-content: space-around; align-items: center;"> <div style="text-align: center;">  <p>11a⁴⁻</p> </div> <div style="text-align: center;">  <p>11b⁴⁻</p> </div> </div>			
Atom1–Atom2	Bond length in 11a⁴⁻ (exp)	Bond length in 11b⁴⁻ (exp)	Bond length (calc)
Ga–Bi	2.694(3), 2.698(3), 2.711(3)	2.714(3), 2.730(3), 2.742(3)	2.746, 2.746, 2.744
Ga–Ga	2.470(5)	2.493(5)	2.500
Bi–Bi	2.9469(16) – 3.0304(15)	2.9320(14) – 3.0196(13)	2.952 – 3.049

Table 7.20: Selected bond angles (in degrees) of the experimental and optimized structures in the cluster anion $(\text{Ga}_2\text{Bi}_{16})^{4-}$ in compound $[\text{K}(\text{crypt-222})]_4\mathbf{11}\cdot\text{solv}$.

Atom1–Atom2–Atom3	Bond angle range in 11a⁴⁻ (exp)	Bond angle range in 11b⁴⁻ (exp)
Ga–Ga–Bi	106.57(15), 109.60(17), 111.21(17)	104.03(13), 110.84(15), 112.74(14)
Ga–Bi–Bi	87.87(7) – 95.56(7)	91.85(7) – 94.76(6)
Bi–Ga–Bi	104.71(9), 111.85(11), 112.97(11)	104.49(8), 112.20(9), 112.76(10)
Bi–Bi–Bi	90.54(4) – 109.11(4)	89.92(3) – 110.84(4)

Table 7.21: Selected interatomic distances (in Å) of the experimental and optimized structures in the cluster anion $\{[(\text{cod})\text{Ru}]_4\text{Bi}_{18}\}^{4-}$ in compound $[\text{K}(\text{crypt-222})]_4\mathbf{12}\cdot\text{solv}$.

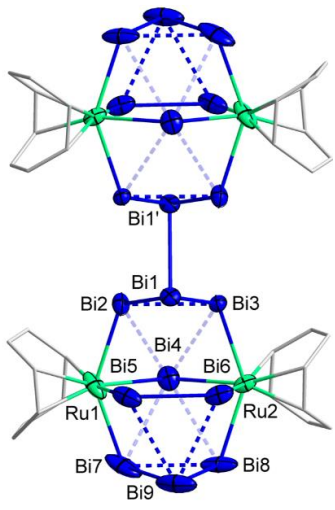
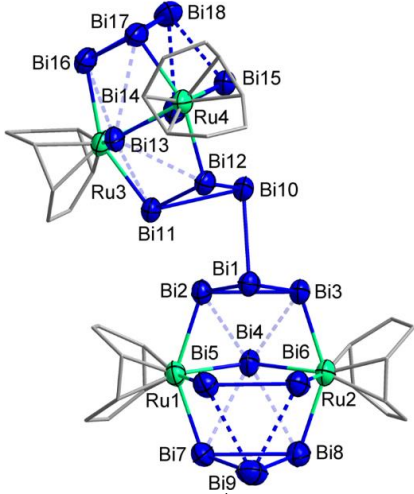
 <p style="text-align: center;">12a⁴⁻</p>			 <p style="text-align: center;">12b⁴⁻</p>		
Atom1–Atom2	Bond length in 12a⁴⁻ (exp)	Bond length in 12a⁴⁻ (calc)	Atom1–Atom2	Bond length in 12b⁴⁻ (exp)	Bond length in 12b⁴⁻ (calc)
Ru–Bi	2.713(2) – 2.7806(19)	2.727 – 2.796	Ru–Bi	2.713(4) – 2.795(4)	2.718 – 2.796
Bi–Bi	2.9569(13) – 3.6330(13)	2.977 – 3.648	Bi–Bi	2.962(3) – 3.662(3)	2.980 – 3.652

Table 7.22: Selected bond angles (in degrees) of the experimental and optimized structures in the cluster anion $\{[(\text{cod})\text{Ru}]_4\text{Bi}_{18}\}^{4-}$ in compound $[\text{K}(\text{crypt-222})]_4\mathbf{12}\cdot\text{solv}$.

Atom1–Atom2–Atom3	Bond angle range in 12a⁴⁻ (exp)	Bond angle range in 12b⁴⁻ (exp)
Ru–Bi–Bi	47.80(5) – 53.24(4), 98.88(5) – 113.33(4)	47.41(8) – 54.77(8), 97.95(9) – 113.13(10),
Ru–Bi–Ru	124.09(6)	122.27(12), 123.89(13)
Bi–Ru–Bi	74.58(5) – 97.77(5), 142.72(8), 142.20(6)	71.47(9) – 98.73(12), 142.06(15) – 143.72(14)
Bi–Bi–Bi	49.05(2) – 73.29(2), 84.56(3) – 105.36(3), 127.36(4) – 149.47(4)	48.56(6) – 74.10(6), 79.92(6), 84.97(6) – 105.98(6), 126.49(8) – 151.60(7)

Table 7.23: Selected interatomic distances (in Å) of the experimental and optimized structures in the complex anion $[(C_7H_{11})(C_7H_{13})Ru]_2Bi_2]^{2-}$ in compound $[K(crypt-222)]_2\mathbf{13}\cdot solv.$

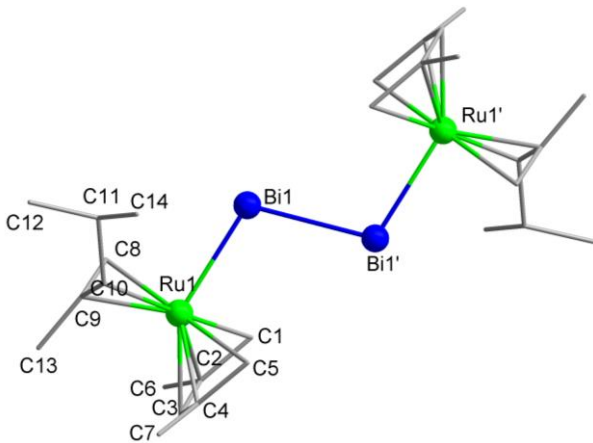
 <p style="text-align: center;">13²⁻</p>				
Atom1–Atom2	Bond length in 13a²⁻ (exp)	Bond length in 13b²⁻ (exp)	Bond length in 13c²⁻ (exp)	Bond length (calc)
Bi–Bi	2.8318(12)	2.8578(3)	2.8623(19)	2.84
Ru–Bi	2.7514(14)	2.7625(3)	2.7679(8)	2.76
Ru–C	2.112(11) – 2.224(11)	2.090(4) – 2.220(4)	2.077(5) – 2.226(6)	2.11 – 2.23
C–C	1.397(18) – 1.540(17)	1.414(5) – 1.549(6)	1.404(10) – 1.536(10)	1.43 – 1.54

Table 7.24: Selected bond angles (in degrees) of the experimental and optimized structures in the complex anion $[(C_7H_{11})(C_7H_{13})Ru]_2Bi_2]^{2-}$ in compound $[K(crypt-222)]_2\mathbf{13}\cdot solv.$

Atom1– Atom2–Atom3	Bond angle range in 13a²⁻ (exp)	Bond angle range in 13b²⁻ (exp)	Bond angle range in 13c²⁻ (exp)	Bond angle range (calc)
Ru–Bi–Bi	108.03(4)	107.867(10)	107.96(3)	108.9
C–Ru–C	36.7(5) – 38.8(4), 67.3(5) – 141.9(4), 173.7(5)	37.53(13) – 39.73(13), 69.33(13) – 145.03(13), 171.44(13), 173.97(13)	37.4(3) – 39.3(3), 68.1(3) – 145.3(3), 171.3(3), 173.7(3)	37.7 – 39.1, 67.7 – 145.7, 171.4, 174.1
C–Ru–Bi	85.5(3) – 93.7(3), 112.2(3), 122.6(4) – 147.3(3)	87.01(9) – 97.10(10), 112.76(10), 124.33(9) – 147.78(9)	86.4(2) – 97.54(19), 112.6(2), 123.44(19) – 147.63(18)	86.0 – 94.2, 110.8, 123.4 – 148.6

7.2 Micro-X-ray Fluorescence Spectroscopy (μ -XFS) Analysis and Energy-Dispersive X-ray Spectroscopy (EDS) Analysis

Several measurements produced unreasonably large values for the % K. Removal of K from the calculations afforded excellent agreement with the expected atomic ratio of close to each compound. It is believed that accumulation of K at the crystal surface upon exposure to air is responsible for the anomalous results. This is observed commonly for these very air-sensitive compounds.

Table 7.25: μ -XFS analysis of $[\text{K}(\text{crypt-222})]_2(\mathbf{1})_{0.9}(\text{Ge}_2\text{As}_2)_{0.1} \cdot 0.9\text{tol}$ (K, Ge, As, Zn).

compound $[\text{K}(\text{crypt-222})]_2(\mathbf{1})_{0.9}(\text{Ge}_2\text{As}_2)_{0.1} \cdot 0.9\text{tol}$					
Element	Element wt %	Weight % err. (1 sigma)	Atom %	Element ratio observed	Element ratio calc
K-K	53.75	0.00	68.01	10.25	2.00
Ge-K	29.00	0.00	19.76	2.98	3.00
As-K	8.48	0.00	5.60	0.84	1.00
Zn-K	8.77	0.00	6.63	1.00	1.00
Total	100.00		100.00		

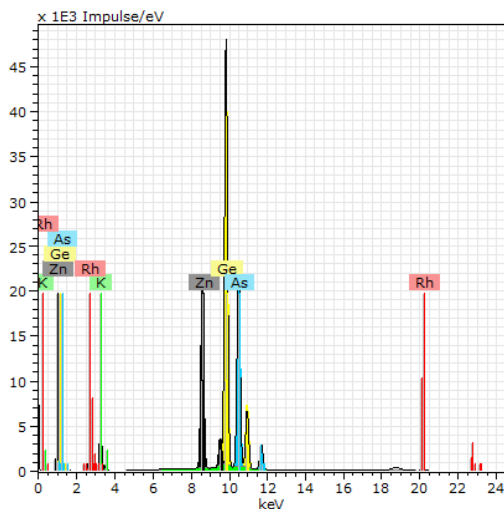


Figure 7.2: Micro X-ray fluorescence spectrum of $[\text{K}(\text{crypt-222})]_2(\mathbf{1})_{0.9}(\text{Ge}_2\text{As}_2)_{0.1} \cdot 0.9\text{tol}$ with the results of the deconvolution algorithm. Colors are used as follows: K (green), Zn (black), Ge (gold), As (light blue), background (green).

Table 7.26: μ -XFS analysis of [K(crypt-222)]₃3 (K, Ge, As, Zn).

compound [K(crypt-222)] ₃ 3					
Element	Element wt %	Weight % err. (1 sigma)	Atom %	Element ratio observed	Element ratio calc
K-K	37.54	0.00	52.72	10.48	3.00
Ge-K	37.60	0.00	28.43	5.69	5.00
As-K	18.97	0.00	13.82	2.75	3.00
Zn-K	5.03	0.00	5.03	1.00	1.00
Total	100.00		100.00		

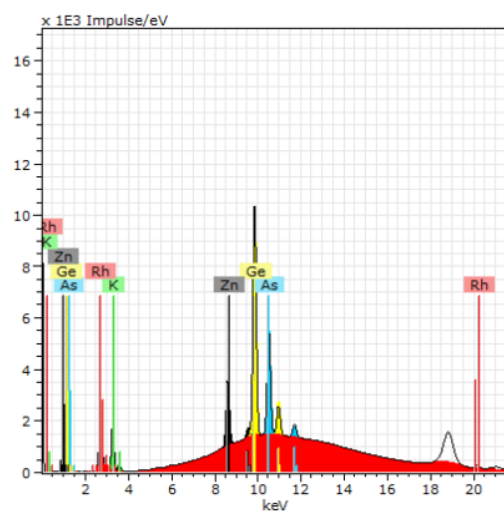


Figure 7.3: Micro X-ray fluorescence spectrum of [K(crypt-222)]₃3 with the results of the deconvolution algorithm. Colors are used as follows: K (green), Zn (black), Ge (gold), As (light blue), background (red).

Table 7.27: μ -XFS analysis of [K(crypt-222)]₉(**5a**)(**5b**)_{0.5}·en (K, Ge, As, Zn).

compound [K(crypt-222)] ₉ (5a)(5b) _{0.5} ·tol					
Element	Element wt %	Weight % err. (1 sigma)	Atom %	Element ratio observed	Element ratio calc
K-K	26.97	0.00	40.53	13.14	6.00
Ge-K	48.75	0.00	39.44	12.79	12.00
As-K	15.72	0.00	12.33	4.00	4.00
Zn-K	8.56	0.00	7.69	2.49	3.00
Total	100.00		100.00		

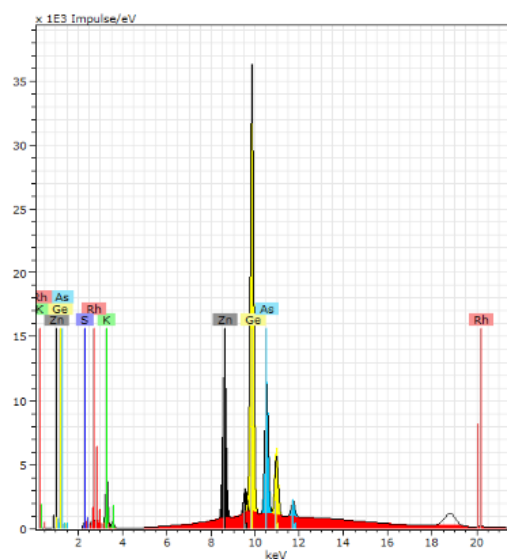


Figure 7.4: Micro X-ray fluorescence spectrum of [K(crypt-222)]₉(**5a**)(**5b**)_{0.5}·en with the results of the deconvolution algorithm. Colors are used as follows: K (green), Zn (black), Ge (gold), As (light blue), background (red).

Table 7.28: μ -XFS analysis of [K(crypt-222)]₂6 (K, Ge, As, Zn).

compound [K(crypt-222)] ₂ 6					
Element	Element wt %	Weight % err. (1 sigma)	Atom %	Element ratio observed	Element ratio calc
K-K	29.47	0.00	43.47	3.69	2.00
Ge-K	44.52	0.00	35.36	3.00	3.00
As-K	15.88	0.00	12.23	1.03	1.00
Zn-K	10.13	0.00	8.94	0.76	1.00
Total	100.00		100.00		

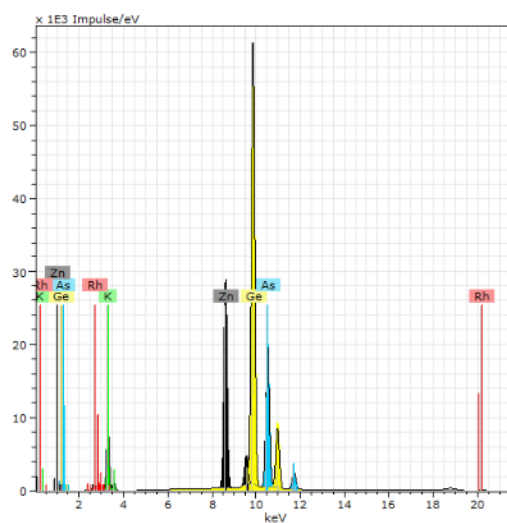


Figure 7.5: Micro X-ray fluorescence spectrum of [K(crypt-222)]₂6 with the results of the deconvolution algorithm. Colors are used as follows: K (green), Zn (black), Ge (gold), As (light blue), background (yellow).

Table 7.29: μ -XFS analysis of [K(crypt-222)]₂7·2en (K, Ge, As, Ni).

compound [K(crypt-222)] ₂ 7·2en					
Element	Element wt %	Weight % err. (1 sigma)	Atom %	Element ratio observed	Element ratio calc
K-K	25.34	0.00	37.87	6.02	2.00
Ge-K	47.65	0.00	38.34	6.09	6.00
As-K	14.37	0.00	11.20	1.78	2.00
Ni-K	12.64	0.00	12.59	2.00	2.00
Total	100.00		100.00		

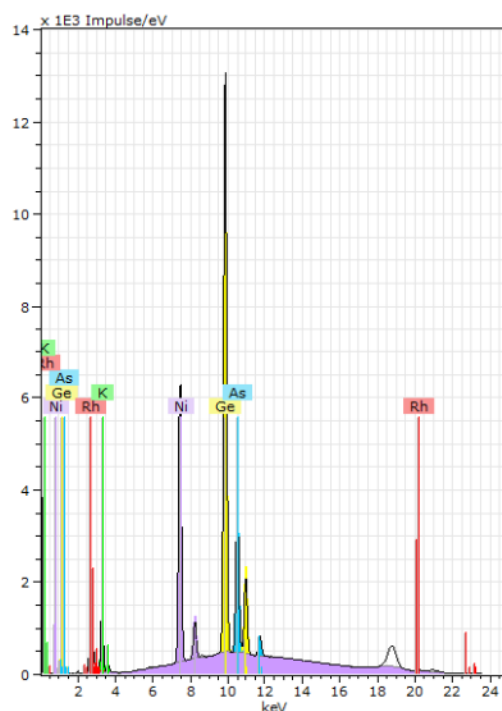


Figure 7.6: Micro X-ray fluorescence spectrum of [K(crypt-222)]₂7·2en with the results of the deconvolution algorithm. Colors are used as follows: K (green), Ni (lavender), Ge (gold), As (light blue), background (lavender).

Table 7.30: μ -XFS analysis of $[\text{K}(\text{crypt-222})]_q\mathbf{8}\cdot\text{solv}$ (K, Ge, As, Mn).

compound $[\text{K}(\text{crypt-222})]_q\mathbf{8}\cdot\text{solv}$					
Element	Element wt %	Weight % err. (1 sigma)	Atom %	Element ratio observed	Element ratio calc
K-K	16.19	0.00	26.06	6.77	
Ge-K	55.91	0.00	48.46	12.59	
As-K	21.17	0.00	17.78	4.62	
Mn-K	6.73	0.00	7.70	2.00	
Total	100.00		100.00		

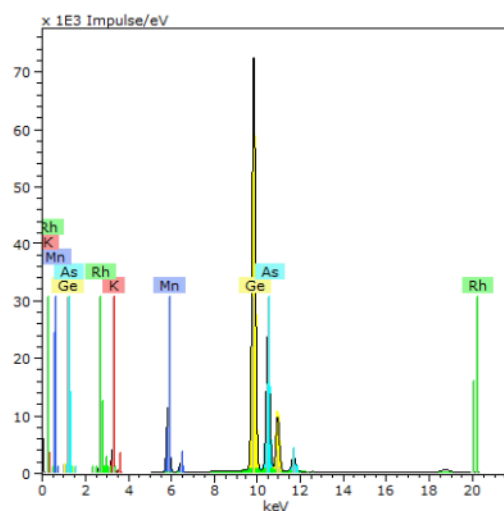


Figure 7.7: Micro X-ray fluorescence spectrum of $[\text{K}(\text{crypt-222})]_q\mathbf{8}\cdot\text{solv}$ with the results of the deconvolution algorithm. Colors are used as follows: K (red), Mn (blue), Ge (gold), As (light blue), background (green).

Table 7.31: μ -XFS analysis of [K(crypt-222)]₂9·solv (K, Ge, As, Ru).

compound [K(crypt-222)] ₂ 9·solv					
Element	Element wt %	Weight % err. (1 sigma)	Atom %	Element ratio observed	Element ratio calc
K-K	6.95	0.00	13.39	1.76	2.00
Ge-K	32.37	0.00	45.55	6.00	6.00
As-K	43.87	0.00	16.92	2.23	2.00
Ru-K	16.81	0.00	24.14	3.18	4.00
Total	100.00		100.00		

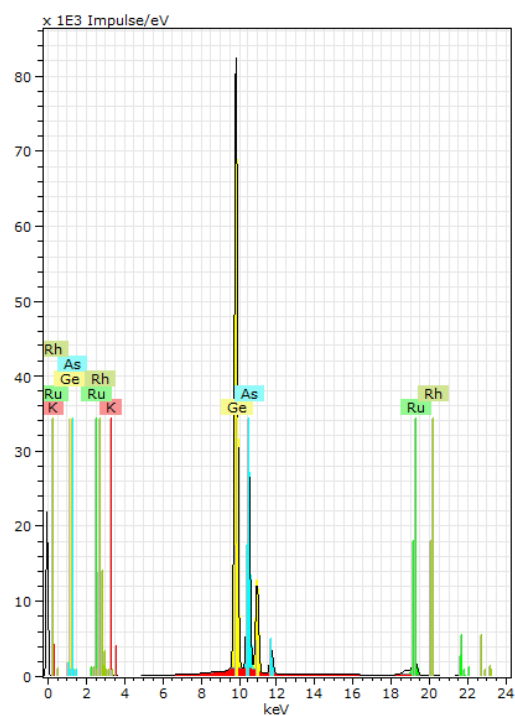
Figure 7.8: Micro X-ray fluorescence spectrum of [K(crypt-222)]₂9·solv with the results of the deconvolution algorithm. Colors are used as follows: K (red), Ru (green), Ge (gold), As (light blue), background (red).

Table 7.32: μ -XFS analysis of [K(crypt-222)]_{3.67}**10** (K, Ga, Bi).

compound [K(crypt-222)] _{3.67} 10					
Element	Element wt %	Weight % err. (1 sigma)	Atom %	Element ratio observed	Element ratio calc
K-K	11.22	0.00	27.41	10.66*	4.00
Ga-K	15.67	0.00	21.46	8.35	8.00
Bi-L	73.11	0.00	33.92	13.00	13.00
Total	100.00		100.00		

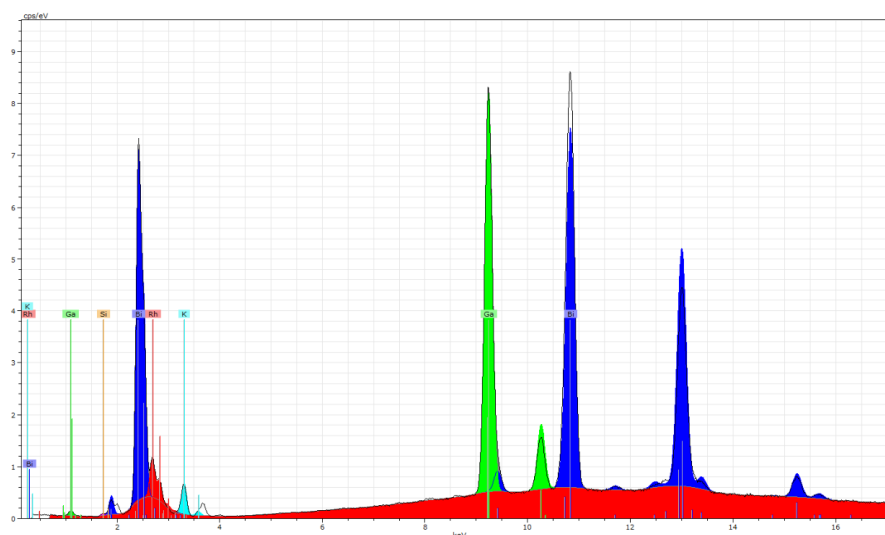


Figure 7.9: Micro X-ray fluorescence spectrum of [K(crypt-222)]_{3.67}**10** with the results of the deconvolution algorithm. Colors are used as follows: K (sky blue), Bi (blue), Ga (green), background (red).

Table 7.33: μ -XFS analysis of [K(crypt-222)]**411a** (K, Ga, Bi).

compound [K(crypt-222)] 411a					
Element	Element wt %	Weight % err. (1 sigma)	Atom %	Element ratio observed	Element ratio calc
K-K	4.22	0.00	17.80	3.94	4.00
Ga-K	4.18	0.00	9.88	2.19	2.00
Bi-L	91.61	0.00	72.32	16.00	16.00
Total	100.00		100.00		

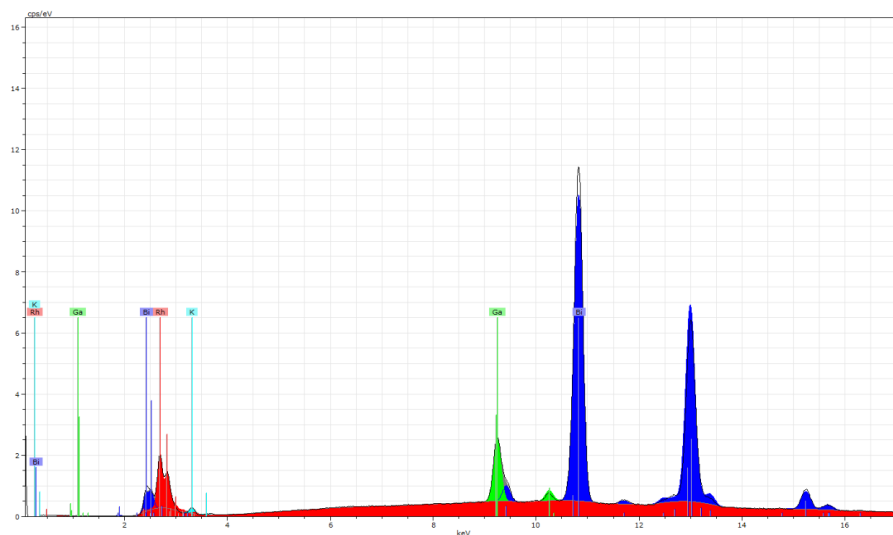
Figure 7.10: Micro X-ray fluorescence spectrum of [K(crypt-222)]**411a** with the results of the deconvolution algorithm. Colors are used as follows: K (sky blue), Bi (blue), Ga (green), background (red).

Table 7.34: μ -XFS analysis of [K(crypt-222)]₄**11b**·4py (K, Ga, Bi).

compound [K(crypt-222)] ₄ 11b ·4py					
Element	Element wt %	Weight % err. (1 sigma)	Atom %	Element ratio observed	Element ratio calc
K-K	6.67	0.00	26.24	6.33*	4.00
Ga-K	3.21	0.00	7.12	1.71	2.00
Bi-L	90.11	0.00	66.55	16.00	16.00
Total	100.00		100.00		

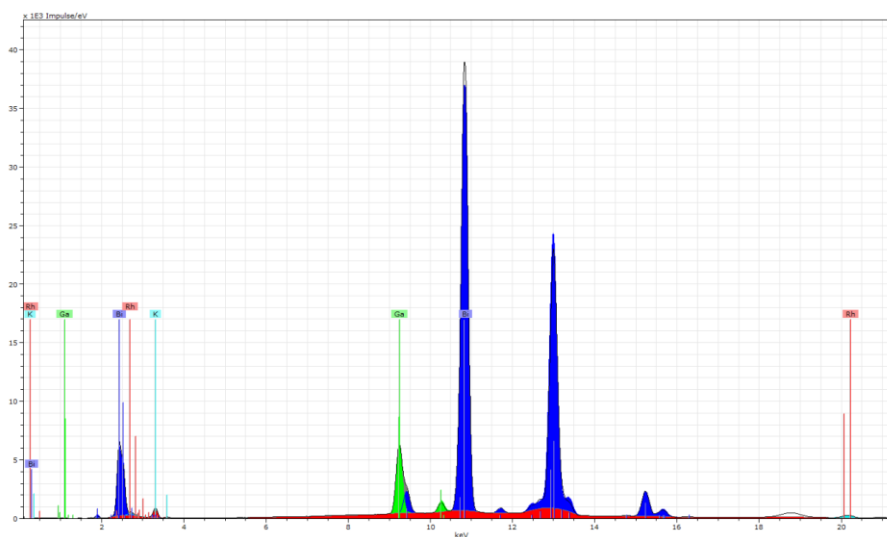


Figure 7.11: Micro X-ray fluorescence spectrum of [K(crypt-222)]₄**11b**·4py with the results of the deconvolution algorithm. Colors are used as follows: K (sky blue), Bi (blue), Ga (green), background (red).

Table 7.35: μ -XFS analysis of [K(crypt-222)]**412a**·4.63THF·2en (K, Ru, Bi).

compound [K(crypt-222)] 412a ·4.63THF·2en					
Element	Element wt %	Weight % err. (1 sigma)	Atom %	Element ratio observed	Element ratio calc
K-K	3.53	0.00	15.05	3.91	4.00
Ru-K	9.54	0.00	15.71	4.08	4.00
Bi-L	86.92	0.00	69.24	18.00	18.00
Total	100.00		100.00		

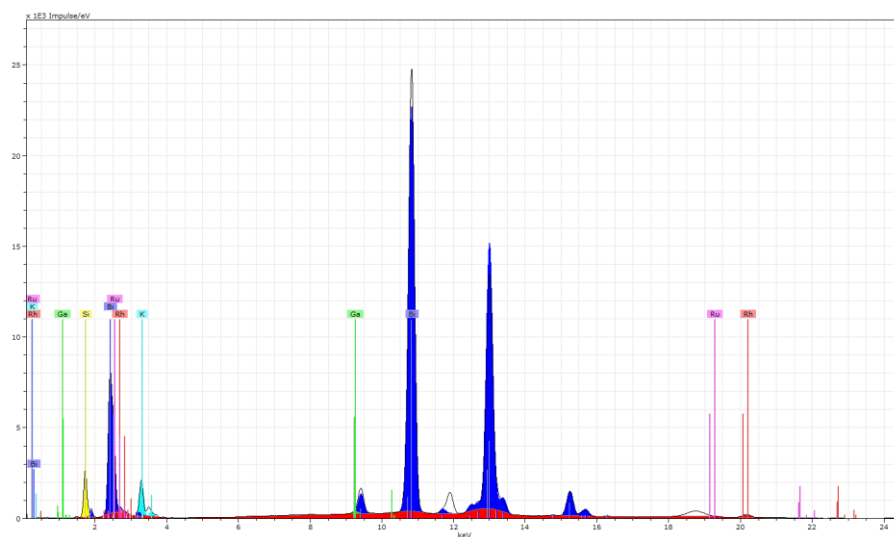
Figure 7.12: Micro X-ray fluorescence spectrum of [K(crypt-222)]**412a**·4.63THF·2en with the results of the deconvolution algorithm. Colors are used as follows: K (sky blue), Ru (purple), Bi (blue), background (red).

Table 7.36: μ -XFS analysis of compound [K(crypt-222)]**213a** (K, Ru, Bi).

compound [K(crypt-222)] 213a					
Element	Element wt %	Weight % err. (1 sigma)	Atom %	Element ratio observed	Element ratio calc
K-K	12.42	0.00	36.74	2.56	2.00
Ru-K	25.05	0.00	28.66	2.00	2.00
Bi-L	62.53	0.00	34.60	2.41	2.00
Total	100.00		100.00		

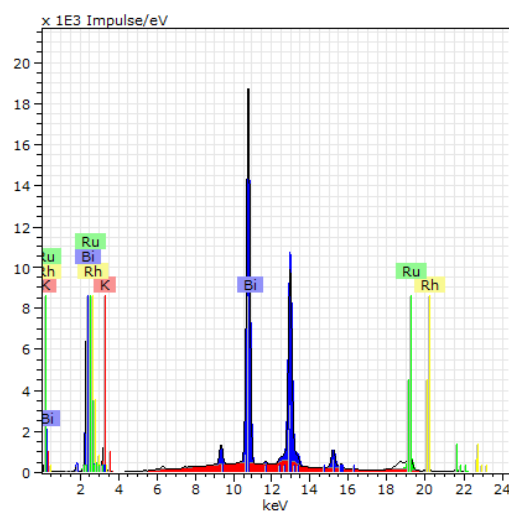


Figure 7.13: Micro X-ray fluorescence spectrum of [K(crypt-222)]**213a** with the results of the deconvolution algorithm. Colors are used as follows: K (red), Ru (green), Bi (blue), background (red).

Table 7.37: μ -XFS analysis of compound [K(crypt-222)]₂**13b**·2tol (K, Ru, Bi).

compound [K(crypt-222)] ₂ 13b ·2tol					
Element	Element wt %	Weight % err. (1 sigma)	Atom %	Element ratio observed	Element ratio calc
K-K	17.06	0.00	46.88	4.02	2.00
Ru-K	22.66	0.00	23.35	2.00	2.00
Bi-L	59.74	0.00	29.77	2.55	2.00
Total	100.00		100.00		

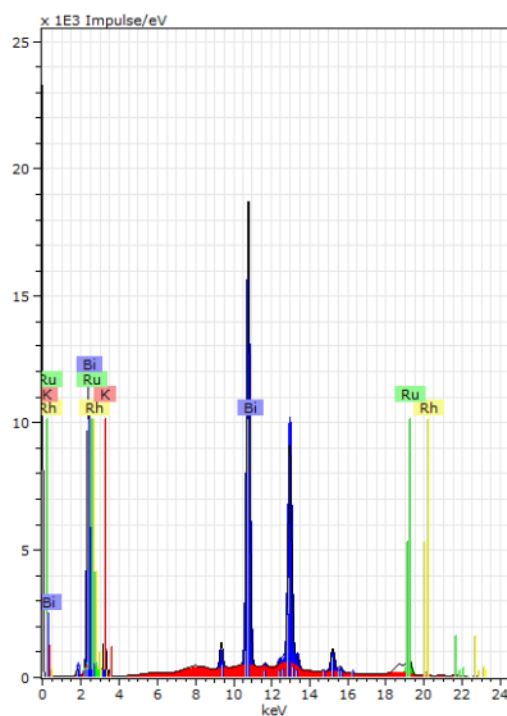
Figure 7.14: Micro X-ray fluorescence spectrum of [K(crypt-222)]₂**13b**·2tol with the results of the deconvolution algorithm. Colors are used as follows: K (red), Ru (green), Bi (blue), background (red).

Table 7.38: μ -XFS analysis of compound [K(crypt-222)]₂**13c**·2tol (K, Ru, Bi).

compound [K(crypt-222)] ₂ 13c ·2tol					
Element	Element wt %	Weight % err. (1 sigma)	Atom %	Element ratio observed	Element ratio calc
K-K	18.60	0.00	48.60	4.32	2.00
Ru-K	22.21	0.00	22.46	2.00	2.00
Bi-L	59.19	0.00	28.94	2.57	2.00
Total	100.00		100.00		

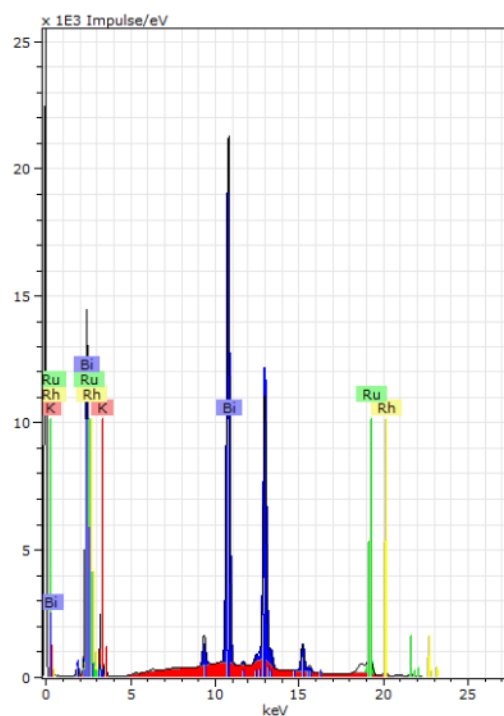
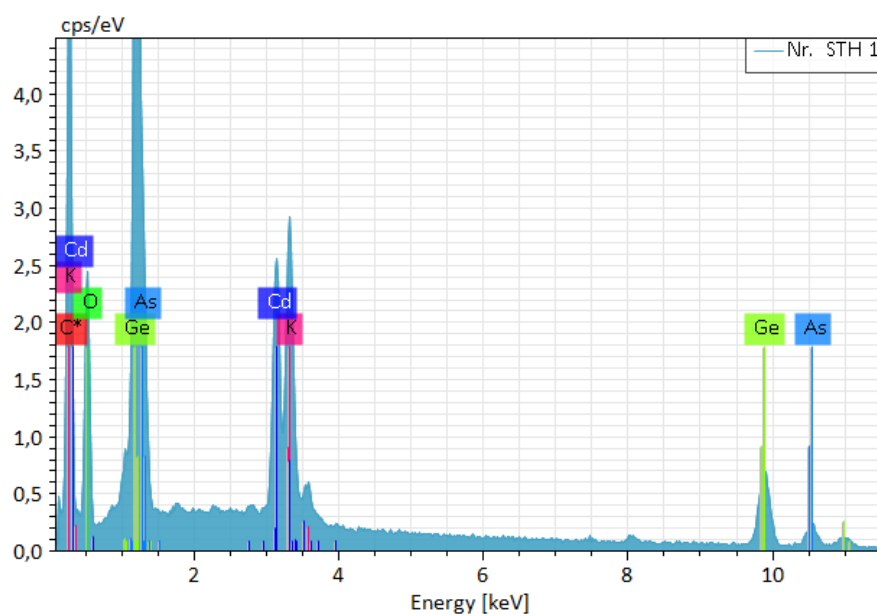


Figure 7.15: Micro X-ray fluorescence spectrum of [K(crypt-222)]₂**13c**·2tol with the results of the deconvolution algorithm. Colors are used as follows: K (red), Ru (green), Bi (blue), background (red).

Table 7.39: EDS analysis of [K(crypt-222)]₃4·tol (K, Ge, As, Cd).

compound [K(crypt-222)] ₃ 4·tol					
Element	Element wt %	Weight % err. (1 sigma)	Atom %	Element ratio observed	Element ratio calc
K-K	10.03	0.00	19.13	1.12	1.00
Ge-K	42.85	0.00	43.98	2.59	3.00
As-K	17.05	0.00	16.96	1.00	1.00
Cd-K	30.07	0.00	19.93	1.17	1.00
Total	100.00		100.00		

Figure 7.16: EDS analysis of [K(crypt-222)]₃4·tol (K, Ge, As, Cd).

7.3 Electrospray Ionization Mass Spectrometry (ESI-MS) Investigations

7.3.1 Mass Spectra of Zintl Solids and Crypt-222 in Solution

The sample of the extraction solution was measured from a fresh en solution (2 mL) of “K₂GeAs” and crypt-222 stirred for 5 mins, filtered with a 0.45 µm PTFE syringe filter and diluted with toluene (2 mL). The sample of the extraction solution was measured from a fresh en solution (2 mL) of “K₅Ga₂Bi₄” and crypt-222 stirred for 5 mins, filtered with a 0.45 µm PTFE syringe filter and diluted with DMF (2 mL).

“K₂GeAs” and crypt-222 in en/tol

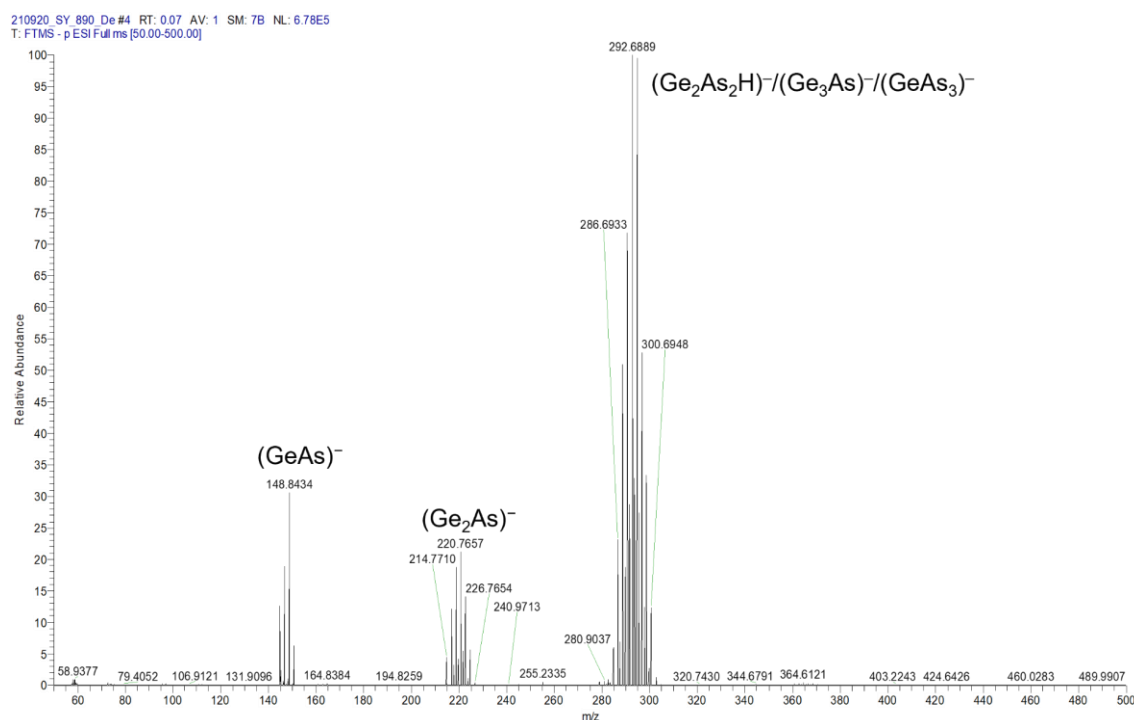


Figure 7.17: Overview of ESI(–) mass spectrum recorded immediately upon injection of a fresh reaction solution of “K₂GeAs” in en/tol.

Table 7.40: Species identified in the overview ESI(–) mass spectrum, recorded immediately upon injection of a fresh solution of “K₂GeAs” in en/tol. The relative strength of the observed signals is given in two categories, strong (s), and medium (m), respectively.

Species	m/z (rel. signal strength)
(GeAs) [–]	148.8433(m)
(Ge ₂ As) [–]	220.7657(s)
(Ge ₄ H) [–] /(Ge ₃ As) [–] /(Ge ₃ AsH ₂) [–] /(Ge ₂ As ₂ H) [–] /(GeAs ₃) [–]	290.6901(s)

“K₅Ga₂Bi₄” and crypt-222 in en/DMF

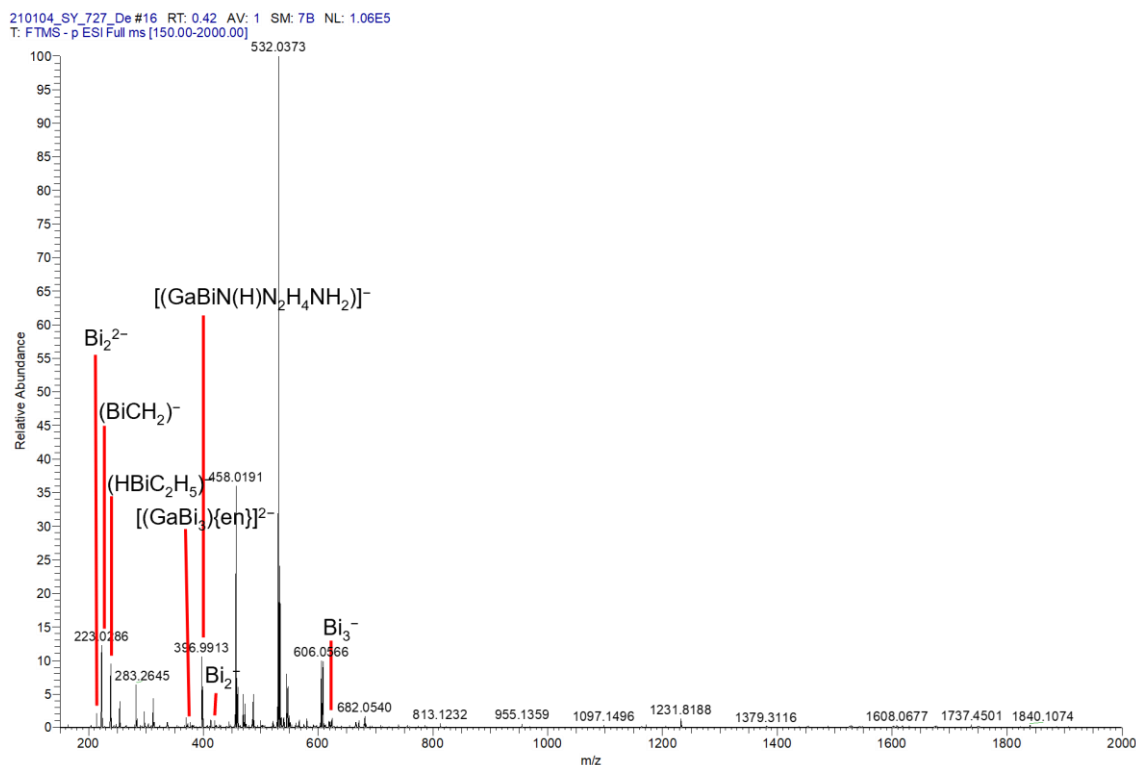


Figure 7.18: Overview of ESI(−) mass spectrum, recorded immediately upon injection of a fresh en solution of “K₅Ga₂Bi₄” and crypt-222 and diluted by DMF, after 5 min reaction time.

Table 7.41: Species identified in the overview ESI(−), recorded immediately upon injection of a fresh en solution of “K₅Ga₂Bi₄” and crypt-222 and diluted by DMF, after 5 min reaction time. The relative strength of the observed signals is given in two categories, medium (m), and weak (w), respectively.

Species	m/z (rel. signal strength)	Assumptive structure (with organic fragments)
Bi ₂ ²⁻	208.9810 (w)	
(BiCH ₂) ⁻	223.0285 (m)	
(HBiC ₂ H ₅) ⁻	239.0598 (w)	
[(GaBi ₃ {en})] ²⁻	378.9840 (w)	
[(GaBiN(H)C ₂ H ₄ NH ₂){en}] ⁻	396.9917 (m)	
Bi ₂ ⁻	417.9605 (w)	
Bi ₃ ⁻	626.9481 (w)	

Table 7.42: Species identified in the overview ESI(–) mass spectrum, recorded immediately upon injection of a fresh solution of re-dissolved single-crystals of compounds $[\text{K}(\text{crypt-222})]_2(\mathbf{1})_{0.9}(\text{Ge}_2\text{As}_2)_{0.1} \cdot 0.9\text{tol}$, $[\text{K}(\text{crypt-222})]_3\mathbf{3}$, and $[\text{K}(\text{crypt-222})]_9(\mathbf{5a})(\mathbf{5b})_{0.5} \cdot \text{en}$ in DMF. The relative strengths of the observed signals are given in only medium (m) categories.

Species	m/z (rel. signal strength)
$(\text{Ge}_2\text{As}_2\text{H})^-$	296.6947(m)
$(\text{Ge}_5\text{H})^-$	364.6106(m)
$(\text{Ge}_3\text{As}_3)^-$	442.5307(m)
$\text{Ge}_7^-/(\text{Ge}_6\text{As})^-$	510.4554(m)
$(\text{KZn}_3\text{Ge}_9\text{As}_3)^{2-}$	556.4043(m)
$(\text{Ge}_5\text{As}_3\text{H})^-$	586.3754(m)
$(\text{KGe}_6\text{As}_2)^-$	624.3391(m)
$(\text{Ge}_6\text{As}_3)^-$	660.2968(m)
$(\text{KGe}_7\text{As}_2)^-$	696.2624(m)
$(\text{Ge}_9\text{AsH}_2)^-$	730.2210(m)
$(\text{KZn}_2\text{Ge}_6\text{As}_2)^-$	754.1943(m)
$(\text{ZnGe}_5\text{As}_5)^-$	804.1432(m)
$(\text{Ge}_9\text{As}_3)^-$	943.9902(m)
$(\text{ZnGe}_9\text{As}_3\text{O}_2)^-$	973.9812(m)
$(\text{ZnGe}_{10}\text{As}_3)^-$	1015.9125(m)
$(\text{Zn}_3\text{Ge}_9\text{As}_3)^-/[\text{K}(\text{crypt-222})\text{Ge}_7\text{As}_2]^-$	1072.5203(m)
$(\text{K}_2\text{Zn}_3\text{Ge}_9\text{As}_3)^-$	1149.7717(m)
$[\text{K}_2(\text{crypt-222})\text{Zn}_2\text{Ge}_7\text{As}_2]^-$	1470.0962(m)
$[\text{K}(\text{crypt-222})\text{Zn}_3\text{Ge}_8\text{As}_4]^-$	1492.0685(m)
$[\text{K}_2(\text{crypt-222})\text{Zn}_3\text{Ge}_9\text{As}_3]^-$	1528.0267(m)
$[\text{K}_2(\text{crypt-222})_2\text{Zn}_3\text{Ge}_7\text{As}_5]^-$	1844.3530(m)
$[\text{K}_2(\text{crypt-222})_2\text{Zn}_3\text{Ge}_9\text{As}_3]^-$	1906.2835(m)

[K(crypt-222)]₂·tol

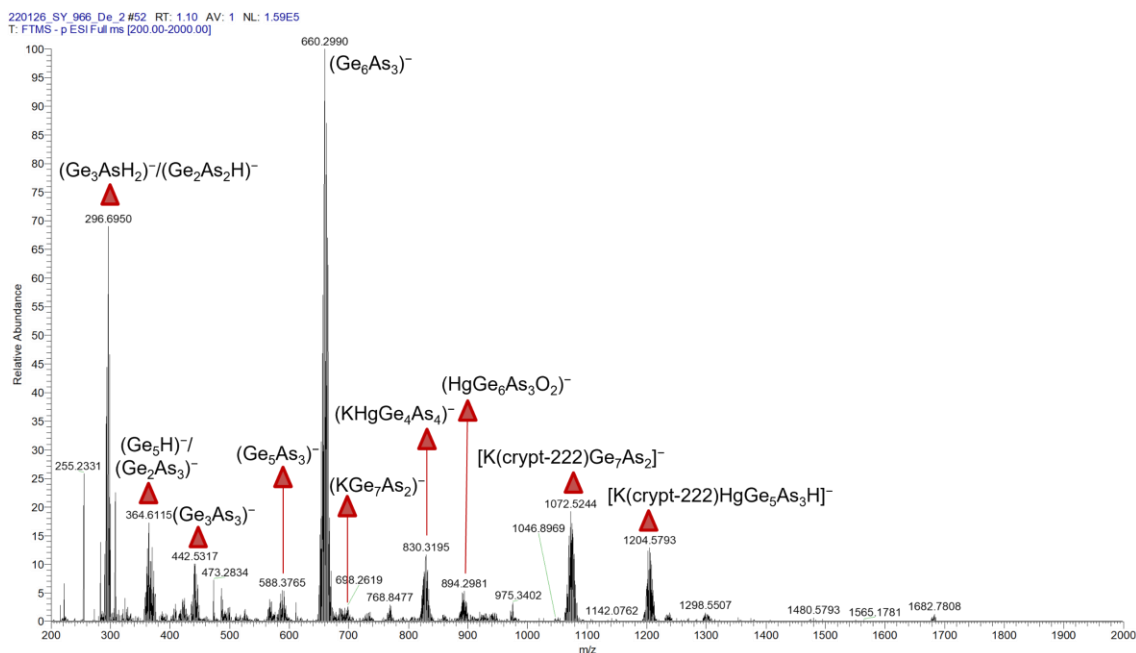


Figure 7.20: Overview of ESI(-) mass spectrum of re-dissolved single-crystals of compound [K(crypt-222)]₂·tol recorded immediately upon injection of a fresh reaction solution of in DMF.

Table 7.43: Species identified in the overview ESI(-) mass spectrum, recorded immediately upon injection of a fresh solution of re-dissolved single crystals of compound [K(crypt-222)]₂·tol in DMF. The relative strength of the observed signals is given in two categories, strong (s), and medium (m), respectively.

Species	m/z (rel. signal strength)
(Ge ₃ As ₂ H ₂) ⁻ /(Ge ₂ As ₂ H) ⁻	296.6950(s)
(Ge ₅ H) ⁻ /(Ge ₂ As ₃) ⁻	364.6114(s)
(Ge ₃ As ₃) ⁻	442.5317(s)
(Ge ₅ As ₃) ⁻	588.3765(m)
(Ge ₆ As ₃) ⁻	660.2990(s)
(KGe ₇ As ₂) ⁻	698.2619(s)
(KHgGe ₄ As ₄) ⁻	830.3195(s)
(HgGe ₆ As ₃ O ₂) ⁻	894.2181(m)
[K(crypt-222)Ge ₇ As ₂] ⁻	1072.5244(s)
[K(crypt-222)HgGe ₅ As ₃ H] ⁻	1204.5793(s)

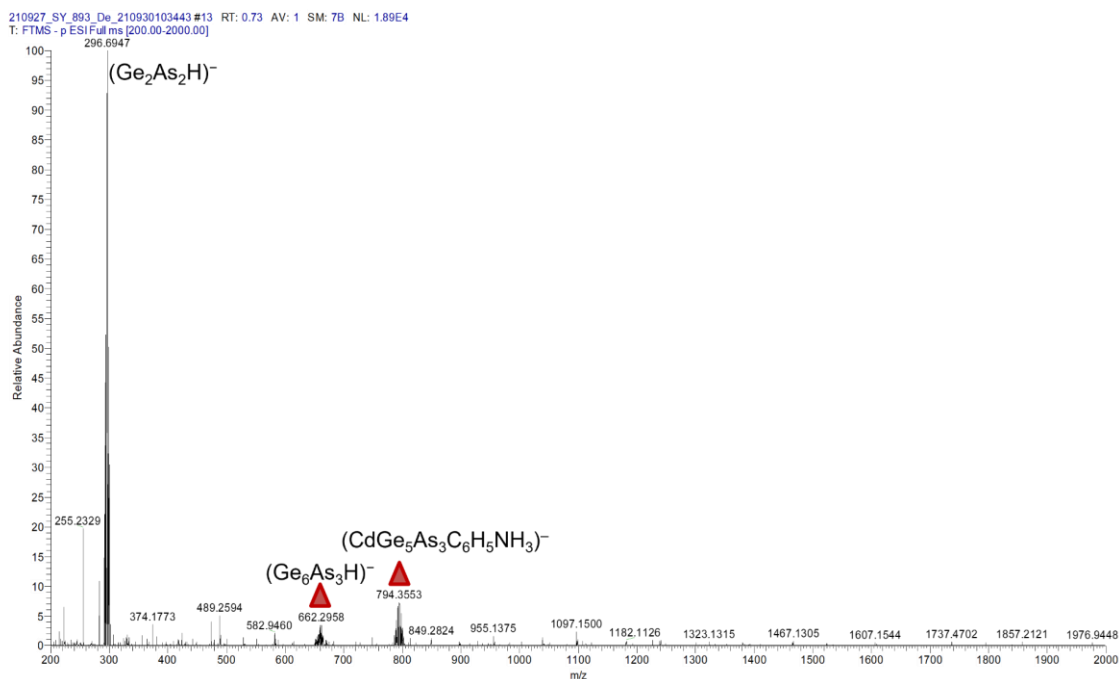
[K(crypt-222)]₃4·tol

Figure 7.21: Overview of ESI(–) mass spectrum of re-dissolved single-crystals of compound [K(crypt-222)]₃4·tol recorded immediately upon injection of a fresh reaction solution of in DMF.

Table 7.44: Species identified in the overview ESI(–) mass spectrum, recorded immediately upon injection of a fresh solution of compound [K(crypt-222)]₃4·tol in DMF. The relative strength of the observed signals is given in three categories, strong (s), medium (m), and weak (w), respectively.

Species	m/z (rel. signal strength)
(Ge ₂ As ₂ H) [–]	296.6947(s)
(Ge ₆ As ₃) [–]	660.2979(w)
(CdGe ₅ As ₃ C ₆ H ₅ NH ₃) [–]	794.3553(m)

[K(crypt-222)]₂·2en

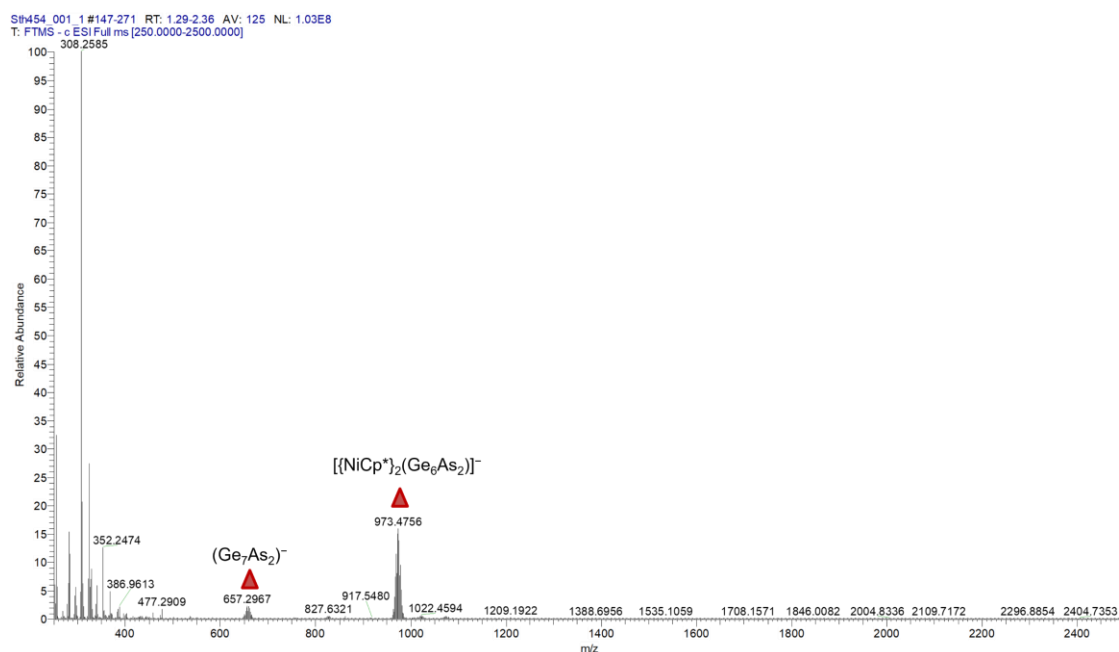


Figure 7.22: Overview of ESI(–) mass spectrum of re-dissolved single-crystals of compound [K(crypt-222)]₂·2en recorded immediately upon injection of a fresh reaction solution of in DMF.

Table 7.45: Species identified in the overview ESI(–) mass spectrum, recorded immediately upon injection of a fresh solution of compound [K(crypt-222)]₂·2en in DMF. The relative strength of the observed signals is given in one category, strong (s).

Species	m/z (rel. signal strength)
(Ge ₇ As ₂) [–]	657.2967(s)
[{Cp*Ni} ₂ (Ge ₆ As ₂)] [–]	973.4756(s)

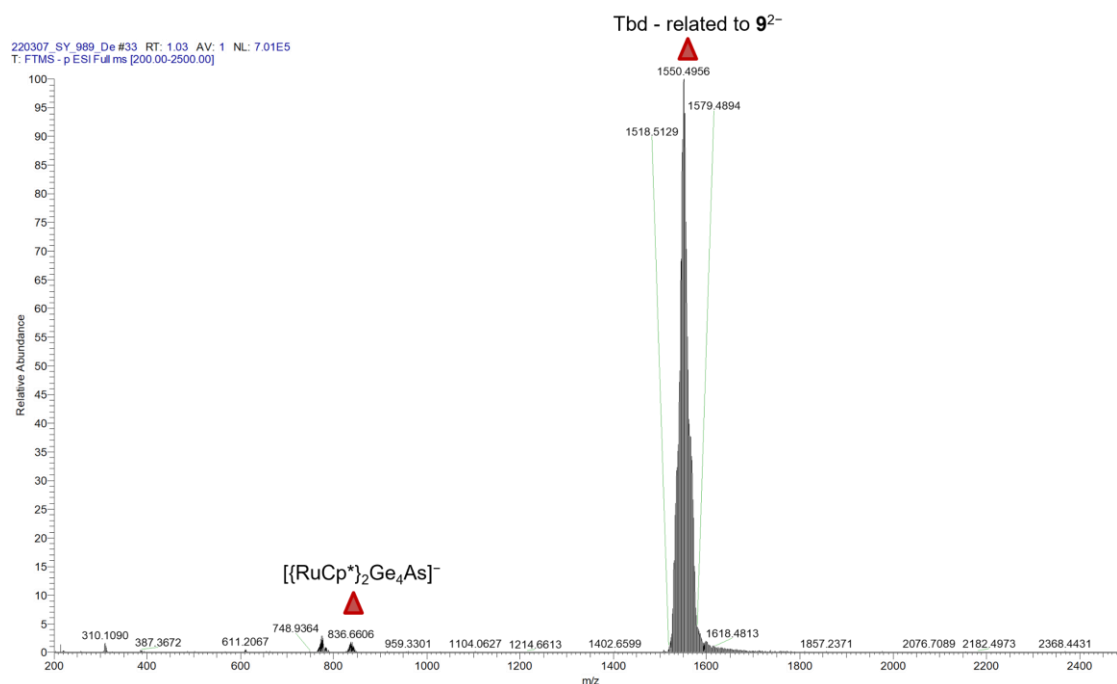
[K(crypt-222)]₂9·solv

Figure 7.23: Overview of ESI(–) mass spectrum of re-dissolved single-crystals of compound [K(crypt-222)]₂9·solv recorded immediately upon injection of a fresh reaction solution of in DMF.

Table 7.46: Species identified in the overview ESI(–) mass spectrum, recorded immediately upon injection of a fresh solution of compound [K(crypt-222)]₂9·solv in DMF. The relative strength of the observed signals is given in two categories, strong (s), and medium (m), respectively.

Species	m/z (rel. signal strength)
$[(RuCp^*)_2Ge_4As]^-$	836.6606(m)
Tbd – related to 9^{2-}	1550.4956(s)

[K(crypt-222)]_{3.67}10

200304_SY_575_De_GaBi-3 #83 RT: 2.50 AV: 1 SM: 7B NL: 7.49E4
T: FTMS -p ESI Full ms [400.00-4000.00]

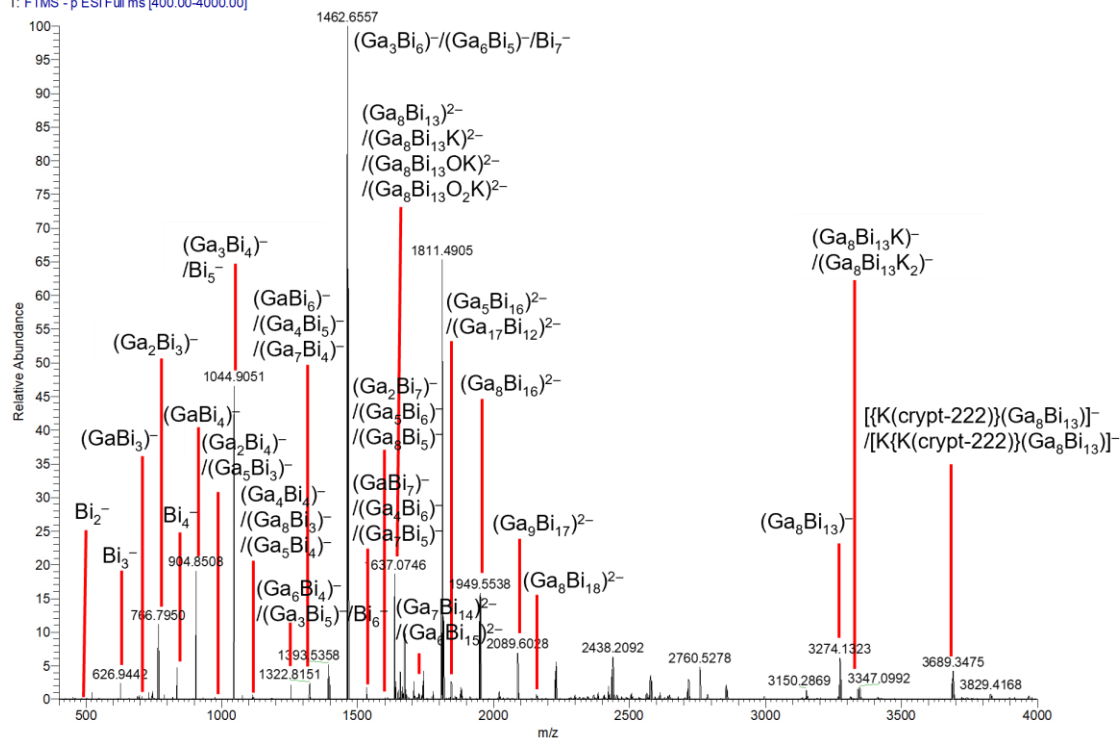


Figure 7.24: Overview of ESI(-) mass spectrum of re-dissolved single-crystals of compound $[\text{K}(\text{crypt-222})]_{3.67}\mathbf{10}$ recorded immediately upon injection of a fresh reaction solution of in DMF.

Table 7.47: Species identified in the overview ESI(–), recorded immediately upon injection of a fresh solution of single-crystals of [K(crypt-222)]_{3.67}**10** in DMF. The relative strength of the observed signals is given in two categories, strong (s), and medium (m), respectively.

Species	m/z (rel. signal strength)
Bi ₂ [–]	417.9574 (m)
Bi ₃ [–]	626.9443 (m)
(GaBi ₃) [–]	695.8698 (m)
(Ga ₂ Bi ₃) [–]	766.7929 (s)
Bi ₄ [–]	835.9259 (m)
(GaBi ₄) [–]	904.8514 (s)
(Ga ₂ Bi ₄) [–] /(Ga ₅ Bi ₃) [–]	975.7733/975.5685 (m)
(Ga ₃ Bi ₄) [–] /Bi ₅ [–]	1044.6987/1044.9015 (s)
(Ga ₄ Bi ₄) [–]	1113.6243 (m)
(Ga ₈ Bi ₃) [–] /(Ga ₅ Bi ₄) [–]	1184.3426/1184.5469 (s)
(Ga ₆ Bi ₄) [–] /(Ga ₃ Bi ₅) [–] /Bi ₆ [–]	1253.4742/1253.6739/1253.8826 (m)
Bi ₆ [–]	1253.8879 (m)
(GaBi ₆) [–] /(Ga ₄ Bi ₅) [–] /(Ga ₇ Bi ₄) [–]	1324.4008/1322.6075/1322.8093 (m)
(Ga ₃ Bi ₆) [–] /(Ga ₆ Bi ₅) [–] /Bi ₇ [–]	1462.6555/1462.4522/1462.8624 (s)
(Ga ₃ Bi ₆) [–]	1462.6564 (s)
(GaBi ₇) [–] /(Ga ₄ Bi ₆) [–] /(Ga ₇ Bi ₅) [–]	1531.7915/1533.5868/1533.3821 (m)
(Ga ₂ Bi ₇) [–] /(Ga ₅ Bi ₆) [–] /(Ga ₈ Bi ₅) [–]	1602.7133/1602.5162/1602.3020 (m)
(Ga ₈ Bi ₁₃) ^{2–}	1637.0746 (s)
(Ga ₈ Bi ₁₃ K) ^{2–}	1656.5522 (m)
(Ga ₈ Bi ₁₃ OK) ^{2–} /(Ga ₈ Bi ₁₃ O ₂ K) ^{2–}	1664.5531/1672.5460 (m)
(Ga ₇ Bi ₁₄) ^{2–}	1707.1023 (s)
(Ga ₆ Bi ₁₅) ^{2–}	1776.1300 (s)
(Ga ₅ Bi ₁₆) ^{2–} /(Ga ₁₇ Bi ₁₂) ^{2–}	1846.1621/1845.6835 (s)
(Ga ₈ Bi ₁₆) ^{2–}	1950.5484 (m)
(Ga ₉ Bi ₁₇) ^{2–}	2089.5007 (m)
(Ga ₈ Bi ₁₈) ^{2–}	2159.5229 (m)
(Ga ₈ Bi ₁₃) [–]	3274.1466 (m)
(Ga ₈ Bi ₁₃ K) [–]	3313.1216 (m)
(Ga ₈ Bi ₁₃ K ₂) [–]	3352.0646 (m)
[{K(crypt-222)}(Ga ₈ Bi ₁₃)] [–]	3689.3687 (m)
[K{K(crypt-222)}(Ga ₈ Bi ₁₃)] [–]	3728.2786 (m)

[K(crypt-222)]₄11a

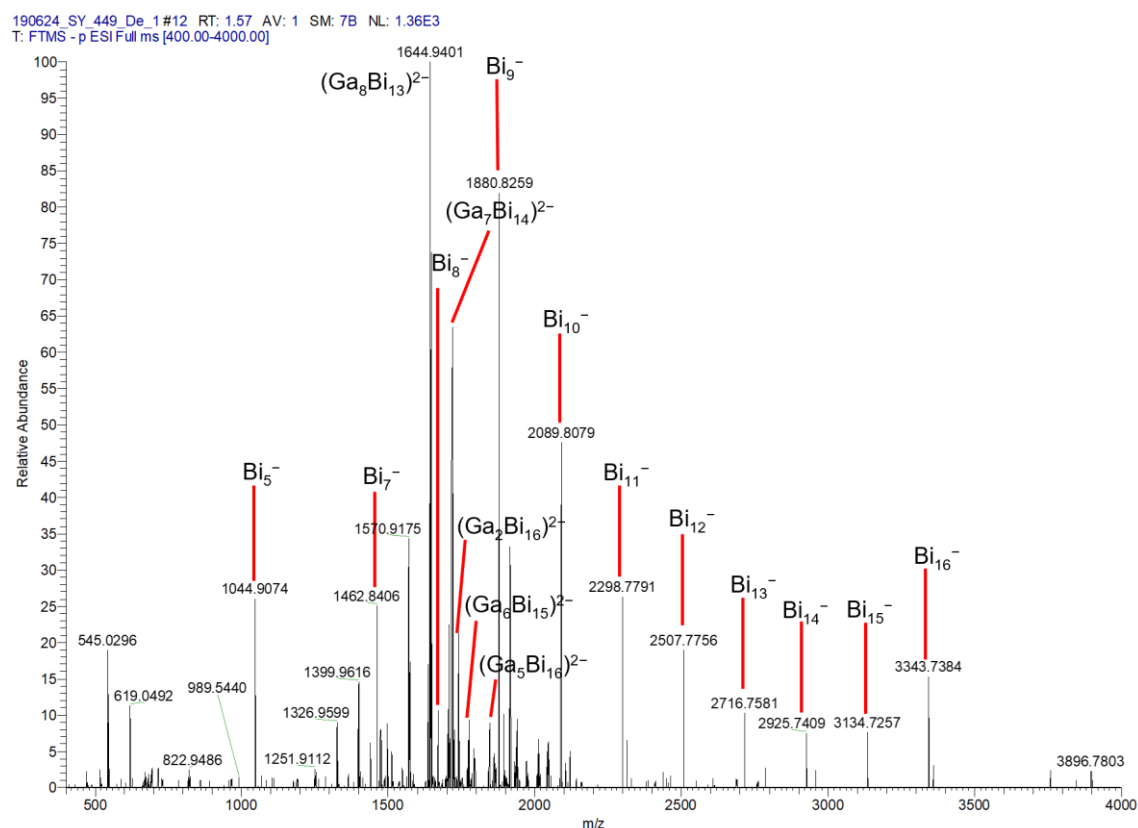


Figure 7.25: Overview of ESI(–) mass spectrum of re-dissolved single-crystals of compound [K(crypt-222)]₄11a recorded immediately upon injection of a fresh reaction solution of in DMF.

Table 7.48: Species identified in the overview ESI(–), recorded immediately upon injection of a fresh solution of single-crystals of [K(crypt-222)]₄11a in DMF. The relative strength of the observed signals is given in two categories, medium (m), and weak (w), respectively.

Species	m/z (rel. signal strength)
Bi ₅ [–]	1044.9070 (m)
Bi ₇ [–]	1462.8769 (m)
(Ga ₈ Bi ₁₃) ^{2–}	1637.0806 (m)
Bi ₈ [–]	1671.8520 (m)
(Ga ₇ Bi ₁₄) ^{2–}	1707.1105 (m)
(Ga ₂ Bi ₁₆) ^{2–}	1741.7760 (m)
(Ga ₆ Bi ₁₅) ^{2–}	1776.1418 (m)
(Ga ₅ Bi ₁₆) ^{2–}	1846.1398 (m)
Bi ₉ [–]	1880.8305 (m)
Bi ₁₀ [–]	2089.8076 (m)
Bi ₁₁ [–]	2298.7988 (m)
Bi ₁₂ [–]	2507.7756 (m)
Bi ₁₃ [–]	2716.7534 (w)
Bi ₁₄ [–]	2925.7328 (w)
Bi ₁₅ [–]	3134.7257 (m)
Bi ₁₆ [–]	3343.6976 (w)

[K(crypt-222)]₄12a

191105_SY_510_De#117 RT: 3.82 AV: 1 SM: 7B NL: 3.36E5
T: FTMS -p ESI Full ms [400.00-4000.00]

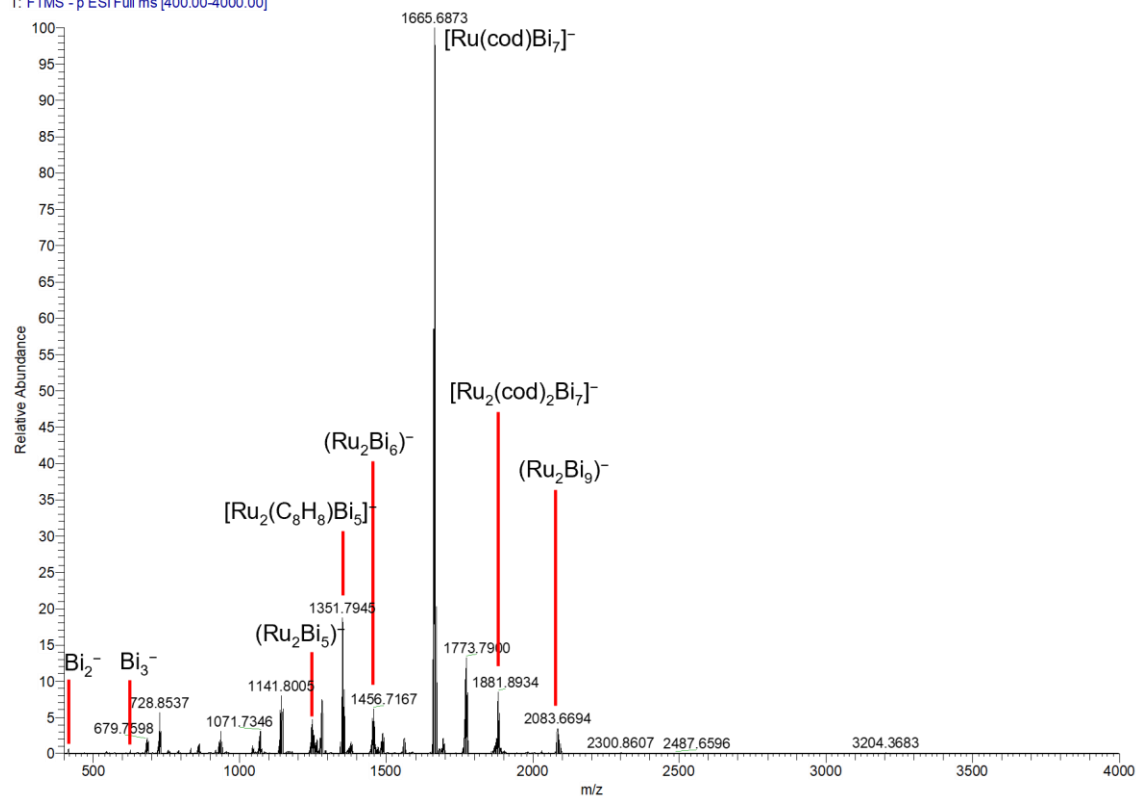


Figure 7.26: Overview of ESI(-) mass spectrum of re-dissolved single-crystals of compound [K(crypt-222)]₄12·solv recorded immediately upon injection of a fresh reaction solution of in DMF.

Table 7.49: Species identified in the overview ESI(-), recorded immediately upon injection of a fresh solution of single-crystals of [K(crypt-222)]₄12·solv in DMF. The relative strength of the observed signals is given in two categories, strong (s), and medium (m), respectively.

Species	m/z (rel. signal strength)
Bi ₂ ⁻	417.9643 (m)
Bi ₃ ⁻	626.9477 (m)
(Ru ₂ Bi ₅) ⁻	1247.7325 (s)
[Ru ₂ (C ₈ H ₈)Bi ₅] ⁻	1351.7945 (s)
(Ru ₂ Bi ₆) ⁻	1456.7167 (s)
[Ru(cod)Bi ₇] ⁻	1672.8724 (m)
[Ru ₂ (cod) ₂ Bi ₇] ⁻	1881.8572 (s)
(Ru ₂ Bi ₉) ⁻	2803.6694 (s)

[K(crypt-222)]₂13a

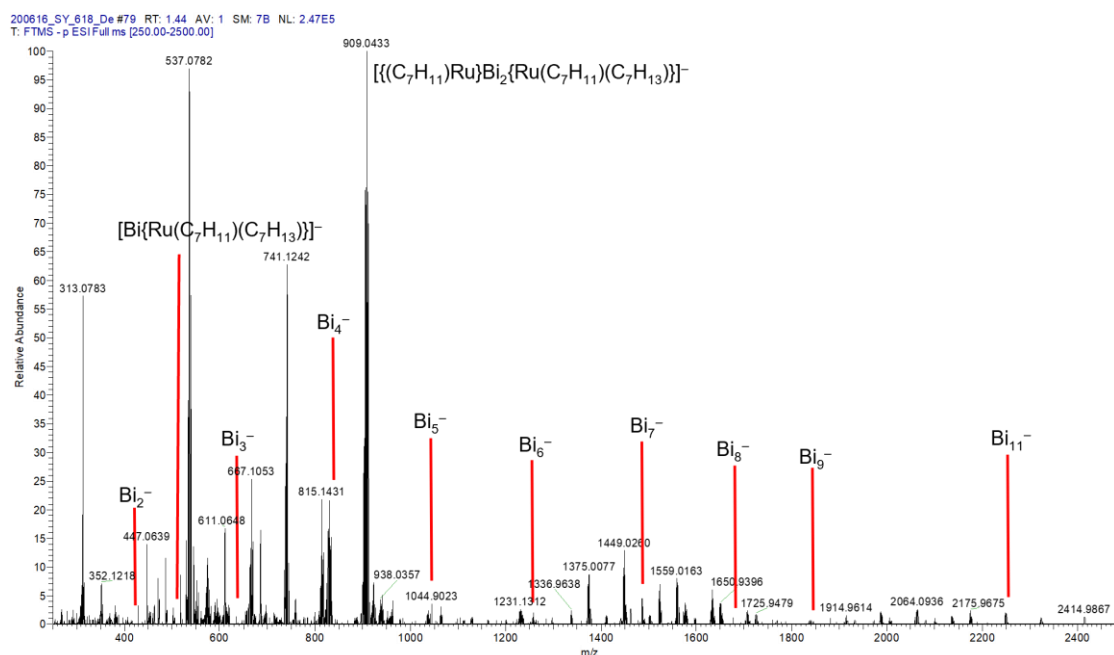


Figure 7.27: Overview of ESI(–) mass spectrum of re-dissolved single-crystals of compound [K(crypt-222)]₂13a recorded immediately upon injection of a fresh reaction solution of in DMF.

Table 7.50: Species identified in the overview ESI(–), recorded immediately upon injection of a fresh solution of single-crystals of [K(crypt-222)]₂13a in DMF. The relative strength of the observed signals is given in two categories, strong (s), and medium (m), respectively.

Species	m/z (rel. signal strength)
$[(C_7H_{11})Ru]Bi_2\{Ru(C_7H_{11})(C_7H_{13})\}^-$	909.0433 (s)
$[Bi\{Ru(C_7H_{11})(C_7H_{13})\}]^-$	503.0740 (m)
Bi_2^-	417.9627 (m)
Bi_3^-	626.9435 (m)
Bi_4^-	835.9241 (m)
Bi_5^-	1044.9060 (m)
Bi_6^-	1253.8863 (m)
Bi_7^-	1462.8694 (m)
Bi_8^-	1671.8598 (m)
Bi_9^-	1880.8304 (m)
Bi_{11}^-	2298.7982 (m)

7.3.3 Time-dependent Mass Spectra of the Reaction Solutions

The samples for time-dependent mass spectra were prepared in a glovebox. The corresponding reactants from Section 6.4 were combined in a vial and stirred, which were filtered with a 0.45 μm PTFE syringe filter at the time intervals specified below. Note that some samples were diluted with DMF or en prior to the measurement.

Time-dependent mass spectrum of the reaction solution during synthesis of compounds $[\text{K}(\text{crypt-222})]_2(\mathbf{1})_{0.9}(\text{Ge}_2\text{As}_2)_{0.1} \cdot 0.9\text{tol}$, $[\text{K}(\text{crypt-222})]_3\mathbf{3}$, and $[\text{K}(\text{crypt-222})]_9(\mathbf{5a})(\mathbf{5b})_{0.5} \cdot \text{en}$ (5 min)

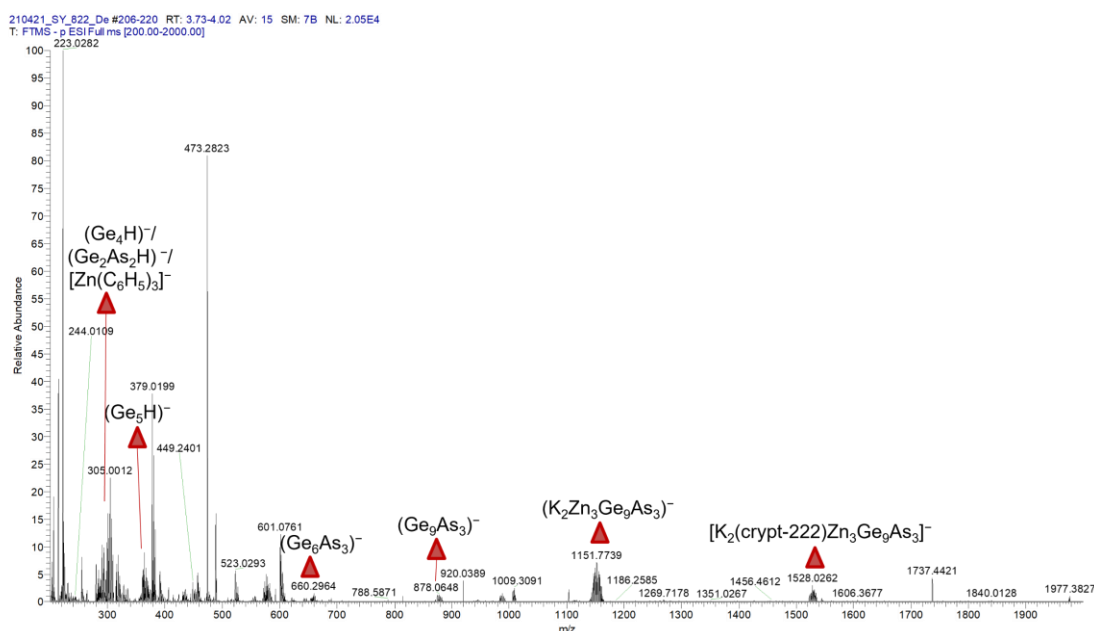


Figure 7.28: Overview of ESI(–) mass spectrum recorded immediately upon injection of a fresh reaction solution for the synthesis of compounds $[\text{K}(\text{crypt-222})]_2(\mathbf{1})_{0.9}(\text{Ge}_2\text{As}_2)_{0.1} \cdot 0.9\text{tol}$, $[\text{K}(\text{crypt-222})]_3\mathbf{3}$, and $[\text{K}(\text{crypt-222})]_9(\mathbf{5a})(\mathbf{5b})_{0.5} \cdot \text{en}$ in en, after 5 min reaction time.

Table 7.51: Species identified in the overview ESI(–) mass spectrum, recorded immediately upon injection of a fresh reaction solution for the synthesis of compounds $[\text{K}(\text{crypt-222})]_2(\mathbf{1})_{0.9}(\text{Ge}_2\text{As}_2)_{0.1} \cdot 0.9\text{tol}$, $[\text{K}(\text{crypt-222})]_3\mathbf{3}$, and $[\text{K}(\text{crypt-222})]_9(\mathbf{5a})(\mathbf{5b})_{0.5} \cdot \text{en}$ in en, after 5 min reaction time. The relative strength of the observed signals is given in two categories, medium (m), and weak (w), respectively.

Species	m/z (rel. signal strength)
$(\text{Ge}_4\text{H})^-/(\text{Ge}_2\text{As}_2\text{H})^-/[\text{Zn}(\text{C}_6\text{H}_5)_3]^-$	290.6896(m)
$(\text{Ge}_5\text{H})^-$	364.6106(w)
$(\text{Ge}_6\text{As}_3)^-$	660.2964(w)
$(\text{Ge}_9\text{As}_3)^-$	878.0648(w)
$(\text{K}_2\text{Zn}_3\text{Ge}_9\text{As}_3)^-$	1151.7739(m)
$[\text{K}_2(\text{crypt-222})\text{Zn}_3\text{Ge}_9\text{As}_3]^-$	1528.0262(w)

Time-dependent mass spectrum of the reaction solution during synthesis of compounds $[\text{K}(\text{crypt-222})]_2(\mathbf{1})_{0.9}(\text{Ge}_2\text{As}_2)_{0.1} \cdot 0.9\text{tol}$, $[\text{K}(\text{crypt-222})]_3\mathbf{3}$, and $[\text{K}(\text{crypt-222})]_9(\mathbf{5a})(\mathbf{5b})_{0.5} \cdot \text{en}$ (1 h)

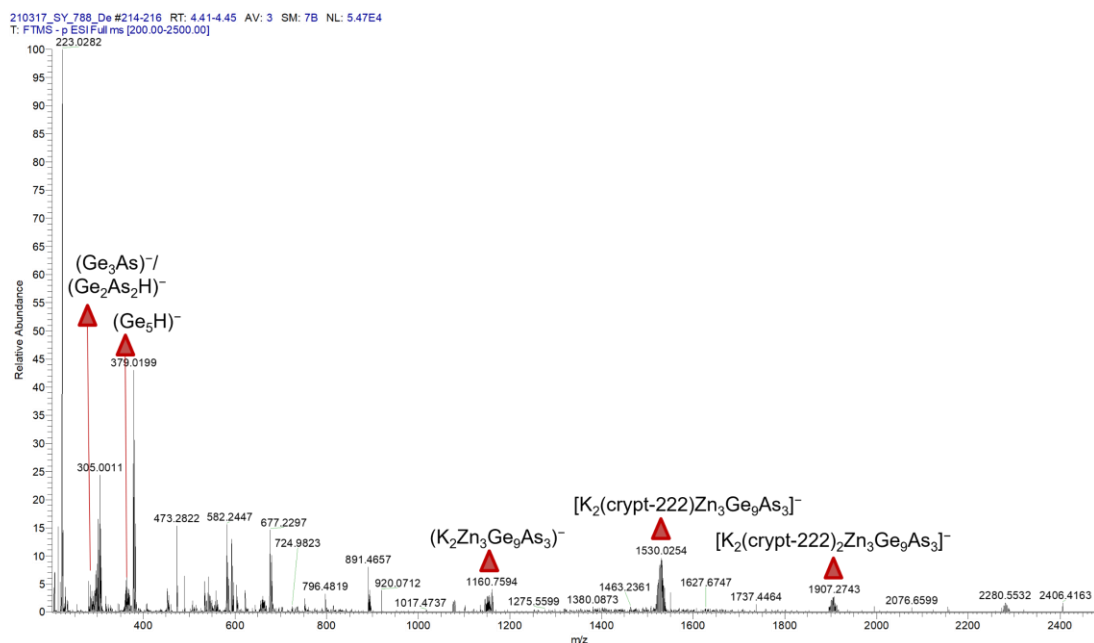


Figure 7.29: Overview of ESI(–) mass spectrum recorded immediately upon injection of a fresh reaction solution for the synthesis of compounds $[\text{K}(\text{crypt-222})]_2(\mathbf{1})_{0.9}(\text{Ge}_2\text{As}_2)_{0.1} \cdot 0.9\text{tol}$, $[\text{K}(\text{crypt-222})]_3\mathbf{3}$, and $[\text{K}(\text{crypt-222})]_9(\mathbf{5a})(\mathbf{5b})_{0.5} \cdot \text{en}$ in en, after 1 h reaction time.

Table 7.52: Species identified in the overview ESI(–) mass spectrum, recorded immediately upon injection of a fresh reaction solution for the synthesis of compounds $[\text{K}(\text{crypt-222})]_2(\mathbf{1})_{0.9}(\text{Ge}_2\text{As}_2)_{0.1} \cdot 0.9\text{tol}$, $[\text{K}(\text{crypt-222})]_3\mathbf{3}$, and $[\text{K}(\text{crypt-222})]_9(\mathbf{5a})(\mathbf{5b})_{0.5} \cdot \text{en}$ in en, after 1 h reaction time. The relative strength of the observed signals is given in two categories, medium (m), and weak (w), respectively.

Species	m/z (rel. signal strength)
$(\text{Ge}_3\text{As})^-/(\text{Ge}_2\text{As}_2\text{H})^-$	296.6947(m)
$(\text{Ge}_5\text{H})^-$	366.6106(s)
$(\text{K}_2\text{Zn}_3\text{Ge}_9\text{As}_3)^-$	1153.7768(m)
$[\text{K}_2(\text{crypt-222})\text{Zn}_3\text{Ge}_9\text{As}_3]^-$	1530.0349(m)
$[\text{K}_2(\text{crypt-222})_2\text{Zn}_3\text{Ge}_9\text{As}_3]^-$	1906.2740(m)

Time-dependent mass spectrum of the reaction solution during synthesis of compounds $[\text{K}(\text{crypt-222})]_2\mathbf{6}$ (3 h)

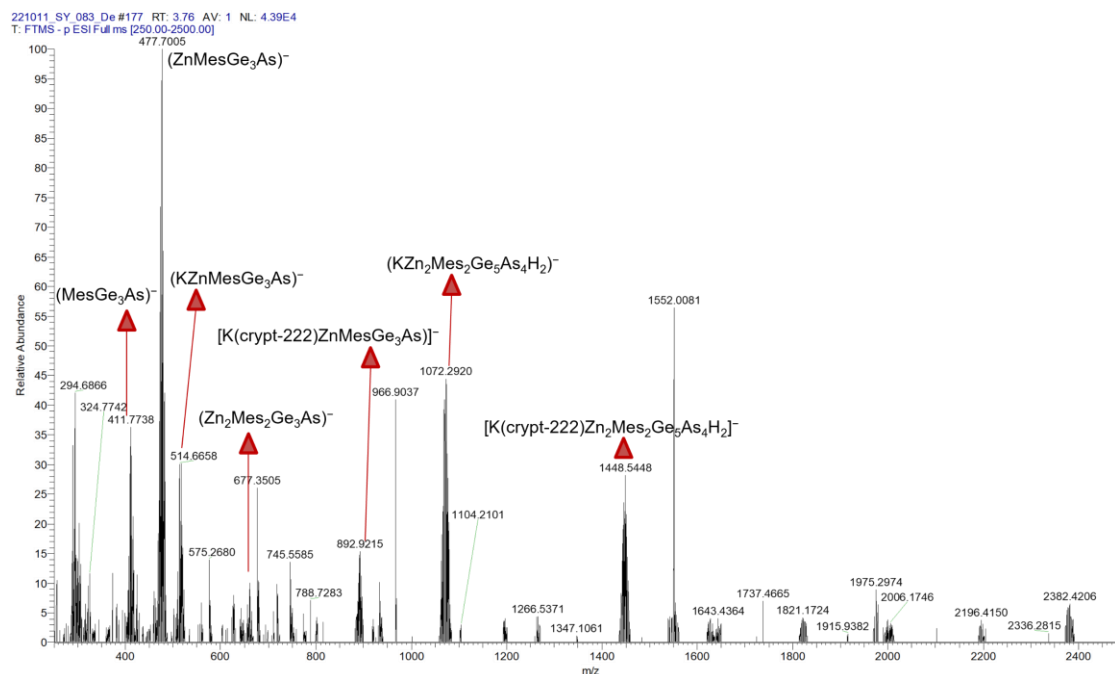


Figure 7.30: Overview of ESI(–) mass spectrum recorded immediately upon injection of a fresh reaction solution for the synthesis of compounds $[\text{K}(\text{crypt-222})]_2\mathbf{6}$ in en, after 3h reaction time.

Table 7.53: Species identified in the overview ESI(–) mass spectrum, recorded immediately upon injection of a fresh reaction solution for the synthesis of compounds $[\text{K}(\text{crypt-222})]_2\mathbf{6}$ in en, after 3h reaction time. The relative strength of the observed signals is given in two categories, strong (s), and medium (m), respectively.

Species	m/z (rel. signal strength)
$(\text{MesGe}_3\text{As})^-$	411.7738(s)
$(\text{ZnMesGe}_3\text{As})^-$	477.7005(s)
$(\text{KZnMesGe}_3\text{As})^-$	516.6649(m)
$(\text{Zn}_2\text{Mes}_2\text{Ge}_3\text{As})^-$	662.7131(m)
$[\text{K}(\text{crypt-222})\text{ZnMesGe}_3\text{As}]^-$	892.9215(m)
$(\text{KZn}_2\text{Mes}_2\text{Ge}_5\text{As}_4\text{H}_2)^-$	1072.2932(s)
$[\text{K}(\text{crypt-222})\text{Zn}_2\text{Mes}_2\text{Ge}_5\text{As}_4\text{H}_2]^-$	1448.5464(s)

Time-dependent mass spectrum of the reaction solution during synthesis of compounds [K(crypt-222)]_{3.67}10 (5 min)

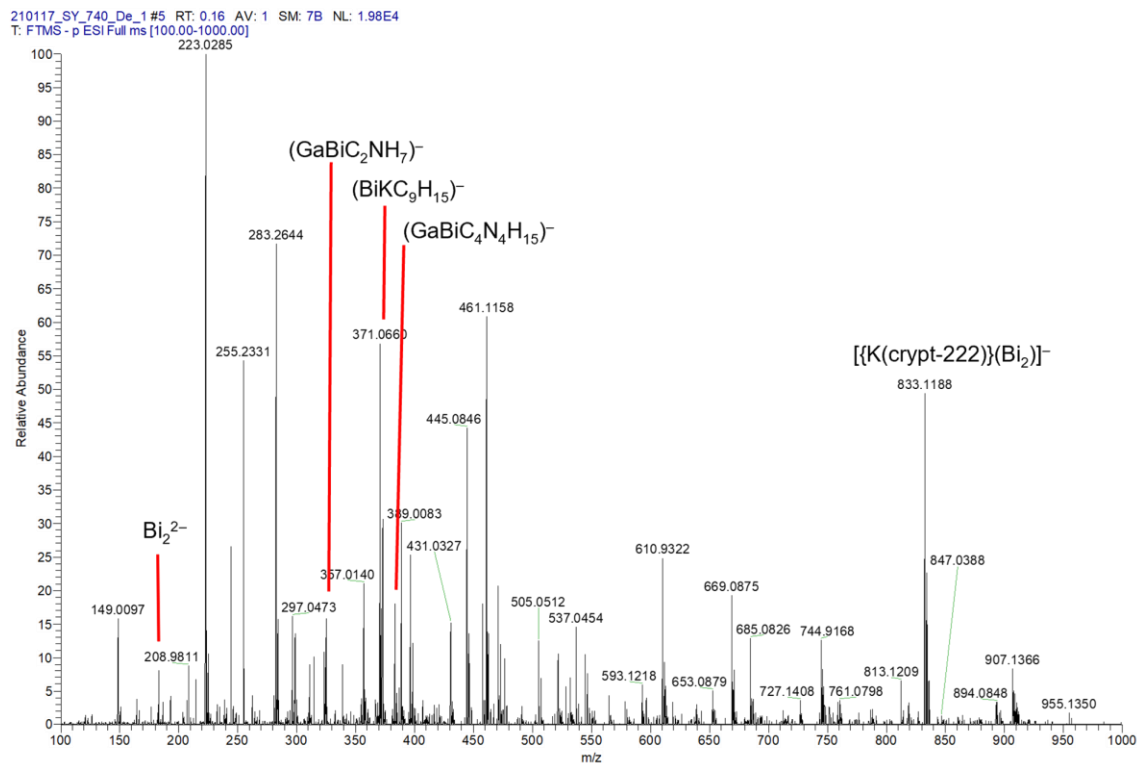


Figure 7.31: Overview of ESI(−) mass spectrum recorded immediately upon injection of a fresh reaction solution for the synthesis of compounds [K(crypt-222)]_{3.67}10 in en/DMF, after 5 min reaction time. All of the other peaks comprise organic fragments, but none of them could be assigned a reasonable composition, suggesting a high reactivity of the intermediates towards the formation of compounds [K(crypt-222)]_{3.67}10 in the gas phase.

Table 7.54: Species identified in the overview ESI(−) mass spectrum, recorded immediately upon injection of a fresh reaction solution for the synthesis of compounds [K(crypt-222)]_{3.67}10 in en/DMF, after 5 min reaction time. The relative strength of the observed signals is given in three categories, strong (s), medium (m), and weak (w), respectively.

Species	m/z (rel. signal strength)	Assumptive structure (with organic fragments)
Bi ₂ ²⁻	208.9811 (w)	
(GaBiC ₂ NH ₇) ⁻	322.9725 (m)	
[(KBiH ₂){C ₅ Me ₄ H}] ⁻	371.0659 (m)	
[(GaBiC ₂ N ₂ H ₇){en}] ⁻	396.9912 (m)	
[[K(crypt-222)](Bi ₂)] ⁻	417.9605 (s)	

Time-dependent mass spectrum of the reaction solution during synthesis of compounds $[\text{K}(\text{crypt-222})]_{3.67}\mathbf{10}$ (1 h)

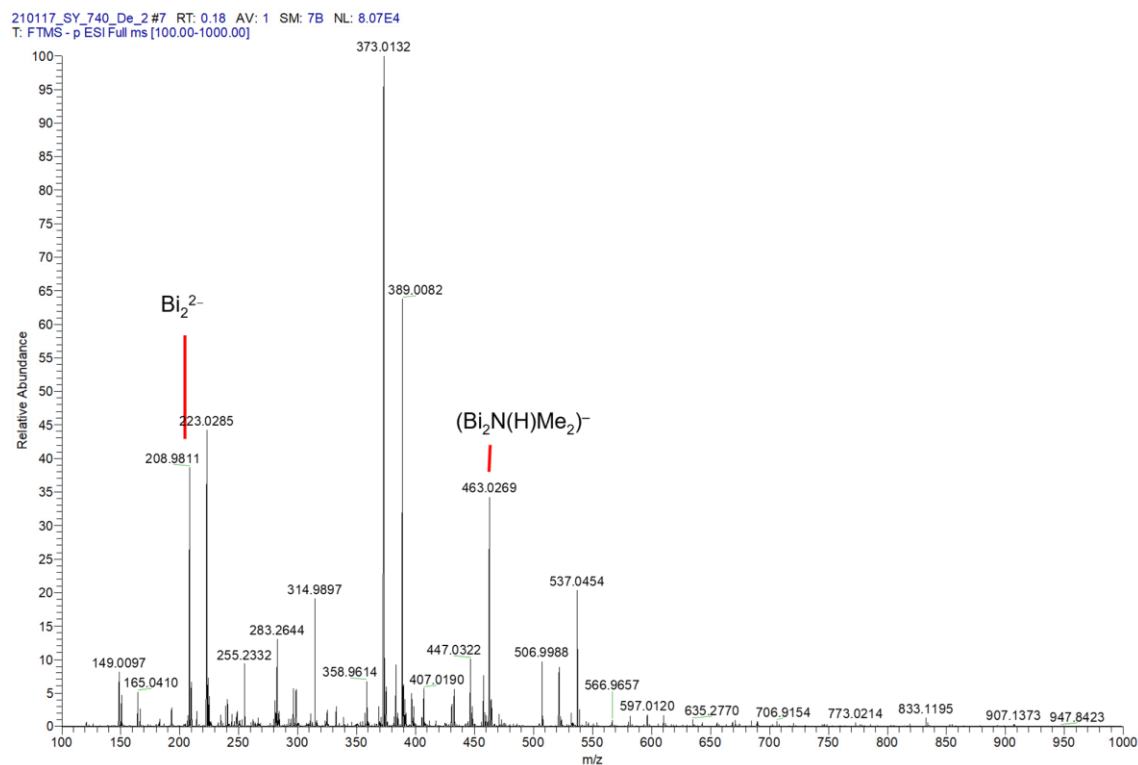


Figure 7.32: Overview of ESI(−) mass spectrum recorded immediately upon injection of a fresh reaction solution for the synthesis of compounds $[\text{K}(\text{crypt-222})]_{3.67}\mathbf{10}$ in en/DMF, after 1 h reaction time.

Table 7.55: Species identified in the overview ESI(−) mass spectrum, recorded immediately upon injection of a fresh reaction solution for the synthesis of compounds $[\text{K}(\text{crypt-222})]_{3.67}\mathbf{10}$ in en/DMF, after 1 h reaction time. The relative strength of the observed signals is given in one category, medium (m).

Species	m/z (rel. signal strength)	Assumptive structure (with organic fragments)
Bi_2^{2-}	208.9811 (w)	
$(\text{Bi}_2\text{N}(\text{H})\text{Me}_2)^-$	463.0270 (m)	

Time-dependent mass spectrum of the reaction solution during synthesis of compounds $[K(\text{crypt-222})]_{3.67}\mathbf{10}$ (3 h)

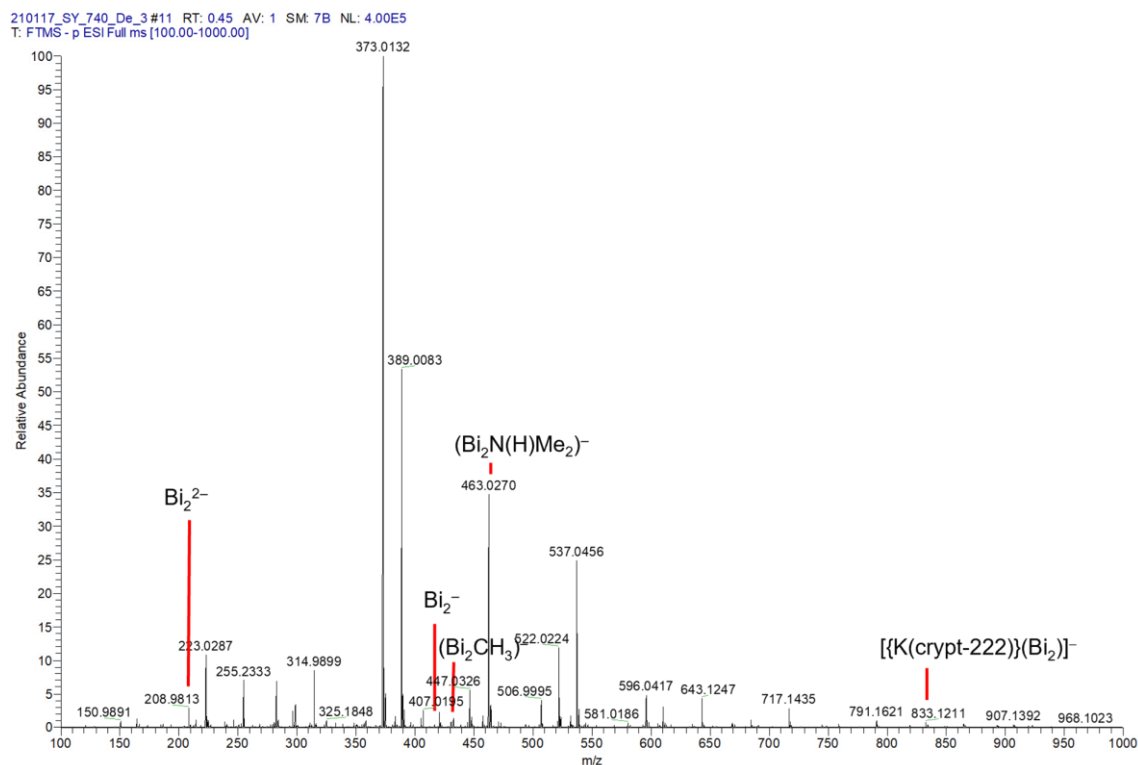


Figure 7.33: Overview of ESI(−) mass spectrum recorded immediately upon injection of a fresh reaction solution for the synthesis of compounds $[K(\text{crypt-222})]_{3.67}\mathbf{10}$ in en/DMF, after 3 h reaction time.

Table 7.56: Species identified in the overview ESI(−) mass spectrum, recorded immediately upon injection of a fresh reaction solution for the synthesis of compounds $[K(\text{crypt-222})]_{3.67}\mathbf{10}$ in en/DMF, after 3 h reaction time. The relative strength of the observed signals is given in two categories, medium (m), and weak (w), and respectively.

Species	m/z (rel. signal strength)	Assumptive structure (with organic fragments)
Bi_2^{2-}	208.9811 (m)	
Bi_2^-	417.9617 (w)	
$(\text{Bi}_2\text{CH}_3)^-$	432.9858 (w)	$\ominus \begin{array}{c} \diagup \text{---} \\ \text{Bi}=\text{Bi}-\text{CH}_3 \\ \diagdown \end{array}$
$(\text{Bi}_2\text{N}(\text{H})\text{Me}_2)^-$	463.0269 (m)	$\left[\begin{array}{c} \text{---} \quad \text{H} \quad \text{CH}_3 \\ \quad \diagup \quad \\ \text{Bi} \quad \text{---} \quad \text{N} \\ \quad \diagdown \quad \\ \ominus \quad \text{Bi} \quad \text{---} \quad \text{CH}_2 \end{array} \right] \ominus$
$[\{\text{K}(\text{crypt-222})\}(\text{Bi}_2)]^-$	833.1201 (m)	

Time-dependent mass spectrum of the reaction solution during synthesis of compounds [K(crypt-222)]_{3.67}10** (1 d)**

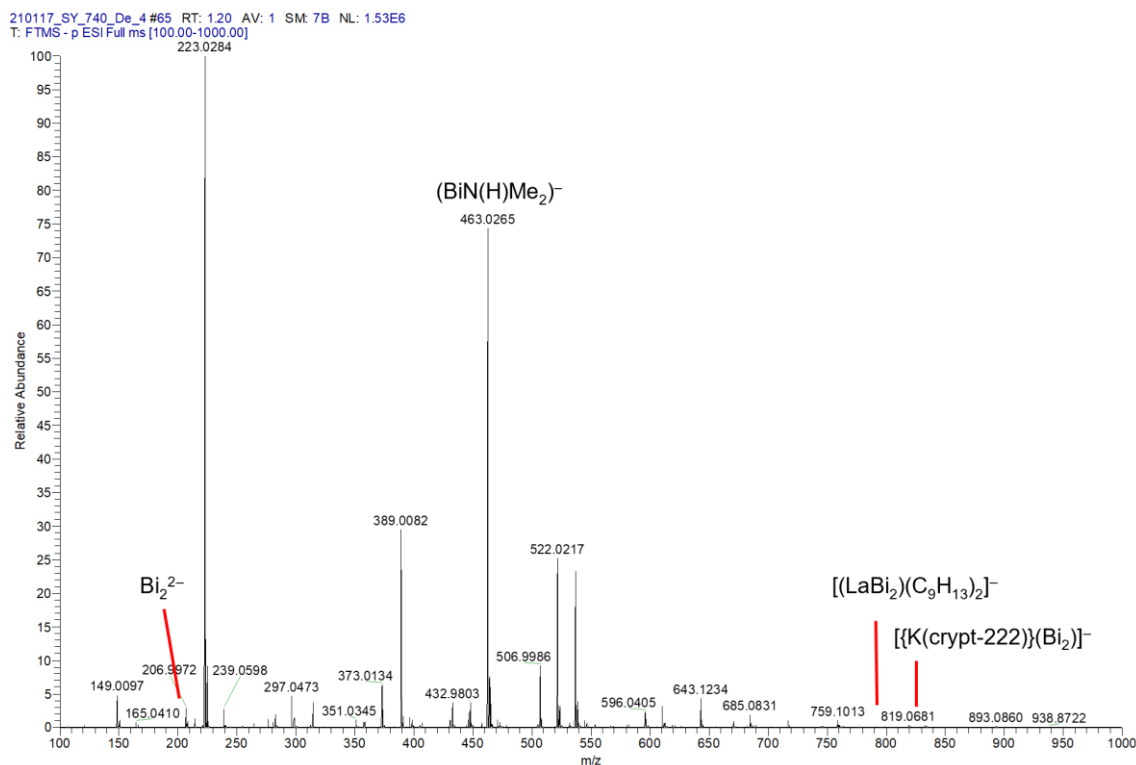


Figure 7.34: Overview of ESI(−) mass spectrum recorded immediately upon injection of a fresh reaction solution for the synthesis of compounds [K(crypt-222)]_{3.67}**10** in en/DMF, after 1 d reaction time.

Table 7.57: Species identified in the overview ESI(−) mass spectrum, recorded immediately upon injection of a fresh reaction solution for the synthesis of compounds [K(crypt-222)]_{3.67}**10** in en/DMF, after 1 d reaction time. The relative strength of the observed signals is given in two categories, strong (s), and weak (w), respectively.

Species	m/z (rel. signal strength)	Assumptive structure (with organic fragments)
Bi ₂ ^{2−}	208.9811 (w)	
(Bi ₂ C ₂ NH ₇) [−]	463.0269 (s)	
[(LaBi ₂)(C ₉ H ₁₃) ₂] [−]	799.0371 (w)	
[{K(crypt-222)}(Bi ₂)] [−]	833.1201 (w)	

Time-dependent mass spectrum of the reaction solution during synthesis of compounds [K(crypt-222)]₄11a (10 min)

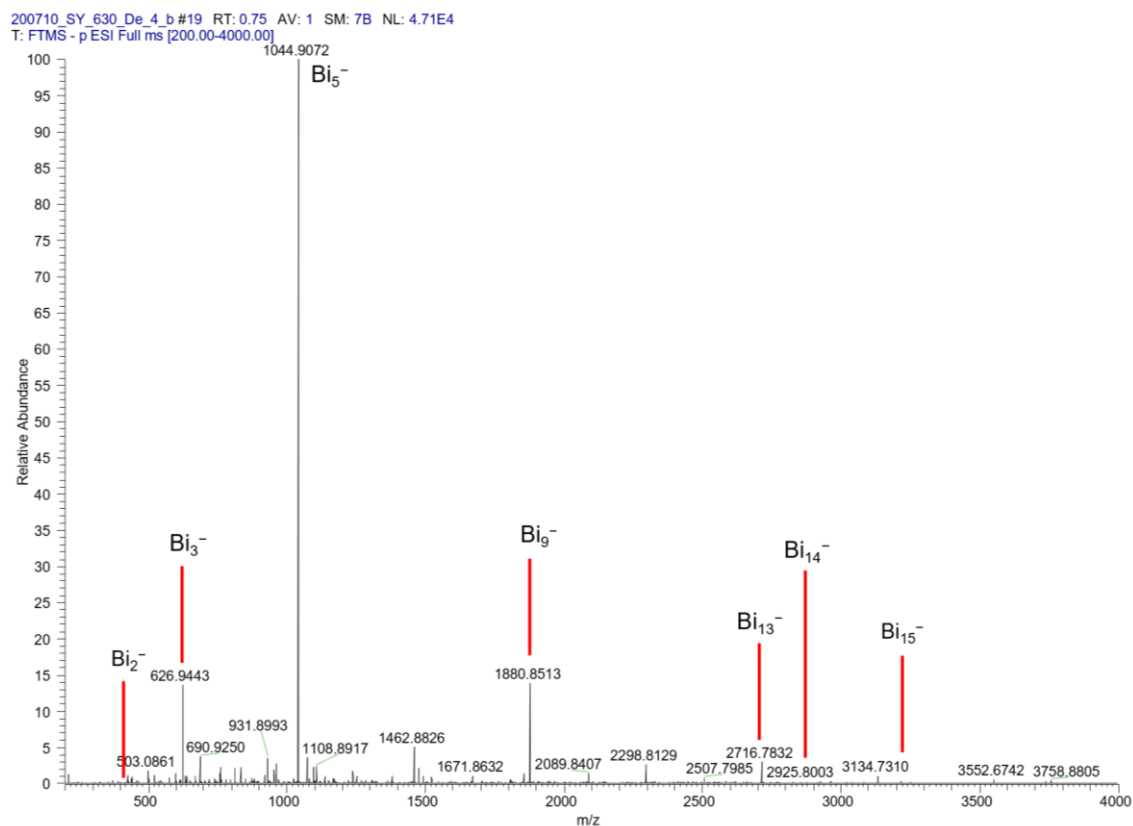


Figure 7.35: Overview of ESI(−) mass spectrum recorded immediately upon injection of a fresh reaction solution for the synthesis of compounds [K(crypt-222)]₄11a in en, after 10 min reaction time.

Table 7.58: Species identified in the overview ESI(−) mass spectrum, recorded immediately upon injection of a fresh reaction solution for the synthesis of compounds [K(crypt-222)]₄11a in en, after 10 min reaction time. The relative strength of the observed signals is given in three categories, strong (s), medium (m), and weak (w), respectively.

Species	m/z (rel. signal strength)
Bi ₂ [−]	417.9557 (w)
Bi ₃ [−]	626.9443 (m)
Bi ₅ [−]	1044.9072 (s)
Bi ₇ [−]	1462.8826 (w)
Bi ₉ [−]	1880.8513 (m)
Bi ₁₃ [−]	2716.7832 (w)
Bi ₁₄ [−]	2925.7127 (m)
Bi ₁₆ [−]	3343.6863 (w)

Time-dependent mass spectrum of the reaction solution during synthesis of compounds [K(crypt-222)]₄11a (1 d)

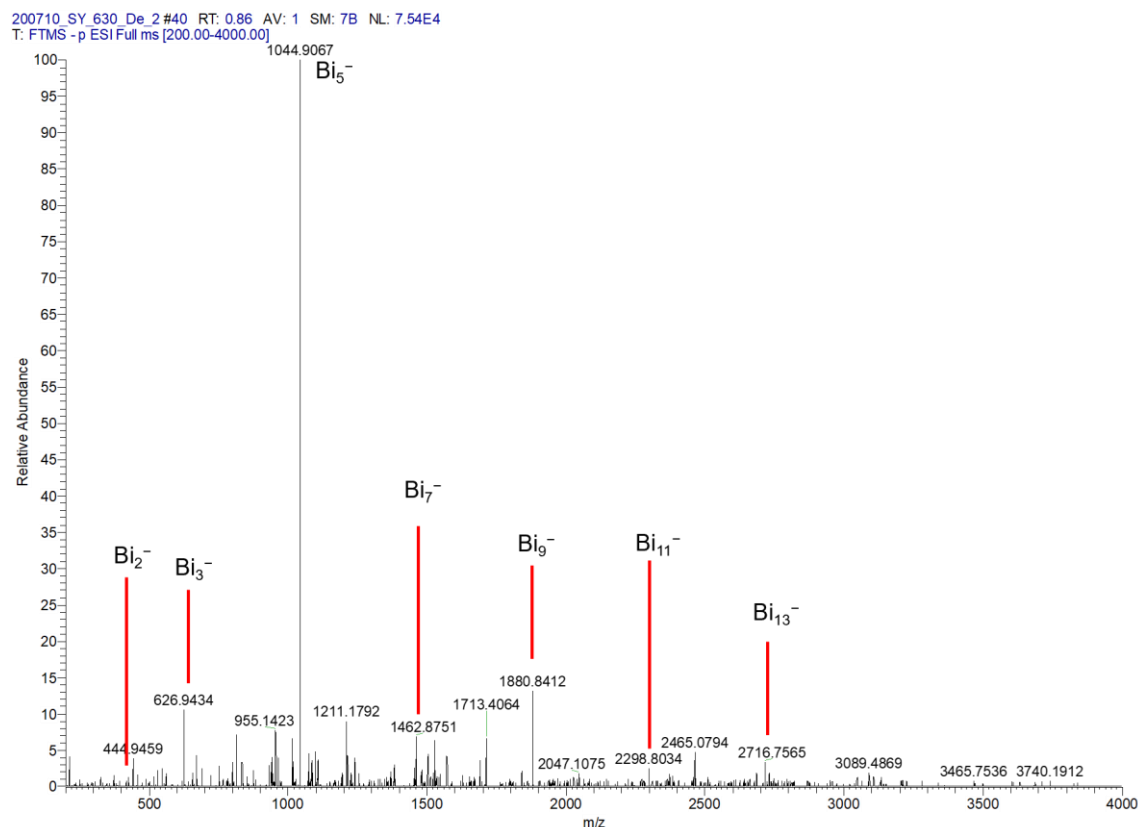


Figure 7.36: Overview of ESI(−) mass spectrum recorded immediately upon injection of a fresh reaction solution for the synthesis of compounds [K(crypt-222)]₄11a in en, after 1 d reaction time.

Table 7.59: Species identified in the overview ESI(−) mass spectrum, recorded immediately upon injection of a fresh reaction solution for the synthesis of compounds [K(crypt-222)]₄11a in en, after 1 d reaction time. The relative strength of the observed signals is given in three categories, strong (s), medium (m), and weak (w), respectively.

Species	m/z (rel. signal strength)
Bi ₂ [−]	417.9612 (w)
Bi ₃ [−]	626.9443 (m)
Bi ₅ [−]	1044.9120 (s)
Bi ₇ [−]	1462.8751 (w)
Bi ₉ [−]	1880.8410 (m)
Bi ₁₁ [−]	2298.7911 (w)
Bi ₁₃ [−]	2716.7491 (w)

Time-dependent mass spectrum of the reaction solution during synthesis of compounds [K(crypt-222)]₄11a (7 d)

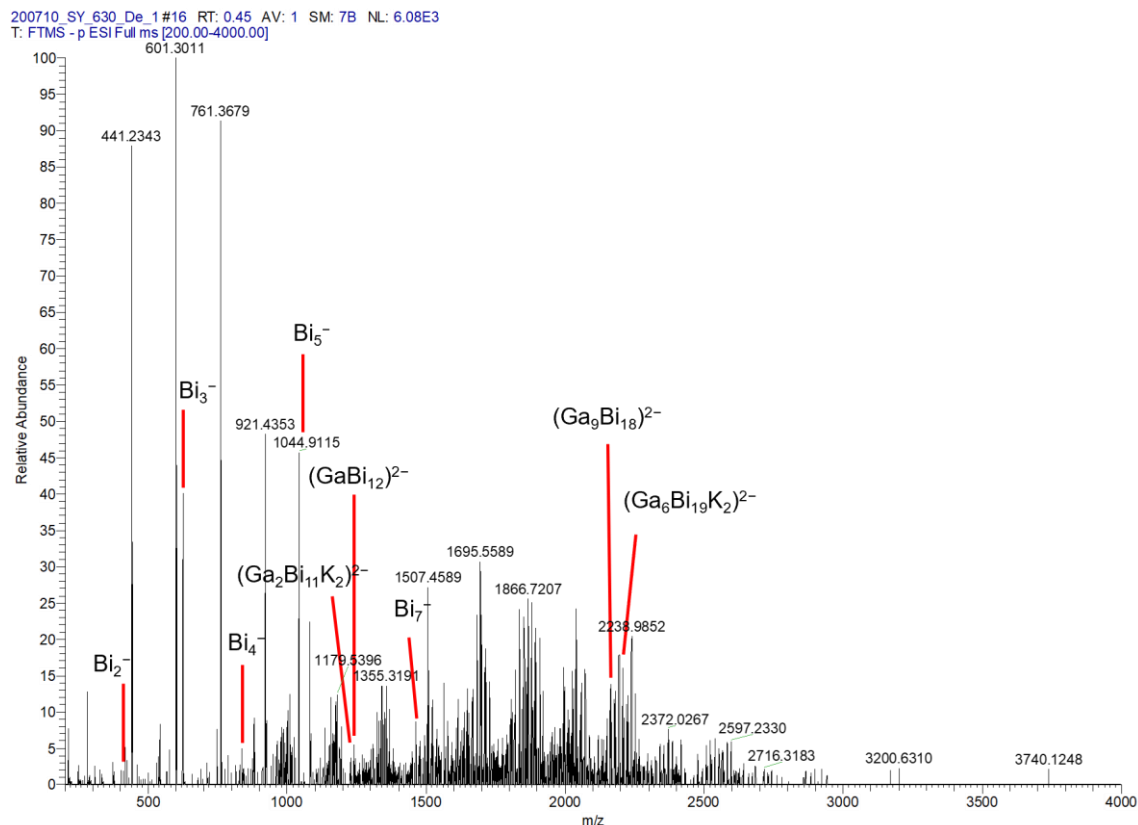


Figure 7.37: Overview of ESI(−) mass spectrum recorded immediately upon injection of a fresh reaction solution for the synthesis of compounds [K(crypt-222)]₄11a in en, after 7 d reaction time.

Table 7.60: Species identified in the overview ESI(−) mass spectrum, recorded immediately upon injection of a fresh reaction solution for the synthesis of compounds [K(crypt-222)]₄11a in en, after 7 d reaction time. The relative strength of the observed signals is given in two categories, medium (m), and weak (w), respectively.

Species	m/z (rel. signal strength)
Bi_2^-	417.9622 (w)
Bi_3^-	626.9440 (m)
Bi_4^-	835.9271 (w)
Bi_5^-	1044.9102 (m)
$(\text{Ga}_2\text{Bi}_{11}\text{K}_2)^{2-}$	1258.3255 (w)
$(\text{GaBi}_{12})^{2-}$	1288.3528 (w)
Bi_7^-	1462.8719 (w)
$(\text{Ga}_9\text{Bi}_{18})^{2-}$	2193.9770 (m)
$(\text{Ga}_6\text{Bi}_{19}\text{K}_2)^{2-}$	2233.0205 (m)

Time-dependent mass spectrum of the reaction solution during synthesis of compounds [K(crypt-222)]₄12 (1 h)

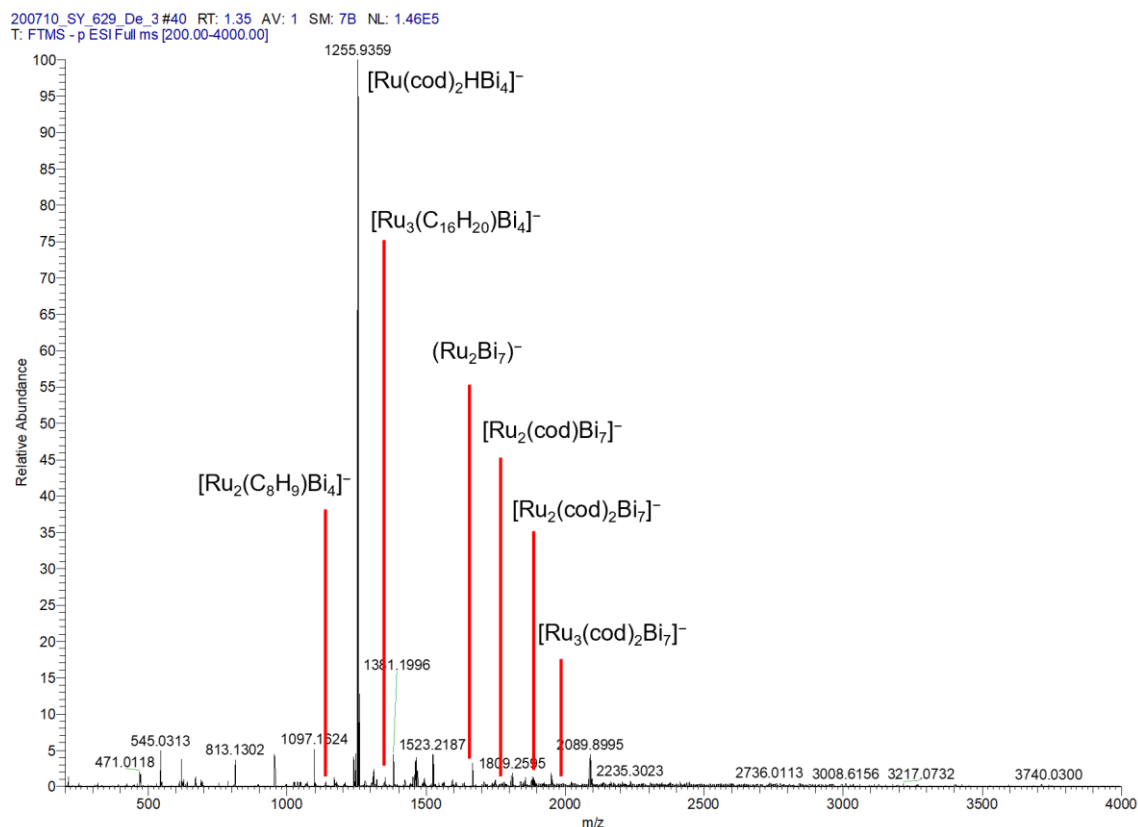


Figure 7.39: Overview of ESI(−) mass spectrum recorded immediately upon injection of a fresh reaction solution for the synthesis of compounds [K(crypt-222)]₄12 in en, after 1 h reaction time.

Table 7.62: Species identified in the overview ESI(−) mass spectrum, recorded immediately upon injection of a fresh reaction solution for the synthesis of compounds [K(crypt-222)]₄12 in en, after 1 h reaction time. The relative strength of the observed signals is given in two categories, strong (s), and weak (w), respectively.

Species	m/z (rel. signal strength)
$[\text{Ru}_2(\text{C}_8\text{H}_9)\text{Bi}_4]^-$	1143.8143 (w)
$[\text{Ru}(\text{cod})_2\text{HBI}_4]^-$	1255.9359 (s)
$[\text{Ru}_3(\text{C}_{16}\text{H}_{20})\text{Bi}_4]^-$	1352.8124 (w)
$(\text{Ru}_2\text{Bi}_7)^-$	1665.7001 (w)
$[\text{Ru}_2(\text{cod})\text{Bi}_7]^-$	1773.7951 (w)
$[\text{Ru}_2(\text{cod})_2\text{Bi}_7]^-$	1881.8858 (w)
$[\text{Ru}_3(\text{cod})_2\text{Bi}_7]^-$	1983.8084 (w)

Time-dependent mass spectrum of the reaction solution during synthesis of compounds [K(crypt-222)]₄12 (7 d)

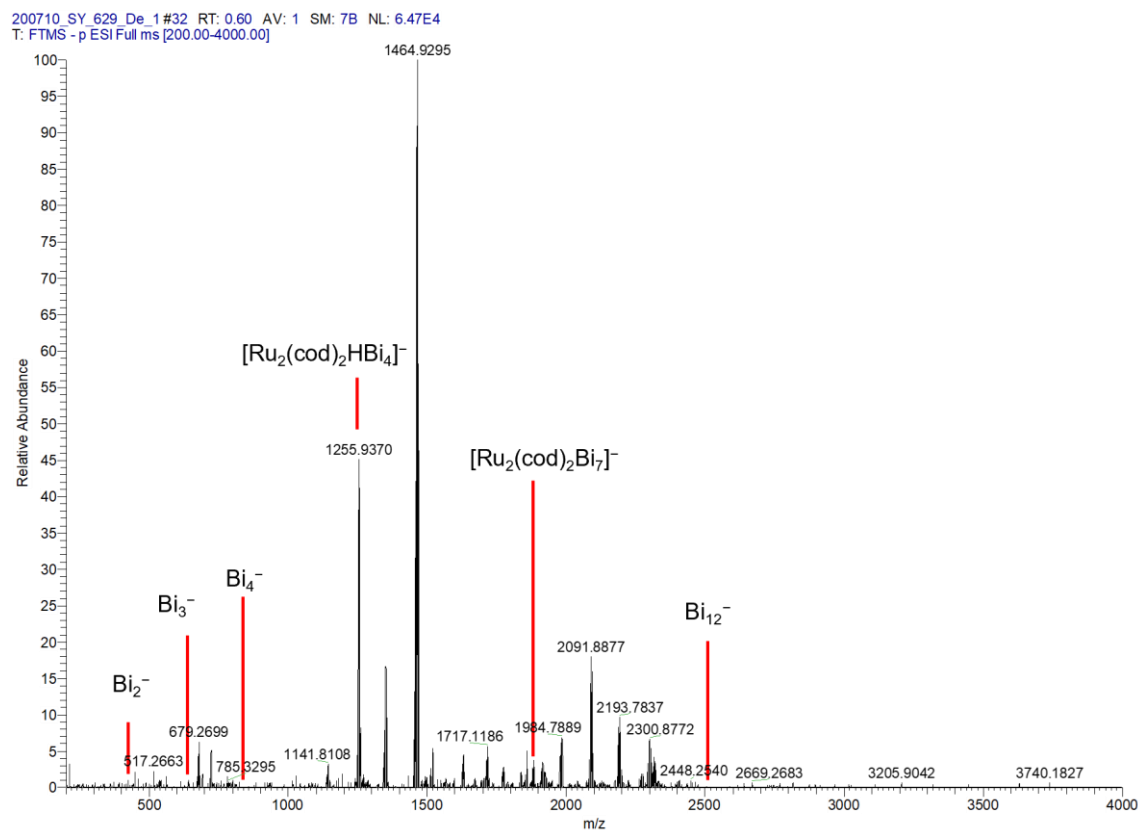


Figure 7.40: Overview of ESI(−) mass spectrum recorded immediately upon injection of a fresh reaction solution for the synthesis of compounds [K(crypt-222)]₄12 in en, after 7 d reaction time.

Table 7.63: Species identified in the overview ESI(−) mass spectrum, recorded immediately upon injection of a fresh reaction solution for the synthesis of compounds [K(crypt-222)]₄12 in en, after 7 d reaction time. The relative strength of the observed signals is given in one category, medium (m).

Species	m/z (rel. signal strength)
Bi_2^-	417.9621 (m)
Bi_3^-	626.9486 (m)
Bi_4^-	835.9143 (m)
$[\text{Ru}_2(\text{cod})_2\text{HBi}_4]^-$	1255.9329 (m)
$[\text{Ru}_2(\text{cod})_2\text{Bi}_7]^-$	1881.8783 (m)
Bi_{12}^-	2507.8065 (m)

7.4 Quantem Chemical Investigations

For compounds $[\text{K}(\text{crypt-222})]_2(\mathbf{1})_{0.9}(\text{Ge}_2\text{As}_2)_{0.1} \cdot 0.9\text{tol}$ – $[\text{K}(\text{crypt-222})]_2\mathbf{6}$, and $[\text{K}(\text{crypt-222})]_{3.67}\mathbf{10}$ – $[\text{K}(\text{crypt-222})]_2\mathbf{13} \cdot \text{solv}$, DFT studies were performed by Dr. Lukas Guggolz. For compounds $[\text{K}(\text{crypt-222})]_2\mathbf{7} \cdot 2\text{en}$, and $[\text{K}(\text{crypt-222})]_2\mathbf{9} \cdot \text{solv}$, DFT studies were performed by Marcel Lukanowski, and Prof. Dr. Florian Weigend. For compound $[\text{K}(\text{crypt-222})]_4\mathbf{8} \cdot \text{solv}$, DFT studies were performed by Kjell Janke, Prof. Dr. Florian Weigend, and Dr. Lukas Guggolz.

7.4.1 Compounds $[\text{K}(\text{crypt-222})]_2(\mathbf{1})_{0.9}(\text{Ge}_2\text{As}_2)_{0.1} \cdot 0.9\text{tol}$ – $[\text{K}(\text{crypt-222})]_2\mathbf{6}$

7.4.1.1 Methods

Quantum chemical investigations were undertaken using the program system Turbomole V7.5.1.^[242,312] We employed density functional theory (DFT)^[313,314] methods throughout these studies. We used the TPSS^[315] functional and basis sets of quality dhf-TZVP^[316,317] with additional use of auxiliary basis sets^[318] and effective core potentials^[319] at the Cd and Hg atoms. Negative charges were compensated with the conductor-like screening model (COSMO).^[320] Partial charges were calculated by means of Mulliken^[321] and natural population analyses (NPA).^[322] Shared electron numbers (SEN) were calculated with a population analysis based on occupation numbers (Paboon).^[323] Localized molecular orbitals (LMOs) were obtained according to Boys' method.^[292] The plots of LMOs and of canonical MOs were plotted using the Chemcraft software.^[324]

All geometry optimizations were performed without any symmetry restrictions (see below), except for $(\text{Ge}_3\text{As})^{3-}$, which was optimized in point group C_{3v} (Figure 3.6).

7.4.1.2 Detailed DFT studies

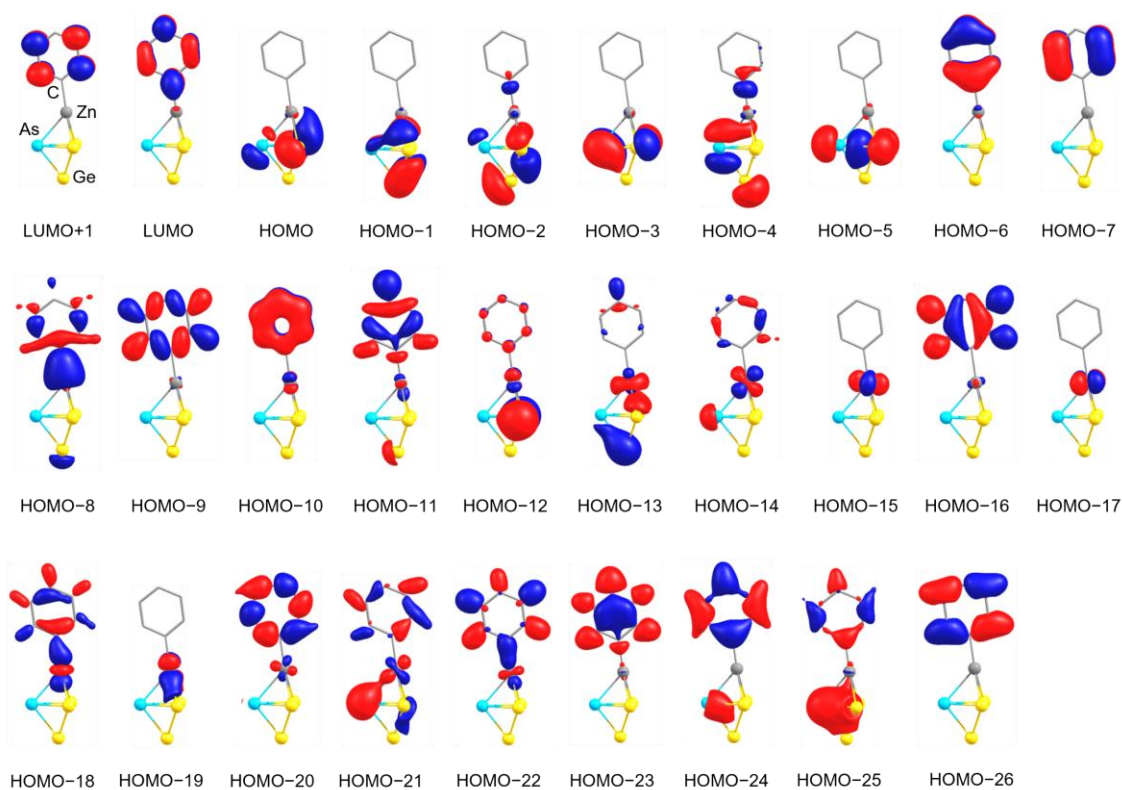


Figure 7.41: Canonical MOs of cluster anion $\mathbf{1}^{2-}$. Contour values are drawn at ± 0.05 a.u.; H atoms are omitted in the images for clarity.

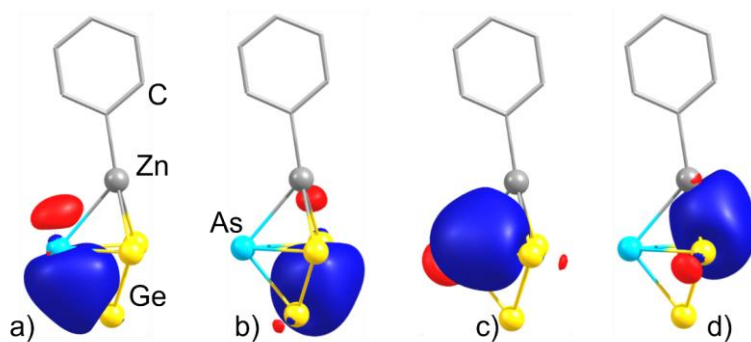


Figure 7.42: LMOs of cluster anion $\mathbf{1}^{2-}$ representing regular two-electron two-center Ge-As (a) and Ge-Ge (b) bonds, and two-electron three-center bonds between the *pseudo*-tetrahedral moiety and the $(\text{PhZn})^+$ fragment (c, d). Contour values are drawn at ± 0.05 a.u.; H atoms are omitted in the images for clarity.

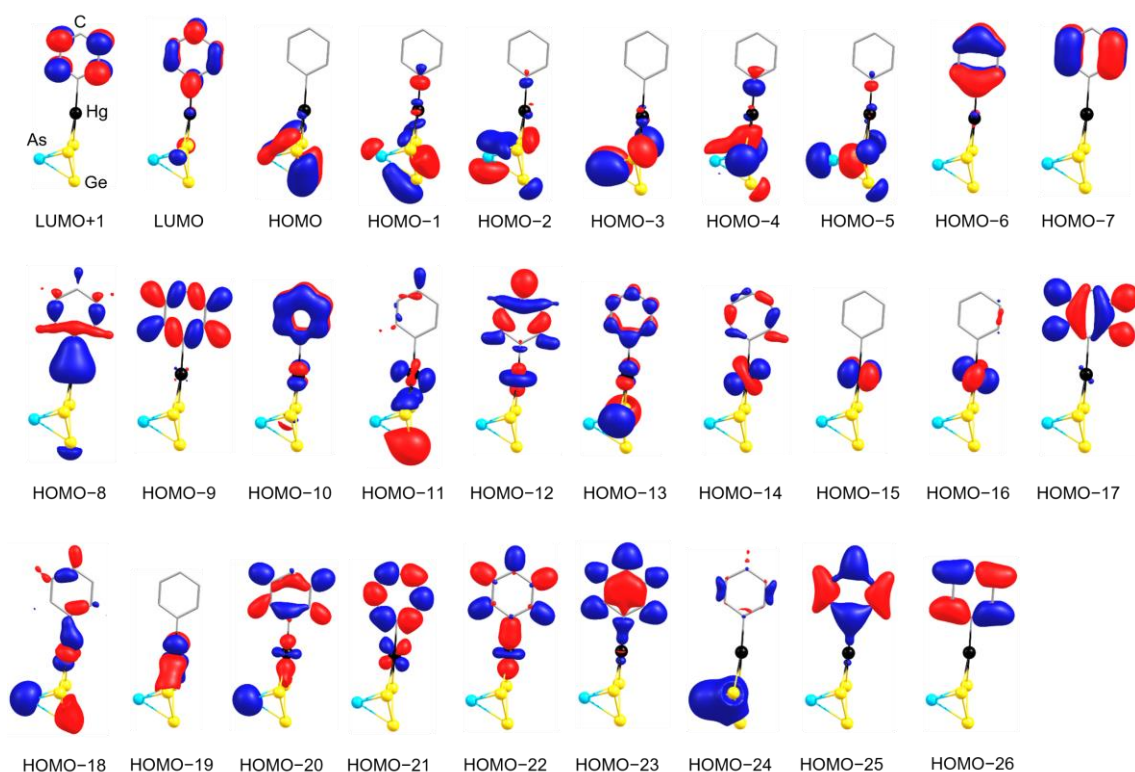


Figure 7.43: Canonical MOs of cluster anion 2^{2-} . Contour values are drawn at ± 0.05 a.u.; H atoms are omitted in the images for clarity.

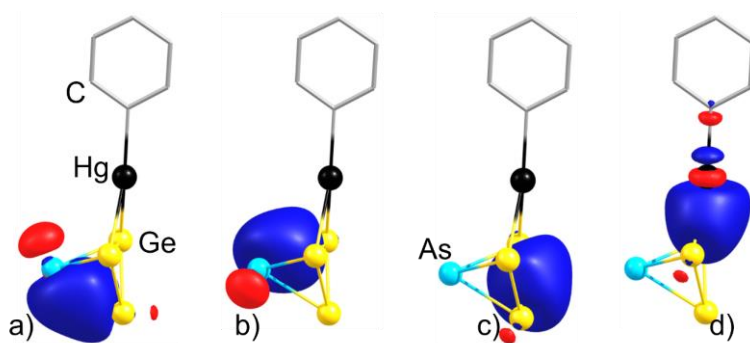


Figure 7.44: LMOs of cluster anion 2^{2-} representing regular two-electron two-center Ge-As (a, b) and Ge-Ge (c) bonds, and the two-electron three-center bond between the *pseudo*-tetrahedral moiety and the $(\text{PhZn})^+$ fragment (d). Contour values are drawn at ± 0.05 a.u.; H atoms are omitted in the images for clarity.

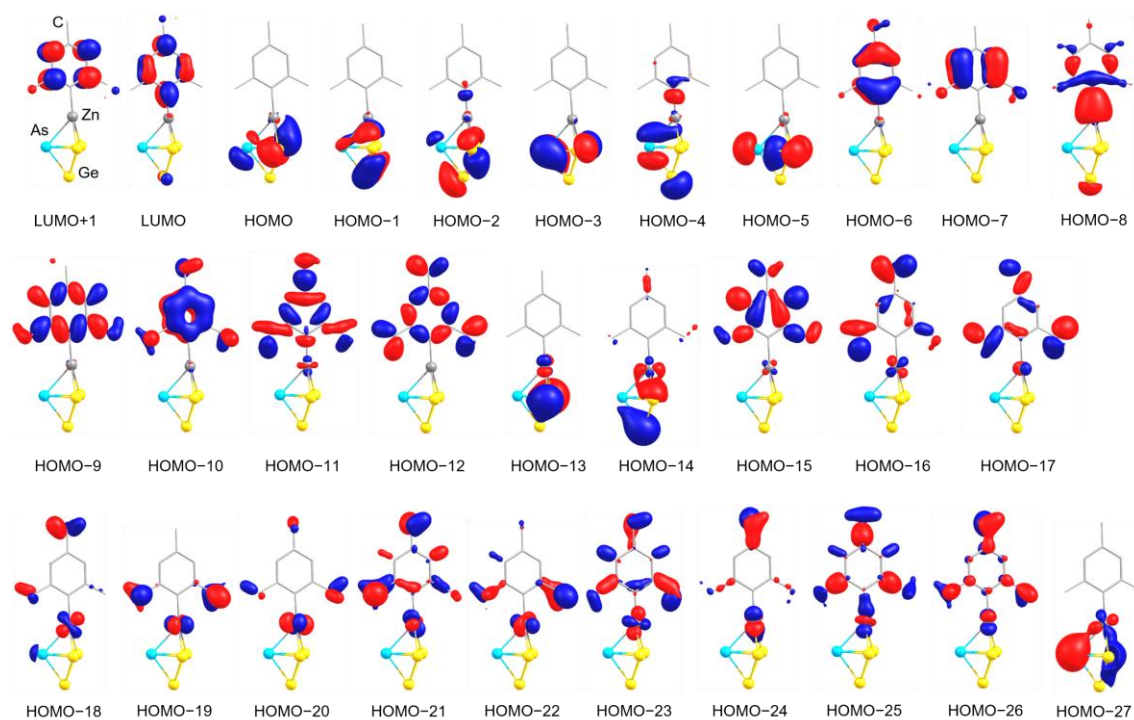


Figure 7.45: Canonical MOs of cluster anion 6^{2-} . Contour values are drawn at ± 0.05 a.u.; H atoms are omitted in the images for clarity.

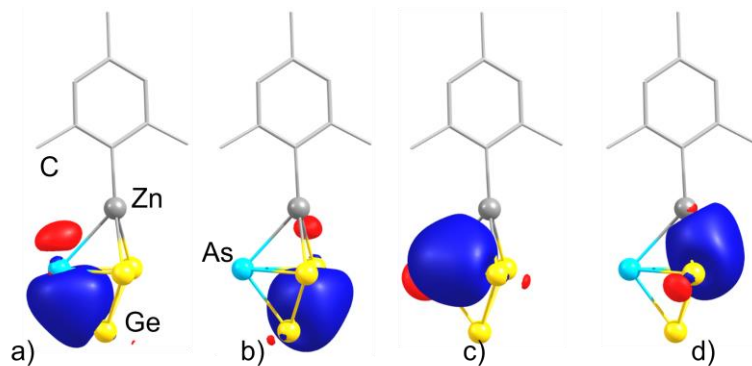


Figure 7.46: LMOs of cluster anion 6^{2-} representing regular two-electron two-center Ge-As (a) and Ge-Ge (b) bonds, and two-electron three-center bonds between the *pseudo*-tetrahedral moiety and the $(\text{MesZn})^+$ fragment (c, d). Contour values are drawn at ± 0.05 a.u.; H atoms are omitted in the images for clarity.

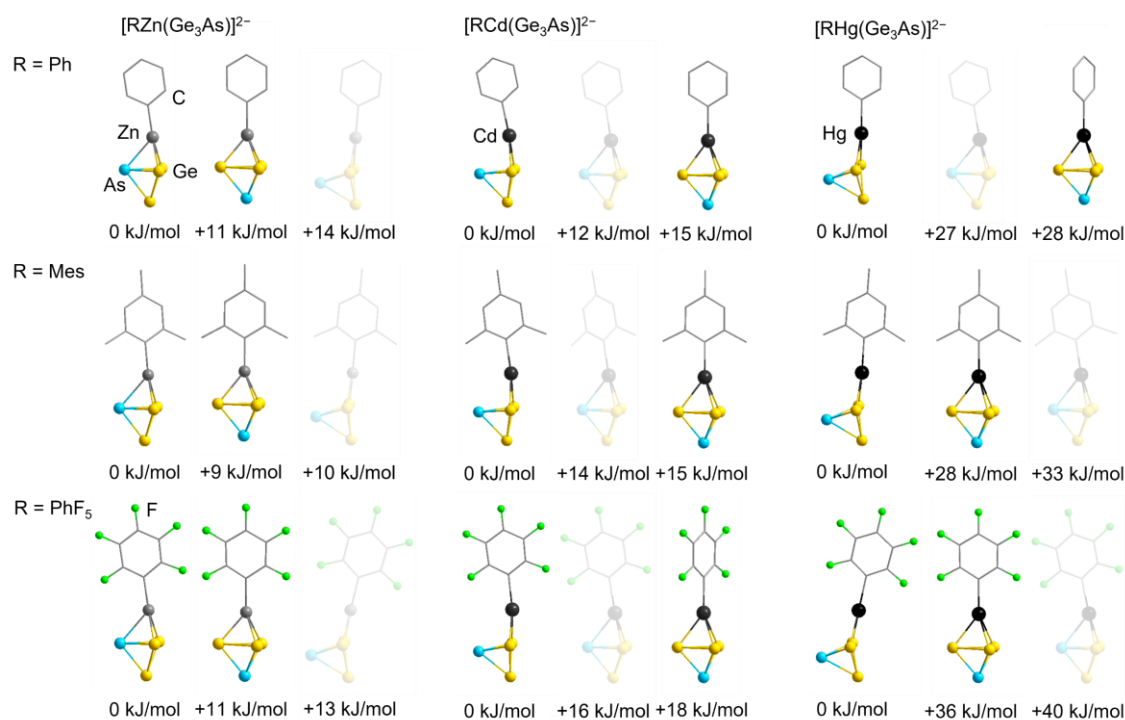


Figure 7.47: Overview of computationally optimized structures for all possible combinations of $[\text{MR}(\text{Ge}_3\text{As})]^{2-}$ ($\text{M} = \text{Zn}, \text{Cd}, \text{Hg}$; $\text{R} = \text{Ph}, \text{Mes}, \text{C}_6\text{F}_5$). The calculated relative energies ΔE of the different conformers are given with respect to the global minimum structure. Conformers that were computed with constrained dihedral angles for comparison with the other structures are shown in semitransparent mode. H atoms are omitted in the images for clarity.

Figure 7.48 displays the calculated Mulliken and natural partial charges for the computationally obtained global minimum structures of all possible combinations of $[\text{MR}(\text{Ge}_3\text{As})]^{2-}$ ($\text{M} = \text{Zn}, \text{Cd}, \text{Hg}$; $\text{R} = \text{Ph}, \text{Mes}, \text{C}_6\text{F}_5$). H atoms are omitted in the images for clarity.

Row (R)	Column (M)	Atom	Mulliken	NPA
R = Ph	M = Zn	Ge ^A	-0.2	-0.7
		Ge ^B	-0.4	-0.3
		As	-0.5	-0.8
		Zn	-0.6	+1.2
		C ^A	-0.1	-0.6
		C ^A	-0.1	-0.6
R = Mes	M = Cd	Ge ^A	-0.3	-0.7
		Ge ^B	-0.5	-0.3
		As	-0.6	-0.7
		Cd	0.0	+1.1
		C ^A	-0.4	-0.5
		C ^{Mes}	-0.4	-0.6
R = PhF ₅	M = Hg	Ge ^A	-0.2	-0.6
		Ge ^B	-0.5	-0.4
		As	-0.6	-0.7
		Hg	-0.1	+0.9
		C ^A	-0.3	-0.5
		C ^{Mes}	-0.3 - -0.4	-0.6
R = Ph	M = Hg	Ge ^A	-0.2	-0.6
		Ge ^B	-0.5	-0.3
		As	-0.6	-0.7
		Hg	-0.1	+0.9
		C ^A	-0.3	-0.5
		C ^{Mes}	-0.3 - -0.4	-0.6
R = Mes	M = Zn	Ge ^A	-0.2	-0.7
		Ge ^B	-0.4	-0.2
		As	-0.5	-0.8
		Zn	-0.5	+1.2
		C ^A	-0.2	-0.6
		F	-0.2	-0.3
R = PhF ₅	M = Cd	Ge ^A	-0.3	-0.6
		Ge ^B	-0.4	-0.3
		As	-0.6	-0.7
		Cd	+0.1	+1.1
		C ^A	-0.4	-0.6
		F	-0.2	-0.3
R = Mes	M = Hg	Ge ^A	-0.2	-0.5
		Ge ^B	-0.4	-0.3
		As	-0.6	-0.7
		Hg	-0.1	+0.8
		C ^A	-0.4	-0.5
		F	-0.2	-0.3

Figure 7.48: Calculated Mulliken and natural partial charges for the computationally obtained global minimum structures of all possible combinations of $[\text{MR}(\text{Ge}_3\text{As})]^{2-}$ ($\text{M} = \text{Zn}, \text{Cd}, \text{Hg}$; $\text{R} = \text{Ph}, \text{Mes}, \text{C}_6\text{F}_5$). H atoms are omitted in the images for clarity.

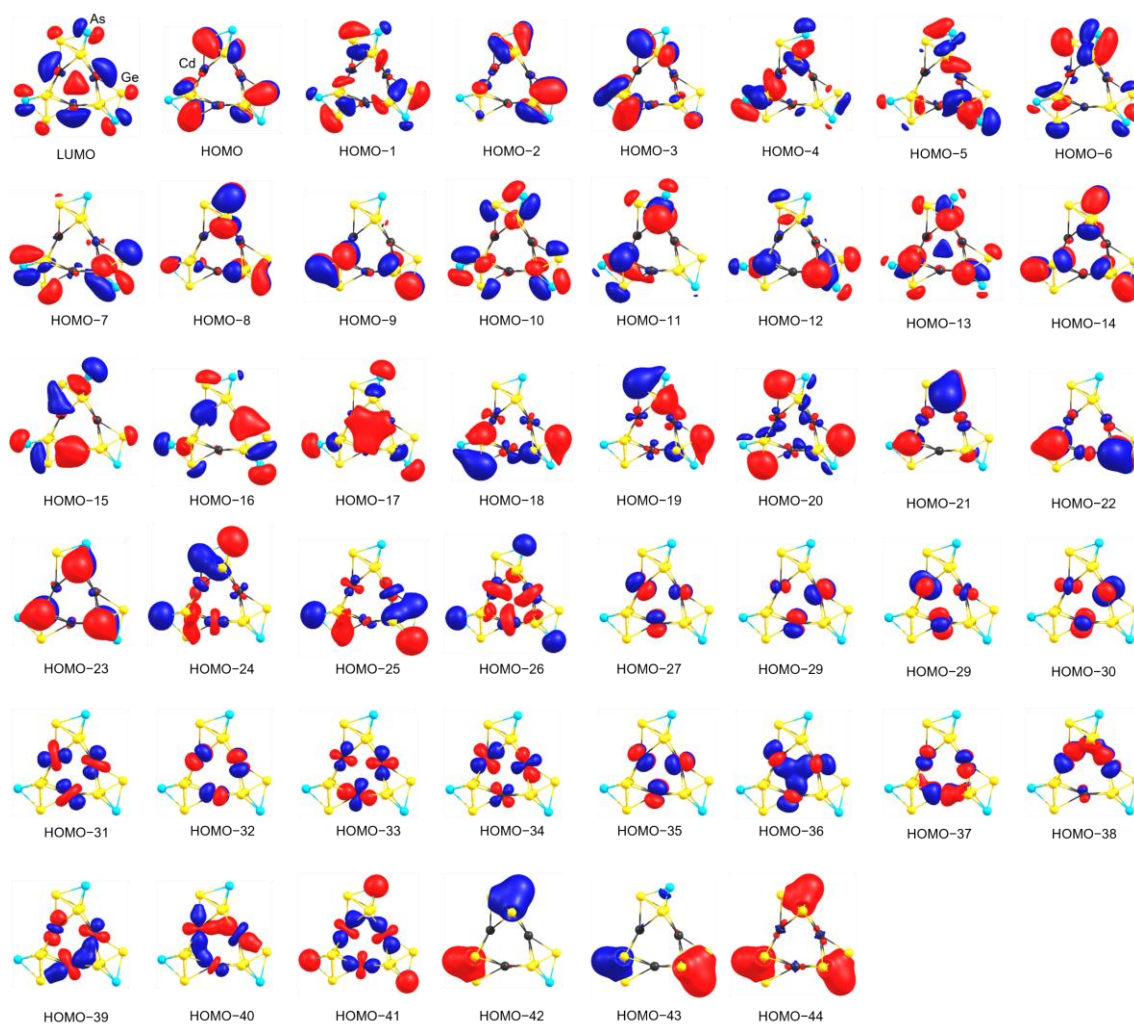


Figure 7.49: Canonical MOs of cluster anion 4^{3-} . Contour values are drawn at ± 0.03 a.u.

7.4.2 Compounds $[K(\text{crypt-222})]_2 7 \cdot 2\text{en} - [K(\text{crypt-222})]_2 9 \cdot \text{solv}$

7.4.2.1 Methods

For anions 7^{2-} and 9^{2-} :

Quantum chemical calculations were carried out using the program package TURBOMOLE (Version 7.8).^[325] Density functional theory (DFT) calculations^[313,314] were carried out using the BP86 functional^[326] and def2-SV(P) basis sets^[316] to figure out the ratio of the investigated compounds while their respective geometries were optimized using DFT with fine grids (gridsize 5), the PBE functional^[327] and def2-TZVP basis sets for cluster anion 7^{2-} and dhf-TZVP for cluster anion 9^{2-} and considering weight derivatives.^[316,317] For all calculations, effective core potentials^[319,328] were used to model the inner electrons of the Ru atoms, the resolution of identity (RI) approximation^[329] with corresponding auxiliary basis sets^[318] was used, and to compensate the negative charge of the calculated compounds, a conductor-like screening model (COSMO) was employed.^[320] The D4 correction from Grimme et al. was used

to empirically include dispersive interactions.^[330] All geometry optimizations were carried out with structures assuming C_1 symmetry and energy convergence to 10^{-9} E_h. All calculated structures were confirmed as energy minimum structures by calculating the force constants and vibrational spectra using the AOFORCE program.

For anion **8**^{q-}:

Quantum chemical investigations were undertaken using the program system Turbomole 7.5.1^[331] and density functional theory (DFT) methods, additionally applying the RI approximation for the Coulomb interaction.^[332,333]

To determine the molecular formula of anion **8**^{q-}, an averaged nuclear charge between 32 for Ge and 33 for As was assigned to each atom. Single-point calculations were then carried out for charge states $q = -4$ and $q = -6$, using the def-SV(P) basis set^[334] and the Becke-Perdew (BP86) functional^[326,335] with Fermi smearing. The relevance of each molecular formula was thus assessed based on the size of the respective HOMO-LUMO gap. For the most probable cluster compositions, elements were assigned to atomic positions by analyzing the electrostatic potential at the nuclear sites.^[336,337]

After the most probable molecular formulas for the clusters were found, geometry optimizations were performed using different functionals.^[326,327,335,338–342] The best results, meaning the best agreement with the experimental results, was achieved with the TPSS functional (grid size 3a).^[315] In contrast to the earlier single-point calculations, the more flexible basis sets x2c-TZVPall^[343] were employed here. Relativistic effects were incorporated using the exact two-component (X2C) decoupling method, which employed the diagonal local approximation (DLU) for the unitary transformation matrices, as well as the finite nucleus model.^[344] The conductor-like screening model (COSMO)^[320] was applied in all calculations to account for solvent effects.

7.4.3 Compounds [K(crypt-222)]_{3.67}**10** – [K(crypt-222)]₄**12**·solv

7.4.3.1 Methods

Density functional theory (DFT) calculations were carried out to optimize the geometric and electronic structure, applying TURBOMOLE^[345,346] using the functional TPSS^[315] and basis sets dhf-TZVP with auxiliary bases.^[316,317] Effective core potentials were applied to model the Bi, Sb, and In atoms.^[347,348] To compensate for the negative charge of the molecule, COSMO^[320] was employed using standard settings and an infinite dielectric constant. Localized molecular orbitals (LMOs) were calculated using the method of Boys,^[292] and representative LMOs are provided below.

7.4.3.2 Detailed DFT Studies

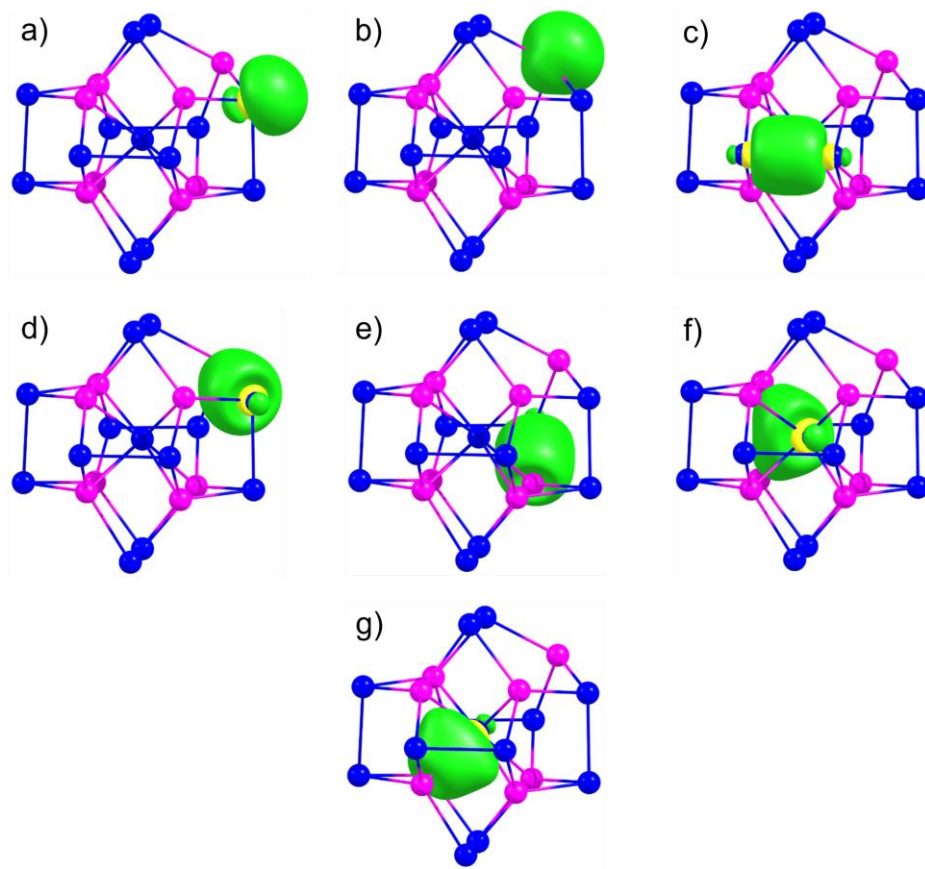


Figure 7.50: Representative localized molecular orbitals (LMOs) for the most stable isomer (A) of the cluster anion $[\text{Bi}@\text{Ga}_8(\text{Bi}_2)_6]^{5-}$ in compound $[\text{K}(\text{crypt-222})]_{3.67}\mathbf{10}$ (Ga: pink, Bi: blue): lone pairs at Bi (a) and the outer Ga (b) atoms, Bi–Bi bond (c), Ga–Bi bonds involving outer (d) or inner (e) Ga atoms, three-center-two-electron bond of the central Bi1 atom with two neighboring Ga atoms (f), and two-center-two electron bond of Bi1 and the Ga atom diagonally opposite of the outer one (g), both of which are polarized towards the central Bi atom.

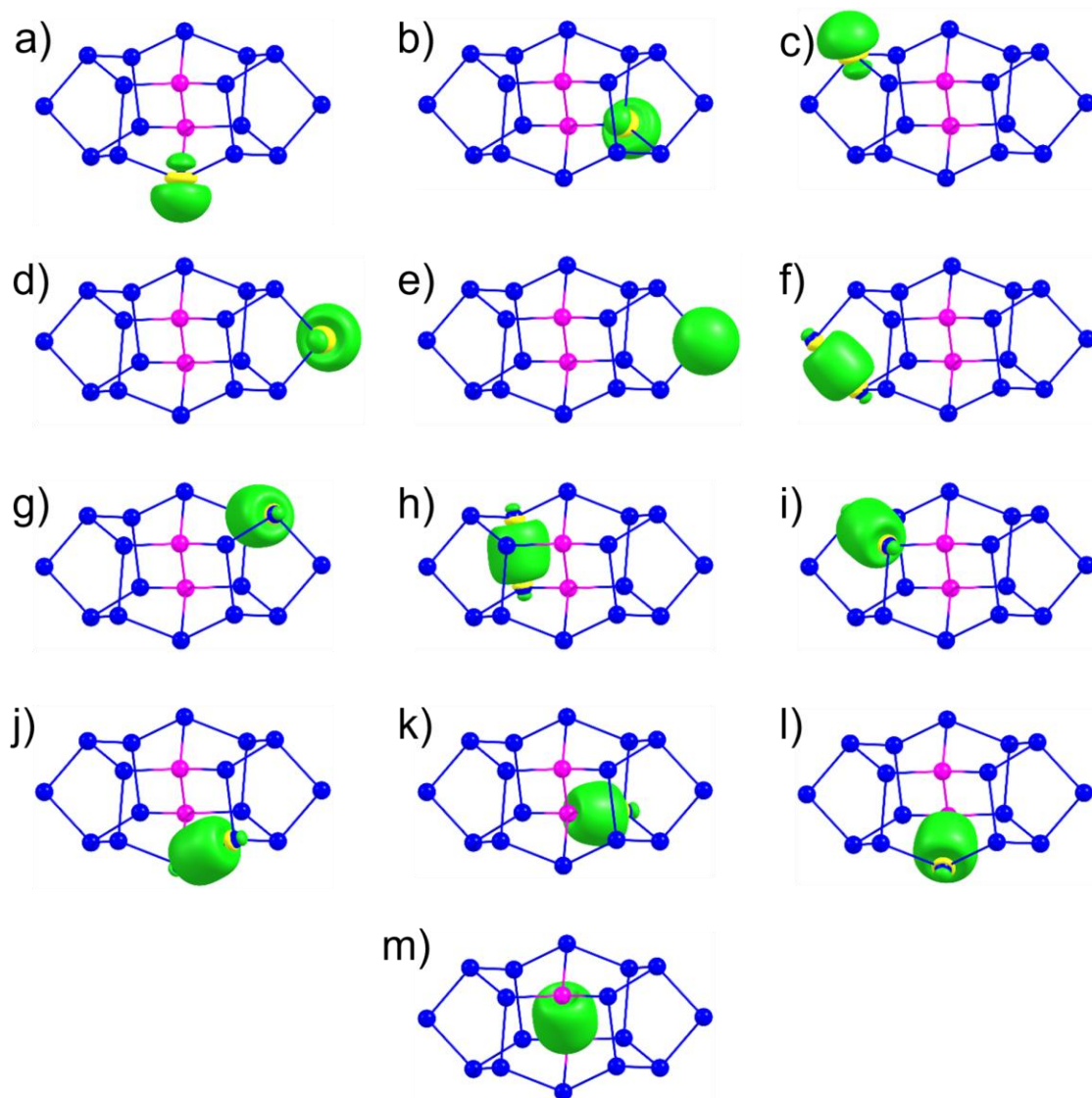


Figure 7.51: Representative LMOs of the cluster anion $(\text{Ga}_2\text{Bi}_{16})^{4-}$ in the compounds $[\text{K}(\text{crypt-222})]_4\mathbf{11a}$ and $[\text{K}(\text{crypt-222})]_4\mathbf{11b} \cdot 4\text{py}$ (Ga: pink, Bi: blue): lone pairs at Bi atoms (a - e), homopolar Bi–Bi bonds (f - j), Ga–Bi bonds that are slightly polarized towards the Bi atom (k, l), and the homopolar Ga–Ga bond (m).

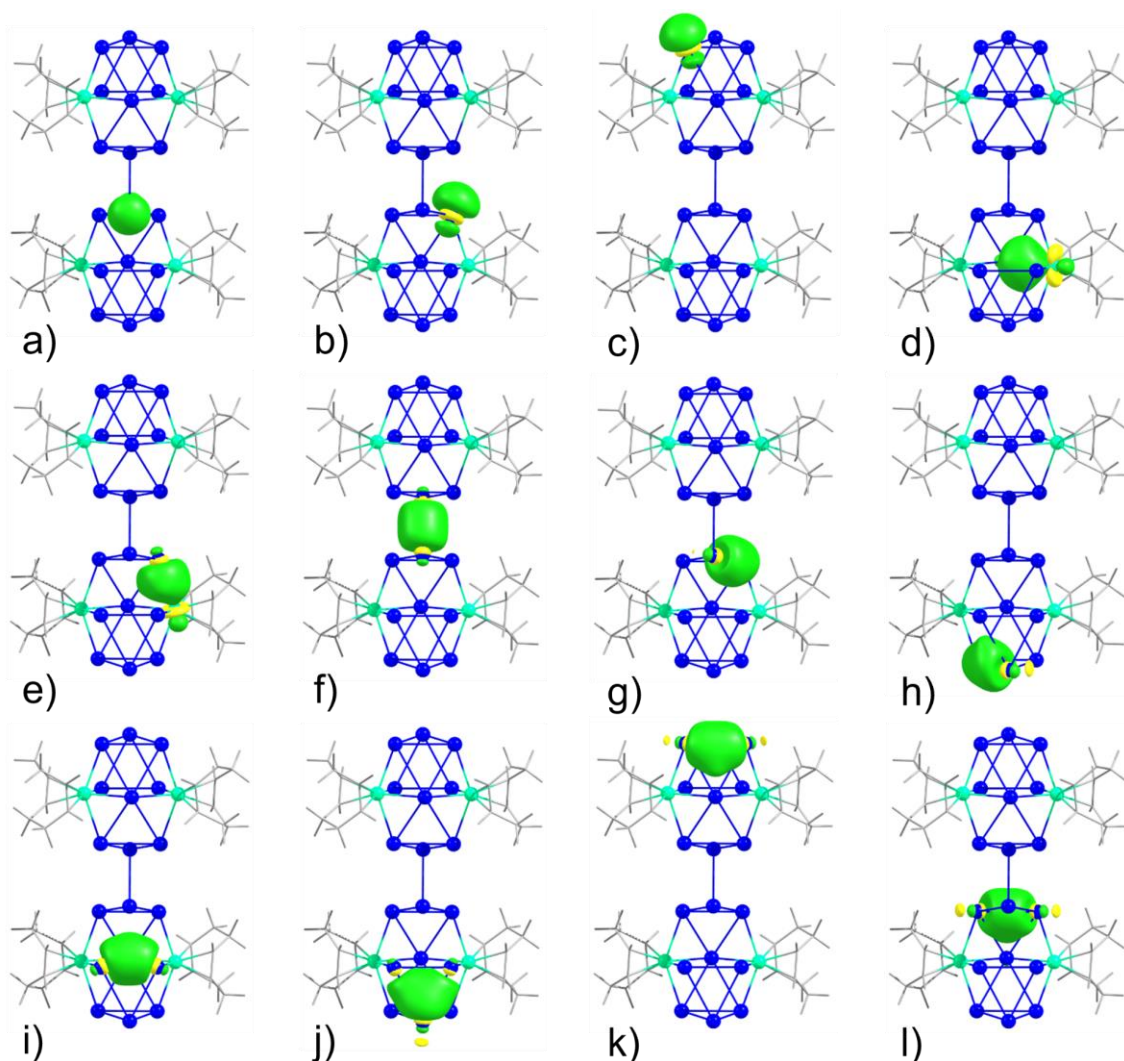


Figure 7.52: Representative LMOs of the cluster anion $[\{(\text{cod})\text{Ru}\}_4\text{Bi}_{18}]^{4-}$ in compound $[\text{K}(\text{crypt-222})]_4\mathbf{12a} \cdot 4.63\text{THF} \cdot 2\text{en}$ (Ru: turquoise, Bi: blue, organic groups as grey/white (C/H) wire-representation): lone pairs at Bi atoms (a - c), Ru-Bi bonds that are strongly polarized towards the Bi atoms (d, e), two-center-two-electron Bi-Bi bonds (f, g), two-center-two-electron Bi-Bi bonds with polarization towards a third Bi atom (h, i), three-center-two-electron Bi-Bi-Bi bonds (j - l). Note: Rotation around the central Bi1-Bi1' bond does not affect the bonding situation within the two subunits, nor does it change the quality of the Bi1-Bi1' bond. Only the LMOs of the anion in compound $[\text{K}(\text{crypt-222})]_4\mathbf{12a} \cdot 4.63\text{THF} \cdot 2\text{en}$ are shown herein.

7.4.4 Compound $[\text{K}(\text{crypt-222})]_2\mathbf{13} \cdot \text{solv}$

7.4.4.1 Methods

The optimizations of the geometric and electronic structures (all without symmetry restrictions) were performed by employing density functional theory (DFT) methods.^[313,314] Calculations were done by using the program system Turbomole^[345] and applying the TPSS functional,^[315] as well as dhf-TZVP basis sets^[316,317] with corresponding auxiliary bases^[318] and effective core potentials^[347,348] at the Ru, Rh, and Bi atoms. The negative charges were compensated with

COSMO^[320] (standard values, $\varepsilon = \infty$). Localized molecular orbitals (LMOs) were calculated using Boys' method.^[292] Mulliken analyses,^[321] natural population analyses (NPA),^[322] and population analyses based on occupation numbers (Paboon)^[323] were employed to further investigate the electronic structures.

All structures were initially optimized without any symmetry restrictions. Bi_2^{2-} and anion $\mathbf{13}^{2-}$ were re-optimized under consideration of the respective higher symmetries (D_{6h} and C_i).

7.4.4.2 Detailed DFT Studies

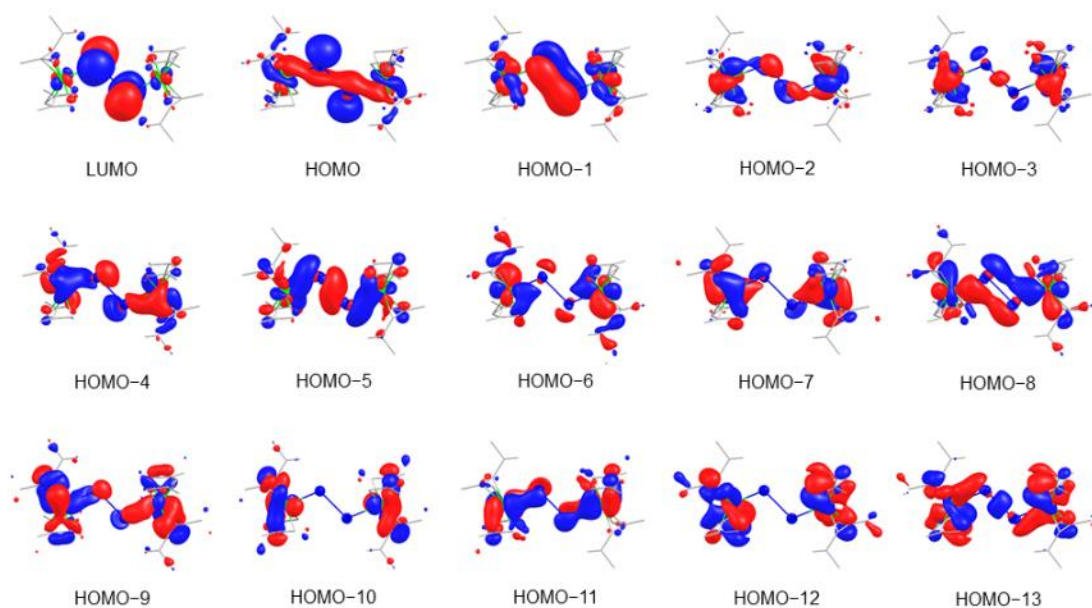


Figure 7.53: Calculated canonical orbitals of complex anion $\mathbf{13}^{2-}$. Only the orbitals with significant Ru or Bi contribution are shown. H atoms are omitted for clarity. Contour values are drawn at ± 0.05 a.u.

Table 7.64: NPA charges at the heavy atoms in complex anion $\mathbf{13}^{2-}$.

Atom Charge	
Bi1	-0.25
Bi1'	-0.25
Ru1	-0.01
Ru1'	-0.01

Bibliography

- [1] M. Joannis, *Hebd. Seances Acad. Sci.* **1891**, 113, 795–798.
- [2] C. A. Kraus, *J. Am. Chem. Soc.* **1922**, 44, 1216–1239.
- [3] F. H. Smyth, *J. Am. Chem. Soc.* **1917**, 39, 1299–1312.
- [4] C. A. Kraus, *Trans. Am. Electrochem. Soc.* **1924**, 45, 175–186.
- [5] E. B. Peck, *J. Am. Chem. Soc.* **1918**, 40, 335–346.
- [6] E. Zintl, J. Goubeaul, W. Dullenkop, *Z. Phys. Chem. Abt. A* **1931**, 154, 1–46.
- [7] E. Zintl, A. Harder, *Z. Phys. Chem. Abt. A* **1931**, 154, 47–91.
- [8] L. Diehl, K. Khodadadeh, D. Kummer, J. Strähle, *Z. Naturforsch. B* **1976**, 109, 3404–3418.
- [9] D. Kummer, L. Diehl, *Angew. Chem. Int. Ed.* **1970**, 9, 895.
- [10] J. D. Corbett, D. G. Adolphson, D. J. Merryman, P. A. Edwards, F. J. Armatas, *J. Am. Chem. Soc.* **1975**, 97, 6267–6268.
- [11] P. A. Edwards, J. D. Corbett, *Inorg. Chem.* **1977**, 16, 903–907.
- [12] L. Diehl, K. Khodadadeh, D. Kummer, J. Strähle, *Chem. Ber* **1976**, 109, 3404–3418.
- [13] J. D. Corbett, P. A. Edwards, *J. Am. Chem. Soc.* **1977**, 99, 3313–3317.
- [14] A. K. Tyagi, Raghurani S. Ningthoujam, in *Handb. Synth. Strateg. Adv. Mater.*, **2021**, pp. 741–784.
- [15] C. B. Xiao, Y. F. Han, S. S. Li, J. X. Song, *Mater. Sci. Technol.* **2003**, 19, 1677–1680.
- [16] B. P. Bewlay, M. Weimer, T. Kelly, A. Suzuki, P. R. Subramanian, *Mater. Res. Soc. Symp. Proc* **2013**, 1516, 49–58.
- [17] R. Pöttgen, D. Johrendt, in *Intermet. Walter Gruyter Berlin, Ger.*, **2019**, pp. 35–243.
- [18] U. Mizutani, H. Sato, *Crystals* **2017**, 7, 9, 1–112.
- [19] W. W. Scanlon, *Science* **1963**, 142, 1265–1269.
- [20] F. Stein, A. Leineweber, *J. Mater. Sci.* **2021**, 56, 5321–5427.
- [21] F. Stein, M. Palm, G. Sauthoff, *Intermetallics* **2004**, 12, 713–720.
- [22] H. Schäfer, B. Eisenmann, W. Müller, *Angew. Chem. Int. Ed.* **1973**, 12, 694–712.
- [23] H. Schäfer, *Annu. Rev. Mater. Sci.* **1985**, 15, 1–41.
- [24] H. Schäfer, *J. Solid State Chem.* **1985**, 57, 97–111.

-
- [25] S. M. Kauzlarich, *Chem. Mater.* **2023**, *35*, 7355–7362.
- [26] F. W. Dorn, W. Klemm, *Z. Anorg. Allg. Chem.* **1961**, *309*, 189–203.
- [27] W. Dahlmann, H. G. v. Schnering, *Naturwissenschaften* **1972**, *59*, 420.
- [28] W. Hönlle, J. Buresch, J. Wolf, K. Peters, J. H. Chang, H. G. von Schnering, *Z. Krist. - New Cryst. Struct.* **2002**, *217*, 489–490.
- [29] F. Emmerling, C. Röhr, *Z. Naturforsch.* **2002**, *57b*, 963–975.
- [30] R. S. P. Turbervill, J. M. Goicoechea, *Chem. Rev.* **2014**, *114*, 10807–10828.
- [31] W. Dahlmann, H. G. v. Schnering, *Naturwissenschaften* **1973**, *60*, 429.
- [32] W. Schmettow, H. G. von Schnering, *Angew. Chem. Int. Ed.* **1977**, *16*, 857.
- [33] V. Manriquez, W. Hönlle, H. G. von Schnering, *Z. Anorg. Allg. Chem.* **1986**, *539*, 95–109.
- [34] R. P. Santandrea, C. Mensing, H. G. Von Schnering, *Thermochim. Acta* **1986**, *98*, 301–311.
- [35] T. Meyer, W. Hönlle, H. G. von Schnering, *Z. Anorg. Allg. Chem.* **1987**, *552*, 69–80.
- [36] C. Hirschle, C. Röhr, *Z. Anorg. Allg. Chem.* **2000**, *626*, 1992–1998.
- [37] W. Hönlle, J. Buresch, K. Peters, J. H. Chang, H. G. von Schnering, *Z. Krist. - New Cryst. Struct.* **2002**, *217*, 485–486.
- [38] W. Hönlle, J. Buresch, K. Peters, J. H. Chang, H. G. von Schnering, *Z. Krist. - New Cryst. Struct.* **2002**, *217*, 487–488.
- [39] O. Sichevych, L. Akselrud, B. Böhme, M. Bobnar, M. Baitinger, F. R. Wagner, Y. Grin, *Z. Anorg. Allg. Chem.* **2023**, *649*, e202300116.
- [40] P. Bordet, M. Affronte, S. Sanfilippo, M. Núñez-Regueiro, O. Laborde, G. L. Olcese, A. Palenzona, S. LeFloch, D. Levy, M. Hanfland, *Phys. Rev. B* **2008**, *81*, 392–397.
- [41] S. J. Kim, M. G. Kanatzidis, *Inorg. Chem.* **2001**, *40*, 3781–3785.
- [42] Z. Weiss, M. Rieder, L. U. Smrcok, V. Petricek, *Z. Krist. - New Cryst. Struct.* **2005**, *220*, 324–326.
- [43] N. Lichtenberger, Y. J. Franzke, W. Massa, F. Weigend, S. Dehnen, *Chem. Eur. J.* **2018**, *24*, 12022–12030.
- [44] L. Xu, S. C. Sevov, *Inorg. Chem.* **2000**, *39*, 5383–5389.
- [45] M. M. Gillett-Kunnath, J. I. Paik, S. M. Jensen, J. D. Taylor, S. C. Sevov, *Inorg. Chem.* **2011**, *50*, 11695–11701.
- [46] S. Joseph, C. Suchentrunk, F. Kraus, N. Korber, *Eur. J. Inorg. Chem.* **2009**, 4641–4647.
- [47] T. Hanauer, M. Grothe, M. Reil, N. Korber, *Helv. Chim. Acta* **2005**, *88*, 950–961.
- [48] J. M. Goicoechea, S. C. Sevov, *Inorg. Chem.* **2005**, *44*, 2654–2658.

- [49] J. M. Goicoechea, S. C. Sevov, *J. Am. Chem. Soc.* **2004**, *126*, 6860–6861.
- [50] S. C. Critchlow, J. D. Corbett, *Inorg. Chem.* **1982**, *21*, 3286–3290.
- [51] D. G. Adolphson, J. D. Corbett, D. J. Merryman, *J. Am. Chem. Soc.* **1976**, *98*, 7234–7239.
- [52] R. Schäfer, W. Klemm, *Z. Anorg. Allg. Chem.* **1961**, *312*, 214–220.
- [53] E. Busmann, *Z. Anorg. Allg. Chem.* **1961**, *313*, 90–106.
- [54] H. G. von Schnering, M. Schwarz, J. H. Chang, K. Peters, E. M. Peters, R. Nesper, *Z. Krist. - New Cryst. Struct.* **2005**, *220*, 525–527.
- [55] T. Goebel, Y. Prots, F. Haarmann, *Z. Krist. - New Cryst. Struct.* **2008**, *223*, 187–188.
- [56] Y. Grin, M. Baitinger, R. Kniep, H. G. Von Schnering, *Z. Krist. - New Cryst. Struct.* **1999**, *214*, 453–454.
- [57] R. E. Marsh, D. P. Shoemaker, *Acta Crystallogr.* **1953**, *6*, 197–205.
- [58] C. H. E. Belin, J. D. Corbett, A. Cisar, *J. Am. Chem. Soc.* **1977**, *99*, 7163–7169.
- [59] R. Adolph, *Chem. Ber.* **2016**, *3418*, 1–23.
- [60] N. Korber, A. Fleischmann, *J. Chem. Soc., Dalt. Trans.*, **2001**, 383–385.
- [61] T. F. Fässler, R. Hoffmann, *J. Chem. Soc., Dalt. Trans.*, **1999**, 3339–3340.
- [62] J. Campbell, D. A. Dixon, H. P. A. Mercier, G. J. Schrobilgen, *Inorg. Chem.* **1995**, *34*, 5798–5809.
- [63] L. Yong, S. D. Hoffmann, T. F. Fässler, *Inorganica Chim. Acta* **2006**, *359*, 4774–4778.
- [64] M. Somer, W. Carrillo-Cabrera, E. M. Peters, K. Peters, H. G. von Schnering, *Z. Anorg. Allg. Chem.* **1998**, *624*, 1105–1110.
- [65] C. Downie, J. Mao, A. M. Guloy, *Inorg. Chem.* **2001**, *32*, 4721–4725.
- [66] C. Suchentrunk, J. Daniels, M. Somer, W. Carrillo-Cabrera, N. Korber, *Z. Naturforsch.* **2005**, *60*, 277–283.
- [67] W. Carrillo-Cabrera, U. Aydemir, M. Somer, A. Kircali, T. F. Fässler, S. D. Hoffmann, *Z. Anorg. Allg. Chem.* **2007**, *633*, 1575–1580.
- [68] T. F. Fässler, R. Hoffmann, *Angew. Chem. Int. Ed.* **1999**, *111*, 526–529.
- [69] R. C. Burns, J. D. Corbett, *Inorg. Chem.* **1985**, *3*, 1489–1492.
- [70] F. Lissner, I. Hartenbach, T. Schleid, *Z. Anorg. Allg. Chem.* **2002**, *628*, 1500–1504.
- [71] T. F. Fässler, *Z. Anorg. Allg. Chem.* **2001**, *627*, 2220–2224.
- [72] M. Driess, K. Merz, H. Pritzkow, R. Janoschek, *Angew. Chem. Int. Ed.* **1996**, *35*, 2507–2510.
- [73] S. C. Critchlow, J. D. Corbett, *Inorg. Chem.* **1984**, *23*, 770–774.

-
- [74] L. G. Perla, A. G. Oliver, S. C. Sevov, *Inorg. Chem.* **2015**, *54*, 872–875.
- [75] N. Korber, J. Daniels, *Acta Crystallogr. Sect. C Cryst. Struct. Commun.* **1996**, *52*, 2454–2457.
- [76] N. Korber, J. Daniels, *Z. Anorg. Allg. Chem.* **1999**, *625*, 189–191.
- [77] F. Kraus, N. Korber, *Chem. Eur. J.* **2005**, *11*, 5945–5959.
- [78] N. Korber, H. Georg, R. Liquid, *Chem. Ber.* **1996**, *49*, 155–159.
- [79] N. Korber, J. Daniels, *Helv. Chim. Acta* **1996**, *79*, 2083–2087.
- [80] U. Bonn, A. Chemie, D.- Bonn, *Z. Krist. - Cryst. Mater.* **1997**, *212*, 139–140.
- [81] K. Hübler, G. Becker, *Z. Anorg. Allg. Chem.* **1998**, *624*, 1492–1496.
- [82] N. Lichtenberger, N. Spang, A. Eichhöfer, S. Dehnen, *Angew. Chem. Int. Ed.* **2017**, *56*, 13253–13258.
- [83] S. Mitzinger, J. Bandemehr, K. Reiter, J. Scott McIndoe, X. Xie, F. Weigend, J. F. Corrigan, S. Dehnen, *Chem. Commun.* **2018**, *54*, 1421–1424.
- [84] S. Mitzinger, L. Broeckert, W. Massa, F. Weigend, S. Dehnen, *Nat. Commun.* **2016**, *7*, 10480–10490.
- [85] K. Beuthert, F. Pan, L. Guggolz, R. J. Wilson, J. Hempelmann, R. Dronskowski, S. Dehnen, *Angew. Chem. Int. Ed.* **2022**, *61*, e202207232.
- [86] F. Lips, I. Schellenberg, R. Pöttgen, S. Dehnen, *Chem. Eur. J.* **2009**, *15*, 12968–12973.
- [87] F. Lips, M. Raupach, W. Massa, S. Dehnen, *Z. Anorg. Allg. Chem.* **2011**, *637*, 859–863.
- [88] S. C. Critchlow, J. D. Corbett, *Inorg. Chem.* **1985**, *24*, 979–981.
- [89] R. Ababei, J. Heine, M. Holynska, G. Thiele, B. Weinert, X. Xie, F. Weigend, S. Dehnen, *Chem. Commun.* **2012**, *48*, 11295–11297.
- [90] K. Beuthert, B. Weinert, R. J. Wilson, F. Weigend, S. Dehnen, *Inorg. Chem.* **2023**, *62*, 1885–1890.
- [91] Y. R. Lohse, B. Weinert, B. Peerless, S. Dehnen, *Z. Anorg. Allg. Chem.* **2024**, *650*, e202300229.
- [92] U. Friedrich, M. Neumeier, C. Koch, N. Korber, *Chem. Commun.* **2012**, *48*, 10544–10546.
- [93] R. J. Wilson, F. Weigend, S. Dehnen, *Angew. Chem. Int. Ed.* **2020**, *59*, 14251–14255.
- [94] U. Friedrich, N. Korber, *ChemistryOpen* **2016**, *5*, 306–310.
- [95] F. Lips, S. Dehnen, *Angew. Chem. Int. Ed.* **2009**, *48*, 6435–6438.
- [96] B. Peerless, A. Schmidt, Y. J. Franzke, S. Dehnen, *Nat. Chem.* **2023**, *15*, 347–356.
- [97] A. Schmidt, B. Peerless, S. Dehnen, *Z. Anorg. Allg. Chem.* **2023**, *649*, e202300121.

- [98] L. Xu, S. Bobev, J. El-Bahraoui, S. C. Sevov, *J. Am. Chem. Soc.* **2000**, *122*, 1838–1839.
- [99] C. B. Benda, T. F. Fässler, *Z. Anorg. Allg. Chem.* **2014**, *640*, 40–45.
- [100] T. Hanauer, N. Korber, *Z. Anorg. Allg. Chem.* **2004**, *630*, 2532–2534.
- [101] S. C. Sevov, J. M. Goicoechea, *Organometallics* **2006**, *25*, 5678–5692.
- [102] A. Schnepf, *Eur. J. Inorg. Chem.* **2008**, 1007–1018.
- [103] C. Schenk, A. Schnepf, *Chem. Commun.* **2009**, *9*, 3208–3210.
- [104] C. Schrenk, I. Schellenberg, R. Pöttgen, A. Schnepf, *Dalton. Trans.* **2010**, *39*, 1872–1876.
- [105] O. Kysliak, C. Schrenk, A. Schnepf, *Inorg. Chem.* **2015**, *54*, 7083–7088.
- [106] L. G. Perla, S. C. Sevov, *J. Am. Chem. Soc.* **2016**, *138*, 9795–9798.
- [107] L. J. Schiegerl, F. S. Geitner, C. Fischer, W. Klein, T. F. Fässler, *Z. Anorg. Allg. Chem.* **2016**, *642*, 1419–1426.
- [108] O. Kysliak, A. Schnepf, *Dalton. Trans.* **2016**, *45*, 2404–2408.
- [109] O. Kysliak, T. Kunz, A. Schnepf, *Eur. J. Inorg. Chem.* **2017**, *2017*, 805–810.
- [110] F. Li, S. C. Sevov, *J. Am. Chem. Soc.* **2014**, *136*, 12056–12063.
- [111] A. Schnepf, *Angew. Chem. Int. Ed.* **2003**, *42*, 2624–2625.
- [112] R. J. Wilson, N. Lichtenberger, B. Weinert, S. Dehnen, *Chem. Rev.* **2019**, *119*, 8506–8554.
- [113] J. E. McGrady, F. Weigend, S. Dehnen, *Chem. Soc. Rev.* **2022**, *51*, 628–649.
- [114] D. E. C. Corbridge, *Phosphorus: Chemistry, Biochemistry and Technology, Sixth Edition*, CRC Press, **2013**.
- [115] M. Scheer, G. Balázs, A. Seitz, *Chem. Rev.* **2010**, *110*, 4236–4256.
- [116] T. Li, S. Kaercher, P. W. Roesky, *Chem. Soc. Rev.* **2014**, *43*, 42–57.
- [117] P. Dapporto, S. Midollini, L. Sacconi, *Angew. Chem. Int. Ed.* **1979**, *18*, 469.
- [118] L. C. Forfar, T. J. Clark, M. Green, S. M. Mansell, C. A. Russell, R. A. Sanguramath, J. M. Slattery, *Chem. Commun.* **2012**, *48*, 1970–1972.
- [119] F. Spitzer, M. Sierka, M. Latronico, P. Mastorilli, A. V. Virovets, M. Scheer, *Angew. Chem. Int. Ed.* **2015**, *54*, 4392–4396.
- [120] Y. Xiong, S. Yao, M. Brym, M. Driess, *Angew. Chem. Int. Ed.* **2007**, *46*, 4511–4513.
- [121] P. Trans, D. B. Clark, M. Fleischmann, D. Pletcher, B. R. Riedel, H. Hausen, *Angew. Chem. Int. Ed.* **1985**, *80*, 1056–1057.
- [122] H. W. Lerner, M. Bolte, *Acta Crystallogr.* **2007**, *E63*, 2006–2007.

-
- [123] M. P. Nrar, C. E. Laplaza, W. M. Davis, C. C. Cummins, *Angew. Chem. Int. Ed.* **1995**, 3–5.
- [124] L. Giusti, V. R. Landaeta, M. Vanni, J. A. Kelly, R. Wolf, M. Caporali, *Coord. Chem. Rev.* **2021**, 441, 213927–214026.
- [125] A. Belendorf, *Ann. Chem. Pharm.* **1867**, 144, 110–114.
- [126] Y. Morino, T. Ukaji, T. Ito, *Bull. Chem. Soc. Jpn.* **1966**, 39, 64–71.
- [127] C. Schwarzmaier, A. Schindler, C. Heindl, S. Scheuermayer, E. V. Peresyphkina, A. V. Virovets, M. Neumeier, R. Gschwind, M. Scheer, *Angew. Chem. Int. Ed.* **2013**, 52, 10896–10899.
- [128] D. Yang, J. Zhao, L. Yu, X. Lin, W. Zhang, H. Ma, A. Gogoll, Z. Zhang, Y. Wang, X. J. Yang, B. Wu, *J. Am. Chem. Soc.* **2017**, 139, 5946–5951.
- [129] C. Schwarzmaier, A. Y. Timoshkin, M. Scheer, *Angew. Chem. Int. Ed.* **2013**, 52, 7600–7603.
- [130] C. Schwarzmaier, M. Sierka, M. Scheer, *Angew. Chem. Int. Ed.* **2013**, 52, 858–861.
- [131] M. Seidl, G. Balázs, M. Scheer, *Chem. Rev.* **2019**, 119, 8406–8434.
- [132] V. Queneau, S. C. Sevov, *J. Am. Chem. Soc.* **1997**, 119, 8109–8110.
- [133] E. Todorov, S. C. Sevov, *Angew. Chem. Int. Ed.* **1999**, 38, 1775–1777.
- [134] U. Zachwieja, M. Jürgen, J. Wlodarski, *Z. Anorg. Allg. Chem.* **1998**, 624, 853–858.
- [135] F. Fendt, C. Koch, S. Gärtner, N. Korber, *J. Chem. Soc. Dalton. Trans.* **2013**, 42, 15548–15550.
- [136] C. B. Benda, M. Waibel, T. Köchner, T. F. Fässler, *Chem. Eur. J.* **2014**, 20, 16738–16746.
- [137] T. Henneberger, W. Klein, J. V. Dums, T. F. Fässler, *Chem. Commun.* **2018**, 54, 12381–12384.
- [138] M. Waibel, F. Kraus, S. Scharfe, B. Wahl, T. F. Fässler, *Angew. Chem. Int. Ed.* **2010**, 49, 6611–6615.
- [139] M. Waibel, G. Raudaschl-Sieber, T. F. Fässler, *Chem. Eur. J.* **2011**, 17, 13391–13394.
- [140] S. Stegmaier, M. Waibel, A. Henze, L.-A. Jantke, A. J. Karttunen, T. F. Fässler, *J. Am. Chem. Soc.* **2012**, 134, 14450–14460.
- [141] H. Xu, I. A. Popov, N. V. Tkachenko, Z. Wang, A. Muñoz-Castro, A. I. Boldyrev, Z. Sun, *Angew. Chem. Int. Ed.* **2020**, 132, 17439–17443.
- [142] C. Knapp, B. Zhou, M. S. Denning, N. H. Rees, J. M. Goicoechea, *Dalton. Trans.* **2010**, 39, 426–436.
- [143] S. Mandal, A. C. Reber, M. Qian, R. Liu, H. M. Saavedra, S. Sen, P. S. Weiss, S. N. Khanna, A. Sen, *Dalton. Trans.* **2012**, 41, 12365–12377.

- [144] N. Lichtenberger, W. Massa, S. Dehnen, *Angew. Chem. Int. Ed.* **2019**, *58*, 3222–3226.
- [145] F. Pan, R. Ababei, W. Massa, S. Dehnen, *Eur. J. Inorg. Chem.* **2024**, *27*, 14–19.
- [146] C. M. Knapp, J. S. Large, N. H. Rees, J. M. Goicoechea, *Dalton. Trans.* **2011**, *40*, 735–745.
- [147] C. M. Knapp, C. S. Jackson, J. S. Large, A. L. Thompson, J. M. Goicoechea, *Inorg. Chem.* **2011**, *50*, 4021–4028.
- [148] N. K. Chaki, S. Mandal, A. C. Reber, M. Qian, H. M. Saavedra, P. S. Weiss, S. N. Khanna, A. Sen, *ACS Nano* **2010**, *4*, 5813–5818.
- [149] S. Charles, B. W. Eichhorn, A. L. Rheingold, S. G. Bott, *J. Am. Chem. Soc.* **1994**, *116*, 8077–8086.
- [150] M. J. Moses, J. Fetting, B. Eichhorn, *J. Am. Chem. Soc.* **2002**, *124*, 5944–5945.
- [151] M. J. Moses, J. C. Fetting, B. W. Eichhorn, *Inorg. Chem.* **2007**, *46*, 1036–1038.
- [152] B. W. Eichhorn, S. P. Mattamana, D. R. Gardner, J. C. Fetting, *J. Am. Chem. Soc.* **1998**, *120*, 9708–9709.
- [153] B. Kesanli, J. Fetting, B. Eichhorn, *J. Am. Chem. Soc.* **2003**, *125*, 7367–7376.
- [154] B. Kesanli, J. Fetting, B. Scott, B. Eichhorn, *Inorg. Chem.* **2004**, *43*, 3840–3846.
- [155] M. J. Moses, J. C. Fetting, B. W. Eichhorn, *Science* **2003**, *300*, 778–780.
- [156] Y. Wang, M. Moses-DeBusk, L. Stevens, J. Hu, P. Zavalij, K. Bowen, B. I. Dunlap, E. R. Glaser, B. Eichhorn, *J. Am. Chem. Soc.* **2017**, *139*, 619–622.
- [157] Z. Li, H. Ruan, L. Wang, C. Liu, L. Xu, *Dalton. Trans.* **2017**, *46*, 3453–3456.
- [158] S. Scharfe, F. Kraus, S. Stegmaier, A. Schier, T. F. Fässler, *Angew. Chem. Int. Ed.* **2011**, *50*, 3630–3670.
- [159] V. Angilella, C. Belin, *J. Chem. Soc. Faraday Trans.* **1991**, *87*, 203–204.
- [160] T. F. Fässler, M. Hunziker, *Inorg. Chem.* **1994**, *33*, 5380–5381.
- [161] T. F. Fässler, U. Schütz, *Inorg. Chem.* **1999**, *38*, 1866–1870.
- [162] A. Ugrinov, S. C. Sevov, *Chem. Eur. J.* **2004**, *10*, 3727–3733.
- [163] L. Xu, S. C. Sevov, *J. Am. Chem. Soc.* **1999**, *121*, 9245–9246.
- [164] R. Hauptmann, T. F. Fässler, *Z. Anorg. Allg. Chem.* **2003**, *629*, 2266–2273.
- [165] A. Ugrinov, S. C. Sevov, *J. Am. Chem. Soc.* **2002**, *124*, 10990–10991.
- [166] L. Yong, S. D. Hoffmann, T. F. Fässler, *Z. Anorg. Allg. Chem.* **2005**, *631*, 1149–1153.
- [167] A. Ugrinov, S. C. Sevov, *Inorg. Chem.* **2003**, *42*, 5789–5791.
- [168] C. Downie, J.-G. Mao, H. Parmar, A. M. Guloy, *Inorg. Chem.* **2004**, *43*, 1992–1997.

-
- [169] A. Nienhaus, R. Hauptmann, T. F. Fässler, *Angew. Chem. Int. Ed.* **2002**, *41*, 3213–3215.
- [170] C. Downie, Z. Tang, A. M. Guloy, *Angew. Chem. Int. Ed.* **2000**, *39*, 337–340.
- [171] A. Ugrinov, S. C. Sevov, *J. Am. Chem. Soc.* **2003**, *125*, 14059–14064.
- [172] B. W. Eichhorn, R. C. Haushalter, W. T. Pennington, *J. Am. Chem. Soc.* **1988**, *110*, 8704–8706.
- [173] B. W. Eichhorn, R. C. Haushalter, *J. Chem. Soc. Chem. Commun.* **1990**, 937–938.
- [174] J. Campbell, H. P. A. Mercier, H. Franke, D. P. Santry, D. A. Dixon, G. J. Schrobilgen, *Inorg. Chem.* **2002**, *41*, 86–107.
- [175] L. Yong, S. D. Hoffmann, T. F. Fässler, *Eur. J. Inorg. Chem.* **2005**, *2005*, 3663–3669.
- [176] L. Yong, S. D. Hoffmann, T. F. Fässler, *Z. Krist. - New Cryst. Struct.* **2005**, *220*, 53–57.
- [177] J. M. Goicoechea, S. C. Sevov, *Organometallics* **2006**, *25*, 4530–4536.
- [178] H. He, W. Klein, L. Jantke, T. F. Fässler, *Z. Anorg. Allg. Chem.* **2014**, *640*, 2864–2870.
- [179] J. M. Goicoechea, S. C. Sevov, *J. Am. Chem. Soc.* **2006**, *128*, 4155–4161.
- [180] D. Rios, M. M. Gillett-Kunnath, J. D. Taylor, A. G. Oliver, S. C. Sevov, *Inorg. Chem.* **2011**, *50*, 2373–2377.
- [181] S. Scharfe, T. F. Fässler, S. Stegmaier, S. D. Hoffmann, K. Ruhland, *Chem. Eur. J.* **2008**, *14*, 4479–4483.
- [182] C. Liu, L. Li, X. Jin, J. E. McGrady, Z. Sun, *Inorg. Chem.* **2018**, *57*, 3025–3034.
- [183] B. Kesanli, J. Fettingner, D. R. Gardner, B. Eichhorn, *J. Am. Chem. Soc.* **2002**, *124*, 4779–4786.
- [184] E. N. Esenturk, J. Fettingner, B. Eichhorn, *Polyhedron* **2006**, *25*, 521–529.
- [185] F. S. Kocak, P. Zavalij, B. Eichhorn, *Chem. Eur. J.* **2011**, *17*, 4858–4863.
- [186] Z. Sun, Y. Zhao, J. Li, L. Wang, *J. Clust. Sci.* **2009**, *20*, 601–609.
- [187] F. Li, S. C. Sevov, *Inorg. Chem.* **2015**, *54*, 8121–8125.
- [188] F. Henke, C. Schenk, A. Schnepf, *Dalton. Trans.* **2011**, *40*, 6704–6710.
- [189] O. Kysliak, D. D. Nguyen, A. Z. Clayborne, A. Schnepf, *Inorg. Chem.* **2018**, *57*, 12603–12609.
- [190] M. Binder, C. Schrenk, T. Block, R. Pöttgen, A. Schnepf, *Chem. Commun.* **2017**, *53*, 11314–11317.
- [191] E. N. Esenturk, J. Fettingner, Y.-F. Lam, B. Eichhorn, *Angew. Chem. Int. Ed.* **2004**, *43*, 2132–2134.
- [192] E. N. Esenturk, J. Fettingner, B. Eichhorn, *J. Am. Chem. Soc.* **2006**, *128*, 9178–9186.
- [193] C. Liu, X. Jin, L. Li, J. Xu, J. E. McGrady, Z. Sun, *Chem. Sci.* **2019**, *10*, 4394–4401.

- [194] J. Wang, S. Stegmaier, B. Wahl, T. F. Fässler, *Chem. Eur. J.* **2010**, *16*, 1793–1798.
- [195] C. Liu, L. Li, I. A. Popov, R. J. Wilson, C. Xu, J. Li, A. I. Boldyrev, Z. Sun, *Chinese J. Chem.* **2018**, *36*, 1165–1168.
- [196] L. Li, F. Pan, F. Li, Z. Chen, Z. Sun, *Inorg. Chem. Front.* **2017**, *4*, 1393–1396.
- [197] B. Zhou, T. Krämer, A. L. Thompson, J. E. McGrady, J. M. Goicoechea, *Inorg. Chem.* **2011**, *50*, 8028–8037.
- [198] G. Espinoza-Quintero, J. C. A. Duckworth, W. K. Myers, J. E. McGrady, J. M. Goicoechea, *J. Am. Chem. Soc.* **2014**, *136*, 1210–1213.
- [199] J. M. Goicoechea, S. C. Sevov, *J. Am. Chem. Soc.* **2005**, *127*, 7676–7677.
- [200] Z. Sun, H. Xiao, J. Li, L. Wang, *J. Am. Chem. Soc.* **2007**, *129*, 9560–9561.
- [201] L. Guggolz, S. Dehnen, *Chem. Eur. J.* **2020**, *26*, 11819–11828.
- [202] B. Cordero, V. Gómez, A. E. Platero-Prats, M. Revés, J. Echeverría, E. Cremades, F. Barragán, S. Alvarez, *Dalton. Trans.* **2008**, 2832–2838.
- [203] A. L. Allred, *J. Inorg. Nucl. Chem.* **1961**, *17*, 215–221.
- [204] T. Andersen, H. K. Haugen, H. Hotop, *J. Phys. Chem. Ref. Data* **1999**, *28*, 1511–1533.
- [205] R. Tang, X. Fu, Y. Lu, C. Ning, *J. Chem. Phys.* **2020**, *152*, 114303.
- [206] C. W. Walter, N. D. Gibson, D. J. Carman, Y.-G. Li, D. J. Matyas, *Phys. Rev. A* **2010**, *82*, 32507.
- [207] C. W. Walter, N. D. Gibson, S. E. Spielman, *Phys. Rev. A* **2020**, *101*, 52511.
- [208] F. Pan, L. Guggolz, F. Weigend, S. Dehnen, *Angew. Chem. Int. Ed.* **2020**, *59*, 16638–16643.
- [209] S. Mitzinger, L. Broeckaert, W. Massa, F. Weigend, S. Dehnen, *Chem. Commun.* **2015**, *51*, 3866–3869.
- [210] F. Pan, L. Li, Z. Sun, *Chin. J. Struct. Chem.* **2016**, *35*, 1099–1106.
- [211] F. Pan, M. Lukanowski, F. Weigend, S. Dehnen, *Angew. Chem. Int. Ed.* **2021**, *60*, 25042–25047.
- [212] R. J. Wilson, L. Broeckaert, F. Spitzer, F. Weigend, S. Dehnen, *Angew. Chem. Int. Ed.* **2016**, *55*, 11775–11780.
- [213] Y. Xu, N. V. Tkachenko, I. A. Popov, L. Qiao, A. Muñoz-Castro, A. I. Boldyrev, Z. Sun, *Nat. Commun.* **2021**, *12*, 4465.
- [214] R. J. Wilson, F. Hastreiter, K. Reiter, P. Büschelberger, R. Wolf, R. M. Gschwind, F. Weigend, S. Dehnen, *Angew. Chem. Int. Ed.* **2018**, *57*, 15359–15363.
- [215] F. Lips, M. Hołyńska, R. Clérac, U. Linne, I. Schellenberg, R. Pöttgen, F. Weigend, S. Dehnen, *J. Am. Chem. Soc.* **2012**, *134*, 1181–1191.

-
- [216] R. Ababei, W. Massa, B. Weinert, P. Pollak, X. Xie, R. Clérac, F. Weigend, S. Dehnen, *Chem. Eur. J.* **2015**, *21*, 386–394.
- [217] N. Lichtenberger, R. J. Wilson, A. R. Eulenstein, W. Massa, R. Clérac, F. Weigend, S. Dehnen, *J. Am. Chem. Soc.* **2016**, *138*, 9033–9036.
- [218] R. J. Wilson, S. Dehnen, *Angew. Chem. Int. Ed.* **2017**, *56*, 3098–3102.
- [219] R. Ababei, W. Massa, K. Harms, X. Xie, F. Weigend, S. Dehnen, *Angew. Chem. Int. Ed.* **2013**, *52*, 13544–13548.
- [220] F. Lips, S. Dehnen, *Angew. Chem. Int. Ed.* **2011**, *50*, 955–959.
- [221] F. Lips, R. Clérac, S. Dehnen, *J. Am. Chem. Soc.* **2011**, *133*, 14168–14171.
- [222] F. Pan, L. Guggolz, S. Dehnen, *CCS Chem.* **2021**, *4*, 809–824.
- [223] F. Pan, L. Guggolz, S. Dehnen, *Nat. Sci.* **2022**, *2*, e202103302.
- [224] A. R. Eulenstein, Y. J. Franzke, N. Lichtenberger, R. J. Wilson, H. L. Deubner, F. Kraus, R. Clérac, F. Weigend, S. Dehnen, *Nat. Chem.* **2021**, *13*, 149–155.
- [225] J. Rienmüller, A. Schmidt, N. J. Yutronkie, R. Clérac, C. G. Werncke, F. Weigend, S. Dehnen, *Angew. Chem. Int. Ed.* **2022**, *61*, e202210683.
- [226] N. V Tkachenko, X. Zhang, L. Qiao, C. Shu, D. Steglenko, A. Muñoz-Castro, Z. Sun, A. I. Boldyrev, *Chem. Eur. J.* **2020**, *26*, 2073–2079.
- [227] B. Weinert, F. Weigend, S. Dehnen, *Chem. Eur. J.* **2012**, *18*, 13589–13595.
- [228] B. Weinert, F. Müller, K. Harms, R. Clérac, S. Dehnen, *Angew. Chem. Int. Ed.* **2014**, *53*, 11979–11983.
- [229] B. Weinert, A. R. Eulenstein, R. Ababei, S. Dehnen, *Angew. Chem. Int. Ed.* **2014**, *53*, 4704–4708.
- [230] A. R. Eulenstein, Y. J. Franzke, P. Bügel, W. Massa, F. Weigend, S. Dehnen, *Nat. Commun.* **2020**, *11*, 5122.
- [231] W. Klemm, *P. Chem. Soc.* **1958**, 329–364.
- [232] K. Wade, *J. Chem. Soc. D Chem. Commun.* **1971**, 792–793.
- [233] D. M. P. MINGOS, *Nat. Phys. Sci.* **1972**, *236*, 99–102.
- [234] K. Wade, in *Struct. Bond. Patterns Clust. Chem.* (Eds.: H.J. Emeléus, A.G. Sharpe, A. in I.C. and Radiochemistry), Academic Press, **1976**, pp. 1–66.
- [235] W. N. Lipscomb, *Science* **1977**, *196*, 1047–1055.
- [236] D. M. P. Mingos, *Acc. Chem. Res.* **1984**, *17*, 311–319.
- [237] D. M. P. Mingos, *J. Chem. Soc. Chem. Commun.* **1983**, 706–708.
- [238] D. M. P. Mingos, *Pure Appl. Chem.* **1991**, *63*, 807–812.

- [239] A. Spiekermann, S. D. Hoffmann, T. F. Fässler, *Angew. Chem. Int. Ed.* **2006**, *45*, 3459–3462.
- [240] S. Bobev, S. C. Sevov, *Angew. Chem. Int. Ed.* **2000**, *39*, 4108–4110.
- [241] M. Waibel, T. Henneberger, L.-A. Jantke, T. F. Fässler, *Chem. Commun.* **2012**, *48*, 8676–8678.
- [242] C. Steffen, K. Thomas, U. Huniar, A. Hellweg, O. Rubner, A. Schroer, *J. Comput. Chem.* **2010**, *31*, 2967–2970.
- [243] C. Wallach, K. Mayer, T. Henneberger, W. Klein, T. F. Fässler, *Dalton. Trans.* **2020**, *49*, 6191–6198.
- [244] Y. Wang, P. Zavalij, B. Eichhorn, *Chem. Commun.* **2018**, *54*, 11917–11920.
- [245] A.-M. Li, Y. Wang, P. Y. Zavalij, F. Chen, A. Muñoz-Castro, B. W. Eichhorn, *Chem. Commun.* **2020**, *56*, 10859–10862.
- [246] P. Zhang, F. Benner, N. F. Chilton, S. Demir, *Chem* **2022**, *8*, 717–730.
- [247] P. Zhang, R. Nabi, J. K. Staab, N. F. Chilton, S. Demir, *J. Am. Chem. Soc.* **2023**, *145*, 9152–9163.
- [248] S. Reichl, C. Riesinger, R. Yadav, A. Y. Timoshkin, P. W. Roesky, M. Scheer, *Angew. Chem. Int. Ed.* **2024**, *63*, e202316117.
- [249] L. Lin, Y. Wang, L. Xu, *Organometallics* **2022**, *41*, 450–455.
- [250] M. Haimerl, C. Graßl, M. Seidl, M. Piesch, M. Scheer, *Chem. Eur. J.* **2021**, *27*, 18129–18134.
- [251] C. Liu, L. J. Li, Q. Pan, Z. Sun, *Chem. Commun.* **2017**, *53*, 6315–6318.
- [252] V. Heintl, M. Schmidt, M. Eckhardt, M. Eberl, A. E. Seitz, G. Balázs, M. Seidl, M. Scheer, *Chem. Eur. J.* **2021**, *27*, 11649–11655.
- [253] S. Scharfe, T. F. Fässler, *Eur. J. Inorg. Chem.* **2010**, *2010*, 1207–1213.
- [254] D. O. Downing, P. Zavalij, B. W. Eichhorn, *Eur. J. Inorg. Chem.* **2010**, *2010*, 890–894.
- [255] Y. Wang, Q. Qin, J. Wang, R. Sang, L. Xu, *Chem. Commun.* **2014**, *50*, 4181–4183.
- [256] H. Jamali, R. Mozafarinia, A. Eshaghi, *J. Alloys Compd.* **2015**, *646*, 360–367.
- [257] Z. Wang, N. V Tkachenko, L. Qiao, E. Matito, A. Muñoz-Castro, A. I. Boldyrev, Z. Sun, *Chem. Commun.* **2020**, *56*, 6583–6586.
- [258] M. W. Hull, S. C. Sevov, *Angew. Chem. Int. Ed.* **2007**, *46*, 6695–6698.
- [259] C. B. Benda, J.-Q. Wang, B. Wahl, T. F. Fässler, *Eur. J. Inorg. Chem.* **2011**, *2011*, 4262–4269.
- [260] M. W. Hull, S. C. Sevov, *J. Am. Chem. Soc.* **2009**, *131*, 9026–9037.
- [261] M. W. Hull, A. Ugrinov, I. Petrov, S. C. Sevov, *Inorg. Chem.* **2007**, *46*, 2704–2708.

-
- [262] M. M. Gillett-Kunnath, A. G. Oliver, S. C. Sevov, *J. Am. Chem. Soc.* **2011**, *133*, 6560–6562.
- [263] A. Hershaft, J. D. Corbett, *Inorg. Chem.* **1963**, *2*, 979–985.
- [264] M. Ruck, *Z. Anorg. Allg. Chem.* **1998**, *624*, 521–528.
- [265] R. C. Burns, R. J. Gillespie, W.-C. Luk, *Inorg. Chem.* **1978**, *17*, 3596–3604.
- [266] B. Krebs, M. Hücke, C. J. Brendel, *Angew. Chem. Int. Ed.* **1982**, *21*, 445–446.
- [267] M. Ruck, S. Hampel, *Polyhedron* **2002**, *21*, 651–656.
- [268] M. Knies, M. Kaiser, A. Isaeva, U. Müller, T. Doert, M. Ruck, *Chem. Eur. J.* **2018**, *24*, 127–132.
- [269] B. Wahl, L. Kloo, M. Ruck, *Angew. Chem. Int. Ed.* **2008**, *47*, 3932–3935.
- [270] B. Wahl, M. Ruck, *Z. Anorg. Allg. Chem.* **2008**, *634*, 2267–2275.
- [271] U. Müller, A. Isaeva, J. Richter, M. Knies, M. Ruck, *Eur. J. Inorg. Chem.* **2016**, *2016*, 3580–3584.
- [272] M. F. Groh, U. Müller, A. Isaeva, M. Ruck, *Z. Anorg. Allg. Chem.* **2019**, *645*, 161–169.
- [273] M. F. Groh, U. Müller, A. Isaeva, M. Ruck, *Z. Anorg. Allg. Chem.* **2017**, *643*, 1482–1490.
- [274] B. Wahl, M. Erbe, A. Gerisch, L. Kloo, M. Ruck, *Z. Anorg. Allg. Chem.* **2009**, *635*, 743–752.
- [275] M. Ruck, V. Dubenskyy, T. Söhnle, *Angew. Chem. Int. Ed.* **2003**, *42*, 2978–2982.
- [276] M. F. Groh, A. Wolff, B. Wahl, B. Rasche, P. Gebauer, M. Ruck, *Z. Anorg. Allg. Chem.* **2017**, *643*, 69–80.
- [277] M. F. Groh, A. Isaeva, C. Frey, M. Ruck, *Z. Anorg. Allg. Chem.* **2013**, *639*, 2401–2405.
- [278] F. Gascoin, S. C. Sevov, *Inorg. Chem.* **2001**, *40*, 5177–5181.
- [279] P. Alemany, M. Llunell, E. Canadell, *Inorg. Chem.* **2005**, *44*, 1644–1646.
- [280] J. M. Goicoechea, S. C. Sevov, *Angew. Chem. Int. Ed.* **2006**, *45*, 5147–5150.
- [281] L. Xu, A. Ugrinov, S. C. Sevov, *J. Am. Chem. Soc.* **2001**, *123*, 4091–4092.
- [282] Z. Li, D. Ouyang, L. Xu, *Chem. Commun.* **2019**, *55*, 6783–6786.
- [283] Z. Li, C. Liu, J. Wu, Z. Lin, L. Xu, *Dalton. Trans.* **2019**, *48*, 12013–12017.
- [284] S. Chen, Z. Li, B. Yuan, L. Lin, M.-H. Whangbo, L. Xu, *Inorg. Chem.* **2020**, *59*, 10628–10633.
- [285] M. Kaas, N. Korber, *Z. Anorg. Allg. Chem.* **2019**, *645*, 146–148.
- [286] J. M. Goicoechea, M. W. Hull, S. C. Sevov, *J. Am. Chem. Soc.* **2007**, *129*, 7885–7893.
- [287] L. G. Perla, S. C. Sevov, *Inorg. Chem.* **2015**, *54*, 8401–8405.

- [288] F. Lips, R. Clérac, S. Dehnen, *Angew. Chem. Int. Ed.* **2011**, *50*, 960–964.
- [289] C. Liu, N. V Tkachenko, I. A. Popov, N. Fedik, X. Min, C. Xu, J. Li, J. E. McGrady, A. I. Boldyrev, Z. Sun, *Angew. Chem. Int. Ed.* **2019**, *58*, 8367–8371.
- [290] J. Tillmann, J. H. Wender, U. Bahr, M. Bolte, H.-W. Lerner, M. C. Holthausen, M. Wagner, *Angew. Chem. Int. Ed.* **2015**, *54*, 5429–5433.
- [291] J. Teichmann, M. Wagner, *Chem. Commun.* **2018**, *54*, 1397–1412.
- [292] S. F. Boys, in *P.O. Löwdin (Ed.), Quantum Theory Atoms, Mol. Solid State, Acad. Press., 1966*, pp. 253–262.
- [293] R. W. Henning, J. D. Corbett, *Inorg. Chem.* **1997**, *36*, 6045–6049.
- [294] A. Cisar, J. D. Corbett, *Inorg. Chem.* **1977**, *16*, 2482–2487.
- [295] B. Twamley, C. D. Sofield, M. M. Olmstead, P. P. Power, *J. Am. Chem. Soc.* **1999**, *121*, 3357–3367.
- [296] H. M. Weinert, C. Wölper, J. Haak, G. E. Cutsail, S. Schulz, *Chem. Sci.* **2021**, *12*, 14024–14032.
- [297] L. Tuscher, C. Helling, C. Wölper, W. Frank, A. S. Nizovtsev, S. Schulz, *Chem. Eur. J.* **2018**, *24*, 3241–3250.
- [298] G. Prabusankar, C. Gemel, P. Parameswaran, C. Flener, G. Frenking, R. A. Fischer, *Angew. Chem. Int. Ed.* **2009**, *48*, 5526–5529.
- [299] J. Krüger, C. Wölper, S. Schulz, *Inorg. Chem.* **2020**, *59*, 11142–11151.
- [300] A. M. Arif, A. H. Cowley, N. C. Norman, M. Pakulski, *Inorg. Chem.* **1986**, *25*, 4836–4840.
- [301] W. J. Evans, S. L. Gonzales, J. W. Ziller, *J. Am. Chem. Soc.* **1991**, *113*, 9880–9882.
- [302] J. J. Dunsford, E. R. Clark, M. J. Ingleson, *Angew. Chemie* **2015**, *127*, 5780–5784.
- [303] B. C. Boren, S. Narayan, L. K. Rasmussen, L. Zhang, H. Zhao, Z. Lin, G. Jia, V. V Fokin, *J. Am. Chem. Soc.* **2008**, *130*, 8923–8930.
- [304] C. S. Wei, C. A. Jiménez-Hoyos, M. F. Videa, J. F. Hartwig, M. B. Hall, *J. Am. Chem. Soc.* **2010**, *132*, 3078–3091.
- [305] C. F. Kins, D. Dudenko, D. Sebastiani, G. Brunklaus, *Macromolecules* **2010**, *43*, 7200–7211.
- [306] B. Eisenmann, J. Klein, *J. Less Common Met.* **1991**, *175*, 109–117.
- [307] M. Boyko, V. Hlukhyy, T. F. Fässler, *Z. Anorg. Allg. Chem.* **2020**, *646*, 659–664.
- [308] G. M. Sheldrick, *Acta Crystallogr. Sect. A* **2015**, *71*, 3–8.
- [309] G. M. Sheldrick, *Acta Crystallogr. Sect. C* **2015**, *71*, 3–8.
- [310] Diamond - Crystal and Molecular Structure Visualization, Crystal Impact - Dr. H. Putz &

Dr. K. Brandenburg GbR, Kreuzherrenstr. 102, 53227 Bonn, Germany,
<http://www.crystalimpact.com/diamond>.

- [311] A. L. Spek, *Acta Crystallogr. Sect. C* **2015**, *71*, 9–18.
- [312] TURBOMOLE V7.5.1 2021, a development of University of Karlsruhe and Forschungszentrum Karlsruhe GmbH, 1989–2007, TURBOMOLE GmbH, since 2007; available from <http://www.turbomole.com>.
- [313] K. Eichkorn, O. Treutler, H. Öhm, M. Häser, R. Ahlrichs, *Chem. Phys. Lett.* **1995**, *240*, 283–290.
- [314] K. Eichkorn, F. Weigend, O. Treutler, R. Ahlrichs, *Theor. Chem. Acc.* **1997**, *97*, 119–124.
- [315] J. Tao, J. P. Perdew, V. N. Staroverov, G. E. Scuseria, *Phys. Rev. Lett.* **2003**, *91*, 146401.
- [316] F. Weigend, R. Ahlrichs, *Phys. Chem. Chem. Phys.* **2005**, *7*, 3297–3305.
- [317] F. Weigend, A. Baldes, *J. Chem. Phys.* **2010**, *133*, 174102.
- [318] F. Weigend, *Phys. Chem. Chem. Phys.* **2006**, *8*, 1057–1065.
- [319] D. Andrae, U. Häußermann, M. Dolg, H. Stoll, H. Preuß, *Theor. Chim. Acta* **1990**, *77*, 123–141.
- [320] A. Klamt, G. Schüürmann, *J. Chem. Soc. Perkin Trans. 2*, **1993**, 799–805.
- [321] R. S. Mulliken, *J. Chem. Phys.* **1955**, *23*, 2338–2342.
- [322] A. E. Reed, R. B. Weinstock, F. Weinhold, *J. Chem. Phys.* **1985**, *83*, 735–746.
- [323] C. Ehrhardt, R. Ahlrichs, *Theor. Chim. Acta* **1985**, *68*, 231–245.
- [324] Chemcraft - graphical software for visualization of quantum chemistry computations. <https://www.chemcraftprog.com>.
- [325] TURBOMOLE V7.8 2023, a development of University of Karlsruhe and Forschungszentrum Karlsruhe GmbH, 1989–2007, TURBOMOLE GmbH, since 2007; available from <http://www.turbomole.org>.
- [326] A. D. Becke, *Phys. Rev. A* **1988**, *38*, 3098–3100.
- [327] J. P. Perdew, K. Burke, M. Ernzerhof, *Phys. Rev. Lett.* **1996**, *77*, 3865–3868.
- [328] K. A. Peterson, D. Figgen, M. Dolg, H. Stoll, *J. Chem. Phys.* **2007**, *126*, 124101.
- [329] J. L. Whitten, *J. Chem. Phys.* **1973**, *58*, 4496–4501.
- [330] E. Caldeweyher, J.-M. Mewes, S. Ehlert, S. Grimme, *Phys. Chem. Chem. Phys.* **2020**, *22*, 8499–8512.
- [331] R. Ahlrichs, M. Bär, M. Häser, H. Horn, C. Kölmel, *Chem. Phys. Lett.* **1989**, *162*, 165–169.
- [332] O. Treutler, R. Ahlrichs, *J. Chem. Phys.* **1995**, *102*, 346–354.

- [333] M. Sierka, A. Hogekamp, R. Ahlrichs, *J. Chem. Phys.* **2003**, *118*, 9136–9148.
- [334] A. Schäfer, H. Horn, R. Ahlrichs, *J. Chem. Phys.* **1992**, *97*, 2571–2577.
- [335] J. P. Perdew, *Phys. Rev. B* **1986**, *33*, 8822–8824.
- [336] F. Weigend, C. Schrod, R. Ahlrichs, *J. Chem. Phys.* **2004**, *121*, 10380–10384.
- [337] F. Weigend, C. Schrod, *Chem. Eur. J.* **2005**, *11*, 3559–3564.
- [338] C. Lee, W. Yang, R. G. Parr, *Phys. Rev. B* **1988**, *37*, 785–789.
- [339] J. P. Perdew, M. Ernzerhof, K. Burke, *J. Chem. Phys.* **1996**, *105*, 9982–9985.
- [340] J. P. Perdew, Y. Wang, *Phys. Rev. B* **1992**, *45*, 13244–13249.
- [341] K. Raghavachari, *Theor. Chem. Acc.* **2000**, *103*, 361–363.
- [342] V. N. Staroverov, G. E. Scuseria, J. Tao, J. P. Perdew, *J. Chem. Phys.* **2003**, *119*, 12129–12137.
- [343] P. Pollak, F. Weigend, *J. Chem. Theory Comput.* **2017**, *13*, 3696–3705.
- [344] D. Peng, N. Middendorf, F. Weigend, M. Reiher, *J. Chem. Phys.* **2013**, *138*, 184105.
- [345] TURBOMOLE V7.5 2020, a development of University of Karlsruhe and Forschungszentrum Karlsruhe GmbH, 1989–2007, TURBOMOLE GmbH, since 2007; available from <http://www.turbomole.com>.
- [346] S. G. Balasubramani, G. P. Chen, S. Coriani, M. Diedenhofen, M. S. Frank, Y. J. Franzke, F. Furche, R. Grotjahn, M. E. Harding, C. Hättig, A. Hellweg, B. Helmich-Paris, C. Holzer, U. Huniar, M. Kaupp, A. Marefat Khah, S. Karbalaei Khani, T. Müller, F. Mack, B. D. Nguyen, S. M. Parker, E. Perlt, D. Rappoport, K. Reiter, S. Roy, M. Rückert, G. Schmitz, M. Sierka, E. Tapavicza, D. P. Tew, C. van Wüllen, V. K. Voora, F. Weigend, A. Wodyński, J. M. Yu, *J. Chem. Phys.* **2020**, *152*, 184107.
- [347] D. Figgen, G. Rauhut, M. Dolg, H. Stoll, *Chem. Phys.* **2005**, *311*, 227–244.
- [348] B. Metz, H. Stoll, M. Dolg, *J. Chem. Phys.* **2000**, *113*, 2563–2569.

Publication List

1. Silke Wolf, Shangxin Wei, Wim Klopper, Stefanie Dehnen, Claus Feldmann,* *Inorg. Chem.* **2020**, 59, 12895–12902.
 2. Fuxing Pan,[‡] Shangxin Wei,[‡] Lukas Guggolz, Armin R. Eulenstein, Frank Tambornino, Stefanie Dehnen,* *J. Am. Chem. Soc.* **2021**, 143, 7176–7188.
 3. Shangxin Wei, Benjamin Peerless, Lukas Guggolz, Stefan Mitzinger, Stefanie Dehnen,* *Angew. Chem. Int. Ed.* **2023**, e202303037.
-

[‡] Both authors contributed equally.